Cosmological distances of type II supernovae from radiative transfer modeling

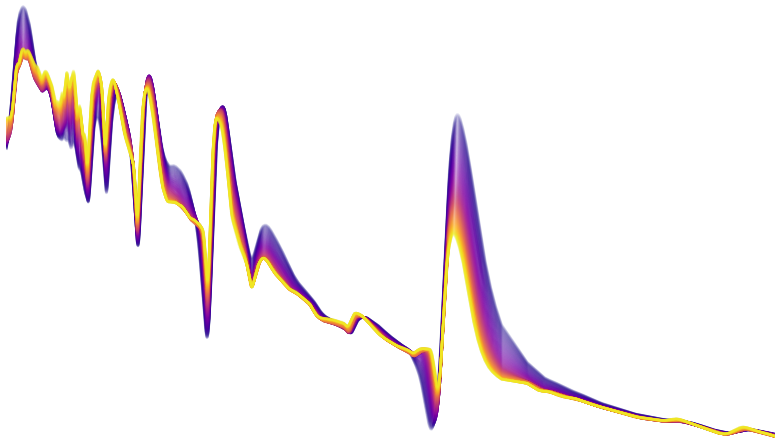

Dissertation

Christian Vogl

TECHNISCHE UNIVERSITÄT MÜNCHEN

MAX-PLANCK-INSTITUT FÜR ASTROPHYSIK

Cosmological distances of type II supernovae from radiative transfer modeling

Christian Vogl

Vollständiger Abdruck der von der Fakultät für Physik der Technischen Universität München zur Erlangung des akademischen Grades eines

Doktors der Naturwissenschaften (Dr. rer. nat.)

genehmigten Dissertation.

Vorsitzende(r): Prof. Dr. Stefan Schönert

Prüfer der Dissertation:

1. Hon.-Prof. Dr. Wolfgang Hillebrandt
2. Prof. Dr. Bruno Leibundgut

Die Dissertation wurde am 07.04.2020 bei der Technischen Universität München eingereicht und durch die Fakultät für Physik am 24.06.2020 angenommen.

Abstract

There is a great need for independent accurate determinations of the Hubble constant (H_0). We establish a new one-step method to measure H_0 based on radiative transfer modeling of type II supernovae. Our approach relies on luminosity estimates from the tailored-expanding-photosphere method. As a starting point, we create a new type II supernova radiative transfer code through substantial extensions of the Monte Carlo spectral synthesis code TARDIS. This allows us to calculate large grids of radiative transfer models fast but accurately. The model grids serve as training data for a machine learning emulator, which reproduces the output of our simulations with high precision ($\lesssim 1\,\%$) but $\sim 10^7$ times faster. This tremendous speedup makes it possible, for the first time, to fit type II supernova spectra in a reproducible manner through numerical optimization. We demonstrate the utility of the developed tools in a proof-of-principle H_0 measurement. In this first-ever application of the tailored-expanding-photosphere method in the Hubble flow, we find $H_0{=}72.3^{+2.9}_{-2.8}\,\mathrm{km\,s^{-1}\,Mpc^{-1}}$ in good agreement with state-of-the-art measurements. Currently, the small set of available observational data limits the accuracy. Our dedicated observing program will significantly improve this situation and pave the way towards a highly competitive H_0 determination in the near future.

Zusammenfassung

Der Bedarf an unabhängigen, genauen Bestimmungen der Hubble-Konstante (H_0) ist groß. Wir etablieren hier eine neue direkte Methode zur Messung von H_0 basierend auf Modellrechnungen zum Strahlungstransport in Typ-II-Supernovae. Unser Ansatz beruht auf einer Bestimmung der Supernova-Helligkeiten mithilfe von „maßgeschneiderten EPM“. Hierzu entwickeln wir einen neuen Typ-II-Supernova-Strahlungstransportcode durch umfassende Erweiterungen des existierenden Monte-Carlo-Codes TARDIS. Dies ermöglicht es uns, große Gitter von Strahlungstransportmodellen schnell und genau zu berechnen. Die Modellgitter dienen als Trainingsdaten für einen Emulator der auf Basis maschinellen Lernens die Ergebnisse unserer Simulationen mit hoher Präzision ($\lesssim 1\,\%$), aber $\sim 10^7$ mal schneller reproduziert. Diese enorme Zeitersparnis macht es erstmals möglich, Strahlungstransportmodelle von Typ-II-Supernovae für individuelle beobachtete Spektren numerisch zu optimieren. Anhand einer H_0-Messung demonstrieren wir, dass die neu entwickelte Methode funktioniert. Diese erste Anwendung der „maßgeschneiderten EPM“ auf Supernovae im Hubble-Fluss ergibt ein H_0 von $72.3^{+2.9}_{-2.8}\,\mathrm{km\,s^{-1}\,Mpc^{-1}}$, in guter Übereinstimmung mit anderen modernen Messungen. Derzeit begrenzt die geringe Menge an verfügbaren Beobachtungsdaten die Genauigkeit. Unser dediziertes Beobachtungsprogramm wird diese Situation maßgeblich verbessern und eine konkurrenzfähige Messung von H_0 ermöglichen.

Contents

List of Figures

List of Tables

Part I.

Introduction and methodology

1. The expanding Universe

The Universe is expanding: the distance between our Milky Way and faraway galaxies is increasing constantly with time. As photons propagate through this expanding cosmos, their wavelength is stretched alongside the space they are moving in; in observations of distant galaxies, the position of known atomic transitions is shifted to longer (redder) wavelengths. Figure 1.1 illustrates this effect in the Hubble Ultra Deep Field: as we observe longer wavelengths more and more distant galaxies start to appear. In the early twentieth century, the discovery of this cosmological redshift—and its approximately linear correlation with distance—provided the first conclusive proof that we are living in a dynamic, expanding cosmos. The local rate of this expansion—the Hubble constant (H_0)—follows from the observed redshift-distance relation; it is tightly connected to the scale and age of the Universe we are living in. The Hubble constant is a key parameter in our model of the Universe. A precise knowledge of H_0 is a prerequisite for constraining most cosmological parameters. From the discovery of cosmic expansion in 1927 until today, a quest for ever more accurate determinations of H_0 has been one of the most important driving forces for a better understanding of our Universe.

The goal of this thesis is to establish distance measurements of Type II supernovae (SNe II) based on radiative transfer modeling as an independent one-step method to measure H_0. We will set the stage for this endeavor with a short recap of the discovery of the expanding Universe and the first measurements of H_0 in Sect. 1.1. Section 1.2 then reviews the basics of cosmography. We present the current state of the extragalactic distance scale in Chapter 2. The current tension between late and early Universe measurements of H_0—a potential first crack in the ΛCDM concordance cosmological model—serves as the backdrop for this review. The tension highlights the need for complementary ways to determine H_0 independent of the cosmic distance ladder. In Chapter 3, we showcase radiative transfer modeling of SNe II as one of the most promising avenues towards this goal. We break this down into an introduction to SNe II in Sect. 3.1 and a presentation of the expanding photosphere method (EPM), which forms the basis for our distance measurements, in Sect. 3.2. The realization of the full potential of the EPM for cosmology requires new tools. Part II describes the development of a custom-built SN II radiative transfer code based on TARDIS (Kerzendorf & Sim, 2014; Kerzendorf et al., 2019) to facilitate rapid spectral modeling of observations. In Part III, we introduce an innovative machine-learning framework for automated fitting of SN spectra; this novel approach eases the distance determination from spectral fits substantially and allows, for the first time, the study of large SN samples. The developed tools put us in a prime position for an independent, high-precision measurement of

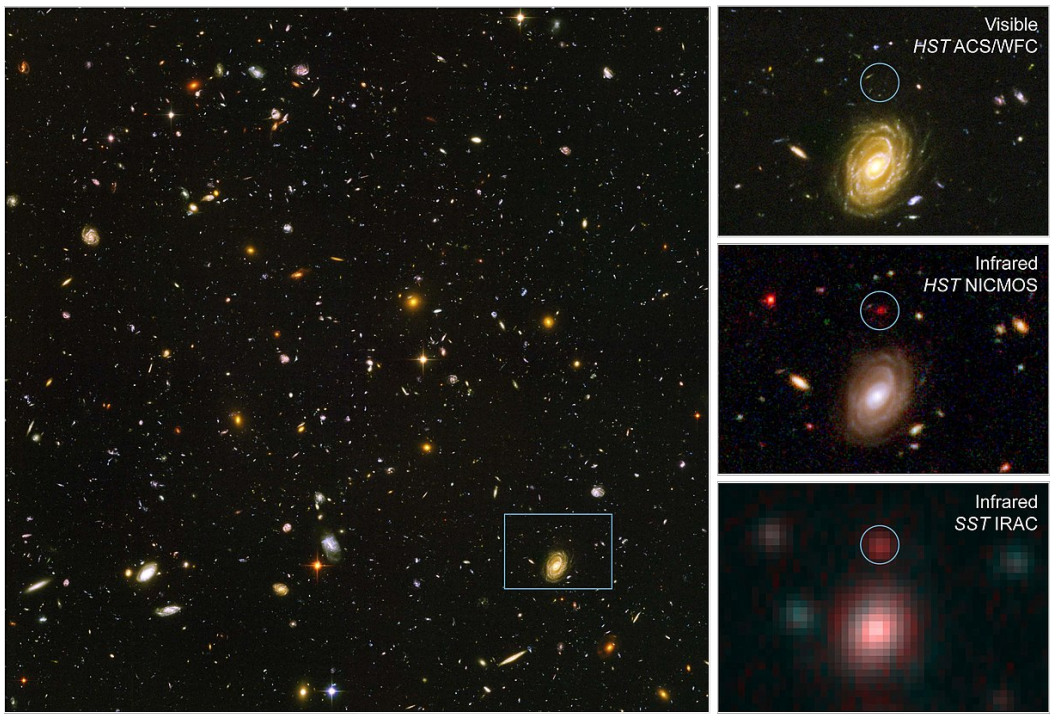

Figure 1.1.: A multi-wavelength view of the expanding Universe: the Hubble Ultra Deep Field. On its way toward us, the wavelength of light from distant galaxies is stretched alongside the fabric of space itself—a phenomenon known as the cosmological redshift. This behavior is illustrated in the close-ups on the right, which show the same region as observed in different wavelength bands. The wavelength increases from top to bottom. As we move from visible light to near-infrared, and finally mid-infrared, a galaxy starts to appear inside the circle: HUDF-JD2. In the course of the 13 billion years needed for this radiation to reach us, the Universe has multiplied in size and the wavelength of the emitted radiation along with it. Figure courtesy of NASA, ESA, and B. Mobasher (STScI/ESA).

H_0 as described in Part IV. Chapter 20 outlines our efforts to obtain the necessary observational data: the needed high-quality spectral time series for SNe II in the Hubble flow are not available from the literature. Finally, in Chapter 21, we conclude with a proof-of-principle measurement of H_0 based on a small SN sample. Having demonstrated that highly-competitive constraints on H_0 from radiative transfer modeling of SNe II are within close reach, we end with a summary and an outlook on the bright future of this method (Chapter 22).

1.1. History

The discovery of the expansion of the Universe in the early twentieth century required breakthroughs at the interface of theoretical physics and observational astronomy. Einstein laid the theoretical foundation for understanding a dynamical cosmos with his field equations of general

relativity in 1915 (Einstein, 1915)—the culmination of an endeavor that started years earlier (Einstein, 1908). Einstein himself, however, was not initially a proponent of a dynamical cosmos: after realizing that his theory predicted an initially stationary universe to collapse due to gravity, he introduced an additional repulsive term into his field equations—the cosmological constant (Einstein, 1917). The sole purpose of this constant was to counterbalance gravity and to guarantee that the Universe is static.[1] The possibility of dynamic cosmological models was first introduced by Friedmann (1922, 1924); this included expanding models of the Universe (but also, among others, oscillating ones). A generic prediction of any expanding cosmological model is that the redshift of faraway galaxies should increase with their distance (see, e.g, Peebles, 1993). The observational confirmation of this behavior in the late 1920s led to an abrupt paradigm shift in our understanding of the Universe—from static to expanding.

The groundbreaking discovery rested on two observational pillars: the accurate determination of the redshifts of galaxies and a reliable extragalactic distance scale. The first field of research was advanced mostly by the Lowell Observatory astronomer Vesto Slipher; in 1913, Slipher published the first measurement of the shift in the spectral lines of another galaxy: the Andromeda nebula (Slipher, 1913). Over the next years, Slipher continued to determine redshifts for many more galaxies (Slipher, 1913, 1915, 1917, 1921). By 1923, his dataset contained 41 objects—36 of these appeared to move away from us. This alone provided a compelling piece of evidence for the expansion of the Universe; Eddington calls the "great speed of the spiral nebulae" and the "great preponderance of velocities of recession from the solar system 'one of the most perplexing problems of cosmogony'" in his book "The Mathematical Theory of Relativity" (Eddington, 1923), which collects the radial velocity measurements. Eddington correctly placed the data in the context of the "Curvature of Space and Time"—but did not yet establish a connection to the cosmological redshift in an expanding Universe.

The other stepping stone to the discovery was the development of robust methods for measuring extragalactic distances. Here, the crucial breakthrough came through the work of Leavitt (1908) and Leavitt & Pickering (1912); they established a relation between the period and luminosity of Cepheids—the Leavitt law. Cepheids—variable, pulsating stars—are thousand times more luminous than the Sun. This put the nearest galaxies within reach with the observational equipment of the time. In 1923, Edwin Hubble identified the first Cepheid in another galaxy (Andromeda) using the world's largest telescope at the time—the 100-inch Hooker telescope (Hubble, 1925a). Many more Cepheids in Andromeda and other nearby galaxies followed over the next years (Hubble, 1925a,b; M33 and NGC 6822). The Cepheids themselves are not sufficiently bright to probe far enough into the cosmos to see the expansion—but they can be used to calibrate more far-reaching distance indicators; in Hubble's case, these were the brightest stars in a galaxy and the galaxies themselves. Both were assumed to always have approximately the same luminosity; the distance of such standard candles follows directly from their apparent brightness. In 1926, Hubble published

[1] In fact, not even the cosmological constant could save Einstein's notion of an unmoving Universe: as proven by Eddington (1930) only shortly after, Einsteins's static universe is unstable, that is to say, prone to expand or collapse at the slightest perturbation.

the apparent magnitudes of 42 galaxies along with a calibrated value for their mean absolute magnitude (Hubble, 1926)—in essence, their distances. These distances, in combination with Slipher's redshifts set the stage for the discovery of the expanding Universe.

Less than a year later, the Belgian astrophysicist Georges Lemaître combined the observational pieces of evidence for a relation between the redshift and distance of galaxies—and explained it in the context of the relativistic expansion of space (Lemaître, 1927). His theory is that of "A Homogeneous Universe of Constant Mass and Increasing Radius accounting for the Radial Velocity of Extra–Galactic Nebulae"[2], as expressed in the title of his seminal work. Lemaître calculated the first estimate for the rate of expansion—$680\,\mathrm{km\,s^{-1}\,Mpc^{-1}}$—from the mean radial velocity and mean distance of the galaxies in his observational data.[3] Lemaître's breakthrough went largely unnoticed for the next years; instead, the work of Edwin Hubble acted as the catalyst for the paradigm shift from a static to an expanding Universe. The key piece of evidence was Hubble's diagram of the radial velocities of galaxies as a function of their distance (Hubble, 1929);[4] the graph, reproduced in Fig. 1.2, revealed an approximately linear correlation between redshift and distance. Hubble & Humason (1931) put the final doubts about the redshift-distance relation to rest: they demonstrated its validity out to the Leo cluster at a recession velocity of $19\,600\,\mathrm{km\,s^{-1}}$—roughly twenty times farther than their previous analysis. For the next decades, Hubble was largely credited as the discoverer of the expanding Universe: the redshift-distance relation was named Hubble's law and its proportionality constant—the expansion rate of the Universe—the Hubble constant. Recent years have witnessed increased efforts to set the historical omission of Lemaître's contribution straight: in a landmark decision, the International Astronomical Union (IAU) has voted to rename the Hubble law to Hubble-Lemaître law.[5]

Whereas the work of Hubble (1929) and Hubble & Humason (1931) largely settled the debate on whether the Universe is static or expanding, the rate of this expansion remained controversial. In 1931, observational cosmology had a long way to go: the Hubble constant of $558\,\mathrm{km\,s^{-1}\,Mpc^{-1}}$, confidently reported by Hubble & Humason (1931) with an estimated error of less than 10%, is roughly ten times larger than the currently favored value. The first doubts about Hubble's distance scale were put forward a year later by the Dutch astronomer Jan Hendrik Oort: Oort (1932) criticized that, if Hubble is to be believed, the Milky Way must be considerably larger than any other nearby galaxy (except for Andromeda). He published a revised value for H_0 that was only half as big as Hubble's. It took more than two decades for the faults in Hubble's distance scale to be finally corrected. Baade (1954) fixed the first mistake—the mixing of two types of Cepheids with different period-luminosity relations. Sandage (1958) resolved the second problem: in many cases, Hubble mistook H II regions for the brightest stars in a galaxy; by using the wrong standard candles, he consistently underestimated their distance. Together, these

[2] Translated from French.

[3] Redshifts from Stromberg (1925; largely based on the work of Slipher) and distances from Hubble (1926).

[4] The idea to plot redshift versus distance, however, is not original to Hubble: similar diagrams can be found in Lundmark (1924) and Stromberg (1925). Both studies knowingly include globular clusters in addition to galaxies; the correlation between redshift and distance is weak.

[5] https://www.iau.org/news/pressreleases/detail/iau1812/

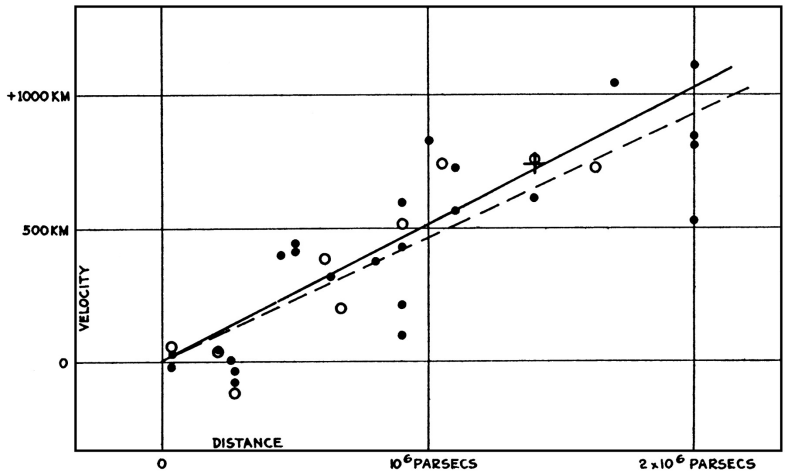

Figure 1.2.: The original Hubble diagram. Radial velocities of galaxies (in units of km/s) as a function of their distance; the diagram extends out to the Virgo cluster. Filled circles indicate measurements for 24 individual galaxies; open circles represent a clustering of the same data in velocity and distance. The cross marks the mean distance and recession velocity of 22 galaxies for which individual measurements were not feasible. The data shows an approximately linear increase of the radial velocities with distance—indicative of an expanding Universe. Fits to the unclustered (solid line) and clustered (dashed line) data yield on the order of $500\,\mathrm{km\,s^{-1}\,Mpc^{-1}}$ for the rate of the expansion—roughly ten times larger than the currently favored value. The figure, a reproduction of the original from Hubble (1929), is from Kirshner (2004).

changes pushed the Hubble constant down to $75\,\mathrm{km\,s^{-1}\,Mpc^{-1}}$—very close to the currently favored value. The uncertainties, however, were still considerable: Sandage (1958) estimated that their result is accurate to $25\,\mathrm{km\,s^{-1}\,Mpc^{-1}}$. As astronomers strove for higher precision over the next decades, measurements continued to show significant scatter, covering roughly a range from $50\,\mathrm{km\,s^{-1}\,Mpc^{-1}}$ to $100\,\mathrm{km\,s^{-1}\,Mpc^{-1}}$. In the quest for a more reliable extragalactic distance scale, the Hubble Space Telescope (HST), launched in 1990, played a central role; the determination of the Hubble constant with an accuracy of 10% was one of its three key projects (e.g., Freedman et al., 1994). The hope put in the new technology was high: as stated by Marc Aaronson—one of the initiators of the program—"The distance scale path has been a long and tortuous one, but with the imminent launch of HST there seems good reason to believe that the end is finally in sight." The high resolving power of the space telescope extended the range for the Cepheid distance scale by a factor of ten; this, in turn, allowed a more robust calibration of secondary distance indicators such as surface brightness fluctuations (SBF), the Tully–Fisher relation (TFR), or Type Ia supernovae (SNe Ia). All of these methods had only a handful or, in the worst cases, no Cepheid calibrators before the start of HST. The final results of the Key project are published in 2001—marking the successful end of a multi-decade and 30 paper strong effort. The Hubble constant as inferred from a weighted average of the different secondary distance indicators was $72 \pm 8\,\mathrm{km\,s^{-1}\,Mpc^{-1}}$ (Freedman et al., 2001). Figure 1.3 illustrates the long and

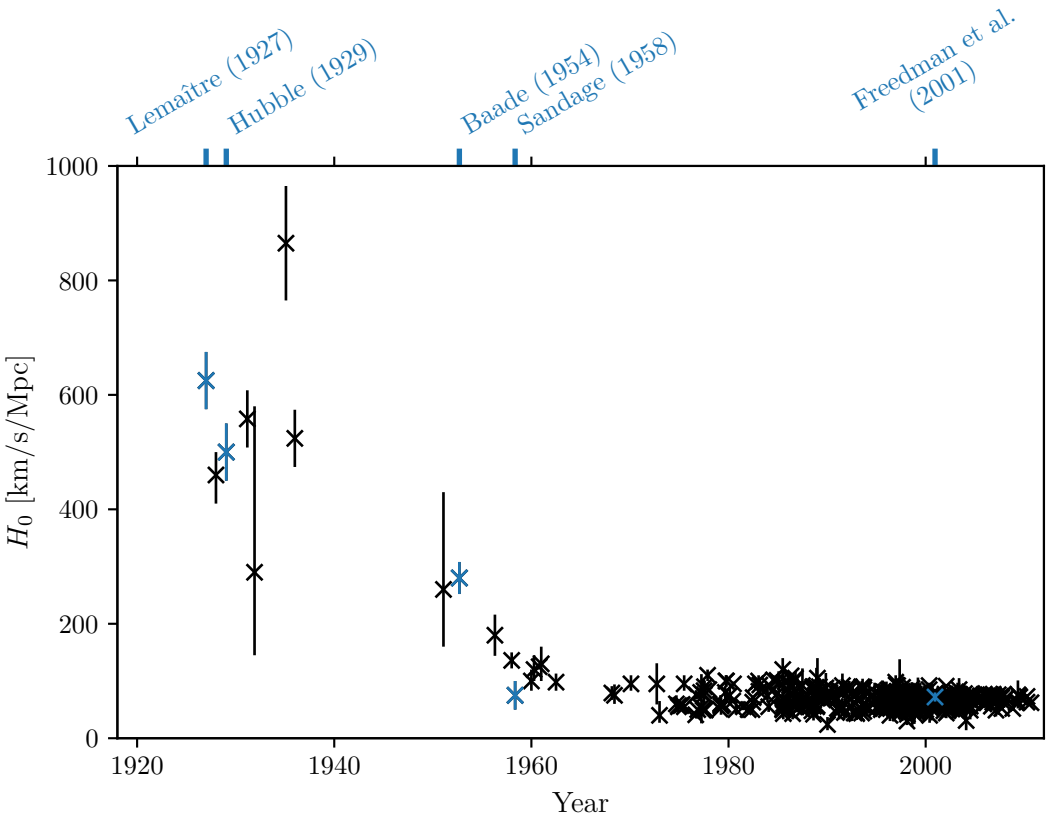

Figure 1.3.: Published measurements of the Hubble constant H_0 from 1927 to 2010. We have highlighted some works of historical importance in color: Lemaître (1927)—the first published value of H_0, Hubble (1929)—the first use of a Hubble diagram (see, Fig. 1.2), and Freedman et al. (2001)—the final results of the HST H_0 Key Project. The data in this plot has been assembled by John Huchra as part of the NASA/HST Key Project on the Extragalactic Distance Scale.[6]

stony path from Hubble's initial efforts to the Key project: the figure provides a comprehensive history of H_0 measurements.

1.2. Basics of cosmography

Cosmography (from the Greek kosmos "world" and -graphia "description of") is the science of measuring the Universe. In this quick review, we will focus mainly on the different ways to measure distances in an expanding cosmos and how these distances connect to the underlying properties of the Universe—its geometry, energy content and so forth. For a more complete presentation of

[6] https://www.cfa.harvard.edu/~dfabricant/huchra/hubble.plot.dat

common cosmographic parameters, we refer the reader to the concise summary of Hogg (1999), or for a more rigorous description to the textbooks of Peebles (1993) and Dodelson (2003).

The Universe, as viewed from Earth, is isotropic on large scales as evidenced by the distribution of galaxies and the cosmic microwave background (CMB). This observation, combined with the assumption that our place in the Universe is not special, yields the cosmological principle—one of the cornerstones of cosmology. The cosmological principle states that the Universe is, on average, homogeneous and isotropic;[7] homogeneity follows directly from isotropy given that isotropy is assumed to apply for all observers. The cosmological principle strongly restricts the possibilities for the evolution of the Universe: the dynamics of spacetime can be described by a single time-dependent scalar quantity—the scale factor $a(t)$; it describes how the proper distance l between two objects changes with time t due to the expansion or contraction of the Universe:

$$l = l_0 \cdot a(t). \tag{1.1}$$

Proper distance, simply put, is the separation between objects as measured by a ruler for a given cosmological time. The change is measured relative to the current proper distance l_0—the so-called comoving distance; by definition, the scale factor at the current time is equal to one: $a(t_0) \equiv 1$. Figure 1.4 illustrates the relation between scale factor, proper- and comoving distance for three galaxies in the Hubble flow: the galaxies are comoving with the cosmic expansion and their distance changes solely due to the expansion of the Universe.

1.2.1. Cosmological redshift

A fundamental observational consequence of the expansion of the Universe is the cosmological redshift of radiation: photons emitted by a faraway object are observed at longer (redder) wavelengths than they have been originally emitted. This is particularly apparent for light that is emitted (or absorbed) in well-known atomic transitions, for example, the Lyα line of star-forming galaxies. Figure 1.5 illustrates how the typical emission and absorption lines of galaxies change in wavelength as we look further and further into the Universe. To understand this effect, we follow the path of light from emission to detection. The propagation of the photons through spacetime is described by the Friedmann–Lemaître–Robertson–Walker (FLRW) metric (e.g., Peacock, 1999);[8] the spacetime interval along the trajectory is given by

$$ds^2 = (c\,dt)^2 - a^2(t)\left(\frac{dr^2}{1-kr^2}\right).^{9} \tag{1.2}$$

[7] The potential existence of very large structures in the Universe, such as the Huge Large Quasar Group (Clowes et al., 2013) or the Giant GRB Ring (Balázs et al., 2015), with dimensions of the order of a Gpc, challenges the notion of an isotropic and homogeneous Universe.

[8] Given that the cosmological principle holds.

[9] For a suitable choice of coordinates ($\theta = \Phi = 0$)

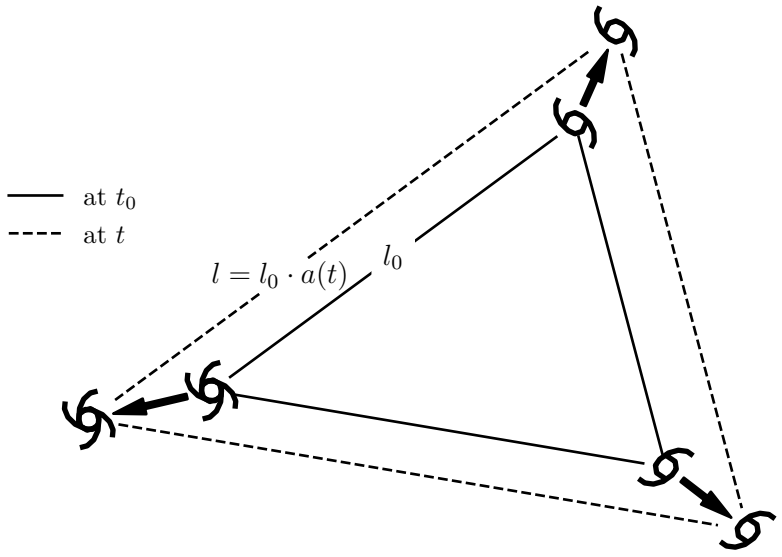

Figure 1.4.: Cosmic expansion illustrated. Figure adapted from Peebles (1993).

Here, r is a radial comoving coordinate, dt is a time interval, c is the speed of light, and $a(t)$ is the aforementioned scale factor. The constant k determines the curvature of the Universe. The wavelength of light is directly proportional to the time interval Δt between successive crests of the electromagnetic wave ($\lambda = c\Delta t$); if we trace the change of this interval between emission and detection, we know the change in wavelength. Let us assume that the first crest was emitted at time t_e and observed at time t_0. As in Minkowski space ($c\,dt - d\mathbf{x}^2 = 0$), the spacetime element ds^2 vanishes for light-like trajectories and Eq. (1.2) yields

$$\int_{t_\mathrm{e}}^{t_0} \frac{dt}{a(t)} = \frac{1}{c}\int_0^r \frac{dr}{\sqrt{1-kr^2}} \tag{1.3}$$

for the first crest. Similarly, for the second crest, which was emitted at $t_\mathrm{e} + \Delta t_\mathrm{e}$ and observed at $t_0 + \Delta t_0$ we obtain

$$\int_{t_\mathrm{e}+\Delta t_\mathrm{e}}^{t_0+\Delta t_0} \frac{dt}{a(t)} = \int_{t_\mathrm{e}}^{t_0} \frac{dt}{a(t)} + \int_{t_0}^{t_0+\Delta t_0} \frac{dt}{a(t)} - \int_{t_e}^{t_e+\Delta t_e} \frac{dt}{a(t)} = \frac{1}{c}\int_0^r \frac{dr}{\sqrt{1-kr^2}}. \tag{1.4}$$

Subtracting the two equations yields

$$\int_{t_0}^{t_0+\Delta t_0} \frac{dt}{a(t)} = \int_{t_e}^{t_e+\Delta t_e} \frac{dt}{a(t)}. \tag{1.5}$$

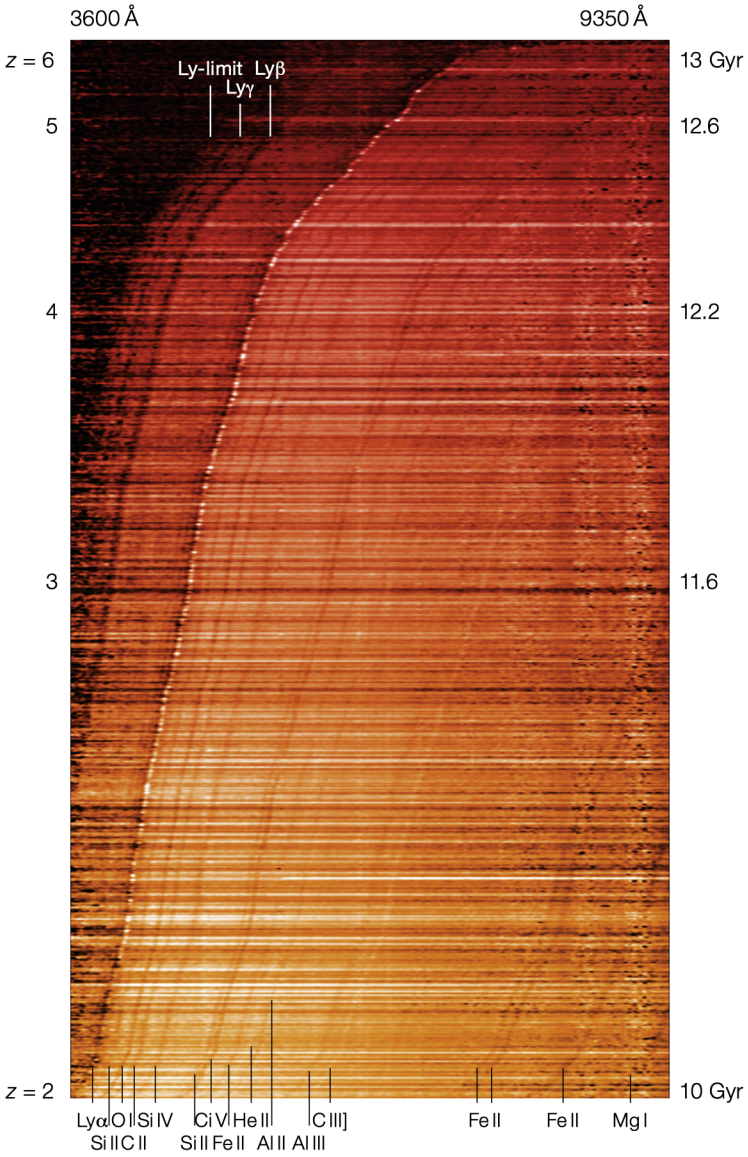

Figure 1.5.: Cosmological redshift of galaxy lines [from Le Fèvre et al. (2014)]. The figure shows spectra of ∼ 6000 galaxies from the VIMOS Ultra Deep Survey: the spectra are sorted by redshift—increasing from bottom to top—and their scaled flux is color-coded. Each spectrum shows localized suppressions and amplifications of the flux that arise from absorption or emission of radiation in specific atomic line transitions; one example is the Lyα transition that connects the ground state and the first excited level of neutral hydrogen H I. Other prominent features are indicated by their absorbing/emitting ion. The observed wavelengths of the transitions are shifted compared to their rest wavelengths due to the expansion of space itself; the shift is proportional to the change in size of the Universe between the time of emission of the photons and today—the longer the photon travels the more redshifted its wavelength. For example, a Lyα photon that has been emitted with a wavelength of 1215.67 Å (e.g., Kramida et al., 2019) 10 Gyr ago, is detected at ∼ 3600 Å today ($z \approx 2$).

The time interval for integration is much smaller than the time scale for changes in the scale factor;[10] we can safely assume that the scale factors are constant. From this, we obtain

$$\frac{\Delta t_0}{a(t_0)} = \frac{\Delta t_\mathrm{e}}{a(t_\mathrm{e})}. \tag{1.6}$$

Thus, the ratio between emitted λ_e and observed λ_o wavelength

$$\frac{\lambda_\mathrm{o}}{\lambda_\mathrm{e}} = \frac{a(t_0)}{a(t_\mathrm{e})} \tag{1.7}$$

is equal to the change in the size of the Universe—the wavelength is stretched similar to space itself. In terms of the redshift

$$z \equiv \frac{\lambda_\mathrm{o}}{\lambda_\mathrm{e}} - 1, \tag{1.8}$$

this translates to

$$1 + z = \frac{a(t_0)}{a(t_\mathrm{e})}. \tag{1.9}$$

The redshift is commonly expressed in terms of the recession velocity v that would produce a special relativistic Doppler shift of the same size:

$$z = \sqrt{\frac{1 + v/c}{1 - v/c}} - 1 \approx \frac{v}{c}. \tag{1.10}$$

It is often stated that it is wrong to view the cosmological redshift as resulting from radial velocities instead of the stretching of space (e.g., Harrison, 2000). Nevertheless, many people argue in favor of an interpretation as a Doppler shift[11] (Bunn & Hogg, 2009), or a combination of a Doppler- and a gravitational redshift Bondi (1947); Peacock (2008); Chodorowski (2011).

In practice, every redshift has an unambiguous kinematic component: all objects show peculiar motions due to local gravitational fields.[12] The observed redshift z is then given by

$$1 + z = (1 + \bar{z})(1 + z_\mathrm{p}), \tag{1.11}$$

where $\bar{z}$ is the normal cosmological redshift and z_p is the special relativistic redshift for the peculiar velocity v_p [see Eq. (1.10)]. We illustrate this in Fig. 1.6 using two galaxies that are receding from each other. For low peculiar velocities and low redshifts, Eq. (1.11) simplifies to

$$z \approx \bar{z} + z_\mathrm{p}. \tag{1.12}$$

[10] For optical light with a wavelength of 650 nm the time between two successive wave crests Δt_0 is approximately 10^{-15} s, whereas the current cosmological time scale is on the order of billions of years (10^{17} s).

[11] More accurately, infinitely many infinitesimal Doppler shifts.

[12] For example, the Local Group of galaxies moves at a velocity of approximately 600 km s^{-1} compared to the rest frame defined by the CMB (e.g., Tully et al., 2014).

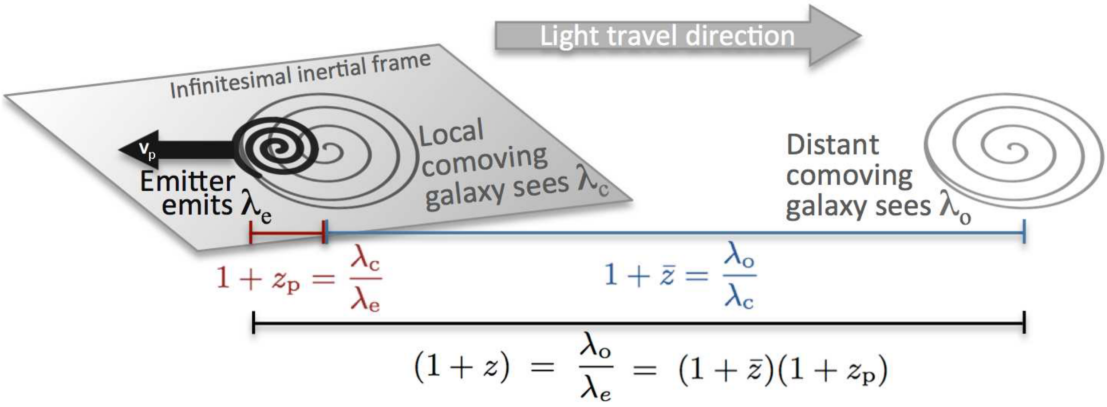

Figure 1.6.: Impact of peculiar velocities on the observed redshift [from Davis & Scrimgeour (2014)]. A photon is emitted at wavelength λ_e from a galaxy that has a peculiar velocity component v_p in the direction opposite to the emission. Later, an observer in a distant comoving galaxy detects the photon at wavelength λ_o—and thus redshift $z = \lambda_o/\lambda_e - 1$. The measured z is a combination of a special relativistic and a cosmological redshift. First, the wavelength of the emitted light is transformed from the inertial frame of the emitter (λ_e) to a local comoving frame (λ_c) according to the laws of special relativity: $1 + z_p = \lambda_c/\lambda_e$, where $z_p \approx v_p/c$ [see, Eq. (1.10)]. Second, the photon suffers the normal cosmological redshift between the local comoving frame and the distant comoving galaxy: $1 + \bar{z} = \lambda_o/\lambda_c$. In combination, this yields the observed redshift: $1 + z = \lambda_o/\lambda_e = (\lambda_o/\lambda_c)(\lambda_c/\lambda_e) = (1 + \bar{z})(1 + z_p)$.

Thus, a typical peculiar velocity on the order of $300\,\mathrm{km\,s^{-1}}$ to $400\,\mathrm{km\,s^{-1}}$ (e.g., Léget et al., 2018) contributes an additional redshift of ± 0.001 to the observation. In galaxy clusters, where the gravitational fields are particularly large, the peculiar velocities can even exceed $1000\,\mathrm{km\,s^{-1}}$, leading to a correction of around ± 0.003 (see, e.g., Ruel et al., 2014; Léget et al., 2018).

1.2.2. Cosmological time dilation

The cosmological redshift results from the change of the time interval between successive crests of electromagnetic waves between emission and detection. This physical effect—cosmological time dilation—is not specific to radiation but applies to all observable time intervals. Equation (1.6) tells us that the duration of an event Δt_0 as measured on Earth is longer than the original time span Δt_e at the redshift z where the event occurred:

$$\frac{\Delta t_0}{\Delta t_\mathrm{e}} = 1 + z. \tag{1.13}$$

One exemplary consequence is that the light curves of SNe Ia appear broader for higher redshifts (e.g., Leibundgut et al., 1996; Goldhaber et al., 1997).

1.2.3. Hubble-Lemaître law

The linear correlation between redshift and distance of faraway objects —the Hubble-Lemaître law—provides one of the most compelling pieces of evidence for the expansion of the Universe; to date, accurate measurements of this relation are crucial to our understanding of cosmology. The Hubble-Lemaître law is a direct consequence of the proportionality between the cosmological redshift and the change in the size of the Universe [Eq. (1.9)].

Let us define the Hubble parameter $H(t)$ as the logarithmic derivative of the scale factor $a(t)$ with respect to cosmic time t:

$$H(t) = \frac{\dot{a}(t)}{a(t)}. \tag{1.14}$$

The Hubble parameter is thus a measure of the relative rate of expansion of the Universe; it has dimensions of inverse time but it is commonly specified in units of $\mathrm{km\,s^{-1}\,Mpc^{-1}}$ (due to its alternative interpretation as a proportionality constant between radial velocity and distance). In the calculation of the cosmological redshift, we can use the current Hubble parameter $H(t_0)$ to approximate the scale factor $a(t_\mathrm{e})$ at the time of emission by its first order Taylor expansion $a(t_e) \approx a(t_0)(1 + (t_\mathrm{e} - t_0)H(t_0))$. In the limit of small distances, the cosmological redshift is then given by[13]

$$z = \frac{a(t_0)}{a(t_\mathrm{e})} - 1 \approx \frac{1}{1 + (t_\mathrm{e} - t_0)H(t_0)} - 1 \approx (t_0 - t_\mathrm{e})H(t_0). \tag{1.15}$$

[13] With the additional approximation that $(1 - x)^{-1} \approx x$ for small x, where x is $(t_0 - t_\mathrm{e})H(t_0)$.

By replacing the time interval $(t_0 - t_e)$ with the corresponding distance $D = c(t_0 - t_e)$,[14] we obtain the Hubble-Lemaître law:

$$cz = H(t_0)D \tag{1.16}$$

or in terms of the recession velocity v

$$v = H(t_0)D. \tag{1.17}$$

For observed objects, peculiar velocities lead to deviations of the measured redshift from a strict Hubble-Lemaître law.

1.2.4. Hubble constant and related parameters

The current Hubble parameter $H(t_0)$ is commonly called the Hubble constant and is abbreviated H_0. Often, H_0 is parametrized in terms of a dimensionless parameter h—the scaled Hubble constant:

$$H_0 = 100\,h\,\mathrm{km\,s^{-1}\,Mpc^{-1}}. \tag{1.18}$$

As far as we know, h is around 0.7 (Riess et al., 2019; e.g.,). The Hubble constant is connected tightly to the age and size of the Universe. The Hubble time

$$t_\mathrm{H} \equiv \frac{1}{H_0} = \frac{9.78 \times 10^9\,\mathrm{yr}}{h} \tag{1.19}$$

and the Hubble distance

$$D_\mathrm{H} \equiv \frac{c}{H_0} = \frac{3000\,\mathrm{Mpc}}{h} \tag{1.20}$$

provide convenient units for these quantities. The Hubble time is equal to the age of the Universe if the expansion rate is constant throughout cosmic time; the latter is only strictly realized for an empty universe, where there are no forces to decelerate or accelerate the expansion.

1.2.5. Distance measures

In addition to the proper distance, which we introduced earlier, there are many more ways to specify distances in the expanding Universe. The two most important for cosmography are the angular diameter distance and the luminosity distance; the two relate to directly measurable quantities: angular sizes and observed fluxes.

Their definitions are the same as in non-expanding space: we estimate the distance to a faraway galaxy of know size in the same way as for a church tower in the neighbouring village. The angular

[14] Strictly speaking, D is the so-called light-travel distance—one of the many ways to specify distances in cosmology. However, the differences between the various distance measures vanishes in the low-redshift limit.

diameter distance D_A of a terrestrial or extraterrestrial object of size x with angular diameter θ is

$$D_\mathrm{A} \equiv \frac{x}{\theta}. \tag{1.21}$$

Objects of know size—so-called standard rulers—can thus be used to map our Universe. An important example in cosmology is Baryon acoustic oscillations (BAO): these density waves in the primordial plasma have left imprints of a characteristic scale on the distribution of baryonic matter [which can be measured, for example, through galaxy clustering (Eisenstein et al., 2005; Cole et al., 2005)].

We can use not only objects of known size as distance indicators but also objects of known bolometric luminosity L. The distance to such standard candles is called the luminosity distance and is calculated from the total (frequency integrated) flux F as follows:

$$D_\mathrm{L} \equiv \sqrt{\frac{L}{4\pi F}}. \tag{1.22}$$

Standard candles are ubiquitous in cosmography: famous examples are Cepheid variable stars and SNe Ia.

Luminosity and angular diameter distance are only identical in the local Universe: at higher redshifts, we have to use Etherington's distance-duality equation (Etherington, 1933)

$$D_\mathrm{L} = (1+z)^2 D_\mathrm{A} \tag{1.23}$$

to convert between the two. Similarly, the linear relation between redshift and distance—the Hubble-Lemaître law—only holds for small redshifts; for faraway objects, both distance measures are sensitive to the cosmic expansion history (and, in turn, the energy content of the Universe). To illustrate, we expand the luminosity distance to second order in redshift:

$$D_\mathrm{L} = \frac{cz}{H_0}\left(1 + \frac{1}{2}[1-q_0]z + O(z^2)\right). \tag{1.24}$$

The newly defined deceleration parameter

$$q_0 \equiv -\frac{\ddot{a}_0 a_0}{\dot{a}_0^2} \tag{1.25}$$

depends on the matter and dark energy density in the Universe via

$$q_0 = \Omega_\mathrm{M}/2 - \Omega_\Lambda \tag{1.26}$$

(see, e.g., Peebles, 1993; Eq. 13.7).[15] Here, Ω_M and Ω_Λ are the dimensionless density parameters for matter and dark energy as defined for instance by Hogg (1999; Eq. 5, 6 & 7). To the best of

[15] As long as the radiation energy density is negligible and dark energy is a cosmological constant.

our knowledge, $\Omega_\mathrm{M} \approx 0.3$ and $\Omega_\Lambda \approx 0.7$ (e.g., Planck Collaboration et al., 2018); thus the current deceleration parameter is $q_0 \approx -0.55$. This implies that even for a moderate redshift of 0.05 the deviation from a strict Hubble expansion is already on the order of 5 %. This is an important effect for the observational determination of the Hubble constant, where typically objects in a redshift range between 0.01 and 0.15 are used (e.g., Riess et al., 2019).

The definition of the luminosity distance in Eq. (1.22) in terms of bolometric luminosity and total flux is particularly simple but of limited practical use: observations hardly ever have sufficient wavelength coverage to allow a reliable reconstruction of the total flux. Usually, we have information about the differential flux F_λ in a limited wavelength window through spectra or broadband photometry. In this context, the cosmological redshift becomes relevant again: the observed flux F_λ at wavelength λ is connected to the emitted luminosity $L_{\lambda/(1+z)}$ at wavelength $\lambda/(1+z)$. The redshift also affects the width of the wavelength intervals between emission and detection: the interval in which the radiation is detected is broader than the one it has been emitted in by a factor $1+z$. In combination, this yields

$$F_\lambda = \frac{1}{1+z} \frac{L_{\lambda/(1+z)}}{4\pi D_\mathrm{L}^2}.^{16} \tag{1.27}$$

We can recover the relation that is valid in non-expanding space by deredshifting the observed flux and multiplying it by $1+z$. For magnitudes this procedure is called a K correction (Humason et al., 1956; Oke & Sandage, 1968).[17]

[16] This can be easily verified by integrating both sides over the observed wavelength, which, through a change of variables on the right-hand side, recovers Eq. (1.22).

[17] Detailed derivations of the K correction equations are given by Hogg et al. (2002).

2. The cosmic distance scale and the Hubble tension

There is an ongoing tension between determinations of H_0 from late and early Universe probes. The most notable discrepancy is found between the local distance ladder of the SH0ES project, built from Cepheids and SNe Ia, and the constraints from CMB anisotropies from the Planck Collaboration et al. (2018). Their determinations of H_0, which currently constitute the most accurate late and early Universe measurements, are in a 4.4σ tension: the local H_0 found by SH0ES of $74.03 \pm 1.42\,\mathrm{km\,s^{-1}\,Mpc^{-1}}$ (Riess et al., 2019) lies significantly above the CMB-based estimate of $67.36 \pm 0.54\,\mathrm{km\,s^{-1}\,Mpc^{-1}}$ from the Planck Collaboration et al. (2018). Figure 2.1 illustrates the steady increase in the discrepancy over the last ten years as measurements at both ends of cosmic time became ever more accurate.

When this tension first emerged in 2013, following a downward correction in the CMB-based estimate between WMAP (Hinshaw et al., 2013) and *Planck* (Planck Collaboration et al., 2014a,b), it ushered in the end of a decade of concordance cosmology. In the preceding years, the flat-ΛCDM model, that is to say, a spatially-flat Universe comprised of baryonic matter, cold dark matter, and dark energy described by a cosmological constant, did an outstanding job at explaining all cosmological observations: with only six free parameters, ΛCDM simultaneously described as diverse probes as the temperature and polarization anisotropies of the CMB, Big Bang nucleosynthesis (BBN), or the formation of large-scale structure. To this day, flat-ΛCDM remains an extremely successful cosmological model, but if the Hubble tension is taken at face value it cannot be the complete model of our Universe.

The CMB at a redshift of a thousand cannot, on its own, constrain H_0—the expansion rate of the Universe at redshift zero: a cosmological model must be assumed to bridge the roughly 13 billion years of cosmological evolution. If the extrapolation from $z \approx 1000$ to $z = 0$ fails, as indicated by the Hubble tension, something might be missing from the adopted cosmological model. There are myriad suggestions for the missing ingredient in the literature including modifications to neutrino physics (Kreisch et al., 2019), time-dependent dark energy (Poulin et al., 2019), non-Gaussianity of the primordial fluctuations (Adhikari & Huterer, 2019), and many more (e.g., Mörtsell & Dhawan, 2018; Di Valentino et al., 2018; Poulin et al., 2019). However, systematic or underestimated errors in either of the analyses might explain the discrepant results just as well. One example would

be a bias in the distance ladder measurement caused by correlations of SN Ia luminosities with environmental and host galaxy properties (e.g., Rigault et al., 2015).[1]

The tension is not limited to the SN Ia distance ladder and CMB anisotropy measurements. Alternative methods paint a similar picture: late Universe probes, including variations of the distance ladder (e.g., Dhawan et al., 2018; Huang et al., 2020), time-delay lensing (Wong et al., 2019), and water masers (Pesce et al., 2020) tend to find high values for H_0. An exception is the Carnegie-Chicago Hubble Program (CCHP; Beaton et al., 2016), which obtains a value intermediate to the local probes and the *Planck* result based on a Tip of the Red Giant Branch (TRGB) calibration of SN Ia distances (Freedman et al., 2019). The low H_0 from the Planck Collaboration et al. (2018), on the other hand, is corroborated through various BAO-based measurements (e.g., Aubourg et al., 2015; Abbott et al., 2018; Addison et al., 2018; Macaulay et al., 2019).[2] The agreement with *Planck* persists even if the sound horizon scale is calibrated independently of CMB anisotropy data (e.g., Abbott et al., 2018; Addison et al., 2018), for example through BAO measurements at significantly different redshifts combined with BBN constraints (Addison et al., 2018).

The Hubble tension with its potentially profound implications calls for additional rigorous checks on both early and late Universe determinations of H_0. One option is high-precision measurements of the local H_0 through independent methods. This is essential to rule out systematics in any individual probe. Our goal in this thesis is to establish competitive distance determinations based on radiative transfer modeling of SNe II. To put this into context, the next chapter reviews three of the most important independent avenues towards local measurements of H_0: the distance ladder, water megamasers, and time-delay lensing. We highlight the strengths and weaknesses of each method to motivate the need for complementary techniques.

The CMB probes physics at vastly different scales and is subject to completely different uncertainties than local measurements. A treatment that does justice to this vast topic is beyond the scope of this thesis. We refer the reader to Hu & Dodelson (2002), Samtleben et al. (2007), and Staggs et al. (2018) for an in-depth discussion.

2.1. Distance ladder

The distance ladder is the most well-established method to measure extragalactic distances: the idea to calibrate a succession of further and further reaching relative distance indicators starting from absolute distances has been used since the earliest attempts to map the Universe (e.g., Hubble, 1926; Hubble & Humason, 1931). The approach was foundational for the development of a reliable cosmic distance scale (e.g., Freedman et al., 2001). To date, the distance ladder provides the most accurate way to measure extragalactic distances—and thus H_0 (e.g., Riess

[1] However, most recent studies (e.g., Jones et al., 2018; Rose et al., 2019) conclude that this bias is not significant enough to alleviate the current Hubble tension.

[2] BAO distances depend on the sound horizon scale at the time of recombination and are therefore early rather than late Universe probes (even though the BAO signal is measured at redshifts of order one or less).

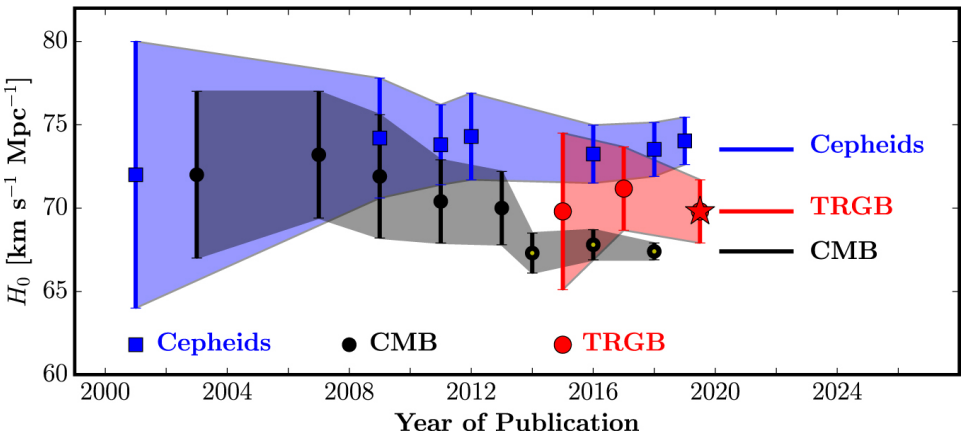

Figure 2.1.: Development of the Hubble tension [from Freedman et al. (2019)]. The figure shows how the estimates of H_0 from local Cepheid-based distance ladders (blue) and the CMB (red) have evolved over time. At the beginning of the millennium, local (HST Key project) and CMB (WMAP) constraints were in perfect agreement. In 2013, the first *Planck* data release put an abrupt end to this consensus. The next years were marked by an ever-increasing tension, as the uncertainties of both the local and the CMB measurements decreased. In 2019, the discrepancy between H_0 as determined by the Planck Collaboration et al. (2018) and SH0ES has reached a significance of 4.4σ. Complementary results from a TRGB-based distance ladder, which are in better agreement with the CMB, are shown in red.

et al., 2019). There are a myriad of ways to combine different distance indicators to reach the Hubble flow. We will focus on one of the currently most competitive avenues: the calibration of SNe Ia through Cepheids as realized by the SH0ES project (Riess et al., 2019). Freedman & Madore (2010) provide a comprehensive review of other commonly used techniques such as the TRGB, surface brightness fluctuations (SBF), or the Tully–Fisher relation (TFR).

First rung: geometric methods

Geometric or mostly geometric methods form the lowest rung of the distance ladder. Out of the available techniques only parallaxes, detached eclipsing binaries (DEB), and masers are relevant for state-of-the-art distance ladders; other probes, such as moving cluster distances (e.g., Mamajek, 2005) or the distance to the ring of SN 1987A (e.g., Panagia et al., 1991), are not as precise or can only be applied to a limited number of objects.

The parallax is the oldest of the three methods: Robert Hooke[3] first attempted to measure a stellar parallax in 1669 and Friedrich Bessel succeeded in 1838 (Bessel, 1838a,b). The method is based on the Earth's motion around the Sun: over the course of a year, the apparent position of a nearby star changes relative to that of more distant ones due to the change in viewpoint.

[3]Robert Hooke—a true renaissance man—excelled not only in astronomy but also in many other fields including architecture, microscopy, paleontology, and classical mechanics (e.g., Andrade, 1950). He is most famously known for this work on elasticity—and specifically the discovery of Hooke's law.

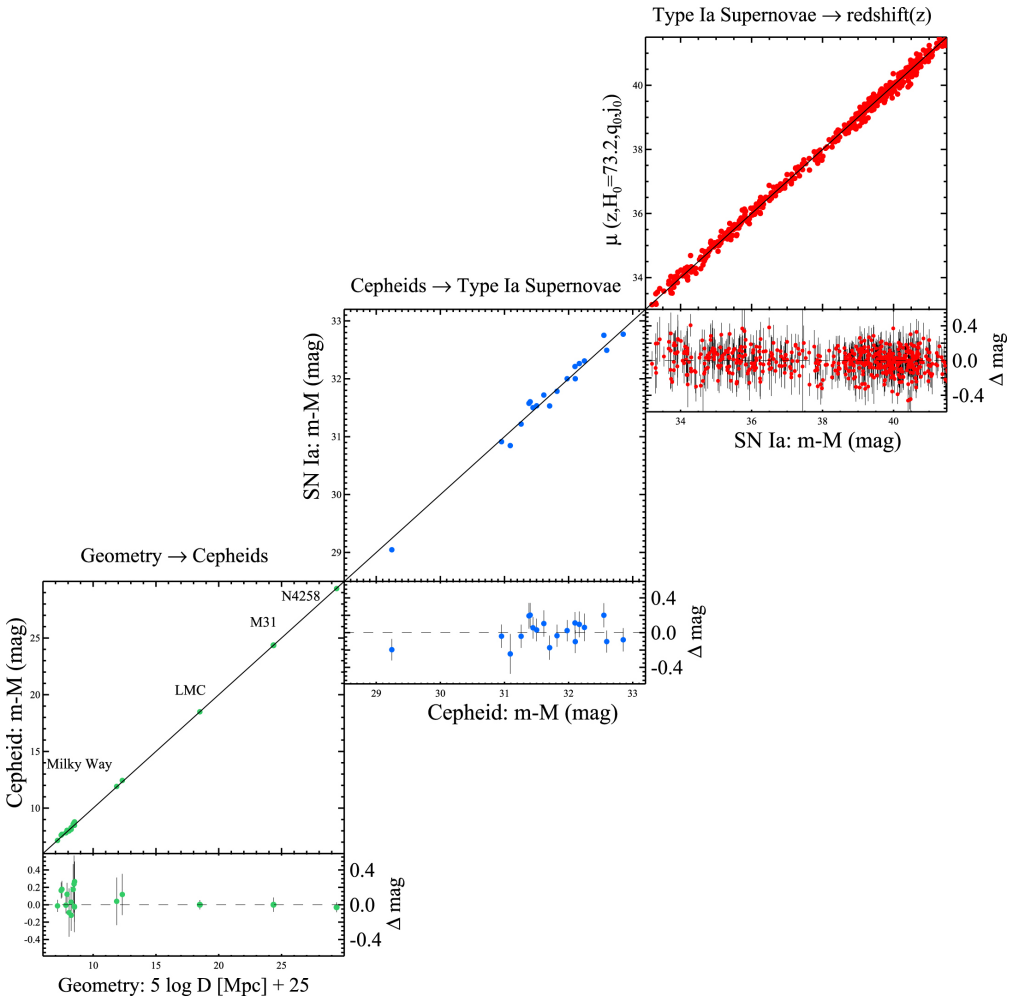

Figure 2.2.: Cosmic distance ladder [from Riess et al. (2016)]. The basic principle is to calibrate successively further-reaching relative distance indicators starting from absolute distances. In state-of-the-art distance ladders, two calibration steps—often called rungs—are needed to reach the Hubble flow. In the SH0ES project, the first step standardizes the luminosities of Cepheid variable stars based on geometric distances from Milky Way parallaxes, DEBs in the LMC, and the megamaser galaxy NGC 4258. This is illustrated in the bottom left panel. In the second step, shown in the central panel, the calibrated Cepheids provide distances to the host galaxies of nearby SNe Ia. The standardized SNe Ia are then used to probe the smooth Hubble flow and measure H_0 as illustrated in the top right subplot.

The maximum difference in position—the parallax p—is inversely proportional to the distance $D = (1''/p)\,\mathrm{pc}$. The effect is minuscule: the closest star system, Alpha Centauri, at a distance of 1.33 pc has a parallax of only $0.747''$ (Söderhjelm, 1999). We require a precision of roughly 10 µas to probe a significant fraction of the Milky Way, which has a radius on the order of 10 kpc (e.g., López-Corredoira et al., 2018). At optical wavelengths, atmospheric seeing and refraction, as well as seasonal changes in the observing conditions limit the accuracy (e.g., Hubeny & Mihalas, 2014); currently, only space-based measurements from HST (Benedict et al., 2007) or *Gaia* (Gaia Collaboration et al., 2016, 2018) provide the necessary precision to measure parallaxes beyond a kpc.[4]

DEBs reach much further but the method is not purely geometric. With current telescopes, DEBs can be used to determine distances to galaxies in the Local Group including the LMC, Andromeda, and M33—corresponding to a range of around a Mpc (see, Guinan et al., 1998; Ribas et al., 2005; Bonanos et al., 2006; Pietrzyński et al., 2019). The method works by constraining the luminosity of double-line, detached eclipsing binaries. In these systems, the orbital plane is aligned with our line of sight—leading to eclipses whenever the stars pass in front of each other. Since the system is detached, that is to say, there is no mass transfer, the light curve shows two well-separated eclipses: when the primary occults the secondary and vice versa. The relative depths of the light curve dips yield the ratio of the surface brightnesses of the stars F_2/F_1; the shapes provide the radii (R_1, R_2) in units of the separation (e.g., Paczynski, 1997). For double-line binaries, which show spectral lines from both stars, the separation can be inferred from the radial velocity curves. Together with the surface brightness of the primary F_1, these observables allow us to determine the distance

$$D = \left(\pi R_1^2 F_1 \left[1 + \frac{R_2^2}{R_1^2}\frac{F_2}{F_1}\right] / F_\lambda^{\mathrm{dered}}\right)^{\frac{1}{2}} \tag{2.1}$$

from the measured dereddened flux $F_\lambda^{\mathrm{dered}}$. The surface brightness of the primary can be obtained from stellar atmosphere models (e.g., Milone et al., 1992; Guinan et al., 1998; Fitzpatrick et al., 2002; Ribas et al., 2002) or in the case of late-type stars from an empirical surface brightness–color relation. The latter can be calibrated with an accuracy of less than one percent based on Very Large Interferometer array (VLTI) measurements of the stellar angular diameters for red clump giant stars (Pietrzyński et al., 2019).

Masers cannot match this accuracy but they can be observed well into the Hubble flow. This makes them valuable both as an anchor for the distance ladder and as an independent one-step method to measure H_0. We will discuss the latter application and the physics of masers in Sect. 2.2. The only relevant maser for the calibration of the distance ladder is NGC 4258 (D=7.54 Mpc), whose distance is known to an accuracy of 2.6 % (Humphreys et al., 2013; Riess et al., 2016).

[4] At radio wavelengths, Very Long Baseline Interferometry (VLBI) provides comparable or better precision from the ground (e.g., Reid & Honma, 2014).

Second rung: Cepheids

Geometric methods provide absolute distances, but they have limited range: apart from masers none of the presented techniques can be applied outside of the Local Group. We need to calibrate further-reaching, relative distance indicators to make our way into the Hubble flow. One option is classical Cepheids. These yellow (super-)giant stars can be observed up to distances of around 40 Mpc (Riess et al., 2016) due to their high luminosities ($-2 < M_V < -6$; Freedman & Madore, 2010).

Cepheids are variable stars: their brightnesses fluctuate by around 0.5 to 2 magnitudes with periods in the range of days to months. The period correlates strongly with the luminosity: the longer the period, the brighter the star. This period-luminosity relationship—called the Leavitt law after its discoverer (Leavitt & Pickering, 1912)—provides the basis for the use of Cepheids as distance indicators. The variability is driven by radial pulsations, which occur in certain evolutionary stages of intermediate-mass stars ($3 - 10\,M_\odot$; Anderson et al., 2017). In this mass range, stars can make multiple passes through the instability strip of the Hertzsprung–Russell diagram during the post main sequence evolution (e.g., Chiosi, 1990)—each time resulting in a phase of pulsational instability. The crossing time scale is longest for stars on a blue loop, which, as a result, make up the bulk of observed Cepheids (e.g., Turner et al., 2006; Anderson et al., 2017). The pulsations are related to changes in the helium ionization zone (e.g., Cox, 1980). Since the opacity of doubly ionized helium (He III) is much higher than that of singly ionized helium (He II), the zone acts similar to a valve, which alternately traps and releases radiative energy. When the valve is closed (He III), the internal pressure below the layer increases, which leads the star to expand. As the material rises, it cools due to expansion work and the work against gravity. Once the temperature drops sufficiently for helium to recombine, the valve opens again and the built-up pressure is released; the expansion stops. As the star contracts, the temperature rises and the material again becomes fully ionized: the valve closes and the cycle starts anew.[5]

The changes of the radius and temperature of the stellar surface drive the variation in luminosity. The intrinsic dispersion of the period-luminosity relation is caused mainly by the non-zero width of the instability strip in temperature. The correlation thus tightens at longer wavelengths as the luminosity becomes increasingly insensitive to temperature (Madore & Freedman, 1991, 2012). In this regime, the effect of reddening is also minimized—leading to a further reduction in the dispersion. Figure 2.3 illustrates this for optical to near-infrared period-luminosity relations of Galactic and LMC Cepheids. State-of-the-art measurements rely on observations at near-infrared (Riess et al., 2019) or mid-infrared wavelengths (Freedman et al., 2012). Multi-filter photometry is used to construct Wesenheit magnitudes (Madore, 1982) from a weighted average of the individual bandpasses. The weights are chosen such that for a plausible reddening law the intrinsic value of the Wesenheit magnitude is identical to that of the reddened observation (see, e.g., Freedman & Madore, 2010). This reduces not only the dispersion caused by reddening but also the intrinsic

[5] Hydrodynamical modeling of this process reproduces the observed period-luminosity relation reasonably well (e.g., Caputo, 2008).

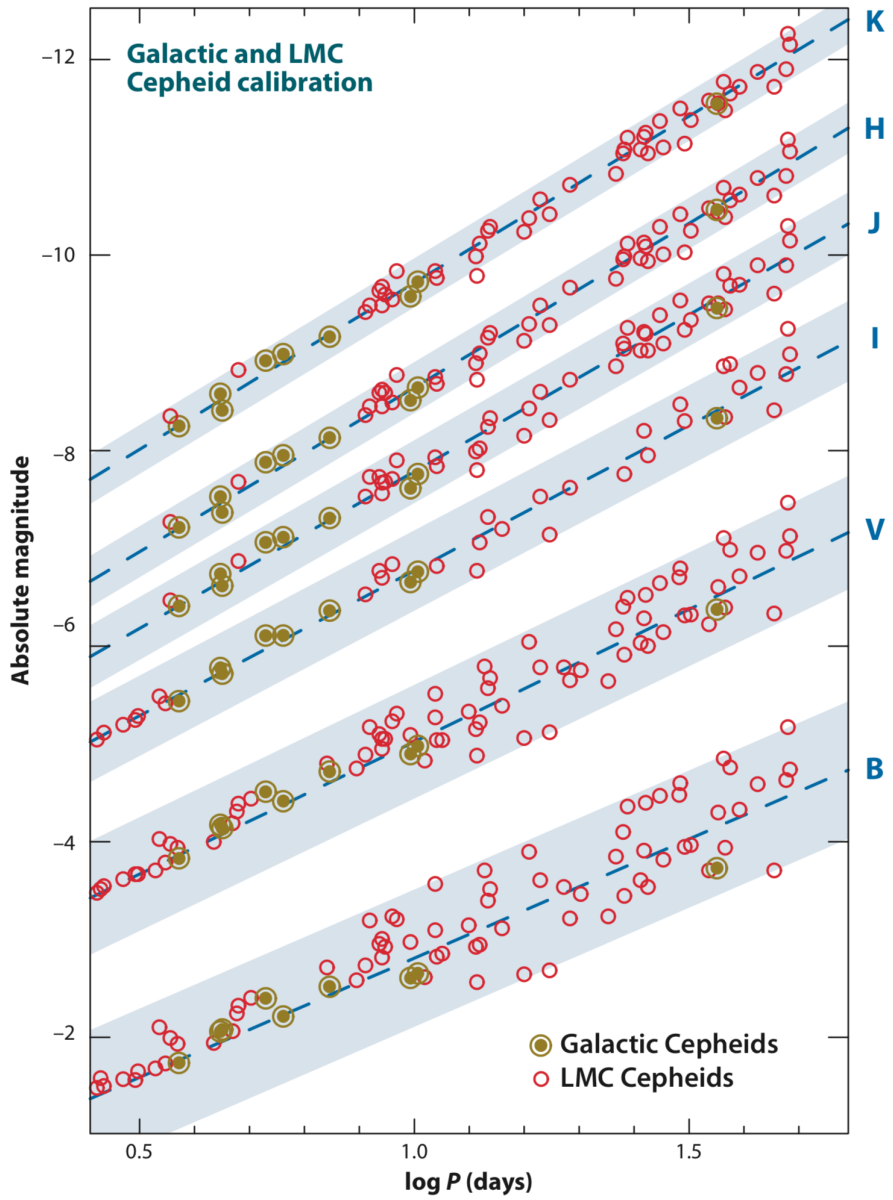

Figure 2.3.: Optical to near-infrared Cepheid period-luminosity relations [from Freedman & Madore (2010)].

one (e.g., Riess et al., 2019). Riess et al. (2019), based on a Fitzpatrick (1999) law, construct a near-infrared (V, I, H) Wesenheit period-luminosity relation with a scatter of only around 3 % in distance. Their Leavitt law includes a dependence of the luminosity on the metallicity (e.g., Romaniello et al., 2008) and allows for a break in the slope at 10 d (e.g., Bhardwaj et al., 2016). The sensitivity to metallicity is of particular concern for the use of the LMC as an anchor: its metallicity is significantly lower than that of the SN Ia host galaxies, whose distances are measured with the calibrated Cepheids (e.g, Romaniello et al., 2008).

Third rung: type Ia supernovae

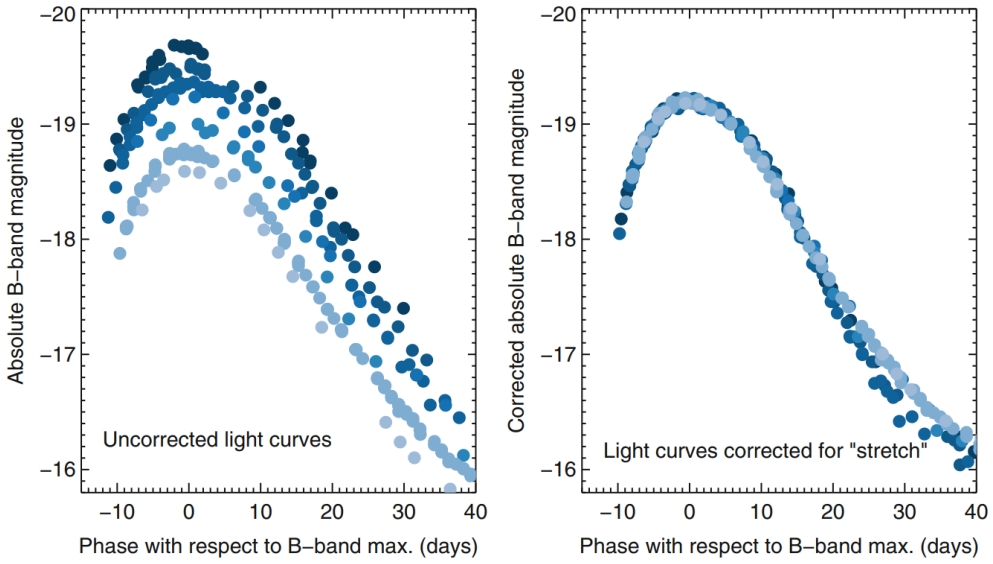

Figure 2.4.: Type Ia supernovae as standardizable candles [from Maguire (2017)]. Observed SN Ia light curves, as shown on the left-hand side, cover a wide range of peak absolute magnitudes and light curve widths. On the right-hand side, the light curves have been standardized to high precision by applying a stretch factor to the light-curve timescale. The remaining scatter in the peak luminosity is only a few hundredth magnitudes—making SNe Ia excellent standardizable candles.

Type Ia supernovae, finally, allow us to probe the smooth Hubble flow. The radioactive decay of ^{56}Ni, synthesized in these thermonuclear explosions of white dwarves, powers luminous transients with absolute magnitudes between -18 and -19.5 mag (e.g., Maguire, 2017). This puts SNe Ia among the brightest events in the Universe and makes it possible to observe them up to redshifts of $z \approx 2$ (e.g., Jones et al., 2013; Rodney et al., 2015). The majority of SNe Ia show remarkably similar spectroscopic evolution—and their relative absolute luminosities can be standardised based on observational properties similar to Cepheids (Phillips, 1993; Riess et al., 1996; Tripp, 1998; Phillips et al., 1999). Normal, standardisable SNe Ia can be distinguished from their peculiar brethren, such as 91T-like or 91bg-like SNe Ia, through their spectra (see, e.g., Taubenberger, 2017; for the spectroscopic differences between the subclasses). The homogeneity of normal SNe Ia

provides the foundation for their decades-long use as distance indicators (e.g., Kowal, 1968),[6] which culminated in the discovery of the accelerated expansion of the Universe by Riess et al. (1998) and Perlmutter et al. (1999).

The success of SNe Ia as one of the best standard candles rests on the relation between their peak luminosities and post-maximum decline rates: more luminous SNe Ia have slower declining light curves. This was first realized by Rust (1974) and Pskovskii (1977, 1984). In the advent of CCD technology, Phillips (1993) put the relation on a robust foundation using improved photometric data. He showed that there is a strong correlation between the peak magnitude in the B-band and $\Delta m_{15}(B)$—the decline in magnitudes in the first 15 d after the light curve peak. Early on, so-called stretch factors have replaced $\Delta m_{15}(B)$ as the indicator of the light-curve-decline rate in most practical applications. The stretch factors, as first proposed by Perlmutter et al. (1997), are based on the idea that light curves of different SNe Ia can be brought into agreement through stretching or compressing them in time. This is illustrated in Fig. 2.4. The advantage of stretch-based techniques is the use of the complete light curve shape instead of a simple point estimate. Modern light curve fitters like SALT2 (Guy et al., 2007) go even further: the standardization is performed on multi-color light curves instead of only the B-band.

The peak magnitudes of SNe Ia correlate not only with the light curve shape but also with the color at maximum light. As first demonstrated by Tripp (1998), SNe Ia with bluer $B - V$ colors have higher peak luminosities. This is likely related to the intrinsic SN colors and not only to interstellar extinction (e.g., Phillips & Burns, 2017). After stretch and color corrections, the scatter in the standardized peak magnitudes of modern SN Ia cosmology samples is only around 0.02 mag (e.g., Betoule et al., 2014). This provides the foundation for precision measurements of H_0 and other cosmological parameters.

Joining the rungs

Figure 2.2 illustrates how the SH0ES project assembles the distance ladder from its parts. To start with, geometric distances are used to calibrate the Cepheid period-luminosity relation based on three distinct anchors: the Milky Way, the LMC, and NGC 4258. In the Milky way, distances to the individual objects come from HST spatial scanning (Riess et al., 2018a) and *Gaia* parallaxes (Riess et al., 2018b). The distances to the LMC and NGC 4258 are constrained by DEBs (Pietrzyński et al., 2019) and masers (Humphreys et al., 2013; Riess et al., 2016) respectively with precisions of 1.2 % and 2.6 %.

The calibrated Cepheids put the host galaxies of nearby SNe Ia in reach. The small maximum range of ~ 40 Mpc and the restriction to star-forming spiral galaxies limit the number of suitable calibrators. Only 19 SNe Ia remain, after additional considerations, such as low-reddening or the existence of pre-maximum observations, are taken into account (Riess et al., 2019). These objects set the absolute magnitude scale of SNe Ia. In the final step, more than 300 hundred SNe Ia in the

[6] This study, which presents the first supernova Hubble diagrams, predates the identification of SNe Ia as a distinct subclass of hydrogen-poor supernovae by Elias et al. (1985).

Hubble flow ($0.01 < z < 0.15$) provide a precise determination of H_0 from the redshift-distance relation.

Decades-long efforts have established the distance ladder as the most accurate direct way to measure H_0. However, the many steps of the analysis make it difficult to control all possible systematics. The distance ladder is particularly prone to biases that result from systematic differences between the samples used for the calibration and the final distance measurement. Dependencies of the luminosities on environmental properties are a potential source of such differences. Correlations of this nature are well established: the Cepheid period-luminosity relation depends on metallicity (e.g., Romaniello et al., 2008) and SN Ia luminosities are likely influenced by environmental or host galaxy properties (e.g., Rigault et al., 2015, 2018; Roman et al., 2018; Jones et al., 2018; Rose et al., 2019). The resulting biases in the distance measurements have been put forward as possible explanations of the Hubble tension (e.g., Rigault et al., 2015), although this is widely disputed (e.g., Jones et al., 2018; Rose et al., 2019). The basic point still stands: the procedure of locally calibrating distance indicators and then applying them elsewhere under potentially different conditions carries the risk of introducing systematic errors. This is exacerbated by the multitude of methods used to construct the distance ladder.

2.2. Maser galaxies

Stimulated emission of microwave radiation can give rise to considerable amplifications of the radiation field in an atomic or molecular transition—so-called masers (microwave amplification by stimulated emission of radiation). Astrophysical masers are excellent probes of the kinematic of the underlying system because their nearly monochromatic radiation allows the accurate determination of Doppler shifts; this enables, for example, precise measurements of black hole masses (e.g., Kuo et al., 2011), and more importantly for our purposes, absolute distances (e.g., Herrnstein et al., 1999).

The physical conditions needed for masers do not naturally occur on Earth but are realized in many astrophysical plasmas: the low densities of these environments make it possible for the necessary population inversions to develop and strong energy sources, such as stars or AGN, provide the required energy input through radiation or shocks. As a result, masers are a common occurrence both in our Galaxy (Weaver et al., 1965; Cheung et al., 1969)[7] and in other galaxies (e.g., Dos Santos & Lepine, 1979). Of particular importance are so-called megamasers, which are associated with the nuclear regions of galaxies. Megamasers are characterized by high luminosities of $10^2\,L_\odot$ to $10^4\,L_\odot$ (e.g., Lo, 2005), which is roughly a million times more luminous than Galactic masers (hence megamaser); this makes it possible to observe them well into the Hubble flow. Most megamasers originate from only three different molecules: water (H_2O; Dos Santos & Lepine, 1979), hydroxyl (OH; Baan et al., 1982), and formaldehyde (H_2CO; Baan et al., 1986). Only

[7] The initial discovery of galactic OH maser emission by Weaver et al. (1965) was so unexpected that they attributed the line to a yet unknown substance—aptly named 'mysterium'—in spite of their correct identification of the other features as OH transitions.

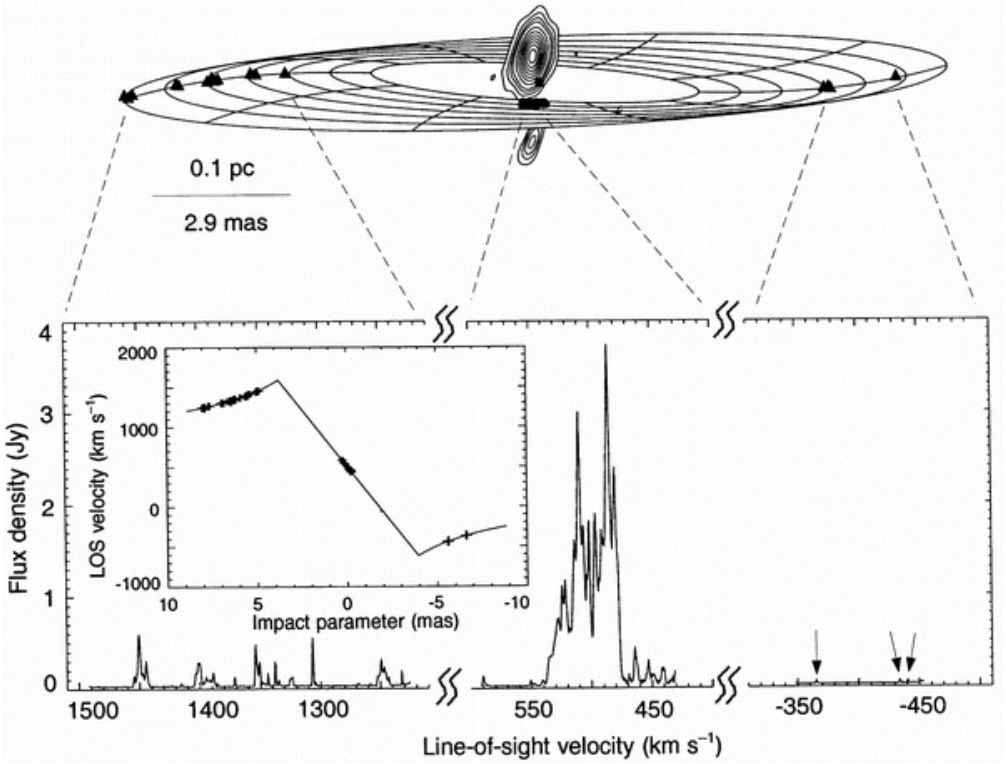

Figure 2.5.: Observations and reconstructed geometry of the water megamaser in NGC 4258 [from Herrnstein et al. (1999)]. The top of the plot shows the measured positions of maser sources (black circles/triangles) in the accretion disk around the AGN; the necessary submilliarcsecond spatial resolution is achieved through VLBA observations. The bottom shows a spectrum of the total emission from the region, revealing a complicated combination of many narrow emission lines; each line is associated with one of the masers from the imaging and provides, through its Doppler shift, important information about the kinematics of the system. The observations can be understood in the context of a thin warped disk in Keplerian motion: the bulk of the emission occurs close to the peculiar velocity of the galaxy ($\approx 470\,\mathrm{km\,s^{-1}}$) corresponding to material that is moving through the line of sight; the masers on the left-hand side are moving away from us and thus appear redshifted; the masers on the right-hand side move towards us and are blueshifted. The combination of imaging and spectra yields the rotation curve in the inset on the left; the observations are in excellent agreement with a Keplerian disk model as illustrated by the solid fit line.

water masers are suitable for distance measurements. Water masers, which emit in the 22.2 GHz rotational transition, are found in the accretion disks of AGN; the emission is confined to many small regions of enhanced density, which serve as tracer particles of the disk kinematics. We can reconstruct the physical size and geometry of the accretion disk from the motion of these test particles—yielding the angular diameter distance as a byproduct.[8] Single-dish spectra provide radial velocities of the orbiting masers and VLBI imaging their projected positions. Figure 2.5 illustrates how these observables relate to the structure and kinematics of the accretion disk. Over the course of years, changes in the projected positions and radial velocities (i.e. radial accelerations) can also be measured. All this provides a wealth of information for constraining a Keplerian disk model. This is most easily illustrated for the accelerations of masers moving across our line of sight—the so-called systemic masers. For Keplerian motion, the acceleration is given by $a \approx v_{\mathrm{rot}}^2/R$, where v_{rot} is the rotation velocity and R the radius of the disk. Since we know the rotation velocity v_{rot} from the Doppler shifts at the edges of the disk, we can infer the radius R. The distance follows from the ratio of the physical size R and the angular diameter. The latter is determined from VLBI images.

Masers are a valuable addition to the cosmic distance scale because they provide accurate absolute distances based on a simple physical model. Out of the geometric methods considered in this chapter masers have the furthest range by far; this allows them to be both an anchor for the distance ladder and a one-step way to measure H_0. For the former, the nearby maser galaxy NGC 4258 (D=7.54 Mpc) is used, whose distance is known to an accuracy of 2.6 % (Humphreys et al., 2013; Riess et al., 2016); for example, Efstathiou (2014) and Riess et al. (2019) calibrate their Cepheid luminosities on this object. NGC 4258 also serves as an important test case for other distance indicators; almost all common methods have been compared against its maser distance: Cepheids (e.g., Maoz et al., 1999; Fausnaugh et al., 2015), the TFR (e.g., Sorce et al., 2014), the TRGB (e.g., Madore et al., 2009), SBF (Tonry et al., 2001), and the standardized candle method (SCM) for SNe II (Polshaw et al., 2015).

More distant masers provide distance-ladder-independent probes of the cosmic expansion. The most important program in this context is the Megamaser Cosmology Project (MCP; Reid et al., 2009). To date, the MCP has published distances to six galaxies with redshifts between 0.002 and 0.034 (Reid et al., 2013; Kuo et al., 2013, 2015; Gao et al., 2016; Pesce et al., 2020)—yielding $H_0 = 73.9 \pm 3.0\,\mathrm{km\,s^{-1}\,Mpc^{-1}}$ (Pesce et al., 2020). The small sample size limits the accuracy of the measurement. The low redshifts of the masers and the associated uncertainties from peculiar velocities exacerbate this further. This is unlikely to change completely until the Square Kilometre Array (e.g., Dewdney et al., 2009) starts scientific observations in the late 2020s.

[8] For Hydroxyl and formaldehyde masers, which predominately occur in the nuclear regions of luminous infrared galaxies (LIRGs) and ultra-luminous infrared galaxies (ULIRGs), the simple picture of test particles in Keplerian motion around a central black hole does not apply—prohibiting their use as distance indicators.

More complicated physics might also impact the accuracy of the method. Potential sources of systematic errors are self-gravity effects in the disk, non-circular orbits,[9] and non-physical motions of the maser images due to radiative transfer effects (e.g., Freedman & Madore, 2010).

2.3. Time-delay cosmography

In addition to standard candles and standard rulers, we can probe the cosmic expansion through the measurement of time delays in multiply imaged gravitationally lensed systems. This provides highly complementary constraints on cosmological parameters and specifically H_0.

A distant source can be strongly lensed if there is a massive object, for example, a galaxy, in proximity to the line of sight. Photons that are not emitted towards the observer can then be deflected into the line of sight by the gravitational potential of the lens. The perceived origin of the photons is offset from the source and depends on the initial direction; images form in directions from which photons preferentially arrive. The time needed by the photons to the reach the observer differs between images. For two images i and j with apparent positions θ_i and θ_j, the difference in arrival time is given by

$$\Delta t_{ij} = \frac{D_{\Delta t}}{c}\left[\frac{(\theta_i-\beta)^2}{2} - \Psi(\theta_i) - \frac{(\theta_j-\beta)^2}{2} + \Psi(\theta_j)\right], \tag{2.2}$$

where β is the source position, $D_{\Delta t}$ the time-delay distance, and Ψ the lens potential (e.g., Treu & Marshall, 2016). Two effects contribute to the time delay. The first is the deviation of the light path from a straight line as described by the term $(\theta_i-\beta)^2/2$. The second is the gravitational time delay, which is proportional to the lens potential Ψ. The arrival time difference depends on the angular diameter distances to the source D_s and lens D_d through the time-delay distance:

$$D_{\Delta t} = (1+z_\mathrm{d})\frac{D_\mathrm{d} D_\mathrm{s}}{D_\mathrm{ds}}. \tag{2.3}$$

Here, D_ds is the distance between the source and the lens and z_d is the lens redshift. The time-delay distance is inversely proportional to H_0 because the distances that enter are. This is the primary dependence even at source redshifts of around one: the effects of other cosmological parameters partly cancel in the ratio of angular diameter distances (e.g., Coe & Moustakas, 2009; Linder, 2011).

Refsdal (1964) was the first to recognize the possibility of determining H_0 from time-delay measurements of multiply imaged time-variable sources such as SNe and quasars.[10] Lensed SNe

[9] Deviations from circular orbits are difficult to detect because almost all masers are located either near the projected center or edge of the disk. In other locations, the maser emission in the direction of the observer Doppler shifts out of resonance with the material in the fluid restframe due to the rotation of the disk. This prevents significant amplifications of the radiation field.

[9] In the cosmological context $D_\mathrm{ds} \neq D_\mathrm{s} - D_\mathrm{d}$.

[10] Refsdal (1964, 1966)—with great foresight—realized the potential of quasars for time-delay cosmography at a time where they were a new and poorly understood phenomenon (Matthews & Sandage, 1963). The notions

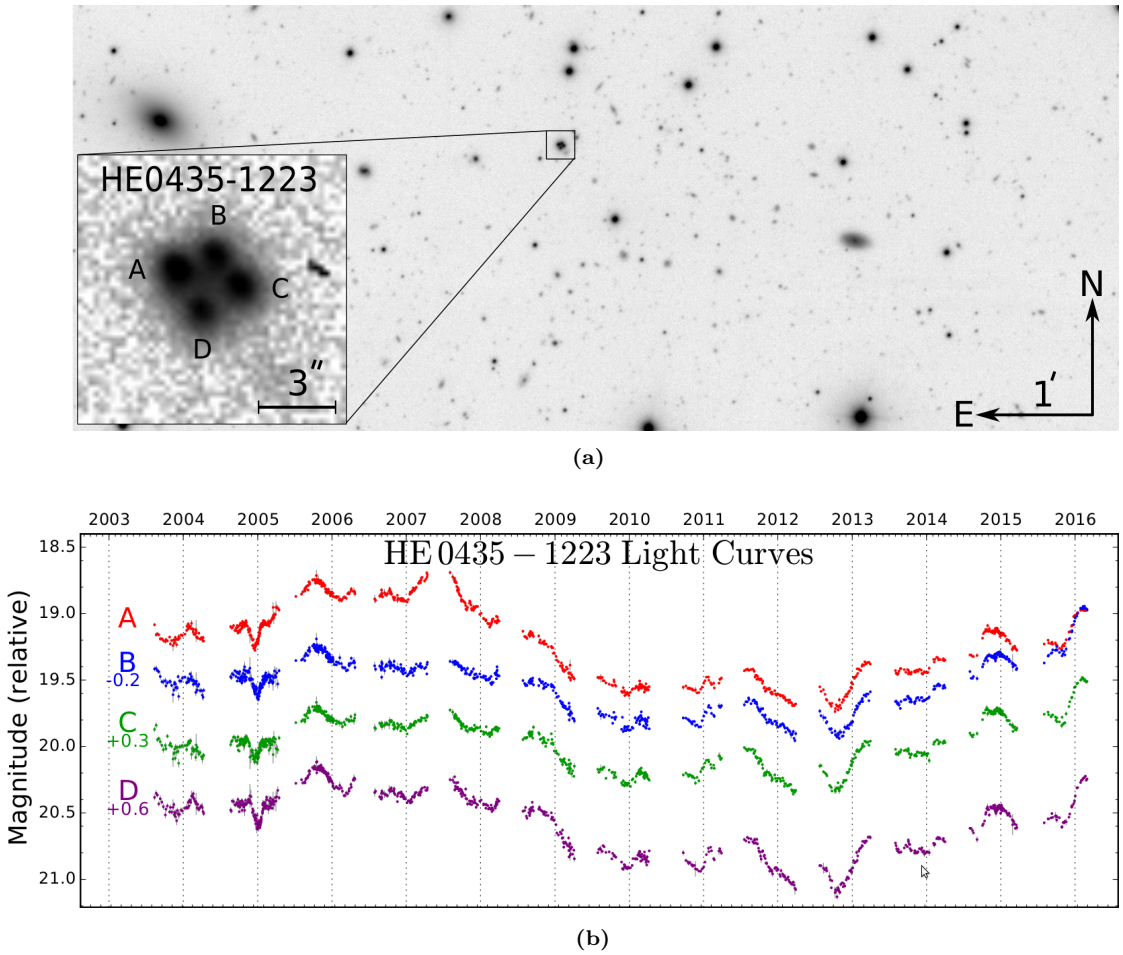

Figure 2.6.: Optical image (a) and light curves (b) of the gravitationally lensed quasar HE 0435-1223 (Bonvin et al., 2017). The inset in the top shows a zoom-in on the quasar, which reveals four lensed images. The bottom plot shows 13-year-long light curves from the COSMOGRAIL project for each image. Gravitational lens time delays shift the variability patterns by a few days between images. Microlensing by stars in the lensing galaxy introduces additional differences between the light curves, which complicates the determination of the time delays. Images courtesy of S. Suyu.

have been discovered only in recent years (Kelly et al., 2015; Goobar et al., 2017) and their use in cosmography is still in its infancy. AGN-time-delay cosmology is a more mature field: the discovery of multiply imaged quasars dates back to the late seventies (Walsh et al., 1979) and a couple hundred systems are known today (e.g., Anguita et al., 2018); long-term photometric monitoring through dedicated projects such as COSmological MOnitoring of GRAvItational Lenses (COSMOGRAIL; Courbin et al., 2005) now provides time delays with an accuracy of a few percent. Figure 2.6 shows exemplary decade-long quasar light curves. With an accurate model of the lens mass distribution, which predicts the source position β and the lens potential Ψ in Eq. (2.2), the time delays yield H_0. The lens model is constrained through the measured image positions and flux ratios; this requires high-resolution imaging because typical image separations are on the order of an arcsecond. The inference is complicated by a fundamental degeneracy between the density profile of the lens and H_0—the mass-sheet degeneracy: the lens mass distribution can be modified without changing any of the lensing observables (i.e., image positions, flux ratios) apart from the time delays, which are used to determine H_0 (e.g., Koopmans et al., 2003). Stellar-velocity-dispersion measurements provide additional information about the lens mass distribution—and can break the degeneracy (e.g., Grogin & Narayan, 1996); high precision measurements even allow the determination of the angular diameter distance to the lens in addition to the time delay distance (Paraficz & Hjorth, 2009; Jee et al., 2015). Mass along the line of sight is an additional source of systematic errors: weak gravitational lensing by galaxies and clusters can bias the inference of H_0 (e.g., Fassnacht et al., 2006). Here, again the mass-sheet degeneracy comes into play, which makes it almost impossible to constrain this effect through the lens model alone (e.g., Wong et al., 2019); additional wide-field imaging and spectroscopy are needed to characterize the mass distribution along the line of sight.

State-of-the-art time-delay cosmography requires a multitude of data including multi-year light curves, high-resolution space or adaptive optics imaging, and stellar-velocity-dispersion measurements; this limits the sample size considerably. The currently best constraints on H_0 come from the analysis of only six lensed quasars: the H_0 Lenses in COSMOGRAIL's Wellspring (H0LiCOW; Suyu et al., 2017) collaboration find $H_0 = 73.3^{+1.7}_{-1.8}\,\mathrm{km\,s^{-1}\,Mpc^{-1}}$ for a flat-ΛCDM cosmology (Wong et al., 2019); this corresponds to an accuracy of 2.4 %—comparable to that of modern distance-ladder approaches (e.g., Riess et al., 2019). This result is based on fundamental physics and is completely independent of other local measurements. However, it depends more strongly on the adopted background cosmology than other late Universe probes due the considerable redshifts of the lensed systems; if the assumption of a flat-ΛCDM cosmology is relaxed, the uncertainties in H_0 become significant. This can be partly mitigated by combining the lensing data with SNe Ia in an inverse distance ladder approach (e.g., Taubenberger et al., 2019); this restricts H_0 to a range of $73\,\mathrm{km\,s^{-1}\,Mpc^{-1}}$ to $78\,\mathrm{km\,s^{-1}\,Mpc^{-1}}$ (Wong et al., 2019) but is no longer completely

that quasars are at high redshift (Schmidt, 1963) and that they show time variability (Sandage, 1964) were just emerging in this period.

[10] Only the angular diameter distance to the lens, which can be derived if high precision stellar-kinematics measurements are available, is unaffected by additional mass along the line of sight (e.g., Wong et al., 2019).

independent of the most competitive distance ladders because these also utilize SNe Ia. Of concern for precision cosmology are also potential biases and underestimated errors that result from the use of simple parametric lens models (e.g., Kochanek, 2019).[11] A careful study of these and other systematic uncertainties in time-delay cosmography can be found in Millon et al. (2019).

[11] Simple parametric lens models are needed to break the mass-sheet degeneracy in combination with stellar kinematics measurements

3. Type II supernovae: the Hubble constant in one step

In light of the increasing Hubble tension, the H_0 measurements from the distance ladder—as the driving force behind the discrepancy—must be subjected to rigorous checks. The best tests are completely independent local determinations of H_0. Currently, only few techniques have the required level of precision. Time-delay lensing (e.g., Wong et al., 2019) and masers (e.g., Pesce et al., 2020) are the only competitive probes that are entirely disconnected from the distance ladder. Each method has its challenges: megamaser cosmology suffers from small sample sizes and uncertainties from peculiar velocities (see Sect. 2.2); time-delay lensing, with typical lens redshifts of around one, is not a local measurement and requires a cosmological model to make meaningful predictions for H_0 (see Sect. 2.3).

The number of complementary probes with the power to provide absolute distances in the Hubble flow is extremely limited. Most, like standard sirens (Abbott et al., 2017; Feeney et al., 2019; Soares-Santos et al., 2019), are far from reaching the necessary level of sophistication.

Type II supernovae, currently, provide the most promising avenue towards an independent one-step determination of H_0. These stellar explosions are bright, abundant, and physically comparatively simple—making them ideal distance indicators. We substantiate this in the following sections starting with a primer on SN II physics (Sect. 3.1). This foundation is then used to explain how SN II luminosities can be constrained through simple supernova emission models in the EPM (Sect. 3.2). Here, we highlight how tailored radiative transfer modeling enables state-of-the-art distance measurements with the EPM.

3.1. Type II supernova basics

Supernovae are powerful cosmic explosions that can briefly match the luminosity of up to a billion stars. They shape our Universe through the injection of energy and heavy elements: the energy release regulates the growth and star formation rate of galaxies; the high-velocity ejection of synthesized and preexisting elements determines their chemical evolution (Edmunds, 2017). As drivers of galactic winds, the influence of SNe extends as far as the intergalactic medium and from there indirectly to other galaxies (Heckman & Thompson, 2017). Supernovae shape the astrophysical environments around us as sources of dust (Sarangi et al., 2018), cosmic rays (Tatischeff & Gabici, 2018), as well as heat and turbulence in the interstellar medium (Cox, 2005).

The nature and appearance of these transients is highly varied: the literature differentiates between dozens of classes and subclasses based on properties of their spectra and light curves (Turatto, 2003; Gal-Yam, 2017). The most basic distinction is made based on the presence or absence of spectroscopic signatures of hydrogen—most prominently that of the Balmer Hα line (Minkowski, 1941). According to this criterion, hydrogen-poor SNe are dubbed type I and hydrogen-rich SNe type II. In the first weeks after the explosion, the presence of hydrogen leads to a well-defined photosphere that radiates like a dilute blackbody. This provides a simple physical picture for the emission, which can be leveraged to constrain the SN luminosity. Type II supernovae are thus well suited for absolute distance determinations. We review the relevant aspects of their physics in the following.

There are five main classes of SNe II: IIP, IIL, IIn, IIb, and 87A-likes (Arcavi, 2017). We focus on SNe of type IIP and IIL, which make up around 80 % of SNe II per volume (Li et al., 2011); we will refer to these events as normal SNe II. The remaining classes are less suited for measuring distances: in type IIn, the interaction with a dense circumstellar medium, which produces the characteristic narrow emission lines, complicates the picture. Type IIb SNe likely have only a small residual hydrogen envelope as indicated by the rapid fading of the hydrogen lines. Finally, 87A-like SNe, which are characterized by their long rise to the light curve peak ($\sim$50 d to 100 d), are too rare to be useful distance indicators (Taddia et al., 2016).

Normal SNe II are the most common type of supernova: they account for roughly half of the explosions in the local Universe (Li et al., 2011).[1] Out of these, the majority are SNe IIP with SNe IIL contributing only $\sim 15\,\%$ of the total rate.

3.1.1. Progenitors

Type IIP and type IIL SNe differ in the shapes of their light curves: the class identifiers P and L abbreviate the distinctive features, which are a plateau and a linear decline (Barbon et al., 1979). Both subclasses are thought to be the explosions of massive stars ($\gtrsim 8\,M_\odot$; Smartt, 2009), which have retained more than a solar mass of their hydrogen envelopes during their evolution (e.g., Blinnikov, 2017). Indirect evidence, such as the strong correlation between the SN II and massive star-formation rate of galaxies (e.g., Kennicutt, 1984), have long pointed towards a massive star origin. In recent years, progenitor identifications of nearby ($\lesssim 30$ Mpc) SNe II in archival high-resolution images have provided conclusive proof for this association (e.g., Smartt, 2009, 2015): of the dozen or so SNe IIP, with progenitor detections, all are explosions of single red supergiants with masses in the range of $\sim 8\,\mathrm{M}_\odot$ to $17\,\mathrm{M}_\odot$ (e.g., Smartt, 2015; Van Dyk, 2017). These stars have extended hydrogen envelopes with a few hundred to more than a thousand times the radius of the Sun (e.g, Levesque et al., 2005). Figure 3.1 illustrates how pre- and post-explosion images reveal the red supergiant precursor of SN 2008bk. The identification of the progenitors of SNe IIL has proven to be more difficult—mostly due to their intrinsic rareness. Tentative detections have been reported only for two likely events: SN 2009kr (Elias-Rosa et al., 2010) and

[1] In a volume-limited sample.

SN 2009hd (Elias-Rosa et al., 2011). In both cases, the classification as SNe IIL is not proven beyond reasonable doubt (Elias-Rosa et al., 2011; Fraser et al., 2010). Elias-Rosa et al. (2010) propose that SN 2009kr is the explosion of a yellow supergiant, which is a hotter, more compact star than a red supergiant. For SN 2009hd, limits on the absolute magnitude and intrinsic color of the progenitor, point towards a red (or possibly yellow) supergiant star (Elias-Rosa et al., 2011). Both results should be taken with a grain of salt (see, e.g., Maund et al., 2015).

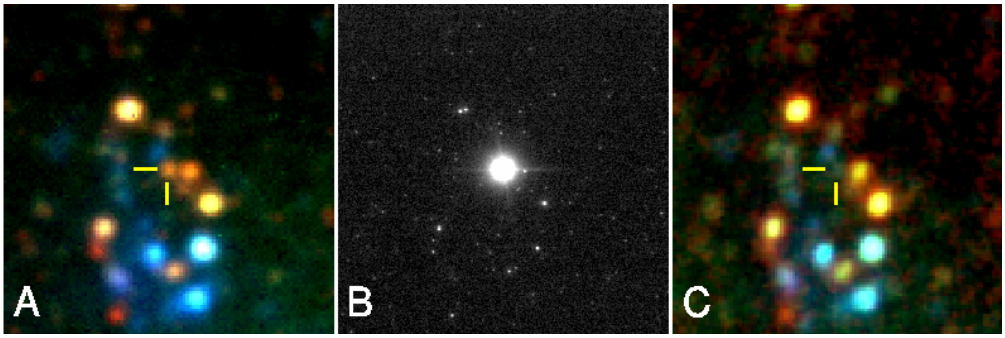

Figure 3.1.: Life, death, and disappearance of a red supergiant [from Mattila et al. (2010)]. The first panel (A) shows a pre-explosion VLT (VIK_s) image of the location of SN 2008bk. The image reveals a red point source at the future position of the SN: its red supergiant progenitor. Shortly after the explosion, the stellar remains outshine their surroundings, as illustrated by the picture (K_s) in the central panel (B). In the final NTT (VIK_s) image, which was taken more than two years later, the SN has faded; the disappearance of the red point source at the SN position confirms the progenitor detection.

3.1.2. Explosion mechanism

In their lifetime, the massive-star progenitors of SNe II form iron cores of around $1.4\,M_\odot$, which are supported by electron-degeneracy pressure.[2] As the core approaches the effective Chandrasekhar mass, the concurrent increase in the central density accelerates the electron capture and photo-dissociation rates—leading to a reduction of the number of free electrons. This removes the pressure support of the core in a runaway process. The subsequent collapse to a neutron star or black hole releases on the order of 10^{53} erg of gravitational binding energy (e.g., Foglizzo, 2017). Less than one percent of this energy is needed to unbind the star outside of the iron core (e.g., Ugliano et al., 2012). According to the current paradigm, neutrinos and antineutrinos radiated from the hot proto-neutron star deposit the energy needed to power the observed energetic explosions ($\sim 10^{51}$ erg). Janka (2017) summarizes the current understanding of this neutrino-driven scenario, which was first proposed by Colgate & White (1966) and Arnett (1966). The detection of a neutrino pulse from SN 1987A (Hirata et al., 1987; Bionta et al., 1987; Alexeyev

[2]Low mass SN progenitors of around $8\,M_\odot$ to $10\,M_\odot$ are thought to explode in an earlier stage of their evolution, when their degenerate oxygen-neon cores approach the Chandrasekhar mass (Nomoto, 1984; Nomoto & Leung, 2017).

et al., 1988), which agreed with the expected properties of the core-collapse model, lends credence to the theory.

The core-collapse does not always end in a supernova explosion: if the energy transfer to the ejecta is inefficient, the star might implode to become a black hole followed only by a very faint transient (Sukhbold et al., 2016; Sukhbold & Adams, 2019). Tentative detections of such failed SNe have been reported by Gerke et al. (2015), Adams et al. (2017a), and Adams et al. (2017b).

3.1.3. Light curves

In a successful explosion, the neutrinos drive a shock wave through the star, which ejects the material outside of the core with an energy on the order of 10^{51} erg. Initially, the shock-deposited energy is distributed almost equally between kinetic and internal (radiation) energy. The bulk of the radiation energy is quickly converted to kinetic energy through adiabatic cooling of the expanding ejecta: as the stellar remains fly apart with velocities of a few thousand kilometers per second, their size doubles on timescales of less than a day, each time reducing their internal energy by half (e.g., Arnett, 1980). Still, for SNe II, with their extended progenitors, not all of the radiation is lost to the expansion: during the shock-cooling phase, which lasts several months, around a percent of the shock-deposited radiation energy escapes. This powers a luminous transient with a peak absolute magnitude M_V between -16 and -18 (e.g., Anderson et al., 2014); in extreme cases, like SN 1999br, M_V can be as low as -14. Normal SNe II thus span a large range in luminosity with roughly a factor of 40 separating the brightest from the faintest objects. Type IIL SNe are thought to fall on the high luminosity end of this distribution at an average absolute magnitude of around -18 (e.g., Patat et al., 1994; Faran et al., 2014b).[3]

The rise to the peak is typically fast: radiation energy can quickly escape from the outer layers because the shock-deposited energy is distributed over the entire ejecta. The bolometric light curve peaks on a time scale of only hours to days (e.g., Shussman et al., 2016). In the optical, maximum brightness is reached later, since the spectral energy distribution (SED) only gradually shifts to redder wavelengths as the ejecta cool; the rise time generally increases with the effective wavelength of the observation. In the g-band, the median time to reach the peak is $\sim 7.5\,\mathrm{d}$ with deviations of $\sim 4\,\mathrm{d}$ (González-Gaitán et al., 2015); already in the i-band, it takes a few days more to reach the maximum of the light curve.

Normal SNe II show not only a significant variety of peak luminosities but also light curve morphologies as illustrated by Fig. 3.3, which presents V-band light curves for a large SN II sample. Still, most objects follow a similar schematic behavior. After the peak, there is usually an initial luminosity decline, which lasts a few days to weeks. In this stage, the light curve decreases at a higher rate ($\sim$ 3 mag per 100 d) than during the following plateau phase ($\sim$ 1 mag per 100 d; Anderson et al., 2014), which is characterized by a hundred days of approximately constant luminosity. The plateau starts with the onset of hydrogen recombination in the ejecta (e.g.,

[3] There has been speculation about the existence of low-luminosity SNe IIL (see, e.g., Pastorello et al., 2009a; for the case of SN 1999ga).

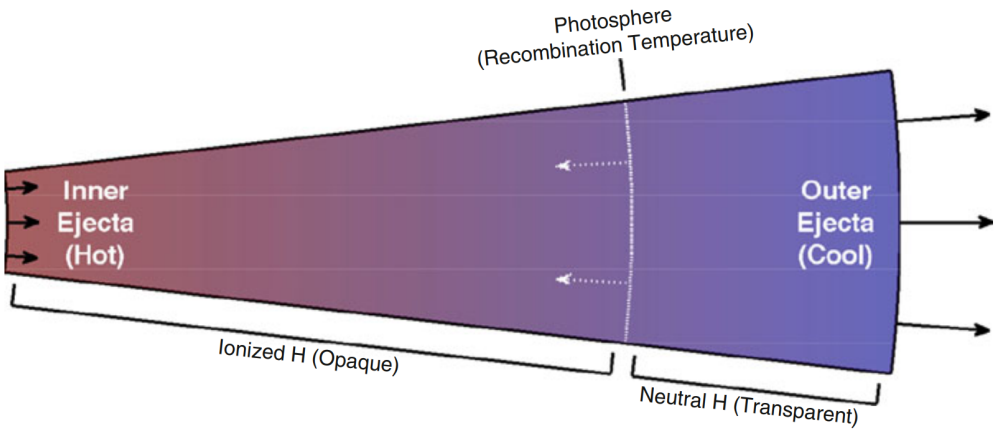

Figure 3.2.: Formation of the photosphere during the plateau phase of SNe II [from Arcavi (2017)].

Dessart et al., 2013): from this point on, the photosphere, from which radiation escapes, closely traces the hydrogen recombination front due to the sharp opacity drop from ionized to neutral hydrogen (see Fig. 3.2). This ties the photospheric temperature to that of hydrogen recombination ($\sim$ 5000 K to 6000 K; Faran et al., 2019). Not only the temperature but also the radius of the photosphere evolves slowly in this phase. Together, the lack of change in the photospheric radius and temperature give rise to the plateau in the bolometric luminosity. The same applies to the color light curves in the redder bands (V, R, I), where the SED is determined by the photospheric temperature rather than metal line blanketing. The plateau ends when the recombination front reaches the helium-rich core and the ejecta become optically thin as the photosphere recedes into the low opacity material (Dessart & Hillier, 2011). After the consecutive light curve drop of $\sim$2.5 magnitudes,[4] a phase of exponential luminosity decay sets in, where the main power source is no longer the release of shock-deposited energy but the radioactive decay of ^{56}Co to ^{56}Fe. In the explosion, between $10^{-3}\,M_\odot$ to $0.3\,M_\odot$ of ^{56}Ni are synthesized, which have been converted almost completely to ^{56}Co by the time the tail is reached (Hamuy, 2003; Spiro et al., 2014; Müller et al., 2017b).[5]

Normal SNe II move through the outlined sequence in highly varied ways. One example is the rate of decline on the plateau, which ranges from more than four magnitudes per 100 d down to slightly negative values (in the V-band; Anderson et al., 2014). Modern studies based on large samples indicate that this transition from classical IIL- to IIP-like behavior is continuous rather than bimodal (Anderson et al., 2014; Sanders et al., 2015; Rubin et al., 2016). The same applies to the distribution of other photometric and spectroscopic properties, such as the color evolution (Galbany et al., 2016) or the Hα morphology (Gutiérrez et al., 2014). This puts the strict subdivision in type IIP and IIL into question. It is not entirely clear what the driving forces

[4] In the V-band.

[5] The Ni mass is correlated with the plateau luminosity: more luminous explosions yield larger amounts of radioactive material and thus have brighter radioactive tails (Hamuy, 2003; Spiro et al., 2014; Müller et al., 2017b).

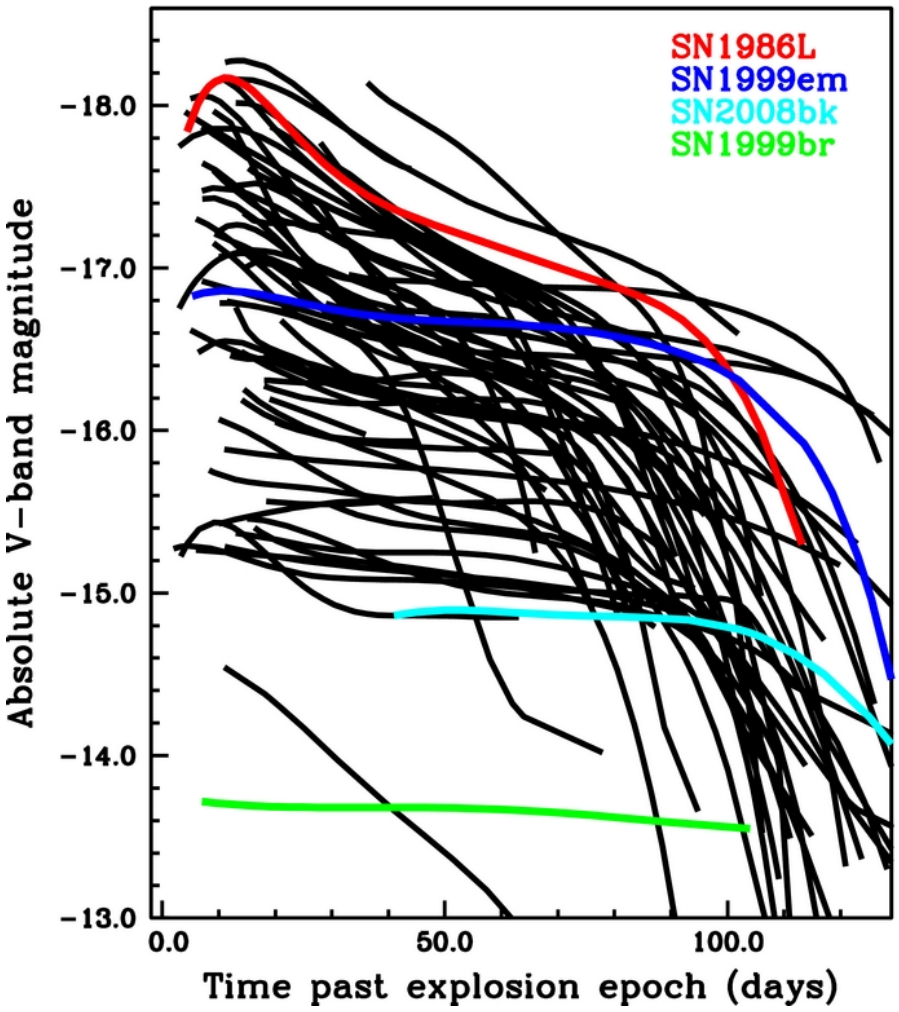

Figure 3.3.: V-band light curves of normal SNe II [from Anderson et al. (2014)].

behind the different light curve decline rates are. At least historically, the most popular hypothesis has been that faster declines are the result of less massive hydrogen envelopes (e.g., Litvinova & Nadezhin, 1983). This is in line with the observation that the transition from an optically thick to thin ejecta and the resulting light curve drop occur earlier for objects with rapidly declining luminosities (Anderson et al., 2014; Valenti et al., 2015): the length of the optically thick phase is thought to be mostly sensitive to the mass of the hydrogen envelope (e.g., Popov, 1993) although the amount and distribution of radioactive nickel also play a role (e.g., Young, 2004; Kasen & Woosley, 2009; Bersten et al., 2011).

3.1.4. Spectra

As illustrated in Fig. 3.4, the spectra of SNe II in the first months after explosion are characterized by a blackbody-like continuum with sawtooth-shaped features superimposed. This type of SED is a generic result of emission from an optically thick expanding medium and is not unique to SNe II (e.g., Sim, 2017). The basic picture is that the continuum is formed in the optically thick regions of the ejecta whereas the line features are imprinted in the optically thin outer layers.[6] In the continuum forming regions, deep inside the atmosphere, the conditions are assumed to be close to thermal equilibrium and the radiation field is approximately a blackbody; the escaping radiation is still vaguely reminiscent of this thermally-created blackbody. Line interactions then imprint the characteristic P-cygni profiles on the smooth continuum emitted from the photosphere. The features are broad with widths of a few hundred Å. The broadening results from the expansion of the ejecta with velocities of a few thousand $\mathrm{km\,s^{-1}}$: photons that are emitted or absorbed at the rest wavelength of the line in the ejecta frame appear red- or blue-shifted to the observer. Figure 3.5 illustrates how scattering of photons into and out of the line of sight produces the characteristic P-cygni shape with a blue-shifted absorption and a rest-wavelength emission component. In practice, the individual P-cygni profiles often blend together due to their significant widths. This produces the highly complex patterns that can be found in SN II spectra, in particular at bluer wavelengths ($\lesssim 5000\,$Å, see Fig. 3.4).

The spectral evolution of SNe II in the photospheric phase is driven mostly by changes in the excitation and ionization state of the spectral forming regions rather than the composition (e.g., Dessart & Hillier, 2011; Dessart et al., 2013). Up to the end of the plateau, the photosphere resides within the hydrogen-rich envelope, whose composition is largely unaffected by the explosion; the elemental abundances at the photosphere trace those of the red supergiant progenitor, which are homogeneous throughout the envelope due to convective mixing (Davies & Dessart, 2019). The composition at the photosphere hardly changes during the first $\sim 70\,$d after explosion as illustrated in Fig. 3.6 for a radiative transfer model of a red supergiant explosion. The figure highlights how well the spectral forming regions are separated from the explosion: during the first half of the plateau ($\lesssim 50\,$d) the photosphere resides in the outermost few tenths solar masses of ejecta. Almost the entire hydrogen-rich envelope, with its many solar masses of material, lies

[6] Here, optically thick and thin refer only to the continuum and not the line optical depth.

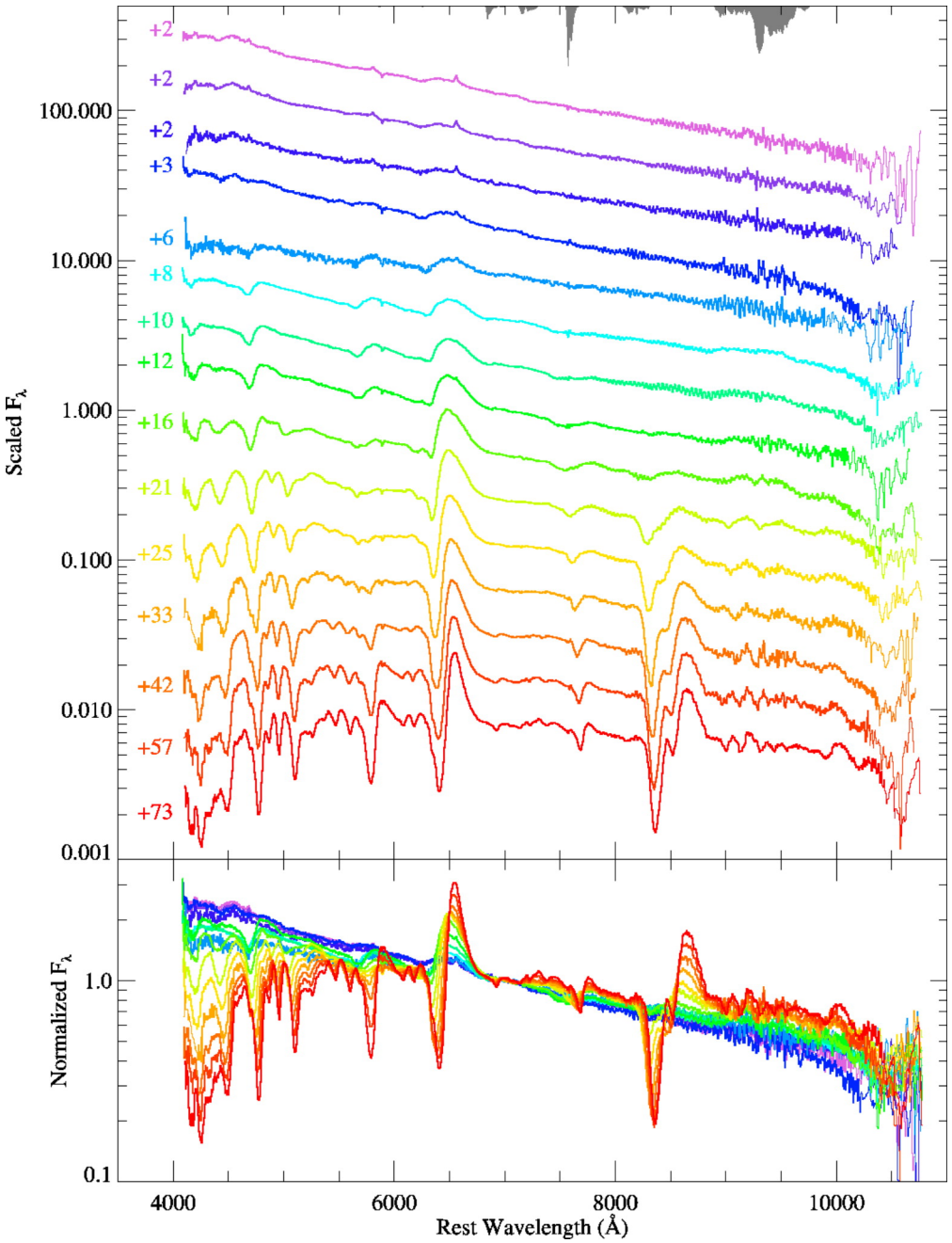

Figure 3.4.: Time series of spectra of the normal SN II 2006bp [from Quimby et al. (2007)]. The observations—which start as early as two days after the explosion and last till the end of the plateau phase—cover most of the photospheric evolution. In the top panel, the individual spectra are scaled and offset for the best visibility and are labeled with the estimated time since explosion. In the bottom panel, all spectra are normalized at ∼7000 Å to highlight the temporal evolution of the continuum and the line features.

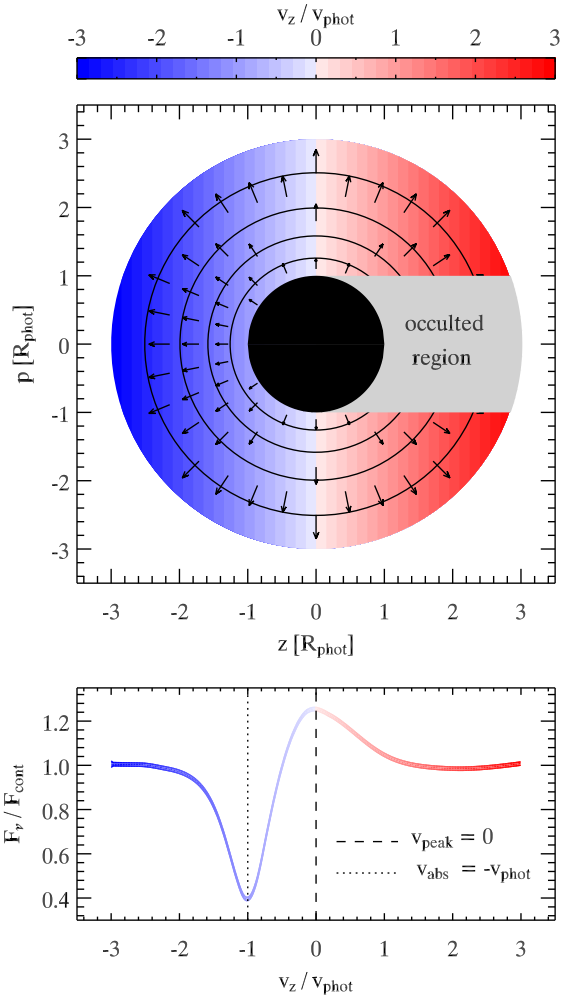

Figure 3.5.: P-cygni line formation. Line interactions add photons to or remove photons from the continuous photospheric SED. In the schematic illustration in the top panel, the observer is on the left-hand side; the optically thick region below the photosphere is indicated in black and the line-forming region in color. Arrows show the velocity of the expanding ejecta. The absorption trough is produced in the material between the observer and the photosphere, where photons can be scattered out of the line of sight; the missing continuum photons appear blue-shifted compared to the rest wavelength of the line, since the absorbing material is moving towards the observer. Scattering into the line of sight, in contrast, is possible from almost all parts of the line-forming region. Only the material behind the optically thick region (gray) is blocked from view. This leads to a small bias of the line emission to blue-shifted wavelengths, since the occulted region is moving away from the observer. Part of the emission is used to fill in the red wing of the absorption trough: the P-cygni profile as the combination of the absorption and emission component peaks close to the rest wavelength of the line (as shown in the bottom panel). The minimum of the P-cygni feature, in turn, is Doppler shifted by approximately the photospheric velocity as long as the line forms close to the photosphere. Figure courtesy of Stephane Blondin.

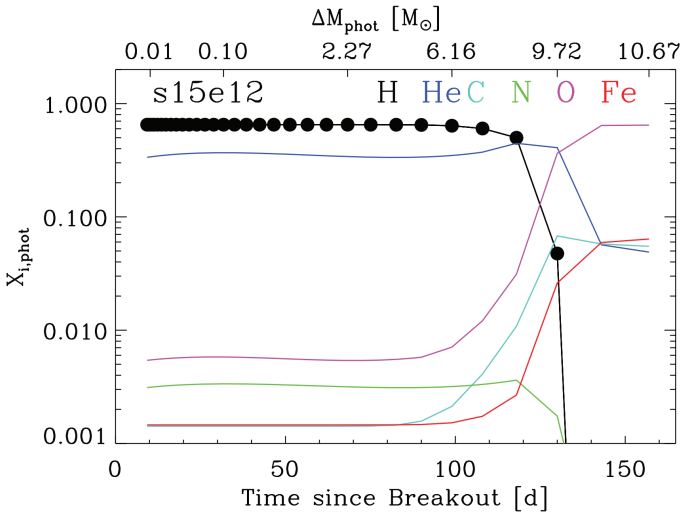

Figure 3.6.: Evolution of the photospheric composition in a SN II [from Dessart & Hillier (2011)]. The plot shows the mass fractions $X_{i,\mathrm{phot}}$ at the photosphere for selected species that are relevant for the spectral formation. The figure illustrates how the composition changes with time as the photosphere moves inward in mass coordinates; the top x-axis indicates how many solar masses the photosphere has receded in mass space at a given time. The results are taken from a time-dependent NLTE radiative transfer calculation for the explosion of a $15\,\mathrm{M}_\odot$ red supergiant.

between the emitting regions and those that have been strongly affected by the explosion, for example through mixing with ^{56}Ni from the explosive nucleosynthesis.

The excitation and ionization state in the spectral forming regions determine which elements and species leave their imprints on the SED. The expansion and cooling of the ejecta are thus the main drivers of the spectroscopic evolution. The flattening of the density profile and the decreasing expansion velocities, which accompany the recession of the photosphere in mass coordinates also play a role: lower velocities make the features narrower and shallower density gradients make them broader and more pronounced.

We will discuss how these effects act together to produce the characteristic spectral evolution at the example of SN 2006bp. Fig. 3.4 shows a time series of spectra for this object from shortly after the explosion to the end of the plateau phase. In the first days after the explosion, the spectral forming regions are very hot and are moving at high velocities: the photospheric temperature and velocity are around 20 000 K and $15\,000\,\mathrm{km\,s^{-1}}$ for the first spectrum taken two days after shock breakout (Dessart et al., 2008). The density profile at this phase is likely extremely steep with a power-law density index close to 50 (Dessart et al., 2008).[7] The rapid drop in density above the photosphere in combination with the high ionization state of the material strongly suppresses line formation; the high velocities dilute the weak features even further. The resulting spectrum is largely featureless with only hints of broad P-cygni lines of hydrogen and He II λ4686. There

[7] The power-law density index is defined as $n = -\,\mathrm{d}\ln\rho/\,\mathrm{d}\ln r$, where r denotes the radius and ρ the density.

are weak narrow emission lines of He II λ4200, He II λ4686, Hβ, C IV $\lambda\lambda$5805, and Hα at the rest wavelength (Quimby et al., 2007). These originate not from the supernova ejecta but from circumstellar material that has been ionized by the intense X-Ray and UV emission of the shock breakout and early shock-cooling phase. The occurrence of flash ionization features, typically from highly-ionized species such He II, N III, or C III, during the first hours to days after explosion is not uncommon (e.g., Niemela et al., 1985; Khazov et al., 2016).[8] A week after the explosion (+8 d), the narrow emission lines have completely faded. The temperature at the photosphere has dropped by half ($\sim$ 12 000 K) and the ionization state in the spectral forming region is lower; the emission from He II has been replaced by He I, with He I λ5876 being the most notable feature. The photosphere has receded by a few thousand km s^{-1} and is now in a region where the density profile is much shallower: the power-law density index is close to ten, which is the value generically predicted for a strong shock moving through the envelope of a massive star (e.g., Imshennik & Nadezhin, 1988; Blinnikov et al., 2000). The flattening of the density profile, the lower ionization, and the decrease in the photospheric velocity have considerably strengthened the P-cygni features—in particular the hydrogen Balmer lines. Over the next days, the spectral forming regions continue to cool rapidly; two weeks after the explosion (+16 d) the temperature has dropped to $\sim$ 8000 K and hydrogen gradually starts to recombine in the spectral forming regions. The Balmer lines have become more pronounced whereas He I λ5876, which originates from a highly excited state, has almost vanished. More and more features from low-ionization species have started to appear in the spectrum: in the near infrared, there are weak lines from O I λ7770 and the Ca II infrared triplet ($\sim$ 8500 Å); in the optical, lines of Fe II including Fe II λ5018 and Fe II λ5169 begin to leave their imprint. By now, the spectral forming regions have stopped cooling rapidly: a month after explosion (+33 d), the photospheric temperature has settled in the range set by hydrogen recombination ($\sim$ 6000 K). Above the photosphere, hydrogen is mostly neutral and the overall ionization level in the spectral forming region is low. The existing lines from low-ionization species have increased significantly in strength; they are joined by others, such as Sc II λ5533 or Na I D (5896-5890 Å). The flux in the blue parts of the spectrum ($\lesssim$ 5400 Å) is strongly suppressed by a dense forest of metal lines—mostly Fe II and Ti II. The spectroscopic evolution for the rest of the plateau phase is slow; most features gradually grow in strength but the qualitative picture stays the same.

The spectral evolution of SN 2006bp—as driven by the cooling and expansion of the ejecta and the accompanying development to lower ionization—is representative for normal SNe II. The details, however, vary significantly between objects. One example is the time scale. To illustrate, for SN 2005cs—a prominent, subluminous SN II—it takes half as long as in SN 2006bp for hydrogen recombination to set in. Significant spectral diversity is also introduced by the wide variety of ejecta velocities. In the middle of the plateau (+50 d), photospheric velocities span a

[8] Flash ionization events are generally associated with the most luminous SNe II (e.g., Khazov et al., 2016). This is challenged by Hosseinzadeh et al. (2018) who found flash ionization features in a low-luminosity, low-velocity SN II.

range from $1500\,\mathrm{km\,s^{-1}}$ to $8000\,\mathrm{km\,s^{-1}}$ (Gutiérrez et al., 2017b).[9] This corresponds to a factor of five difference between the line widths at the low and high velocity end of the distribution.

3.1.5. Polarimetry

Polarimetry makes it possible to probe asymmetries of a supernova without spatially resolving it (Shapiro & Sutherland, 1982). The emission from SNe II is linearly polarized mostly due to electron scattering, which is the dominant continuum opacity source in the spectral forming regions: after an electron scattering, the polarization of a photon is perpendicular to its incident and post-scattering directions (e.g., Chandrasekhar, 1960). Light that is scattered towards the observer is therefore polarized tangentially to the projected photosphere; the degree of polarization is largest at the edge and decreases towards the center.[10] In the observed integrated emission, the polarization signatures from regions with orthogonal polarization directions can cancel; the more spherically symmetric the electron scattering photosphere, the more complete the cancellation. The remaining linear polarization is thus an indicator for asymmetries in the electron distribution of the spectral forming regions (e.g., Wang & Wheeler, 2008).

During their early evolution, SNe II tend to show a low polarization degree of $\sim 0.1\,\%$ (e.g., Leonard et al., 2001, 2006; Chornock et al., 2010). Later on, typically at the end of the plateau phase, this increases to $\sim 1\,\%$.[11] The sudden rise in the polarization is generally understood as the transition from the nearly spherically-symmetric hydrogen envelope to the more asymmetric helium core—which has been shaped by an intrinsically aspherical explosion (e.g., Müller et al., 2017a). Still, even a polarization degree of $\sim 1\,\%$ translates only to asphericities of $\sim 20\,\%$ (Hoflich, 1991; Leonard et al., 2001). Type II supernovae can therefore be considered nearly round, in particular at early epochs.

3.2. Expanding photosphere method

The luminosities—and therefore distances—of SNe II are imprinted in their photospheric spectra: the expansion velocities, as inferred from the P-cygni features, measure the physical size of the emitting regions, and the slope of the blackbody-like continuum their temperatures and consequently surface brightnesses. The size and the surface brightness then give the luminosity of the supernova. This is, in a nutshell, the principle behind the EPM—a variation of the Baade-Wesselink method for pulsating stars (Baade, 1926; Wesselink, 1946).

[9] As inferred from the absorption minimum of Hβ.

[10] In the projected center, all incident directions are viable for electron scattering into the line of sight—leading to a complete cancellation of the polarization signature.

[11] In some objects, the rapid rise in the polarization degree occurs before the end of the plateau phase (e.g., Nagao et al., 2019).

3.2.1. Basic principle

The EPM assumes a sharply-defined, spherically symmetric photosphere as the origin of the blackbody-like emission. This picture is well-justified for SNe II: electron scattering, as the dominant continuum opacity source, provides an almost frequency-independent photosphere at optical wavelengths; the steep density gradient of the ejecta confines the transition from optically thick to thin to a narrow region and polarization measurements show that the electron-scattering photosphere is nearly round (see Sects. 3.1.4 and 3.1.5).

The second prerequisite for the EPM is that the flux at the photosphere f_λ^{ph} can be constrained from physical modeling of the observations. The level of sophistication, in this context, ranges from a simple blackbody at the photometric color temperature (Kirshner & Kwan, 1974) to tailored radiative transfer models that reproduce the entire observed spectrum (Dessart & Hillier, 2006; Dessart et al., 2008).

Given the photospheric flux, the spectra and photometry provide two complementary measurements for the spatial extent of the photosphere: its angular diameter θ and physical size R_{ph}. The angular diameter is determined from the ratio of the model flux at the photosphere and the observed dereddend flux $f_\lambda^{\mathrm{dered}}$:

$$\theta = \frac{R_{\mathrm{ph}}}{D} = \sqrt{\frac{f_\lambda^{\mathrm{dered}}}{f_\lambda^{\mathrm{ph}}}}. \tag{3.1}$$

Here, D is the luminosity distance to the SN. In homologous expansion, R_{ph} is calculated from the photospheric velocity v_{ph} and the time elapsed since the explosion Δt as $R_{\mathrm{ph}} = v_{\mathrm{ph}}\Delta t$. The distance is then determined quasi-geometrically from the ratio of the photospheric radius and angular diameter:

$$D = \frac{R_{\mathrm{ph}}}{\theta} = \frac{v_{\mathrm{ph}}\Delta t}{\theta}. \tag{3.2}$$

This requires knowledge of the time elapsed since the explosion Δt, for example, from a well-sampled early light curve or the detection of the shock-breakout by X-ray or UV satellites. Alternatively, we can constrain the time of explosion within the EPM by measuring the photospheric angular diameter and velocity for multiple epochs. This can be seen by rearranging Eq. (3.2):

$$\frac{\theta}{v_{\mathrm{ph}}} = \frac{\Delta t}{D} = \frac{t - t_0}{D}. \tag{3.3}$$

For homologous expansion, the ratio of the two quantities θ/v_{ph} evolves linearly in time. The slope of the relation is the inverse of the distance D and the intercept with the time axis is the previously unknown time of explosion t_0. Figure 3.7 illustrates how this works in practice for two nearby SNe II.

At cosmological distances, two subtle adjustments to the method become necessary. First, we have to correct the time intervals between spectra for cosmological time dilation [see Eq. (1.13)]. Otherwise, the slope of the regression to θ/v_{ph}—and therefore the distance—will be off by a factor of $1 + z$. Second, we need to account for the fact that the definition of the luminosity

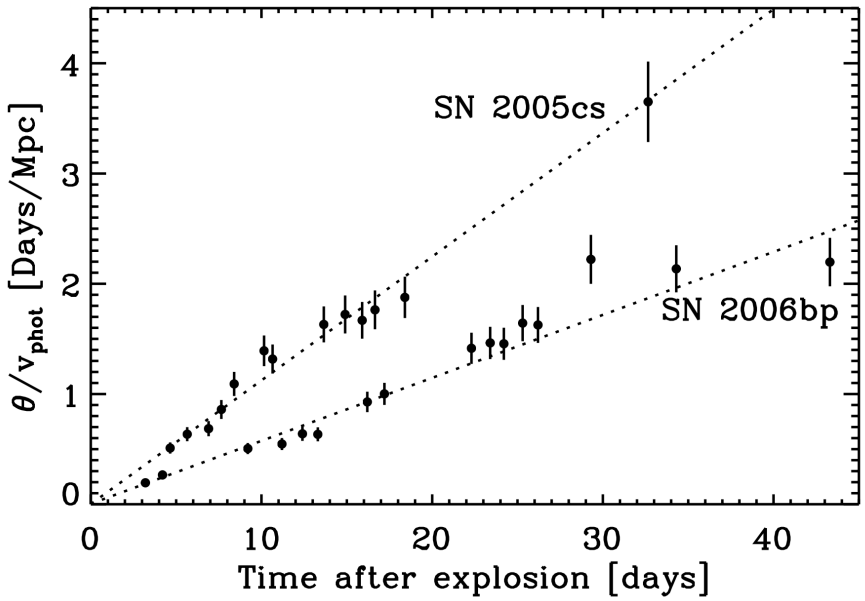

Figure 3.7.: Determination of the distance and time of explosion in the EPM [from Dessart et al. (2008)]. The figure shows the evolution of the ratio of the photospheric angular diameter θ and velocity $v_{\rm ph}$ with time for two nearby SNe II: SN 2005cs and SN 2006bp. The measured datapoints lie approximately on a straight line (dashed); the distance is obtained from the inverse of the slope of this line and the time of explosion from its intercept with the time axis.

distance used in Eq. (3.1) is only applicable at low redshifts. For cosmological distances, we have to transform the observed flux to the SN rest frame as described in Sect. 1.2.5. With the adopted modifications, the EPM yields the correct luminosity distances for high-redshift SNe II (e.g., Gall et al., 2016, 2018).

3.2.2. Challenges

The physical principle at the heart of the EPM is deceptively simple. However, the implementation proves difficult in practice. There are myriad ways to tackle the two most important steps, which are the measurement of photospheric velocities and the construction of a physical model for the photospheric flux. Depending on the approach to these steps, the EPM can yield vastly different results. For example, Jones et al. (2009) find values of H_0 from $52\,\mathrm{km\,s^{-1}\,Mpc^{-1}}$ to $101\,\mathrm{km\,s^{-1}\,Mpc^{-1}}$ by varying the model for the photospheric flux and the treatment of reddening in their analysis of 12 SNe II. For this reason, the EPM is often considered 'an art instead of an objective measurement tool' (Hamuy, 2001). In the following, we highlight the challenges of the different steps and demonstrate how these can be overcome by radiative transfer modeling of individual SNe—an approach known as the tailored EPM (Dessart & Hillier, 2006; Dessart et al., 2008).

Photospheric velocities

The P-cygni features contain information about the velocities in the line-forming region—and thus the photospheric velocity v_{ph}. However, connecting the shapes and wavelength shifts of the lines to v_{ph} is nontrivial: the P-cygni features form over a wide range of projected and actual expansion velocities.

The most common methods are based on measuring the velocity at maximum absorption in line profiles. Weak lines are preferred because their absorption minima are formed close to the photosphere. Figure 3.8 illustrates how the absorption velocities relate to v_{ph} for an exemplary set of lines. The absorption velocities of strong features, such as Hα and Hβ, are significantly higher than v_{ph}: absorption can occur far above the photosphere. Weaker lines, such as Hγ or Fe II λ5169, track v_{ph} more closely. Still, their absorption velocities can overestimate—and underestimate—v_{ph} by as much as 15 %. The fact that the absorption velocity can fall below v_{ph} is a good example of the intricacies associated with interpreting the line profiles. Imagine the idealized scenario of an extremely weak line forming directly above a sharply-defined photosphere. In this case, the absorption always occurs in material that is moving at v_{ph} but the projected velocities, which determine the line profile, range from v_{ph} down to zero. The absorption is almost constant over this velocity window and the center of the absorption trough is at $\sim v_{\mathrm{ph}}/2$.

The absorption velocity depends sensitively on the behavior of the line optical depth and line source function above the photosphere (e.g., Dessart & Hillier, 2005a,b). For example, if a line is much stronger in emission than in absorption (like Hα), this imbalance shifts the

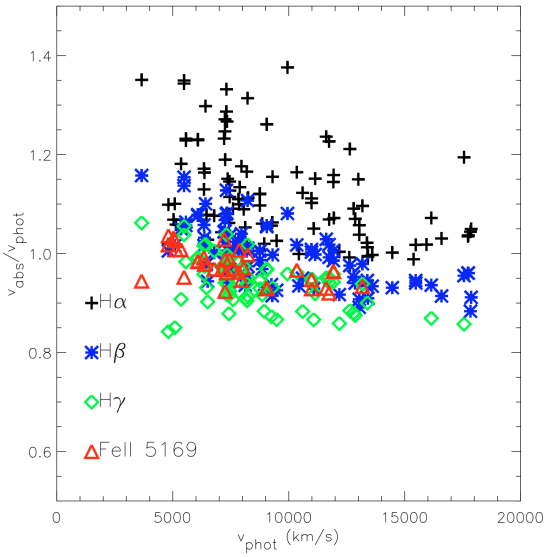

Figure 3.8.: Ratios of line absorption $v_{\rm abs}$ and photospheric velocities $v_{\rm ph}$ [from Dessart & Hillier (2005a)]. The ratios have been extracted from a large set of steady-state SN II radiative-transfer models and are plotted against the photospheric velocity of the model. As in real SNe II, higher velocities generally indicate earlier phases and higher temperatures. The figure includes the three lowest hydrogen Balmer lines and the weak Fe II λ5169 feature. The latter is commonly used as a reliable indicator of the photospheric velocity.

absorption minimum. The only way to capture these effects accurately is through the use of detailed radiative transfer models.[12] On the most basic level, these calculations serve as a guide for selecting transitions that track the photospheric velocity closely: the SN II models in Fig. 3.8 show that measurements of Fe II λ5169 absorption velocities yield $v_{\rm ph}$ with an intrinsic uncertainty of around 5 % to 10 %; this would be satisfactory for most applications. However, Fe II λ5169 is not visible in the first $\sim$ 12 d after the explosion (e.g., Gutiérrez et al., 2017b) and it is difficult to detect in low-signal-to-noise spectra. These are serious limitations when the goal is to measure velocities for the EPM at cosmologically relevant distances: the early epochs are crucial for constraining the time of explosion and noisy spectra are the norm rather than the exception for distant SNe. Many studies resort to using Hβ or even Hα velocities because these indicators are visible at all epochs and are comparatively easy to measure (Nugent et al., 2006; Jones et al., 2009; Gall et al., 2018). These velocities are then converted to $v_{\rm ph}$ through simple relations, which are calibrated either on model atmosphere calculations (e.g., Jones et al., 2009) or on nearby SNe (e.g., Nugent et al., 2006; Gall et al., 2018).[13] The dispersion in the calibration is an additional source of uncertainty in the photospheric velocity measurement. For an individual supernova,

[12] This extends to other effects that we have neglected up to now. These include, for example, additional opacity at the position of the line or the overlap between line and continuum forming regions.

[13] In the latter case, the observed velocities are transformed to Fe II λ5169 velocities, which are assumed to be almost identical to $v_{\rm ph}$.

this error will be systematic rather than statistical. The same applies for a SN sample unless the calibrating objects are completely representative of the SNe that the relation is applied to. This is of particular concern for calibrations based on model atmosphere calculations: the set of radiative transfer models is not necessarily representative of the true population of SNe II.

A better way to measure photospheric velocities at any epoch, and for low signal-to-noise spectra, is radiative transfer modeling of each observation. This uses the line profiles of all features and not only the absorption minimum of a single transition. By using a larger set of velocity indicators—including strong lines—this makes it possible to determine $v_{\rm ph}$ accurately even for noisy spectra. The potential biases of the calibration approaches are largely avoided: the tailored radiative transfer models are representative of the observed SNe by construction.

Photospheric flux

The flux at the photosphere together with its physical size determines the luminosity of the supernova. For blackbody radiation, as originally assumed in the EPM (e.g., Kirshner & Kwan, 1974; Branch et al., 1981), the flux follows directly from the temperature of the emission. The latter can be determined from photometric colors.

Reality is more complicated than this simple model: the emission deviates from that of a blackbody in obvious and less obvious ways, the most apparent being the presence of strong line features. A more subtle, but equally important, difference is that the continuum flux is considerably diluted compared to a blackbody of the same color temperature (e.g., Hershkowitz et al., 1986a,b). This is a direct consequence of the weak coupling between the radiation field and the thermal electron gas in SNe II. The electron scattering opacity greatly exceeds the absorptive opacity in the low-density, ionized, hydrogen-rich environments of SN II atmospheres (e.g., Eastman et al., 1996). Typically, the absorptive component makes up only a few hundredths of the total opacity at the photosphere. Photons are thus coupled to the thermal pool only every few tens of scatterings: a photon that is thermally created at considerable optical depth can escape from the ejecta without being thermalized again. The characteristic optical depth for thermalization $\tau_{\rm thm}$ is proportional to the square root of the expected number of scatterings between absorptions (e.g., Mihalas, 1978):

$$\tau_{\rm thm} \propto \sqrt{\frac{\chi_\nu}{\chi_{\nu,\rm abs}}}. \tag{3.4}$$

Here, χ_ν is the total and $\chi_{\nu,\rm abs}$ the absorptive opacity. Most of the blackbody-like continuum is created close to the thermalization depth: thermal radiation from deeper in the ejecta cannot make it to the surface; radiation from lower optical depths does not couple efficiently to the electron gas and therefore retains the color temperature of the thermalization region. The latter is exacerbated by the steep density gradients of SN II envelopes: the ratio of absorptive to scattering opacity

decreases approximately proportional to the density.[14] Thus, the coupling efficiency between the radiation field and thermal pool drops rapidly in the outer layers.

The continuum radiation is created at optical depths of a few for typical values of $\chi_\nu/\chi_{\nu,\mathrm{abs}} \approx 10^{-2}$ (e.g., Eastman et al., 1996). The mean intensity at this thermalization depth is well approximated by a blackbody. The flux is much lower than the mean intensity because the radiation field is nearly isotropic this deep in the ejecta. On the way to the surface, electron scattering conserves both the shape of the SED and the specific flux set at the thermalization depth.[15] The emergent radiation thus resembles a dilute blackbody. We can estimate the amount of dilution if we approximate the ejecta above the thermalization depth as a plane-parallel, gray, scattering atmosphere. In this case, the flux F_ν according to the Eddington approximation (see, e.g., Mihalas, 1978) is given by

$$F_\nu = \frac{4\pi}{3} J_\nu(\tau) \left(\tau + \frac{2}{3}\right)^{-1} . \tag{3.5}$$

The flux is reduced compared to the mean intensity at the thermalization depth $J_\nu(\tau_{\mathrm{thm}}) = B_\nu$, and thus a blackbody, by around $1/\tau_{\mathrm{thm}}$.[16] For a typical thermalization depth of around five, the emergent flux is only one fifth of that of a blackbody of the same temperature.

The importance of this effect for the EPM was first realized by Wagoner (1981). Hershkowitz et al. (1986a,b), shortly after, introduced the dilution factor ξ to account for continuum flux dilution in the blackbody emission model. The factor was defined as a correction to the distance and not the flux; the reduction in flux is hence given by ξ^2. Later, Eastman et al. (1996) and Dessart & Hillier (2005a) replaced the simple continuum-flux-dilution models used for the initial dilution factors by more detailed radiative transfer calculations. The correction factors, in this case, are determined from the best-fitting dilute-blackbody models for the synthetic spectra. In this way, not only the effect of continuum flux dilution is corrected for but also the other deviations from blackbody emission including lines and limb darkening. The calculated correction factors depend primarily on the color temperature (e.g., Eastman et al., 1996; Dessart & Hillier, 2005a). As can be seen in Fig. 3.9, the dilution factors are weakly sensitive to temperature at color temperatures above 9000 K, but start to increase rapidly at lower temperatures. The latter is related to the onset of metal line blanketing in the ejecta. An easy, approximate way to obtain a correction factor for any color temperature is to use a fit curve to the temperature dependence of the model atmosphere calculations (e.g., Eastman et al., 1996). However, the accuracy of this approach is limited through the considerable variation around the fit relation. In particular at

[14] The scattering opacity scales approximately linearly with density while the absorptive opacity scales with its square.

[15] The latter is a consequence of radiative equilibrium for which the integrated flux is constant throughout the atmosphere. Naturally, for a conserved spectral shape and integrated flux also the specific flux remains unchanged.

[16] The sphericity of the supernova ejecta leads to a small additional dilution of the continuum flux. In a spherically-symmetric atmosphere not the flux F but Fr^2 is conserved in radiative equilibrium, with r being the radius. Thus, the flux between the thermalization radius R_{thm} and the photosphere is reduced by $(R_{\mathrm{thm}}/R_{\mathrm{ph}})^2$. The dilution by scattering ($\sim 1/\tau_{\mathrm{thm}}$), in contrast, scales like $(R_{\mathrm{thm}}/R_{\mathrm{ph}})^{n-1}$, where n is the power-law index of the density profile. For the steep density gradients of SNe II ($n \approx 10$), the spherical dilution of the radiation is only a small modification to that of a plane-parallel atmosphere.

high temperatures, this introduces significant uncertainties on the order of 20 % (e.g., Dessart & Hillier, 2005a; Jones et al., 2009). The scatter reflects the diversity of supernova atmospheres at a given color temperature, which span a wide range of expansion velocities, photospheric densities, and so forth. All of these parameters influence the correction factors.

Radiative transfer modeling of each spectrum provides a way to constrain these quantities and thus reduces the uncertainties in the correction factors. Moreover, the naive fit relation introduces a potential bias in the distance estimation because the atmosphere models are not necessarily representative for a given observational sample. Clearly, this pitfall is avoided through the use of radiative transfer calculations that are tailored to match the observed data.

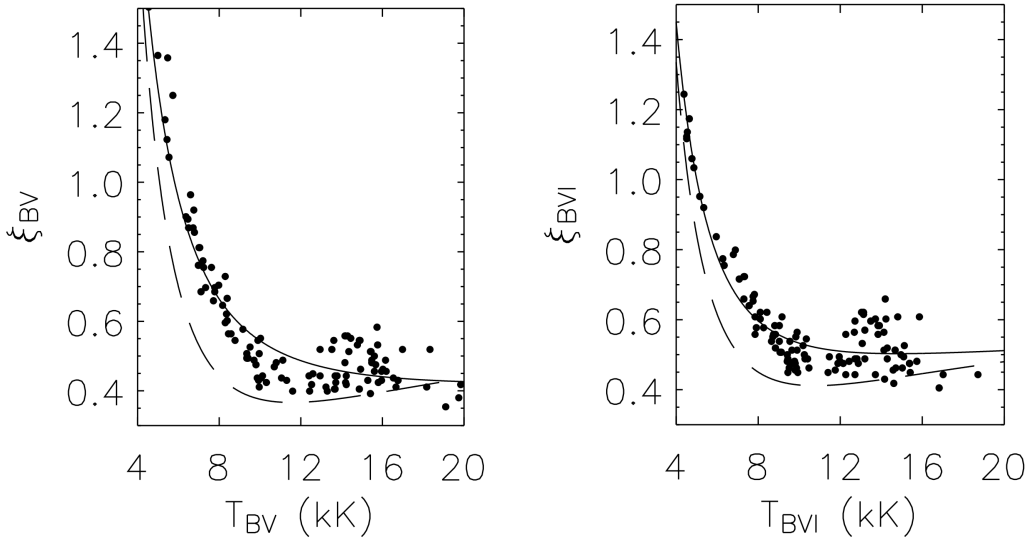

Figure 3.9.: Dilution factors ξ as a function of color temperature for the BV and BVI bandpass combinations [from Dessart & Hillier (2005a)]. Filled circles represent individual steady-state SN II atmosphere models, the solid line a polynomial fit to the full model set. The fit to the calculations of Eastman et al. (1996) is included as the dashed line for comparison purposes.

Part II.

A new type II supernova radiative-transfer code: development and first applications

Summary

An independent measurement of H_0 through the tailored EPM requires modeling large numbers of observed SN II spectra. A fast but accurate radiative transfer code is thus a prerequisite for achieving this goal. We have created the necessary tool through substantial extensions of the Monte Carlo spectral synthesis code TARDIS (Kerzendorf & Sim, 2014). The development and first applications of the new code are published in Vogl et al., A&A, 621, A29, 2019, which is reproduced with permission ©ESO in the following part of the thesis.

The application of TARDIS to SN II spectral synthesis required the implementation of additional physical processes: bound-free, free-free, and collisional interactions. In particular, bound-free processes are essential in SNe II since they are the main channel for thermalizing the radiation field. We account for the significant departures from local thermodynamic equilibrium (LTE), which arise in SNe II due to the low densities and diluted radiation fields, through a full non-LTE (NLTE) excitation and ionization calculation for hydrogen. We improve the determination of the thermal structure by replacing the simplified prescription of the original TARDIS implementation through a detailed thermal-balance calculation based on the heating and cooling rates. Finally, we refine the treatment of relativistic transport effects and optimize the spectral synthesis procedure for the high optical depths of our simulations.

These significant improvements make it possible to produce synthetic spectra that match observed SNe II as demonstrated through the comparison to two exemplary epochs of SN 1999em. As a first application, we investigate the long-standing discrepancy between the two published sets of dilution factors by Eastman et al. (1996) and Dessart & Hillier (2005a). The deviations between the two studies are a major source of uncertainty in the EPM and account for differences of $\sim 20\,\%$ in the distance. We calculate a large number of TARDIS radiative transfer models to derive an independent set of dilution factors. Our results show good agreement with Dessart & Hillier (2005a), which ameliorates the tension between the available corrections factors. We scrutinize the differences between the studies including the setup of the model grid and the treatment of radiative transfer to shed some light on the disagreements in the dilution factors. Finally, we utilize our large model grid to investigate the dependence of the dilution factors on atmospheric parameters such as the density profile or metallicity.

Author contributions I contributed the main driving force to this project. I have developed the extended version of the TARDIS code for spectral modeling of SNe II and I have applied it to calculate a new set of dilution factors for the EPM. I am the main author of the manuscript and I made all the figures. A preliminary, simplified implementation of the bound-free, free-free, and collisional processes was presented previously in my master's thesis (Vogl, 2016). Major improvements in this first step were implemented during my Ph.D. All subsequent steps were performed entirely during the Ph.D.

Spectral modeling of type II supernovae

I. Dilution factors

C. Vogl, S. A. Sim, U. M. Noebauer, W. E. Kerzendorf, and W. Hillebrandt

ABSTRACT We present substantial extensions to the Monte Carlo radiative transfer code TARDIS to perform spectral synthesis for type II supernovae. By incorporating a non-LTE ionization and excitation treatment for hydrogen, a full account of free-free and bound-free processes, a self-consistent determination of the thermal state and by improving the handling of relativistic effects, the improved code version includes the necessary physics to perform spectral synthesis for type II supernovae to high precision as required for the reliable inference of supernova properties. We demonstrate the capabilities of the extended version of TARDIS by calculating synthetic spectra for the prototypical type II supernova SN1999em and by deriving a new and independent set of dilution factors for the expanding photosphere method. We have investigated in detail the dependence of the dilution factors on photospheric properties and, for the first time, on changes in metallicity. We also compare our results with the previously published sets of dilution factors and discuss the potential sources of the discrepancies between studies.

4. Introduction

In recent years the availability of spectral data for hydrogen-rich supernovae (Type II; SNe II) has increased dramatically. Measurements for hundreds of SNe II are now publicly accessible (see, e.g., Poznanski et al., 2009; D'Andrea et al., 2010; Hicken et al., 2017; for recent data releases), providing a dataset that contains a wealth of information about the kinematics of the explosion, the progenitor systems (e.g., Jerkstrand et al., 2012), the circumstellar material (e.g., Quimby et al., 2007), and much more. Most of the analysis of this data has focused on the study of easily measurable spectral parameters such as line absorption velocities or equivalent widths and their correlations (see, e.g., Gutiérrez et al., 2017a,b), omitting the full information contained in the spectra. To establish connections between these parameters and the underlying quantities, such as the metallicity, most studies rely on approximate relations that have been calibrated based on theoretical models (see, e.g., Anderson et al., 2016). In contrast, only a few well-observed type II supernovae, such as SN1999em (Baron et al., 2004; Dessart & Hillier, 2006), SN2005cs (Baron et al., 2007; Dessart et al., 2008) or SN2006bp (Dessart et al., 2008), have been studied using detailed radiative transfer models, which provide a direct way to infer information about the chemical composition, the density profile and other parameters from the full spectral time series. This applies in particular to the use of SNe II as distance indicators, despite the fact that an absolute distance estimate is a natural byproduct of a quantitative spectroscopic analysis (see Baron et al., 1995, 1996a, 2004, 2007; Lentz et al., 2001; Mitchell et al., 2002). SNe II have a long history as cosmological probes (Kirshner & Kwan, 1974; Schmidt et al., 1994) and have regained popularity in recent years due to the increased availability of data at high redshifts (e.g., Poznanski et al., 2009; Gall et al., 2018) and, in the era of high precision cosmology, due to the rising need for independent tests of our cosmological models. Recent efforts have focused mainly on methods that rely on various observed correlations between photometric and spectroscopic parameters such as the standard candle method (SCM) by Hamuy & Pinto (2002), the photometric color method by de Jaeger et al. (2015) or the photospheric magnitude method by Rodríguez et al. (2014). Both Gall et al. (2018) and de Jaeger et al. (2017) demonstrate that with the SCM or the expanding photosphere method (EPM) distance measurements of SNe II up to redshifts of ≈ 0.34 are feasible, highlighting the progress that has been made possible through the availability of new data. In contrast, the determination of distances from radiative transfer modeling has stagnated in recent years. Both the tailored EPM (Dessart & Hillier, 2006; Dessart et al., 2008) and the spectral fitting expanding atmosphere method (SEAM) (Baron et al., 1995, 1996a, 2004, 2007) have never been applied outside the local universe. Nevertheless, their independence of

the cosmic distance ladder as well as their foundation in well-understood physics make them a promising independent tool for cosmology.

Motivated by the wealth of available spectral data and the unique diagnostic abilities of radiative transfer modeling, we have developed a new numerical tool for performing spectroscopic analysis of SNe II. Since our main goal is to provide a tool for parameter inference, we neglect time-dependent effects in favor of computational expediency. Currently, the high computational costs prevent the application of numerical methods that self-consistently simulate the time evolution of the radiation field and the plasma state based on initial conditions (Dessart & Hillier, 2011; Dessart et al., 2013) to this purpose. Our approach is an extension of the Monte Carlo radiative transfer code TARDIS (Kerzendorf & Sim, 2014), which was originally developed for spectral synthesis in type Ia supernovae (SNe Ia). We have extensively modified and improved the physical treatment of radiative transfer implemented in TARDIS to be applicable to the modeling of SNe II atmospheres. This improved version of the code is then used to calculate a new, independent set of dilution factors for the EPM. In the EPM the dilution factors as introduced by Hershkowitz et al. (1986a,b) and Hershkowitz & Wagoner (1987) correct for the deviation of the supernova emission from that of a blackbody of the same color temperature. They provide the possibility to compare our model calculations to previously published numerical results by Eastman et al. (1996; E96 from now on) and Dessart & Hillier (2005a; D05 from now on) in a simple parametrized fashion. Currently, the systematic discrepancies between the two sets of dilution factors constitute one of the most significant sources of uncertainty in the EPM, accounting for differences of roughly 20% in the inferred distance (e.g., Takáts & Vinkó, 2006; Jones et al., 2009; Gall et al., 2016, 2018). This significant uncertainty highlights the need for additional calculations based on independent numerical methods to understand and resolve the current tension.

The structure of the paper is as follows. We begin with a detailed description of the physical extensions and their numerical implementation into TARDIS in Chapter 5. In Chapter 6, we provide a brief review of the EPM and discuss the basic physics of the dilution factors. As a first application of the extended version of TARDIS, we present radiative transfer models for two epochs of the prototypical SN II SN1999em in Chapter 7. The next sections are dedicated to the presentation and discussion of our main application, the calculation of a new set of EPM dilution factors. The setup of the necessary grid of supernova models is described in Chapter 8, followed by an analysis of the calculated dilution factors in Chapter 9. Here, we focus particularly on the differential influence of the model parameters such as photospheric density or metallicity. To put our results into context and to understand the differences between the published set of dilution factors, a comparison to previous studies is given in Chapter 10. We investigate the differences in the adopted numerical approaches and examine the different choices for the atmospheric properties. Finally, we summarize our results and give an outlook in Chapter 11.

5. Method

We present an extended version of the one-dimensional Monte Carlo (MC) radiative transfer code TARDIS (Kerzendorf & Sim, 2014) that has been significantly extended for the application to SNe II. TARDIS is based on the indivisible energy packet MC methods of Lucy (1999a,b, 2002, 2003) and has been developed for rapid spectral modeling of SNe Ia. It has been used to study various aspects of SN Ia explosion physics. Applications include abundance tomographies (Barna et al., 2017), a study of spectral signatures of helium in double-detonation models (Boyle et al., 2017), as well as analyses of SNe Iax spectra (Magee et al., 2016, 2017). In these studies only the effects of Thomson scattering and bound-bound line interactions are simulated in detail. This is a reasonable approximation for SNe Ia but not for SNe II, which have a higher ratio of continuum to line opacity due to the hydrogen-rich composition. To adapt TARDIS to these conditions, we extend our treatment of radiation–matter interactions to include bound-free, free-free as well as collisional processes using the macro atom scheme of Lucy (2002, 2003) as outlined in Sect. 5.1. Further necessary improvements to the code can be motivated based on the peculiarities of radiative transfer in SNe II. SNe II atmospheres are characterized by comparatively low densities at the photosphere and a scattering dominated opacity. Due to the low densities, collisions are ineffective at coupling the level populations and ionization and excitation are mainly controlled by the radiation field. The radiation field is dilute compared to its equilibrium value as a result of the dominance of electron-scattering opacity and thus significant departures from local thermodynamic equilibrium (LTE) arise even far below the photosphere (see, e.g., Dessart & Hillier, 2011). To address this issue, we have extended the code as outlined in Sect. 5.2. Another consequence of the scattering dominated environment is that relatively high optical depths on the order of $\tau \propto \mathcal{O}(10)$ are needed to guarantee a full thermalization of the radiation (see, e.g., Eastman et al., 1996). At such high optical depths the atmospheric structure is strongly affected by relativistic transfer effects as demonstrated by Hauschildt et al. (1991). The inclusion of these effect in TARDIS is described in Sect. 5.1.4.

5.1. Monte Carlo simulations

To find a consistent solution for the plasma state and the radiation field, TARDIS performs a series of Monte Carlo radiative transfer simulations. At every radiative transfer step, a large ensemble of indivisible energy packets (see Abbott & Lucy, 1985; Lucy, 1999a, 2002, 2003) representing monochromatic photon bundles is initialized at the inner boundary. Initial packet properties are

assigned under the assumptions of the LTE diffusion limit. Thus, packet frequencies are sampled from a blackbody distribution at the inner boundary temperature T_i and propagation directions are selected according to zero limb-darkening in the comoving frame. Uniform packet energies are chosen such that the injected packets carry a total comoving frame luminosity $L_\mathrm{i} = 4\pi R_\mathrm{i}^2 \sigma T_\mathrm{i}^4$, where σ is the Stefan-Boltzmann constant and R_i is the radius of the inner boundary. With initial properties assigned, the propagation of the packets is simulated under the assumption of a steady-state, that is to say, neglecting time dependence, as outlined in the following section.

5.1.1. Packet propagation

After initialization, each packet is followed until it leaves the computational domain through the inner or outer boundary. Between the boundaries the supernova atmosphere has been discretized into equidistant, spherical shells. Within each shell the plasma properties such as the opacity or the electron temperature are assumed to be constant. During the propagation the effects of Thomson scattering, hydrogen bound-free, free-free, bound-bound as well as collisional processes are taken into account. As described in Kerzendorf & Sim (2014), line opacity is treated in the Sobolev approximation (see Sobolev, 1957). For micro-turbulent velocities on the order of $100\,\mathrm{km\,s^{-1}}$, this is as accurate as the comoving frame method in describing the formation of the Balmer lines in SNe II (see Duschinger et al., 1995). Following Lucy (2003), the free-free opacity

$$\chi_\mathrm{ff}(\nu) = \alpha_\mathrm{ff}\, \nu^{-3} T_\mathrm{e}^{-1/2} n_\mathrm{e} \left(1 - e^{-h\nu/k_\mathrm{B}T_\mathrm{e}}\right) \sum_{j,k} N_{j,k}(j-1)^2 \tag{5.1}$$

is evaluated with free-free gaunt factors set to unity. Here, $N_{j,k}$ denotes the number density of ionization stage j of element k, T_e is the electron temperature, n_e the electron density and ν the frequency. The prefactor α_ff has the value $3.69 \times 10^8\,\mathrm{cm^5 K^{1/2}/s^3}$. Since hydrogen is the dominant source of bound-free opacity in SNe II, we restrict the inclusion of these processes currently only to this element. However, since an extension to more species is conceptually straightforward, we present the governing equations in their general form. Thus, the opacity resulting from photoionizations of electrons in level i of ion j,k is given by

$$\chi^\mathrm{bf}_{i,j,k}(\nu) = \alpha_{i,j,k\to j+1,k}(\nu) \left(n_{i,j,k} - n^*_{i,j,k} e^{-h\nu/k_\mathrm{B}T_\mathrm{e}}\right), \tag{5.2}$$

where $n_{i,j,k}$ and $n^*_{i,j,k}$ denote the actual and the respective LTE level number densities (see equation 5.25 of Hubeny & Mihalas, 2014). The cross-section for photoionzation $\alpha_{i,j,k\to j+1,k}(\nu)$ is obtained from tabulated values through linear interpolation.

To account for the inclusion of hydrogen bound-free, free-free as well as collisional processes small modifications to the packet propagation procedure of Kerzendorf & Sim (2014; Sect. 2.6) have been necessary. In particular for continuum interactions an additional MC experiment is needed to determine the physical absorption mechanism. The probabilities for bound- free absorption, free-free absorption and Thomson scattering are given by $\chi^\mathrm{bf}/(\chi^\mathrm{bf} + \chi^\mathrm{ff} + \chi^\mathrm{Th})$,

$\chi^{\mathrm{ff}}/(\chi^{\mathrm{bf}}+\chi^{\mathrm{ff}}+\chi^{\mathrm{Th}})$ and $\chi^{\mathrm{Th}}/(\chi^{\mathrm{bf}}+\chi^{\mathrm{ff}}+\chi^{\mathrm{Th}})$ respectively. If a bound-free process is selected, a specific continuum for absorption has to be assigned according to the probabilities $\chi^{\mathrm{bf}}_{i,j,k}/\chi^{\mathrm{bf}}$ for photoionization from specific levels i of ion j,k. Regardless of the type of interaction, we use the macro atom scheme of Lucy (2002, 2003) to select an emission channel as outlined in Sect. 5.1.2. For bound-free and free-free emission, the packet has to be assigned an appropriate frequency before the propagation can be resumed. We employ the approximate sampling rule of Lucy (2003; Eq. 41) for free-free processes and linear interpolation on precomputed values of the emissivity for bound-free interactions.

5.1.2. Macro atom

We use the macro atom scheme of Lucy (2002, 2003) for a general treatment of complicated radiation-matter interactions, such as recombination cascades, fluorescent line emission or cooling emission. In this scheme, packet splitting for processes with multiple emission channels is avoided by assigning the total energy of the packet randomly to one possible interaction channel according to a set of rules derived from the assumption of statistical equilibrium. In Kerzendorf & Sim (2014), only the redistribution of excitation energy created by bound-bound absorption events was simulated using the macro atom machinery. We introduce indivisible packets of thermal kinetic energy (k-packets) and ionization energy (i-packets) in addition to the packets of excitation energy (macro atoms) included in Kerzendorf & Sim (2014) to treat continuum interactions. k-packets can be created by bound-free and free-free absorption events as well as collisional deactivations of i-packets or macro atoms. Since both thermal and ionization energy are created in photoabsorption events, the r-packet is transformed into a k-packet with probability $p^k = \nu_{i,j,k}/\nu'$ and into an i-packet otherwise. Here, $\nu_{i,j,k}$ is the threshold for ionization and ν' is the frequency of the r-packet in the comoving frame. Based on the assumption of radiative balance in the fluid rest frame, all i-packets, macro atoms and k-packets have to be converted in-situ back to r-packets. For k-packets this is done by sampling the rates at which different physical processes cool the electron gas. All treated cooling rates are listed in Sect. 5.2.3. For macro atoms and i-packets, the situation is more complicated due to the possibility of internal transitions. In both cases we sample the internal energy flow rates until a radiative deexcitaton process is selected or a collisional deactivation to a k-packet occurs (see Lucy, 2002, 2003). The needed energy flow rates are calculated with rate coefficients evaluated as described in Sect. 5.2.

5.1.3. Reconstruction of radiation field quantities

For our detailed treatment of ionization and thermal structure (see Sect. 5.2), estimates for the radiative bound-free rates and radiative heating rates are needed. We use volume-based estimators (Lucy, 1999b, 2003) to reconstruct the relevant quantities from the trajectories of the packet ensemble. In this approach, the time-averaged contributions of all trajectory segments, on which the process can in principle occur, are taken into account. Thus, to obtain an estimate

for the photoionization rate coefficient $\gamma_{i,j,k}$ for level i, j, k, we sum over all path segments $\mathrm{d}s$ for which the comoving frame (CMF) frequency ν' of the packet is larger than the threshold for photoionization $\nu_{i,j,k}$

$$\gamma_{i,j,k} = \frac{1}{\Delta t V} \sum_{\nu' \geq \nu_{i,j,k}} \varepsilon'_\nu \frac{\alpha_{i,j,k \to j+1,k}(\nu')}{h\nu'} \, \mathrm{d}s. \tag{5.3}$$

Here, V is the volume of the respective grid cell and ε'_ν is the CMF packet energy. The time interval Δt is a numerical normalization factor that is determined by the energy injection rate at the lower computational boundary. Similarly, the estimator for the stimulated recombination rate coefficient is given by

$$\alpha^{\mathrm{stim}}_{i,j,k} = \Phi_{i,j,k}(T_\mathrm{e}) \frac{1}{\Delta t V} \sum_{\nu' \geq \nu_{i,j,k}} \epsilon'_\nu \frac{\alpha_{i,j,k \to j+1,k}(\nu')}{h\nu'} e^{-h\nu'/k_\mathrm{B}T_\mathrm{e}} \, \mathrm{d}s. \tag{5.4}$$

Here, the Saha factor

$$\Phi_{i,j,k}(T) = \frac{n^*_{i,j,k}}{n^*_{0,j+1,k} n_\mathrm{e}} \tag{5.5}$$

enters, which connects the LTE level populations $n^*_{i,j,k}$ to the ground state population $n^*_{0,j+1,k}$ of the next higher ionization stage. The heating rate coefficient for photoionization is

$$h^{\mathrm{bf}}_{i,j,k} = \frac{1}{\Delta t V} \sum_{\nu' \geq \nu_{i,j,k}} \varepsilon'_\nu \alpha_{i,j,k \to j+1,k}(\nu') \left(1 - \frac{\nu_{i,j,k}}{\nu'}\right) \mathrm{d}s. \tag{5.6}$$

Finally, the heating rate H^{ff} due to inverse-bremsstrahlung is calculated using

$$H^{\mathrm{ff}} = \frac{1}{\Delta t V} \sum \chi_{\mathrm{ff}}(\nu) \epsilon'_\nu \, \mathrm{d}s, \tag{5.7}$$

with the free-free opacity $\chi_{\mathrm{ff}}(\nu)$ treated according to Eq. (5.1). Before concluding our presentation of the reconstruction of radiation field quantities, we stress again that currently the estimators for the bound-free processes $\gamma_{i,j,k}$, $\alpha^{\mathrm{stim}}_{i,j,k}$ and $h^{\mathrm{bf}}_{i,j,k}$ are only used for hydrogen.

5.1.4. Relativistic transfer

For photospheric-phase SNe II the emergent continuum radiation is created in regions well below the photosphere. In these optically thick regions, the radiation field is essentially isotropic in the fluid rest frame and relativistic frame transformations can significantly modify the energy transport in the ejecta by introducing small anisotropies in the lab frame intensity (see, e.g., Hauschildt et al., 1991; Baron et al., 1996b).

To include relativistic effects in the Monte Carlo simulations, TARDIS uses a mixed-frame approach. Radiation–matter interactions are handled in the comoving frame whereas the packet propagation is carried out in the lab frame. Whenever necessary we transform the relevant packet properties between the frames. Compared to Kerzendorf & Sim (2014), we have refined the

treatment of relativity by including frame transformations of opacities as well as angle aberration. To transform packet energies and frequencies between observer and comoving frame, we use the full Doppler factor instead of an first order approximation. Expressions for the relevant transformations laws can be found in Mihalas & Mihalas (1984) or, specifically for spherical geometries, in Castor (1972). To be consistent with the adopted frame transformations, the distance to the next possible line interaction is now calculated based on the full Doppler-shift formula. As a result, the common-direction frequency surfaces, that is, the surfaces that emit line radiation at the same frequency in the observer frame, are no longer planes perpendicular to the line of sight but have a more complicated geometry as described by the relativistic Sobolev theory of Jeffery (1995).

5.2. Plasma state

The original implementation of TARDIS only features approximate excitation and ionization treatments and a very simplified calculation of the thermal structure. We have considerably refined the determination of the plasma state to adapt the code to SNe II. In particular, we have implemented a full NLTE treatment of excitation and ionization for hydrogen and we employ a thermal balance calculation to infer the temperature structure of the envelope.

The calculation of the plasma state involves a simultaneous determination of the excitation and ionization state of the material as well as the thermal structure. To reduce the complexity of this nonlinear problem, we decouple the solution of the excitation and ionization balance as follows: given an initial guess for the kinetic temperature T_e and the electron density n_e, we calculate level population fractions as outlined in Sect. 5.2.1. Based on the obtained excitation state, we solve for the ionization balance as described in Sect. 5.2.2. Finally, we compute heating and cooling rates (see Sect. 5.2.3), which are needed for the determination of the thermal structure. An outer iteration loop establishes consistency between excitation and ionization and adjusts the temperature such that thermal balance is enforced (see Sect. 5.2.4).

5.2.1. Excitation

TARDIS offers excitation treatments with different levels of sophistication. Level population fractions $f_{i,j,k} = n_{i,j,k}/N_{j,k}$ can be calculated from the Boltzmann excitation equation, a nebular modification thereof (see Abbott & Lucy, 1985) or from the steady-state equations of statistical equilibrium.

For the NLTE excitation calculation, electron number densities have to be specified. In this case, the statistical equilibrium equations for the total system decouple and can be solved for each atomic species individually. In the NLTE treatment of Kerzendorf & Sim (2014), only bound-bound interactions and collisional excitation and deexcitation rates were included. We extend the scheme by including radiative and collisional bound-free processes to obtain a more complete description of hydrogen excitation. The necessary photoionization and recombination

rate coefficients γ_i and α_i are reconstructed from the MC simulation by volume- based estimators (see Sect. 5.1.3). The collisional ionization and recombination rate coefficients $q_{i\kappa}$ and $q_{\kappa i}$ are evaluated according to the approximate formula by Seaton (1962). With these processes included, the rate equation for level i of ion j,k is given by

$$-\left(\gamma_i + q_{i\kappa} n_\mathrm{e} + \sum_{m\neq i} r_{im}\right) f_i + \sum_{m\neq i} r_{mi} f_m = -(\alpha_i + q_{\kappa i} n_\mathrm{e}) \frac{N_{j+1,k} n_\mathrm{e}}{N_{j,k}}. \tag{5.8}$$

Here, r_{mi} and r_{im} denote the total rate coefficients at which radiative and collisional transitions between level i and m populate and depopulate level i. In the Sobolev approximation, the rate coefficient for deexcitation from an upper level u to a lower level l is given by

$$r_{ul} = \beta_{lu} A_{ul} + \beta_{lu} B_{ul} J^\mathrm{b}_{lu} + c_{ul} n_\mathrm{e} \tag{5.9}$$

and the excitation rate coefficient is

$$r_{lu} = \beta_{lu} B_{lu} J^\mathrm{b}_{lu} + c_{lu} n_\mathrm{e}. \tag{5.10}$$

Here, J^b_{lu} is the mean intensity at the blue wing of the line, β_{lu} is the Sobolev escape probability (see, e.g., Sect. 4.3.1 of Lucy, 2002) and A_{lu}, B_{lu} and B_{ul} are the Einstein coefficients. Electron impact excitation rate coefficients c_{lu} are taken from the approximate formula of van Regemorter (1962) with deexcitation rates evaluated according to detailed balance. For hydrogen levels with principal quantum numbers up to $n = 7$ we use collision strengths from the detailed ab initio calculations of Przybilla & Butler (2004).

Despite fixing the electron number densities, the system of rates equations (5.8) remains nonlinear due to the dependence of the Sobolev escape probabilities on the level populations. We use a standard root finding algorithm to solve for the level population fractions $f_{i,j,k} = n_{i,j,k}/N_{j,k}$ and the ion population ratio $N_{j+1,k}/N_{j,k}$.[1] The convergence of the outer iteration loop that establishes a consistent plasma state is accelerated considerably by including the ion population ratio in the solution of the excitation state.

5.2.2. Ionization

In our detailed treatment of ionization we use the derived level population fractions $n_{i,j,k}/N_{j,k}$ and an initial guess for the electron density n_e to calculate the total ionization rate coefficient

$$\Gamma_{j,k} = \sum_i n_{i,j,k} (q_{i,j,k\to j+1,k} n_\mathrm{e} + \gamma_{i,j,k}) / N_{j,k} \tag{5.11}$$

[1] Specifically, we use a modified version of the Powell hybrid method as implemented in SciPy (Jones et al., 2001).

and the total recombination rate coefficient

$$\alpha_{j+1,k} = \sum_i \left(\alpha^{\mathrm{sp}}_{i,j,k} + \alpha^{\mathrm{stim}}_{i,j,k} + q_{i,j,k \leftarrow j+1,k} n_{\mathrm{e}} \right) \tag{5.12}$$

for relevant pairs of ions (j,k), $(j+1,k)$. We only do this for hydrogen in this work. For all other ions, the Saha factor $\Phi_{j,k} = (N_{j+1,k} n_{\mathrm{e}})/N_{j,k}$ and the electron density n_{e} serve as approximations of the total ionization and recombination rate coefficients. The Saha factor $\Phi_{j,k}$ is evaluated according to the Saha equation at the local radiation temperature T_{R} or the nebular ionization formula of Mazzali & Lucy (1993) (see Eqs. 2 and 3 of Kerzendorf & Sim, 2014). Based on these ionization and recombination rate coefficients, we iteratively solve for the ion and electron number densities, assuming ionization equilibrium.

5.2.3. Thermal balance

To complete the description of the plasma state, we need an estimate for the electron temperature T_{e} in the ejecta. In Kerzendorf & Sim (2014), T_{e} was set to $0.9 T_{\mathrm{R}}$ following Mazzali & Lucy (1993). We replace this simplified treatment of the thermal structure by a thermal-balance calculation based on the heating and cooling rates of the gas.

The thermal energy content, and therefore the temperature, is determined by the energy exchange between the kinetic energy of the ejecta, the radiative energy pool and the pool of atomic internal energy. This transfer is mediated by adiabatic cooling, collisional transitions as well as bound-free and free-free interactions. Assuming a steady-state, the rates for heating and cooling of the ejecta by these processes must cancel. Thus the electron temperature T_{e} is fixed by the requirement of thermal balance

$$H^{\mathrm{bf}} + H^{\mathrm{ff}} + H^{\mathrm{deexc}} + H^{\mathrm{recomb}} = C^{\mathrm{fb}} + C^{\mathrm{exc}} + C^{\mathrm{ion}} + C^{\mathrm{ad}} + C^{\mathrm{ff}}. \tag{5.13}$$

Here, H^{bf} and C^{fb} denote the rates of heating and cooling by bound-free interactions, H^{ff} and C^{ff} the respective rates for free-free processes. The contributions from collisional excitation, deexcitation, ionization and recombination are C^{exc}, H^{deexc}, C^{ion} and H^{recomb}. The final term C^{ad} describes adiabatic cooling of the envelope due to expansion work.

Specifically, collisional excitations from lower levels l,j,k to level i,j,k remove energy from the thermal pool with a rate

$$C^{\mathrm{exc}}_{i,j,k} = \sum_l C_{l,j,k \to i,j,k} (\epsilon_{i,j,k} - \epsilon_{l,j,k}), \tag{5.14}$$

where $\epsilon_{i,j,k}$ and $\epsilon_{l,j,k}$ are the respective level energies. Correspondingly, collisional ionizations from bound levels of ion j,k contribute

$$C^{\mathrm{ion}}_{j+1,k} = \sum_l C_{l,j,k \to j+1,k} (\epsilon_{0,j+1,k} - \epsilon_{l,j,k}) \tag{5.15}$$

to the total cooling rate.

In turn, atomic internal energy is transfered to the thermal pool by the inverse processes of collisional recombination and deexcitation at rates

$$H_{j,k}^{\mathrm{recomb}} = \sum_{l} C_{l,j,k\leftarrow j+1,k}(\epsilon_{0,j+1,k} - \epsilon_{l,j,k}) \tag{5.16}$$

and

$$H_{i,j,k}^{\mathrm{deexc}} = \sum_{u} C_{i,j,k\leftarrow u,j,k}(\epsilon_{u,j,k} - \epsilon_{i,j,k}). \tag{5.17}$$

Thermal electrons moving in the field of an ion j,k emit radiative energy according to (see Osterbrock, 1974)

$$C_{j,k}^{\mathrm{ff}} = 1.426 \times 10^{-27}\,(j-1)^2 T_{\mathrm{e}}^{1/2} N_{j,k} n_{\mathrm{e}}, \tag{5.18}$$

which depends on the ionic charge $j-1$, the number density of the respective ion $N_{j,k}$ as well as T_{e} and n_{e}. In addition, energy is continuously removed from the thermal electron pool by radiative recombinations. In terms of the modified rate coefficient

$$\alpha_{i,j,k}^{\mathrm{E,sp}} = 4\pi\,\Phi_{i,j,k}(T_{\mathrm{e}}) \int_{\nu_{i,j,k}}^{\infty} \frac{\alpha_{i,j,k\rightarrow j+1,k}(\nu)}{h\nu_{i,j,k}} \frac{2h\nu^3}{c^2} e^{-h\nu/k_{\mathrm{B}}T_{\mathrm{e}}}\,\mathrm{d}\nu \tag{5.19}$$

the cooling rate by recombinations to level i,j,k can be written as

$$C_{i,j,k}^{\mathrm{fb,sp}} = N_{j+1,k} n_{\mathrm{e}} \left(\alpha_{i,j,k}^{\mathrm{E,sp}} - \alpha_{i,j,k}^{\mathrm{sp}}\right) h\nu_{i,j,k}. \tag{5.20}$$

Photoionizations, in turn, heat the medium with a rate

$$H_{i,j,k}^{\mathrm{bf}} = 4\pi n_{i,j,k} \int_{\nu_{i,j,k}}^{\infty} \alpha_{i,j,k\rightarrow j+1,k}(\nu) \left(1 - \frac{\nu_{i,j,k}}{\nu}\right) J_\nu\,\mathrm{d}\nu. \tag{5.21}$$

Finally, the electron gas continuously loses thermal kinetic due to the expansion of the ejecta. The rate of energy loss resulting from this adiabatic cooling is given by

$$C^{\mathrm{ad}} = 3 n_{\mathrm{e}} k_{\mathrm{B}} T_{\mathrm{e}} / t, \tag{5.22}$$

where t denotes the time of explosion.

5.2.4. Outer plasma iteration

To obtain a consistent solution for the plasma state, the input electron densities that are used in the calculation of the level population fractions have to agree with the results from the ionization calculation. This is achieved by combining the methods described above with an iterative root-finding procedure. Apart from establishing consistency between the excitation and ionization

state, the outer iteration loop is used to determine the thermal structure from the thermal balance equation (5.13).

5.3. Approximations

As established by Utrobin & Chugai (2005), Dessart & Hillier (2008), Dessart & Hillier (2010), Potashov et al. (2017) time-dependent effects in the excitation and ionization balance can play an important role in shaping the spectral energy distribution. This applies in particular to epochs following hydrogen recombination. At these times the inclusion of time-dependent terms induces an overionization compared to the steady state solution, which is crucial in reproducing the observed Hα line strengths. In contrast, for epochs preceding hydrogen recombination the influence of time dependence is modest. Since these epochs are most relevant for the application of EPM (see, e.g., Dessart & Hillier, 2006; Dessart et al., 2008), we do not consider our neglect of these effects a severe limitation to our approach. In fact, Dessart & Hillier (2008) find negligible differences between the dilution factors from their time-dependent calculations and the steady-state results from Dessart & Hillier (2006), Dessart et al. (2008). Only for color temperatures less than 7000 K the correction factors drop systematically below their steady-state counterparts. As an additional approximation in the solution of the statistical equilibrium equations, we assume detailed radiative balance in the Lyman continuum. This prevents MC noise in the estimator for the ground- state photoionization rate from hindering convergence and avoids associated fluctuations in the ionization as well as the heating and cooling balance. This approach follows previous studies of SNe II, such as Takeda (1990, 1991) and Duschinger et al. (1995). Since the Lyman continuum is optically thick as long as the outflow ionization is not extremely high, detailed balance is deemed to be a very good approximation under most conditions of interest. We have verified this by a series of test calculations without this assumption but with increased numbers of MC quanta. The spectra resulting from the two approaches show good agreement for the parameter space that has been investigated in this paper. This is consistent with the results of Duschinger et al. (1995) who have reached the same conclusion for pure hydrogen supernova atmospheres with photospheric temperatures up to 15 000 K.

5.4. Iteration cycle

Tardis alternates between the calculation of the plasma state and MC radiative steps to achieve a self-consistent state for radiation and matter. Generally, less than twenty of these iterations are needed to achieve convergence to a point where only statistical variations remain (see Fig. 5.1). The good convergence properties result from the strict enforcement of radiative equilibrium, the explicit treatment of scattering and the direct dependence of the macro atom emissivities on the current estimate of the radiation field through the macro atom activation rates. At the moment, the number of iterations is set by hand at the beginning of the simulation, since no

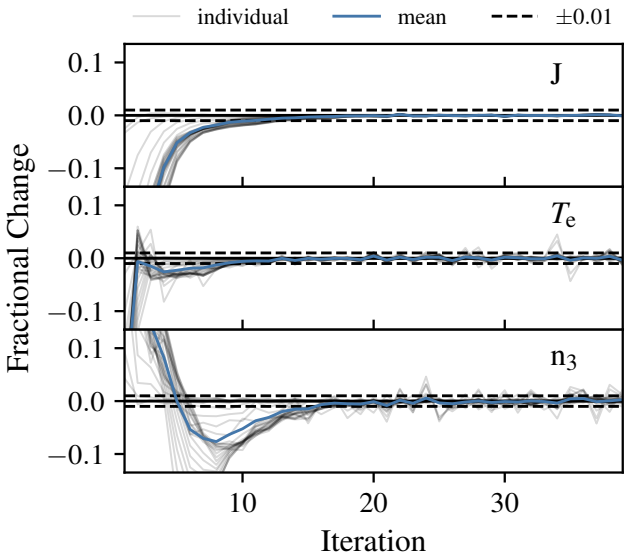

Figure 5.1.: Illustration of the convergence properties of plasma and radiation field quantities. We show the fractional changes between successive iterations for the mean intensity of the radiation field J, the electron temperature T_e and a representative level population, specifically that of the second excited level of hydrogen n_3. In all cases, we include both the changes in each individual shell (gray) as well as their average (blue). The results shown here are taken from our SN1999em model for the 14th of November (see Chapter 7 and Fig. 7.2).

formal convergence criterion is implemented in TARDIS. For the calculations presented in this paper, we have performed 40 iterations in all cases. We have found this to be more than sufficient to guarantee convergence for all used setups.

5.5. Atomic data

We use the hydrogen atomic data as described by Sim et al. (2005). This data set is based on a 20 level model atom with each level corresponding to a principal quantum number n. Frequency-dependent photoionization cross sections are tabulated for every energy state. The tabulated values range from the threshold ionization frequency up to the point at which the cross-section is only about 0.07 % of the value at threshold. This improved hydrogen model atom complements the atomic data already included in TARDIS (see Kerzendorf & Sim, 2014), which is compiled from the line lists of Kurucz & Bell (1995) and the Chianti 7.1 data base (Dere et al., 1997; Landi et al., 2012).

5.6. Spectral synthesis

To calculate synthetic spectra, the properties of escaping packets are recorded and later binned. However, the quality of the spectra that can be obtained from the normal MC quanta is severely affected by MC noise. To improve the signal-to-noise ratio an additional type of MC packet is used in TARDIS. Whenever a normal packet is launched or performs an interaction in the final spectral synthesis run, these so called "virtual" packets (v-packets) are emitted to estimate the contribution of the event to the emergent spectrum. In practice this amounts to optical depth integrations along a number of randomly selected trajectories through the ejecta. The measured optical depths τ_{trj} are then used to weight the contributions of the virtual packets to the spectrum according to the escape probability along the packet path, $\exp(-\tau_{\mathrm{trj}})$. This procedure, commonly called "peeling off", is well established and has found widespread use, in particular in the area of dust MC radiative transfer (see, e.g., Yusef-Zadeh et al., 1984; Wood & Reynolds, 1999; Baes et al., 2011; Steinacker et al., 2013; Lee et al., 2017).

Compared to the implementation described in Kerzendorf & Sim (2014), modifications have been necessary to keep the computational effort reasonable for the high optical depths of our SN II atmospheres. Since the number of interactions scales quadratically with optical depth, the number of virtual packets that have to be tracked for each "real" packet quickly becomes prohibitively large as the optical depth is increased. At the same time, the contribution of the additional v-packets to the spectrum is marginal due to the strong attenuation towards the surface. We apply biasing to the virtual packet emission to tackle this issue. Virtual packets are created only with a probability $\exp(-\tau_{\mathrm{e}})$, where τ_{e} is the electron scattering optical depth. To account for the lower chance of creation, the weight of the spawned packet is increased by the inverse of this probability. Notwithstanding this application of biasing, virtual packets can still accumulate large amounts of optical depth, for example, in line interactions. We use the Russian roulette technique (see, e.g., Carter & Cashwell, 1975; Dupree & Fraley, 2002) to probabilistically remove these low-weight packets.

5.7. Supernova model

TARDIS allows for the use of complex supernova models based on hydrodynamical explosion simulations and with stratified abundances (see Kerzendorf & Sim, 2014; Appendix A). Nevertheless, to facilitate the exploration of the parameter space, we restrict our analysis to simple, highly parameterized models. As in D05, we assume power- law density profiles

$$\rho(r) = \rho_0 (r/r_0)^{-n} \tag{5.23}$$

with density indexes $n = -\,\mathrm{d}\ln\rho/\,\mathrm{d}\ln r$ in the range $n = 6 - 14$. Both hydrodynamic simulations (Chevalier, 1976, 1982; Blinnikov et al., 2000) and spectral modeling (see, e.g., Eastman & Kirshner, 1989; Schmutz et al., 1990; Baron et al., 2007; Dessart & Hillier, 2006; Dessart et al., 2008) have

demonstrated that the outer density distribution is well described by such an ansatz with values close to $n \sim 10$. The composition of the ejecta is taken to be homogeneous. Heavy elements up to nickel are included in the simulations. Following D05 we use CNO-cycle equilibrium values from Prantzos et al. (1986) for the abundances of H, He, C, N, O. The remaining elements are assumed to have solar chemical composition with values taken from Asplund et al. (2009).

6. Expanding photosphere method

6.1. Presentation of the method

The expanding photosphere method (EPM) of Kirshner & Kwan (1974) is based on a simplified model of the supernova as a sharply-defined, spherically-symmetric, expanding photosphere. The radiation emerging from this photosphere is assumed to be that of a blackbody, diluted by an amount given by the dilution factor ξ_ν. This correction factor ξ_ν has originally been introduced by Hershkowitz et al. (1986a,b) and Hershkowitz & Wagoner (1987) to correct for the dilution of continuum flux that occurs in a scattering-dominated environment. In practice, the dilution factors account for all deviations of the spectrum from blackbody emission, such as lines or limb-darkening, in a parametrized fashion (see, e.g., E96; D05). For reasons of simplicity, in the application of EPM it is assumed that the dilution factor only depends on the color temperature. The precise form of this dependence may be reconstructed from supernovae whose distance is known from independent means (see Schmidt et al., 1992). However, to determine absolute distances it is necessary to infer the dilution factors from theoretical models as in E96 and D05, and outlined at the end of this section.

Based on the assumptions given above, the specific luminosity of the supernova is given by

$$L_\nu = 4\pi\xi_\nu^2 R_{\rm ph}^2 \pi B_\nu(T), \tag{6.1}$$

where $R_{\rm ph}$ is the photospheric radius and T is the temperature of the blackbody $B_\nu(T)$. By equating this to the observed de-reddened luminosity $L_\nu^{\rm obs} = 4\pi D^2 f_\nu^{\rm dered}$ the angular size of the expanding photosphere

$$\theta = \frac{2R_{\rm ph}}{D} = 2\sqrt{\frac{f_\nu^{\rm dered}}{\xi_\nu^2 \pi B_\nu(T)}} \tag{6.2}$$

can be inferred from the measured de-reddened flux $f_\nu^{\rm dered}$. The temperature T has to be determined from photometry as will be outlined shortly. Finally, to obtain the distance to the supernova

$$D = \frac{2R_{\rm ph}}{\theta}, \tag{6.3}$$

the photospheric radius must be eliminated from the equations. For homologous expansion this can be achieved via the relation

$$R_{\rm ph} = v_{\rm ph}(t - t_0), \tag{6.4}$$

where t_0 is the time of explosion and $v_{\rm ph}$ is the photospheric velocity. The expansion velocity $v_{\rm ph}$ can be inferred from blueshift velocities of lines, from cross-correlation of the observations with model spectra (see Hamuy et al., 2001) or from tailored radiative transfer calculations (see, e.g., Dessart & Hillier, 2006; Dessart et al., 2008). Finally, by measuring the ratio of photospheric angular diameter and velocity

$$\frac{\theta}{v_{\rm ph}} = \frac{t - t_0}{D} \tag{6.5}$$

for multiple epochs t, the distance is obtained from the slope of the data points. The time of explosion follows from the intercept with the t- axis.

To apply this formalism to observations, we have to recast the relevant equations in terms of photometric magnitudes. For a bandpass $\bar{\nu}$ with a transmission function $\phi_{\bar{\nu},\nu}$ the apparent magnitude $m_{\bar{\nu}}$ of the object can be calculated from the observed flux $f_\nu^{\rm obs}$ according to

$$m_{\bar{\nu}} = -2.5 \log \left(\int_0^\infty {\rm d}\nu \phi_{\bar{\nu},\nu} f_\nu^{\rm obs} \right) + C_{\bar{\nu}}, \tag{6.6}$$

where $C_{\bar{\nu}}$ is the zero-point. Using this definition, we can rewrite Eq. (6.1) for the dilute-blackbody emission as follows:

$$m_{\bar{\nu}} = -5 \log(\xi) - 5 \log(\theta) + A_{\bar{\nu}} + b_{\bar{\nu}}. \tag{6.7}$$

Here, we have introduced the broadband dust extinction $A_{\bar{\nu}}$ and the blackbody magnitude

$$b_{\bar{\nu}} = -2.5 \log \left(\int_0^\infty {\rm d}\nu \phi_{\bar{\nu},\nu} \pi B_\nu(T_S) \right) + C_{\bar{\nu}}, \tag{6.8}$$

where T_S is the color temperature. By minimizing the difference between observed and model magnitudes

$$\mathcal{E} = \sum_{\bar{\nu} \epsilon S} \left(m_{\bar{\nu}} - A_{\bar{\nu}} + 5 \log(\theta \xi_S) - b_{\bar{\nu}}(T_S) \right)^2 \tag{6.9}$$

for a bandpass combination S, the angular diameter θ and the color temperature T_S can be inferred from photometric observations.

To determine dilution factors from a synthetic spectrum, Eq. (6.9) is rewritten in terms of absolute magnitudes $M_{\bar{\nu}}$:

$$\mathcal{E} = \sum_{\bar{\nu} \epsilon S} \left(M_{\bar{\nu}} + 5 \log \xi_S + 5 \log \frac{R_{\rm ph}}{10\,{\rm pc}} - b_{\bar{\nu}}(T_S) \right)^2 . \tag{6.10}$$

In this case, the photospheric radius $R_{\rm ph}$ is known and application of the minimization procedure to the synthetic magnitudes $M_{\bar{\nu}}$ yields the color temperature T_S and the dilution factor ξ_S for the model. In Chapter 9 we will use this procedure to derive an independent set of dilution factors from our TARDIS simulations.

6.2. Dilution factors

To understand the results of our numerical simulations, a firm grasp of the basic physics behind the dilution factors is essential. One of the most important effects in this context and the original motivation for the introduction of the dilution factor (see Hershkowitz et al., 1986a,b) is the dilution of continuum radiation that occurs in a scattering-dominated environment. If, as in SN II, the scattering opacity greatly exceeds the absorptive opacity, a thermally created photon can travel large optical depths before a true absorption event returns it to the thermal energy pool. As a result, these photons can escape the ejecta without thermalizing and can efficiently carry away thermal energy from deep inside the atmosphere. This allows the intensity of the radiation field to fall below the thermal value (B_ν) but to still resemble the spectral energy distribution of a blackbody. From random walk arguments, it can be shown (see, e.g., Mihalas, 1978) that the relevant optical depth for this process, usually referred to as the thermalization depth $\tau_{\rm thm}$, scales roughly like

$$\tau_{\rm thm} \propto \sqrt{\frac{\chi_\nu}{3\chi_{\nu,\rm abs}}}, \tag{6.11}$$

where χ_ν denotes the total opacity and $\chi_{\nu,\rm abs}$ the absorptive component. Under these conditions, the emergent flux resembles that of a blackbody with the temperature at the thermalization depth but is diluted by an amount $\xi^2 \approx 1/\tau_{\rm thm}$.

7. Example spectra

In Chapter 5, a detailed description of our efforts to extend TARDIS for the spectral modeling of SNe II has been given. Here, we apply the extended code to calculate synthetic spectra for two epochs of SN1999em, a prototypical event of this class. Our goal is to demonstrate that, with the implemented changes, we are able to reproduce the spectral properties of such normal hydrogen-rich supernovae. Since we do not aim to perform a quantitative spectroscopic analysis, we have not extensively fine-tuned the model to exactly fit the observations but have adopted parameters similar to those used in previous studies by Baron et al. (2004) and Dessart & Hillier (2006).

As in Dessart & Hillier (2006), we adopt a power-law density profile with index $n = 10$ and a CNO-enhanced composition with an otherwise solar metallicity for both epochs (see Sect. 5.7 for details). Our first model is for the 9th of November, corresponding to around two weeks after explosion. At this point, the hydrogen envelope is still fully ionized but the envelope has already cooled sufficiently for appreciable line blanketing by metals to develop. Apart from the very weak He I 5875 Å feature, helium lines have already disappeared from the spectrum. Since the temperature is still too high for the Ca infrared triplet to form, the spectrum redwards of Hα remains featureless. Our TARDIS model nicely reproduces these characteristics as demonstrated by the comparison to the observations taken by Hamuy et al. (2001) in Fig. 7.1. The observed spectrum has been de-reddened according to a color excess of $E(B-V) = 0.08$, which is slightly less than the value of $E(B-V) = 0.1$ chosen in previous studies by Baron et al. (2004) and Dessart & Hillier (2006). We have blueshifted the observations by 770 km s^{-1} (see Leonard et al., 2002) to correct for the peculiar velocity of the host galaxy. The only major shortcoming of our model is that it underproduces the strength of the Fe II lines at ∼4550 Å and ∼5140 Å. Since this epoch coincides with the recombination from Fe III to Fe II, the predicted strengths of these features are, however, very sensitive to small changes in the parameters and to the adopted ionization treatment.

The second epoch we are modeling corresponds to an intermediate stage in the photospheric-phase evolution of the supernova. On the 14th of November, roughly 3 weeks after explosion, hydrogen recombination has set in and the spectrum shows very prominent Hα emission. Further cooling of the envelope has significantly strengthened the effect of line blanketing compared to the previous epoch. Redwards of Hα the continuum is no longer featureless, since the temperature has dropped sufficiently for the Ca infrared triplet to appear. Figure 7.2 shows a comparison of the spectrum taken by Hamuy et al. (2001) to our TARDIS model. We have corrected the

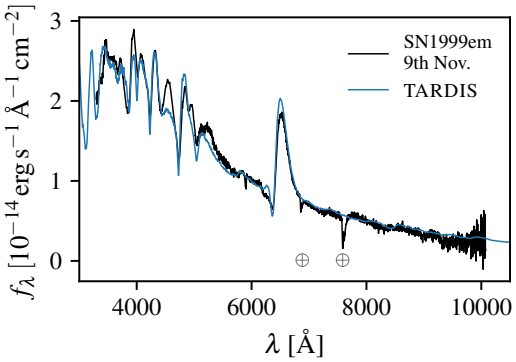

Figure 7.1.: TARDIS spectral model (blue) for the observations of SN1999em (black) taken by Hamuy et al. (2001) on the 9th of November. We have smoothed the Monte Carlo spectrum using a Savitzky-Golay filter (Savitzky & Golay, 1964). The observational data has been taken from the WISeREP archive (Yaron & Gal-Yam, 2012) and has been de-reddened according to the Cardelli, Clayton, & Mathis (1989) law with a color excess of $E(B-V) = 0.08$ (http://www.weizmann.ac.il/astrophysics/wiserep/). To account for the peculiar velocity of the host galaxy, the observations have been blueshifted by 770 km s^{-1} (see Leonard et al., 2002). Finally, the synthetic spectrum has been scaled to match the observed de-reddened flux f_λ. The main telluric features are marked with circled crosses.

observations for reddening and peculiar velocities in the same fashion as for the first epoch. Overall, our synthetic spectrum reproduces the measured SED quite well. The two prominent Ca features, Ca H&K and the infrared triplet, are matched well in both strength and shape. However, our model slightly overestimates the Hα emission, whereas the width of the absorption trough is underestimated. As mentioned by Dessart & Hillier (2006), who found similar problems, the latter might be related to blending with Fe II and Si II lines.

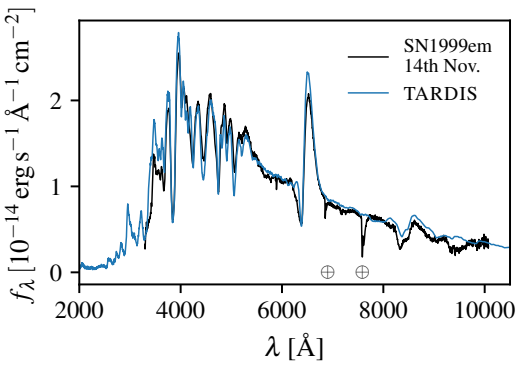

Figure 7.2.: Same as Fig. 7.1 but for the observations of SN1999em on the 14th of November.

8. Model grid

Having established the capabilities of the extended TARDIS version to produce accurate synthetic spectra for SNe II, we use the code to calculate an independent set of dilution factors. To this end, we have set up a grid of 343 models. These have been constructed to cover the interesting physical parameter space of inner boundary temperatures $T_{\rm inner}$ from 9500 K to 24 000 K, photospheric densities $\rho_{\rm ph}$ from 7×10^{-15} g/cm^3 to 8×10^{-14} g/cm^3, power-law density indexes n from 6 to 14 and photospheric velocities $v_{\rm ph}$ from 3000 km s^{-1} to 14 000 km s^{-1}. For these parameters the models span a range of effective temperatures $T_{\rm eff}$ from 4900 K to 12 000 K. We take the photospheric properties $\rho_{\rm ph}$ and $v_{\rm ph}$ to refer to the position at which the electron scattering optical depth is $\tau = 2/3$. In practice, the models are set up by adopting $\rho_0 = \rho_*$ and $r_0 = v_* t$ for the density profile (Eq. (5.23)), where ρ_* and v_* are specific values selected from the desired range of photospheric density and velocity. To ensure that the photosphere of the model will lie at the appropriate depth, t (time since explosion) is estimated using

$$t = \frac{2(n-1) m_H \mu_e}{3 v_* \rho_* \sigma_T}, \tag{8.1}$$

where m_H is the mass of a hydrogen atom, $\mu_{\rm e}$ is the mean molecular weight per electron and σ_T is the Thomson cross section. In making this estimate, it is assumed that μ_e is well-approximated by $\mu_e = 1.52$, as appropriate for a composition of ionized hydrogen and singly-ionized helium. The full calculation is then carried out and the true values of $\rho_{\rm ph}$ and $v_{\rm ph}$ are extracted from the simulation. In general, the true values of the photospheric parameters ($\rho_{\rm ph}$, $v_{\rm ph}$) are very close to the originally selected reference parameters (ρ_*, v_*) from which the model was generated. Nevertheless, we always refer to each model by the derived (simulation) values of $\rho_{\rm ph}$ and $v_{\rm ph}$. We note that the true inner boundary of our computational domain lies considerably deeper than the (approximate) photosphere, typically at $\tau \sim 27$.

The setup of the model grid is done in the form of a latin hypercube design (Stein, 1987). In this approach, each parameter range is subdivided into N equal intervals, where N is the number of models and one random parameter value is selected from each subinterval. This guarantees that, in contrast to a conventional cartesian grid, N distinct values exist for each parameter. This is in particular beneficial if the quantities of interest are only weakly sensitive to a subset of parameters.[1] Finally, to illustrate the properties of our set of models, a projection of the grid in the $T_{\rm eff}$ - $\rho_{\rm ph}$ plane is shown in Fig. 8.1. As can be seen, the desired parameter space is for the

[1] Consider the extreme case that one or more parameters have no influence at all. For the hypercube each point still contains new information, whereas for the cartesian mesh most of the grid has become redundant.

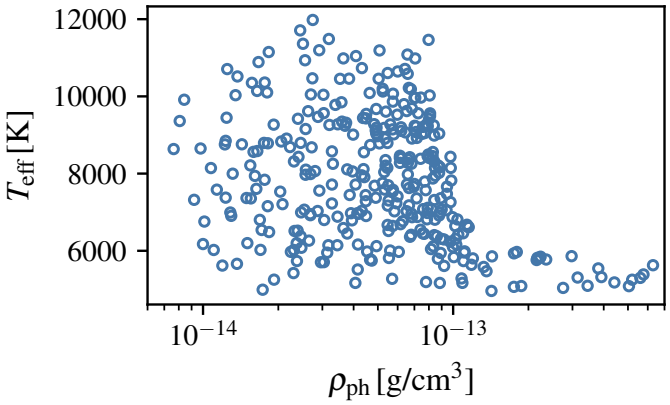

Figure 8.1.: Illustration of the model grid from Chapter 8. The plot shows the effective temperature T_{eff} and the photospheric density ρ_{ph} for all atmosphere models. At low temperatures the actual photospheric density can exceed the targeted upper limit of $8 \times 10^{-14}\,\mathrm{g/cm^3}$, due the development of a strong recombination wave, which complicates the mapping between photospheric properties and the computational grid.

most part uniformly covered. Deviations from the uniform spacing arise from the use of Eq. (8.1) to map between photospheric quantities and the computational grid. This process becomes less reliable as soon as a strong recombination front develops. The main motivation for using a mostly uniform grid is that it allows us to study the differential influence of model parameters, such as the photospheric density, on the dilution factors. In this context, correlations between the input parameters have to be avoided as far as possible. However, since quantities such as photospheric temperature and density are certainly not completely independent in nature, this also means that the grid includes models that are not representative of normal SNe II. One example would be an object with a very high expansion velocity but an extremely low temperature.

9. Results

9.1. Overview

From synthetic photometry of our model spectra, we can derive color temperatures T_S and dilution factors ξ_S according to Eq. (6.10). To facilitate the comparison to the results of E96 and D05, we focus our analysis on the bandpass combinations S=$\{B,V\}$, $\{B,V,I\}$, $\{V,I\}$ and $\{J,H,K\}$ with filter functions taken from Bessell & Brett (1988) and Bessell (1990). Examples of the dilute blackbody models constructed in the synthetic EPM analysis are shown in Fig. 9.1. The results of our analysis are summarized in Fig. 9.2, which displays dilution factors ξ_S and color temperatures T_S for all our models, as well as comparison values from E96 and D05. The color temperatures constitute the most important parameters in the study of the dilution factors, since they account for most of the variance in the correction factors and can be easily inferred from observations. Variations of the remaining parameters such as photospheric density or velocity are in most cases of secondary importance and are responsible for the observed dispersion around the color-temperature trend. In Fig. 9.2 we find good agreement with D05, in particular at low to medium color temperatures. For $\{B,V,I\}$ and $\{V,I\}$ the results match well for temperatures below 12 500 K and for $\{J,H,K\}$ for temperatures below 7000 K. In $\{B,V\}$ the dilution factors are similar to D05 over the entire temperature range. For higher color temperatures in $\{B,V,I\}$, $\{V,I\}$, and $\{J,H,K\}$ our models tend to be systematically more dilute than D05 with values closer to those published by E96. As will be discussed in Sect. 10.2, part of this discrepancy can be attributed to differences in the adopted photospheric densities. We note that for all bandpass combinations the intrinsic scatter of our dilution factors is slightly larger than for the set of models by D05. This was to be expected, since we have constructed our grid of models in such a way that at all temperatures the whole range of remaining parameters is covered (see Chapter 8). In contrast, the dilution factors of E96 show a much smaller dispersion, since only a narrow part of the parameter space is explored in their study. Before concluding our discussion, we stress that this scatter does not correspond to the diversity of real objects but only reflects our ignorance about the parameter space occupied by SNe II. Finally, following E96 and D05 we present third order polynomial fits to the color temperature dependence of our dilution factors $\xi_S = \sum_i a_i (10^4\,\mathrm{K}/T_S)^i$ in Table 9.1.

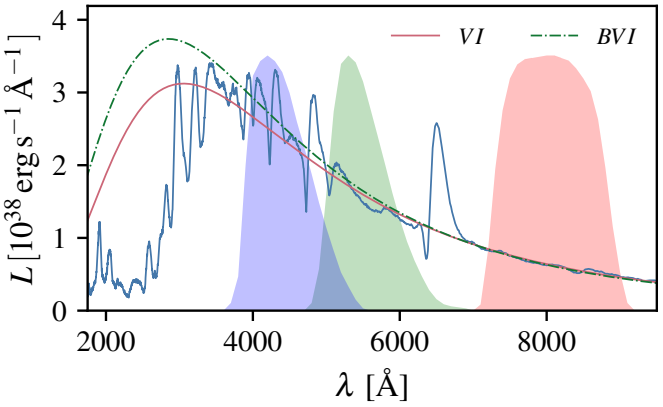

Figure 9.1.: Comparison of the dilute blackbody models from $\{V,I\}$ (red) and $\{B,V,I\}$ synthetic photometry (green) to the original TARDIS spectrum (blue). The spectrum is our SN1999em model for the 9th of November (see Fig. 7.1). The parameters of the blackbody fits are $T_{VI} = 9500\,\mathrm{K}$, $T_{BVI} = 10\,200\,\mathrm{K}$ and $\xi_{VI} = 0.49$, $\xi_{BVI} = 0.45$. We have overplotted the transmission curves for the B, V and I filters from Bessell (1990). The Monte Carlo spectrum has been smoothed using a Savitzky-Golay filter (Savitzky & Golay, 1964).

Table 9.1.: Coefficients a_i of polynomial fits $\xi_S = \sum_i a_i (10^4\,\mathrm{K}/T_S)^i$ to the models for bandpass combinations S=$\{B,V\}$, $\{B,V,I\}$, $\{V,I\}$ and $\{J,H,K\}$.

	$\{B,V\}$	$\{B,V,I\}$	$\{V,I\}$	$\{J,H,K\}$
a_0	0.7417	0.5356	0.2116	−0.0384
a_1	−0.8662	−0.3355	0.3799	0.9918
a_2	0.5828	0.2959	−0.0673	−0.2867

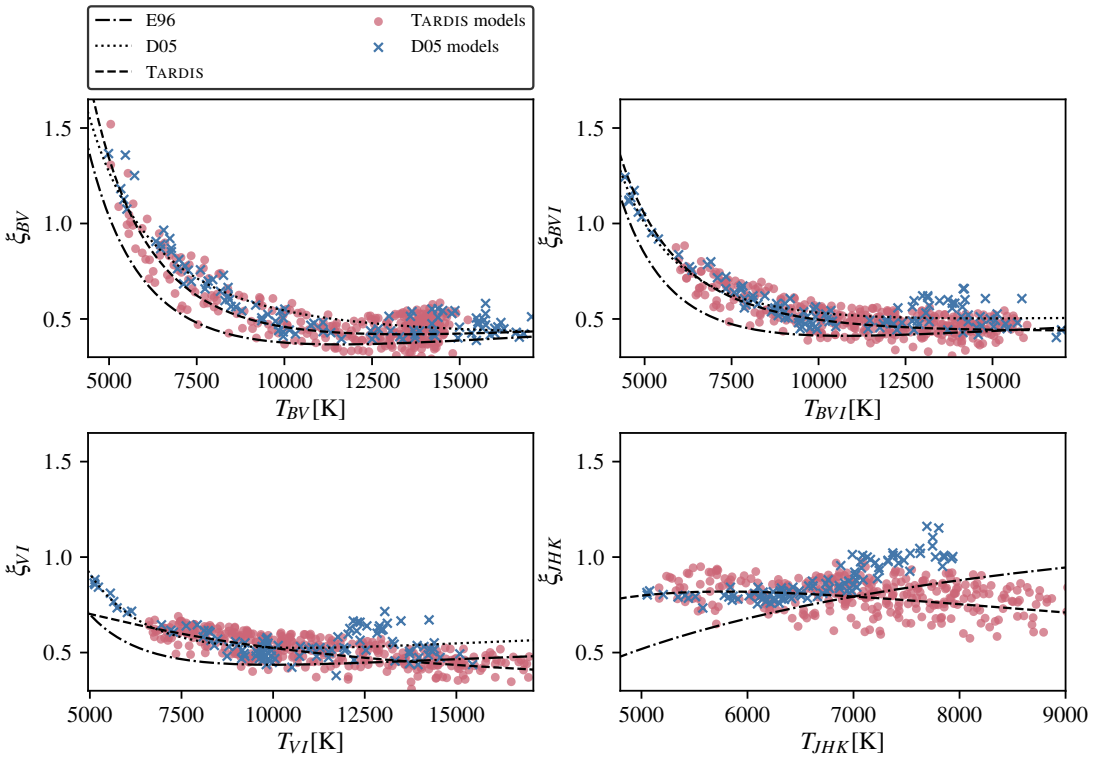

Figure 9.2.: Dilution factors ξ_S as a function of color temperature T_S for filter combinations S={B,V}, {B,V,I}, {V,I} and {J,H,K}. We use a common y-axis scale for all bandpass combinations S to highlight the differences in the scaling behavior of the dilution factors. For comparison purposes, we include the models of D05 as blue crosses. Polynomial fits to the dilution factors are shown for all sets of models (dashed: TARDIS, dashed dotted: E96, dotted: D05). For {J,H,K} the D05 curve is not included due to a misprint in the tabulated fit coefficients in the original paper.

9.2. Influence of atmospheric properties

In the previous section, the dependence of the dilution factors on temperature has been discussed. Here, we will focus on the effects of density. First, we analyze the variation of the dilution factors with photospheric density. Secondly, we investigate the influence of the steepness of the density profile. Finally, to conclude the discussion of the effect of model parameters, we will assess the robustness of the dilution factor fit curves against changes in the metallicity.

Influence of the photopsheric density

Variations in the photospheric density account for most of the dispersion of the models around the general color temperature dependence as illustrated in Fig. 9.3. Since the density cannot be easily constrained from observational data, it is essential to understand its influence on the dilution factors to quantify the associated uncertainties on the mean and the variance of the tabulated fit curves. Figure 9.4 shows the density dependence of our dilution factors and a comparison to the results of D05. In general the dilution factors tend to increase with photospheric density, with the strength of the scaling varying between bandpass combinations. This behavior can be understood by remembering that the amount of continuum flux dilution depends on the ratio of continuum to scattering opacity (see Sect. 6.2). Since the main contribution to the scattering opacity comes from Thomson scattering, it is proportional to the electron density. Thermalization processes, on the other hand, roughly scale with the square of the electron density. As such, we expect the ratio of the two to increase with density, yielding a smaller amount of flux dilution at high densities. To study this behavior in a more quantitative way, we adopt the same ansatz as E96 for the dilution factors:

$$\xi_S = \rho_{\rm ph}^{\gamma} z(T_S). \tag{9.1}$$

Here, $z(T_S)$ denotes a polynomial of the same form as those used in Table 9.1. A least squares fit to our set of models yields the density scaling indexes γ listed in Table 9.2. Overall, the inferred density dependence of our dilution factors is moderate with similar magnitudes for all passbands. The scaling indexes γ are systematically a bit larger than those published in E96 with the largest difference in the infrared (see Table 9.1). However, as illustrated by Fig. 9.4 the density dependence in the infrared is not well described by a single power-law for the entire density range. In Sect. 10.2 we will use the inferred power-law scalings to assess whether differences in the assumed photospheric densities play an import role in understanding the discrepancies between the published sets of dilution factors.

Influence of the density structure

For a power-law atmosphere the ratio of photospheric density and density index n is approximately given by

$$\frac{\rho_{\rm ph}}{n-1} \approx \frac{2}{3} \frac{\mu_{\rm e}}{\sigma_{\rm e} v_{\rm ph} t} \quad . \tag{9.2}$$

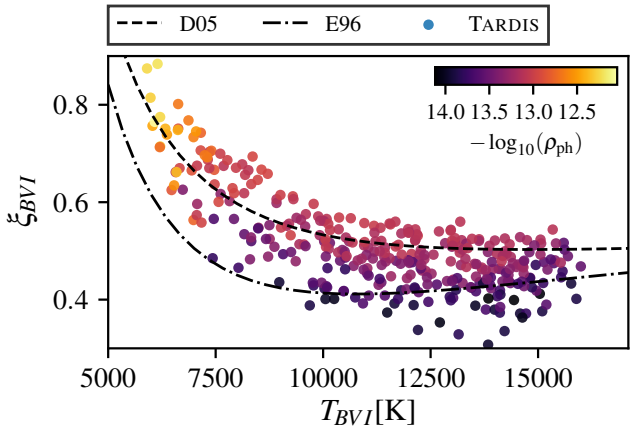

Figure 9.3.: Dilution factors ξ_{BVI} as a function of color temperature T_{BVI}. To illustrate the density dependence of our TARDIS models, the logarithm of the photospheric density $\log_{10}\rho_{\rm ph}$ is color-coded. For comparison purposes we include the polynomial fits to the dilution factors of E96 (dashed-dotted) and D05 (dashed).

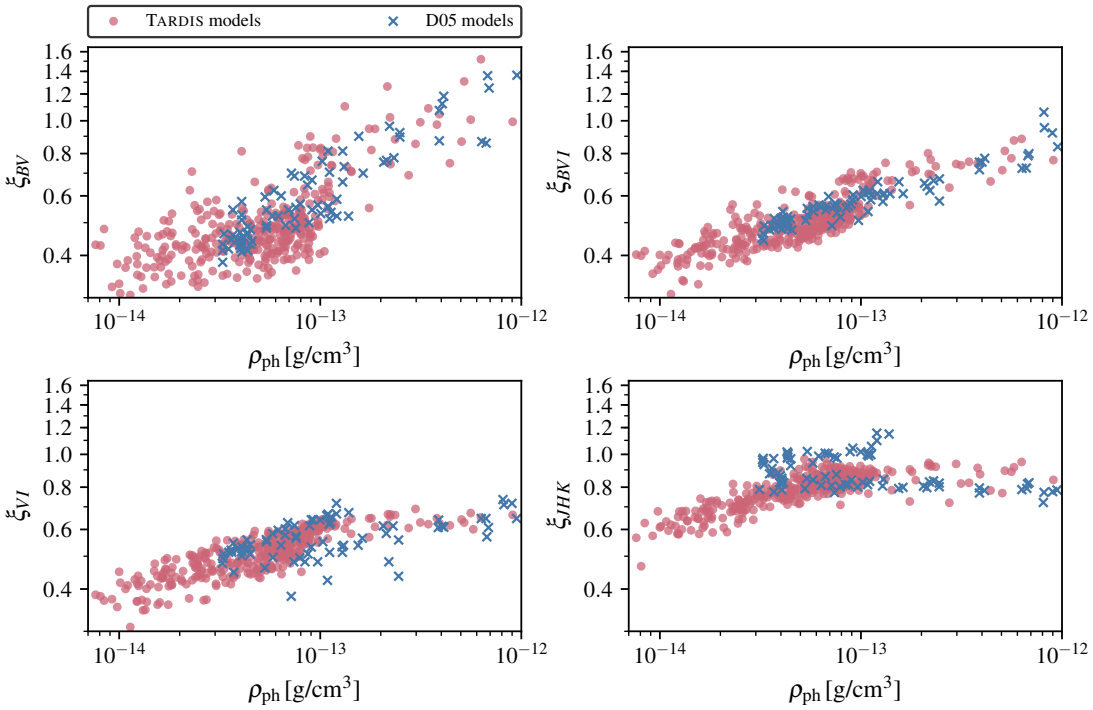

Figure 9.4.: Variation of the dilution factors ξ_S with photospheric density $\rho_{\rm ph}$ for filter combinations S={B,V}, {B,V,I}, {V,I} and {J,H,K}. For comparison purposes the models of D05 are shown as blue crosses.

Table 9.2.: Coefficients γ of polynomial fits $\xi_S = \rho_{\rm ph}^{\gamma} z(T_S)$ to the density dependence of the dilution factors for bandpass combinations S=$\{B,V\}$, $\{B,V,I\}$, $\{V,I\}$ and $\{J,H,K\}$.

	Models	$\{B,V\}$	$\{B,V,I\}$	$\{V,I\}$	$\{J,H,K\}$
γ	TARDIS	0.106	0.137	0.133	0.116
	E96	0.0776	0.0933	0.0769	0.0307

Notes. Here, $z(s) = \sum_i a_i (10^4\,\mathrm{K}/T_S)^i$ denotes a polynomial of the same form as used in Table 9.1 but with different fitted values for the coefficients.

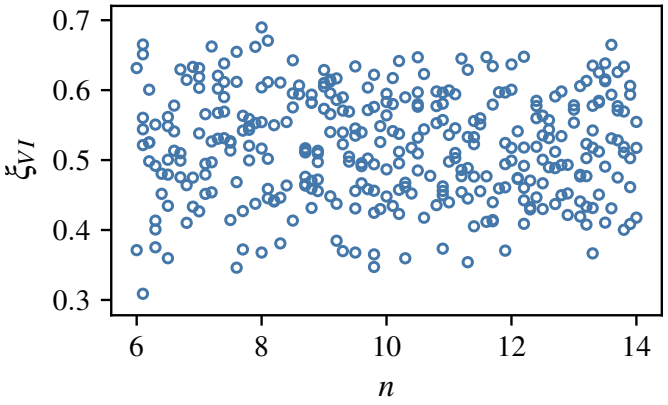

Figure 9.5.: Dilution factors ξ for the bandpass combination $\{V,I\}$ as a function of the density indexes $n = -\,\mathrm{dln}\,\rho/\,\mathrm{dln}\,r$ of the power-law model atmospheres.

For a given outflow ionization, time of explosion and expansion velocity, an increase in the density index n results in higher photospheric densities $\rho_{\rm ph}$ and therefore less flux dilution. However, if the density structure is treated as an independent parameter, the dilution factors do not show a strong dependence on n as illustrated by Fig. 9.5. For a possible explanation, we refer the reader to E96, who have found the same behavior and have proposed a physical motivation in their §3.3.

Influence of metallicity

Line blanketing by metals, in particular iron group elements, plays an important role in shaping the spectral energy distribution of SNe II and the resulting influence of metallicity on the emergent spectrum has been discussed in detail in the literature (see, e.g., Dessart & Hillier, 2005b). However, neither E96 nor D05 discuss in depth how this effect translates into changes in the dilution factors. To investigate the sensitivity of the $\xi - T$ fit curves to changes in metallicity, we have rerun a random subset of 68 models of our solar metallicity grid ($Z = 1$) with a lower metallicity of $Z = 0.2$. The resulting changes in the color temperatures and dilution factors are shown in Fig. 9.6 for

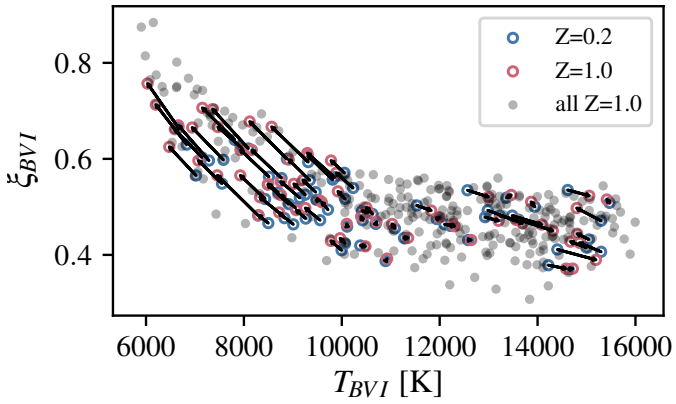

Figure 9.6.: Change of dilution factors ξ_{BVI} with metallicity Z. The subset of the original solar metallicty models for which corresponding calculations with a lower metallicity have been performed are shown in red. The metal-poor models are depicted in blue. Arrows illustrate the changes in model properties induced by the change to the subsolar metallicity of $Z = 0.2$. To facilitate the comparison to the general ξ-T trend, all models of the original grid are included in gray.

the $\{B,V,I\}$ bandpass combination. As expected, at high temperatures ($T_{BVI} \gtrapprox 10\,000\,\mathrm{K}$) the influence of metallicity on the model properties is negligible, since the degree of ionization is too high for significant line blanketing to develop in the optical and near-UV.[1] For moderate and low temperatures large changes in the color temperature up to thousands of degrees are observed. However, the associated changes in the dilution factors are approximately aligned with the general scaling of ξ with T. Compared to the intrinsic scatter of the models, the induced changes in the functional behavior of ξ with T are of secondary importance. Thus, in the investigated regime, ranging from solar to distinctly subsolar, the tabulated fit curves are robust against modifications of the metallicity.

[1] The seemingly random displacements for models at high color temperatures are an artifact resulting from the flattening of the color-color temperature relationship. As a consequence small changes in the fluxes can induce large changes in the inferred temperatures.

10. Comparison to previous studies

10.1. Radiative transfer

To put our results into context, we review differences in the radiative transfer modeling between the CMFGEN code used by D05, the EDDINGTON code used by E96 and TARDIS and discuss possible effects on the dilution factors. The main differences lie in the ionization treatment of metal species, the handling of line opacity and the inclusion of relativistic transfer effects.

For the calculations presented by D05, only the effect of the Doppler shift on the frequency of the radiation field is taken into account. E96 follow a different approach based on the premise that radiation-field time dependence can be included in a quasi-static treatment by enforcing a constant luminosity in the comoving frame. In this case, the time-dependent comoving-frame transport equation reduces to a much simpler expression that differs from D05 only by an additional term $\beta I_\nu / r$, where I_ν is the specific intensity of the radiation field. This term is formally identical to the part of the full transport equation that describes the redshift of photons in the scattering process and thus the adiabatic loss of radiation energy. However, the sign is changed and the magnitude decreased by a factor of three. Both approaches neglect the so-called advection term that arises from the frame transformation of angles (see, e.g., Pistinner & Shaviv, 1994; for a discussion). This term is generally deemed to be more important than the aberration term (see, e.g., Baron et al., 1996b). Taking into account the additional reduction of the magnitude of the aberration term in E96, we conclude that the differences in handling the relativistic terms between E96 and D05 are small in comparison to our relativistic treatment (Sect. 5.1.4), which corresponds to a full solution of the quasi-static relativistic transport problem. Since we can achieve good agreement with D05 despite this difference, we consider it unlikely that relativistic effects play an important role in explaining the systematic offset between E96 and D05.

Another possible source for discrepancies, which has been discussed previously in the literature (see D05), is the treatment of line interactions. Here, the differences start with the handling of the opacity. Both CMFGEN (D05) and TARDIS treat the contributions of all lines to the opacity individually, in a consistent manner. In contrast, EDDINGTON (E96) adopts the more convenient but approximate expansion opacity formalism of Eastman & Pinto (1993) that combines all line opacity in a wavelength bin. For the opacity calculation, the expansion opacity formalism in E96, as well as the method used in TARDIS, rely on the Sobolev approximation (Sobolev, 1957), whereas CMFGEN adopts the comoving-frame method. For micro-turbulent velocities of less than $100\,\mathrm{km\,s^{-1}}$, as adopted in D05, the Sobolev method is of similar accuracy as the comoving-

frame method in describing the formation of hydrogen lines in SNe II (see Duschinger et al., 1995). In regions where line overlap is possible, in particular in the metal line forest in the blue, the Sobolev approximation may, however, be less accurate than the comoving-frame method.

With respect to line interactions, the final difference between the codes concerns the redistribution of the absorbed radiation. Only CMFGEN computes a full NLTE source function for all included species. In E96 line interactions are treated in detail only for a few selected elements, in most cases only hydrogen. For the remaining species, resonance scattering is assumed and effects such as fluorescence or collisional deexcitations are neglected. TARDIS strikes a balance between the approximate treatment of E96 and the full NLTE calculation of D05. In principle, our implementation of the macro atom scheme of Lucy (2002, 2003) also provides a full NLTE description of the redistribution process. However, in our simulations only radiative and collisional bound-bound transitions are included for species other than hydrogen. Despite this simplification, the approximate NLTE emissivities from the macro atom provide a full treatment of fluorescence. It is also worth pointing out that the predicted emissivities are largely insensitive to errors in the excited states population and therefore to our use of approximate excitation treatments. This has been demonstrated by Lucy (2002) and may be understood by considering that, in the context of the macro atom machinery, the most relevant level number densities are those of the ground state and low-lying metastable levels. Radiative excitations from these states account for most of the activations of the macro atom and their populations are likely to be close to LTE with respect to the ground state. In contrast, the level number densities of excited states, which will be less accurately estimated, are not as important in setting the rate of macro atom activations and enter in the emissivity only through minor modifications of the internal redistribution probabilities for stimulated emission. Thus we argue that the macro atom approach captures most of the essential physics of a full NLTE treatment as opposed to the resonance scattering approximation used in E96. As such, it constitutes a promising source of systematic discrepancies between E96 on the one hand and D05 and TARDIS on the other hand.

To conclude our discussion of the major differences in the numerical treatments, we compare the different methods used for calculating the ionization state of metal species. An accurate solution to the ionization balance is essential in modeling the line blanketing, which shapes the spectral energy distribution in the blue. Due to the use of super-levels, CMFGEN (D05) is able to consistently, though approximately, treat all species in NLTE. In contrast, E96 calculated the ionization using NLTE only for a few selected species and only for a subset of their atmospheric models. For the remaining models and species, LTE at the electron temperature is assumed. Similarly, TARDIS relies on simplified prescriptions for the calculation of the ionization balance of metals. For the results presented in this paper, we have used the nebular ionization approximation of Mazzali & Lucy (1993). In principle, this method should provide a more accurate description of the ionization balance in a diluted, radiation- dominated environment than the assumption of LTE. However, neither assumption can fully replace a detailed photoionization calculation. Still, our spectral models for SN1999em (see Chapter 7) reproduce the observed line blanketing well. This instills

confidence that, at least for the early and intermediate stage evolution, the nebular ionization treatment adequately captures the essential physics.

Ultimately, it is extremely difficult to assess the extent to which, if at all, individual numerical differences contribute to the systematic discrepancy between the sets of dilution factors. Based on qualitative arguments, we have deemed it unlikely that the handling of relativistic terms plays an important role in this context. We have identified the use of the very simple resonance scattering approximation by E96 as one of the main distinguishing features from both our and D05's numerical approaches. As such, it can be regarded as a promising possible contributory factor to the systematic differences. However, these interpretations are speculative and should be taken with a grain of salt.

10.2. Effect of model grid assumptions

In the previous section we have discussed how differences in the radiative transfer calculations can affect the dilution factors. In the context of the discrepancy between E96 and D05 most of the discussion in the literature (see, e.g., Dessart & Hillier, 2005a; Jones et al., 2009) has revolved around these issues. However, another possibly important (albeit banal) source of systematic differences is the choice of model grid properties. To demonstrate this, we have modified the plot depicting the temperature dependence of our dilution factors for the $\{B,V,I\}$ bandpass combination to include the color-coded photospheric density for each model (see Fig. 9.3). From this, it is obvious that the inferred fit curves can easily be moved upwards or downwards by preferentially sampling either the high density or the low density regions of the parameter space. Since the exact distribution and correlation of parameters such as density, temperature and velocity are not known for the population of SNe II, there exists a certain amount of freedom in the setup of the model grid.

To quantitatively illustrate the role such effects may have, we have investigated the influence of density in particular. For a comparative study we need to consider families of models for which color temperature, densities and dilution factors are available – accordingly, we make use of our TARDIS models, the E96 models and the models presented for the tailored EPM analysis of SN1999em, SN2005s and SN2006bp (Dessart & Hillier, 2006; Dessart et al., 2008). This set of 38 models covers the relevant range of color temperatures and generally follows the fit curves published in D05.[1]

Before we compare densities, we approximately correct for changes of the electron densities between the set of models due to differences in composition (specifically, we rescale the densities from E96's models with the estimated ratio of the mean molecular weights per electron). The mean rescaled densities $\langle\rho_{\rm ph}\rangle$ are shown in Fig. 10.1 as a function of $\{B,V,I\}$ color temperature. Overall, the densities used in this paper, and in Dessart & Hillier (2006) and Dessart et al. (2008) tend to

[1] We use the tailored EPM models because the full set of model parameter data has not been published for the calculations presented in D05.

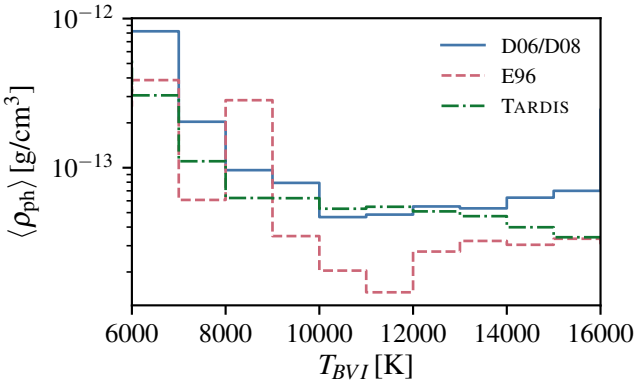

Figure 10.1.: Comparison of the mean photospheric density $\langle\rho_{\rm ph}\rangle$ at a given $\{B,V,I\}$ color temperature for the models from E96 (red dashed), the tailored EPM analyses of Dessart & Hillier (2006) and Dessart et al. (2008) (D06/D08, blue solid), and this paper (green dash-dotted). The plotted densities have been rescaled slightly to account for differences in the composition as outlined in Sect. 10.2.

be larger than those of E96 with maximum differences of a factor of a few. The conspicuous jump in density for the E96 models between 8000 and 9000 K stems from two exponential atmospheres (e12.2,e12.3). To check whether this density mismatch might alleviate some of the tension between the dilution factors by E96, and those of Dessart & Hillier (2005a, 2006) and Dessart et al. (2008), we rescale the dilution factors $\xi_{\rm S}$ using the simple power-law relation $\xi_S \propto \rho_{\rm ph}^{\gamma}$ from Sect. 9.2. For this purpose we do not use the mean densities $\langle\rho_{\rm ph}\rangle$ from Fig. 10.2 but the appropriate average $\langle\rho_{\rm ph}^{\gamma}\rangle^{1/\gamma}$. Fig. 10.2a illustrates the effect of the rescaling on the discrepancy between the two sets of models. Applying the density correction reduces the maximum difference from roughly 40% to 20%, but fails to remove the systematic offset completely. As can be seen in Fig. 10.2b, the procedure is more successful for our set of dilution factors. After rescaling, only a maximum difference of around 8% remains between our calculations and those of Dessart & Hillier (2006) and Dessart et al. (2008). We stress that due to the simplifying assumptions we have made the results above are only qualitative in nature. Nevertheless, our discussion demonstrates that differences in the setup of the model grid, for example, different choices for the photospheric densities, can introduce systematic uncertainties on the 10% level in the dilution factors. This most likely explains part of the discrepancy between the results of E96, and those of Dessart & Hillier (2005a, 2006) and Dessart et al. (2008). To eliminate this additional error source, approaches are needed that strongly constrain the relevant parameters through observational data. One possibility would be to base the dilution factor fit curves on the tailored EPM analyses of a representative set of SNe II.

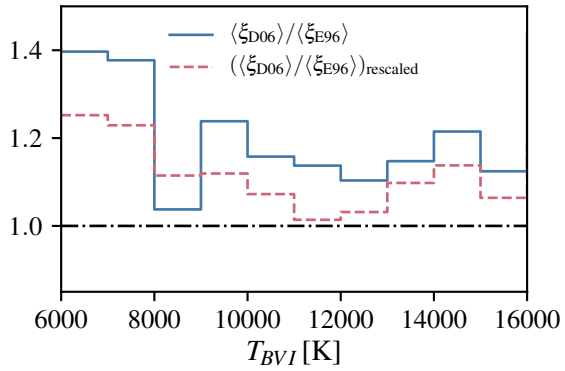

(a)

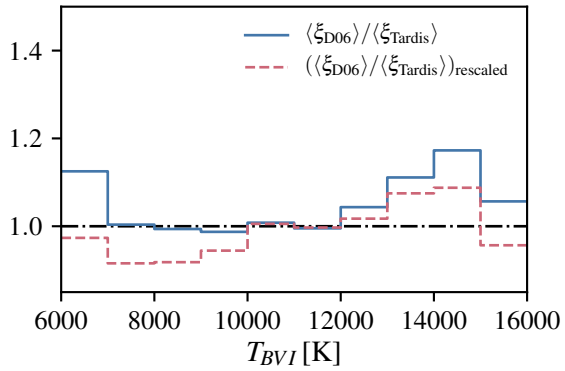

(b)

Figure 10.2.: Comparison of the discrepancy between the dilution factor set in the $\{B,V,I\}$ bandpass combination of Dessart & Hillier (2006) and Dessart et al. (2008) $\langle\xi_{\rm D06}\rangle$, and E96 $\langle\xi_{\rm E96}\rangle$ (upper panel, a), and with respect to the results of this paper $\langle\xi_{\rm Tardis}\rangle$ (lower panel, b). The findings before (blue solid) and after (red dashed) the application of a density correction factor are shown. The details of the procedure are described in Sect. 10.2.

11. Conclusions

In this work, we present an extension of the Monte Carlo radiative transfer code TARDIS to the spectral synthesis of SNe II. The key feature of our numerical approach is an updated radiation–matter interaction scheme, which provides a full treatment of bound-bound, bound-free, free-free and collisional processes based on the macro atom scheme of Lucy (2002, 2003). The second major improvement concerns the calculation of the plasma state. The code now contains a self-consistent determination of the thermal structure from the heating and cooling balance as well as a full NLTE calculation of the ionization and excitation state for hydrogen. Other changes include an improved handling of relativistic effects, an adaption of the spectral synthesis calculation for high optical depths and a different initialization of the plasma state. We demonstrate the capabilities of the extended code by modeling two different epochs of the prototypical SN II SN1999em. For both epochs good agreement with the observed spectra is achieved, instilling confidence that TARDIS is well-suited for quantitative spectroscopic analysis of photospheric-phase, hydrogen-rich supernovae.

In line with our goal to use TARDIS for measuring distances, our final application is the calculation of an independent set of EPM dilution factors. In this context, a long-standing issue has been the systematic discrepancy of around 20% between the results of E96 and D05, which translates into an uncertainty of the EPM distance of the same magnitude. To address this problem, we have performed radiative transfer calculations for a set of 343 TARDIS models, which span a wide range of temperatures, densities and expansion velocities. Despite using significantly different numerical techniques, the dilution factors extracted from these calculations show good agreement with those published by D05. This result helps remove some of the tension between the available sets of distance correction factors. It is still somewhat unclear which differences in the numerical approach make the models of E96 systematically more dilute than ours and D05's. Based on our calculations, we can plausibly rule out only one of the previously suggested explanations, namely differences in the treatment of relativistic effects.

Our other focus lay on investigating the parameter dependences of the dilution factors. Similar to E96 and D05, we identify density as one of the most important parameters in setting the magnitudes of the dilution factors. Our power-law fits to the density dependence yield similar scaling behaviors as for the calculations by E96. As in E96, we do not find a strong effect of the steepness of the density profile. In addition, we have demonstrated that changing the metallicity from solar to decidedly subsolar (Z=0.2) only induces minor modifications in the relationship between color temperature and dilution factors.

Finally, we have investigated differences in the setup of the model grid as an additional source of systematic errors. In our discussion, we have demonstrated that part of the discrepancy between E96 and D05 can plausibly be tracked back to differences in the assumed photospheric densities. This result highlights the need to base tabulated dilution factors on approaches that constrain the model parameters and their correlations more strongly through observational data. One way to achieve this would be to apply the tailored EPM (Dessart & Hillier, 2006; Dessart et al., 2008) to a representative set of SNe II.

In this paper we have established TARDIS as a new independent numerical tool for modeling SNe II and have demonstrated its capability to calculate accurate dilution factors. As a next step we plan to apply the code to measure absolute distances using the tailored EPM (Dessart & Hillier, 2006; Dessart et al., 2008) or SEAM (Baron et al., 1995, 1996a, 2004, 2007). As a consequence of the inclusion of a much more detailed treatment of the radiative transfer process, the typical runtime of the TARDIS spectral synthesis procedure has increased from minutes needed in the original implementation by Kerzendorf & Sim (2014) to hours. However, in light of the ubiquity of machine learning techniques and the continuous increase in computational resources, this increase in computational complexity is of minor concern and it will, for the first time, be feasible to perform the spectral fitting process in an automated manner. In combination with sampling techniques the parameter space can be explored in a systematic manner and uncertainties in the estimated parameters can be obtained. This will put strong constraints on the accuracy of absolute distance measurements of SNe II and will help to assess their promise as tools for cosmology.

Acknowledgements

CV thanks Andreas Floers, Stefan Lietzau and Markus Kromer for stimulating discussions during various stages of this project. The authors gratefully acknowledge Stefan Taubenberger for sharing his enormous expertise in the field of supernovae and for being a key member of the supernova cosmology project that motivated this work. CV would also like to thank Michael Klauser for providing help and guidance during the start of this project. The authors thank the anonymous reviewer for valuable comments. This work has been supported by the Transregional Collaborative Research Center TRR33 “The Dark Universe” of the Deutsche Forschungsgemeinschaft and by the Cluster of Excellence “Origin and Structure of the Universe” at Munich Technical University. SAS acknowledges support from STFC through grant, ST/P000312/1. Data analysis and visualization was performed using MATPLOTLIB (Hunter, 2007), NUMPY (Oliphant, 2006) and SCIPY (Jones et al., 2001).

Part III.

Automated spectroscopic analysis

Summary

An accurate radiative transfer code alone is not enough to measure H_0 with the tailored EPM. We need to fit our radiative transfer models to the observed data to constrain the atmospheric parameters—and thus the luminosity.

The large number of parameters that leave an imprint on the spectrum, ranging from expansion velocities to elemental abundances, make this difficult. Given the high cost of radiative transfer calculations, it is virtually impossible to constrain the relevant properties through conventional optimization techniques. Supernova spectroscopic analysis therefore relies on a "chi by eye" approach where the optimal parameters are identified by an experienced spectroscopist rather than an algorithm (e.g., Stehle et al., 2005; Mazzali et al., 2008; Magee et al., 2017). This reduces the number of needed radiative transfer calculations at the expense of increased human labor. The time-consuming nature of manual fitting is prohibitive for a measurement of H_0 based on a large SN sample. The subjective nature of the optimization further disqualifies the approach from being used in precision cosmology.

We have developed an innovative machine-learning framework for automated spectral fitting to overcome these limitations. Our approach is published in Vogl et al., A&A, 633, A88, 2020, which is reproduced with permission ©ESO in the following part of the thesis. The key ingredient of our method is a machine-learning emulator that is trained to mimic the output of our radiative transfer code to high precision but at a fraction of the computational cost. A few hundred models, spanning a wide range of photospheric velocities, photospheric temperatures, metallicities, time since explosions, and density profiles, serve as the training data for the emulator. We use these examples to create a probabilistic model for the spectrum at any location in the training parameter space through a combination of suitable data preprocessing, principal component analysis (PCA), and Gaussian process (GP) regression. The model reproduces actual radiative transfer calculations with TARDIS with an accuracy better than a percent, as demonstrated through a comparison to a large number of test spectra. Emulation reduces the time for producing a synthetic spectrum from 10^5 s to 10^{-2} s. This tremendous speedup makes automatic fitting of observed SN spectra possible. We demonstrate this for SN 1999em and SN 2005cs—two of the best-studied SNe II. We use the emulator combined with a standard optimization algorithm to perform maximum likelihood estimation for these objects. The inferred parameters are consistent with the conventional spectroscopic analysis of Dessart & Hillier (2006) and Dessart et al. (2008). The distances determined from our fits are in good agreement with Cepheid and TRGB based estimates.

Author contributions I was the main driver of this project. I have performed the involved computations, developed the employed spectral emulator, and conducted the spectroscopic analysis of the investigated SNe. I have written the bulk of the paper and made all the plots.

Spectral modeling of type II supernovae

II. A machine-learning approach to quantitative spectroscopic analysis

C. Vogl, W. E. Kerzendorf, S. A. Sim, U. M. Noebauer, S. Lietzau, and W. Hillebrandt

ABSTRACT There are now hundreds of publicly available supernova spectral time series. Radiative transfer modeling of this data provides insight into the physical properties of these explosions, such as the composition, the density structure, and the intrinsic luminosity, which is invaluable for understanding the supernova progenitors, the explosion mechanism, and for constraining the supernova distance. However, a detailed parameter study of the available data has been out of reach due to the high dimensionality of the problem coupled with the still significant computational expense. We tackle this issue through the use of machine-learning emulators, which are algorithms for high-dimensional interpolation. These use a pre-calculated training dataset to mimic the output of a complex code but with run times that are orders of magnitude shorter. We present the application of such an emulator to synthetic type II supernova spectra generated with the TARDIS radiative transfer code. The results show that with a relatively small training set of 780 spectra we can generate emulated spectra with interpolation uncertainties of less than one percent. We demonstrate the utility of this method by automatic spectral fitting of two well-known type IIP supernovae; as an exemplary application, we determine the supernova distances from the spectral fits using the tailored-expanding-photosphere method. We compare our results to previous studies and find good agreement. This suggests that emulation of TARDIS spectra can likely be used to perform automatic and detailed analysis of many transient classes putting the analysis of large data repositories within reach.

12. Introduction

In recent years, improvements in instrumentation as well as the supply of targets have led to a tremendous increase in the volume of spectral data gathered for astrophysical transients of all kinds. At the same time, public databases such as the WISeREP[1] archive (Yaron & Gal-Yam, 2012) or the Open Supernova Catalog[2] (Guillochon et al., 2017) have made access to this data easier than ever before; WISeREP alone provides 35484 spectra for 10809 transients.[3]

In contrast, our tools for analyzing these large spectral datasets have lagged behind. We can distinguish between two sets of approaches for dealing with such numbers of spectra. The most prevalent approach is to break the spectra down to a few easily measurable diagnostic properties (e.g., line absorption velocities, equivalent widths), which are then studied for correlations (e.g., Gutiérrez et al., 2017a; among many). The second approach is to use the spectra as input for machine-learning techniques; exemplary applications include spectroscopic classification (e.g., Yip et al., 2004) or the detection of sub-classes, for example of type Ia supernovae (Sasdelli et al., 2016). These approaches provide information about the specific measured quantities but do not provide a whole picture of the transient. Radiative transfer models have the power to infer underlying physical properties such as the composition and structure of the ejecta; we constrain these quantities by adjusting parametrized models of the emitting objects such that the simulated and observed spectra match. This provides, for example, information about the progenitor systems of the explosion for many kinds of transients (e.g., Hachinger et al. 2012 for SN Ic, Barna et al. 2017 for SN Iax). The main obstacle is the high cost of radiative transfer simulations; depending on the complexity of the underlying code, the time needed to calculate a single synthetic spectrum ranges between minutes and days. This is exacerbated by high-dimensional parameter spaces; we usually aim to determine a combination of various abundances, the density profile, photospheric temperatures, and velocities (e.g., Dessart & Hillier, 2006; Baron et al., 2007). It is prohibitively expensive to explore this parameter space automatically with radiative transfer models, which would be needed to identify the parameters that best reproduce the observed spectrum; instead, the current standard method is to optimize the agreement by hand, relying heavily on the expertise of the modeler (e.g., Stehle et al., 2005; Magee et al., 2017). This turns each spectroscopic analysis into an extremely time-consuming process that can only be done for very few objects. For example, only for three type IIP supernovae has a full spectral time series been modeled in non-local thermodynamic equilibrium (NLTE) in the last 15 years:

[1] http://www.weizmann.ac.il/astrophysics/wiserep/
[2] https://sne.space/
[3] As of the 13th of June 2019.

SN 1999em (Baron et al., 2004; Dessart & Hillier, 2006), SN 2005cs (Baron et al., 2007; Dessart et al., 2008) and SN 2006bp (Dessart et al., 2008).

One way to overcome the large computational expense of radiative transfer models in spectral fitting is to devise a fast algorithm that mimics the code. A very simple implementation of such an algorithm is interpolation in a pre-computed Cartesian grid. However, high-dimensional problems such as supernovae require the use of more complex algorithms known as emulators. In essence, the emulator learns the mapping from the simulation input to the output from a set of examples; the simulator, in this context, is treated as a black box. Emulators are used extensively, for example in engineering, but have not yet found widespread application in astrophysics. Some of the sparse cases have been the prediction of the nonlinear matter power spectrum (Heitmann et al., 2009), stellar spectra (Czekala et al., 2015), and type Ia supernova spectra (Lietzau, 2017)[4].

In this paper, we apply emulation to perform automated quantitative spectroscopic analysis of type II supernovae (SNe II). We use Gaussian-process interpolation in the principal component analysis (PCA[5]) space to reproduce the output of our radiative transfer code, a modified version of the Monte Carlo (MC) code TARDIS (Vogl et al., 2019). With the emulator, we reduce the time for the calculation of a synthetic spectrum from hours to milliseconds; this in turn makes it possible to fit spectra using conventional optimization methods or to explore the parameter space with a sampler.

We showcase the emulator by inferring distances to type IIP supernovae using the tailored-expanding-photosphere method (tailored EPM; Dessart & Hillier, 2006; Dessart et al., 2008). This method uses spectroscopic analysis of type IIP supernovae to obtain distances with small uncertainties, for example for cosmological studies. A cosmological application requires a large number of uniformly studied supernovae, which will be made possible by the use of emulators. Such an endeavor will provide an independent, physics-based probe of the cosmic expansion history.

Chapter 13 provides a short introduction to supernova models and their use for parameter inference. Chapter 14 describes the library of synthetic spectra that forms the basis of our machine-learning approach. Chapter 15 is dedicated to the presentation of the spectral emulator: the machine-learning techniques, the training process, and the prediction step. In Chapter 16, we assess the predictive performance by comparing emulated and simulated spectra for a set of independent test models. We continue with the application of the emulator to the modeling of spectra of SN 1999em and SN 2005cs in Chapter 18. We show the application of measuring distances using the tailored EPM in Sect. 18.3. Chapter 19 summarizes the results and gives an outlook on future steps.

[4] https://doi.org/10.5281/zenodo.1312512
[5] See Sect. 15.1 for more details on PCA.

13. Parametrized supernova models with TARDIS

We use simple parametrized models of the supernova ejecta to make inferences about the supernova properties. In defining these models, we assume the ejecta to be spherically symmetric and in homologous expansion. This allows us to discretize the spectrum formation region into a set of shells that are specified by their composition, density, and expansion velocity. It is often useful to simplify the model specification further, for example by assuming an analytic form for the density profile (e.g., a power law) or by assuming uniform abundances—this reduces the number of parameters considerably.

Since we do not simulate the creation of the radiation field self-consistently, we treat the radiation field at the inner boundary as a model parameter. Specifically, we assume a blackbody characterized by a temperature T_{inner}; this is well motivated for SNe II since the continuum opacity from hydrogen leads to a full thermalization of the radiation field at high optical depths.

To assess if the thus-defined parametrized model is consistent with observations, we simulate the radiation transport through the discretized ejecta and then compare the synthetic and observed spectra. In TARDIS (Kerzendorf & Sim, 2014), we use a Monte Carlo approach based on the indivisible energy packet scheme of Lucy (1999a,b, 2002, 2003) to this end. The version used in this paper (Vogl et al., 2019) simulates the effects of bound-bound, bound-free, free-free, as well as collisional interactions on the radiation field; it accounts for NLTE effects in the excitation and ionization of hydrogen and calculates the thermal structure of the envelope from the balance of heating and cooling processes.

14. Creation of a SN II spectral training set

As a first step towards the spectral emulator, we need to calculate a set of synthetic SNe II spectra, which will serve as the training data. We selected photospheric velocity $v_{\rm ph}$, photospheric temperature $T_{\rm ph}$, metallicity Z, time of explosion $t_{\rm exp}$, and steepness of the density profile $n = -\,\mathrm{d}\ln\rho/\,\mathrm{d}\ln r$ as the parameters of our model grid. The latter provides a simple parametrization of the density profile, which, as demonstrated for example by Chevalier (1976); Blinnikov et al. (2000), and Dessart & Hillier (2006), describes the outer density distribution with sufficient accuracy.

Most of the spectral evolution of photospheric phase SNe II, as well as the differences between individual objects, can be explained by variations in the expansion velocity, the temperature, and the density profile. As such, the parameters usually considered in quantitative spectroscopic analyses, such as those of Dessart & Hillier (2006) or Dessart et al. (2008) are $v_{\rm ph}$, $T_{\rm ph}$, and n.[1] In addition to these essential parameters, we include the metallicity Z.[2] Observed SNe II show a wide range of metallicities (see e.g., Anderson et al., 2016; Taddia et al., 2016) and the associated changes to the spectrum are significant, in particular in the blue. For the purpose of inferring accurate distances, it is also important to allow for variations in the time of explosion $t_{\rm exp}$. While the effects on the shape of the spectral energy distribution (SED) are small, $t_{\rm exp}$ affects the absolute value of the flux through the modulation of the photospheric density (for any given density profile) and therefore the amount of continuum flux dilution (see e.g., Eastman et al., 1996). Other potentially relevant parameters are the abundances of CNO process elements, which have been investigated for example by Baron et al. (2007), as well as the H/He abundance ratio as studied for example by Dessart & Hillier (2006). For the first demonstration of our method, we refrain from varying these parameters and instead adopt CNO-cycle equilibrium values for the relevant abundances from Prantzos et al. (1986) as in Dessart & Hillier (2005b, 2006).[3]

Table 14.1 lists the ranges of parameters $v_{\rm ph}$, $T_{\rm ph}$, Z, $t_{\rm exp}$, and n covered by our model grid. We have chosen the parameter space such that it allows for the modeling of a large variety of SNe II between roughly one and three weeks after explosion.

[1] We define the photospheric temperature $T_{\rm ph}$ as the temperature of the electron gas at an electron scattering optical depth of $\tau = 2/3$.

[2] We use metallicity to refer to the abundances of all elements except H, He, C, N, and O. The mass fractions of the thus-defined metal species are multiples of the solar neighborhood values $Z_\odot$ of Asplund et al. (2009).

[3] Specifically, we adopt the following number density ratios: H/He = 5, N/He = 6.8×10^{-3}, C/He = 1.7×10^{-4}, and O/He = 10^{-4}. These ratios together with the mass fractions of the metal species specify the composition completely.

Table 14.1.: Parameter range covered by the spectral library.

	$v_{\rm ph}$ [km s^{-1}]	$T_{\rm ph}$ [K]	Z [$Z_\odot$]	$t_{\rm exp}$ [days]	n
Min	3700	6300	0.1	6.5	6
Max	10 500	10 000	3.0	22.0	16

In practice, we cannot directly specify $T_{\rm ph}$ and $v_{\rm ph}$ since both are emergent and not input properties of the simulation; instead, we use the inner boundary temperature $T_{\rm inner}$, that is to say the temperature of the injected blackbody radiation[4], and a simple analytic estimate for the photospheric velocity $v^*_{\rm ph}$. We set up a five-dimensional latin hypercube design (Stein, 1987) in these parameters, which is optimized to fill the space nearly uniformly. In the next step, we perform radiative transfer calculations for the resulting set of 780 models and obtain synthetic spectra as well as the real values of $T_{\rm ph}$ and $v_{\rm ph}$. Figure 14.1 shows pairwise projections for the completed set of parameters $v_{\rm ph}$, $T_{\rm ph}$, Z, $t_{\rm exp}$, and n. The grid of models displays a slight distortion in the $v_{\rm ph}$-$T_{\rm ph}$ plane as a result of our use of $v^*_{\rm ph}$ and $T_{\rm inner}$ as proxies for these quantities.

A common approach in machine learning is to generate a test set in addition to the training set to assess the predictive accuracy. We compute 225 models (in addition to the 780 training models). The parameters for these models are sampled uniformly from the same range of $v^*_{\rm ph}$, $T_{\rm inner}$, Z, $t_{\rm exp}$, and n as covered by the training data. We include the properties of the test data in Fig. 14.1 to facilitate the comparison between the sets of models.

One of the challenges in the setup of the model grid is deciding how large the training set of models really needs to be. Ideally, the number of training models should be large enough to guarantee that the interpolation uncertainty in the spectra is not the dominant contribution to the error in the inferred parameters; at the same time, the training size should be kept as small as possible for reasons of computational expediency. In practice, the best possible trade-off is difficult to identify since the conversion from the interpolation errors in the spectra to errors in the parameters is nontrivial. To be on the safe side however one can aim to have the interpolation uncertainty significantly smaller than the systematic mismatch between model and observation; for the parameter space we consider, this is indeed the case for the training set we used (see Chapter 16).

[4]Typically, the inner edge of our computational domain, where the packets are injected, lies at an electron scattering optical depth of around 20.

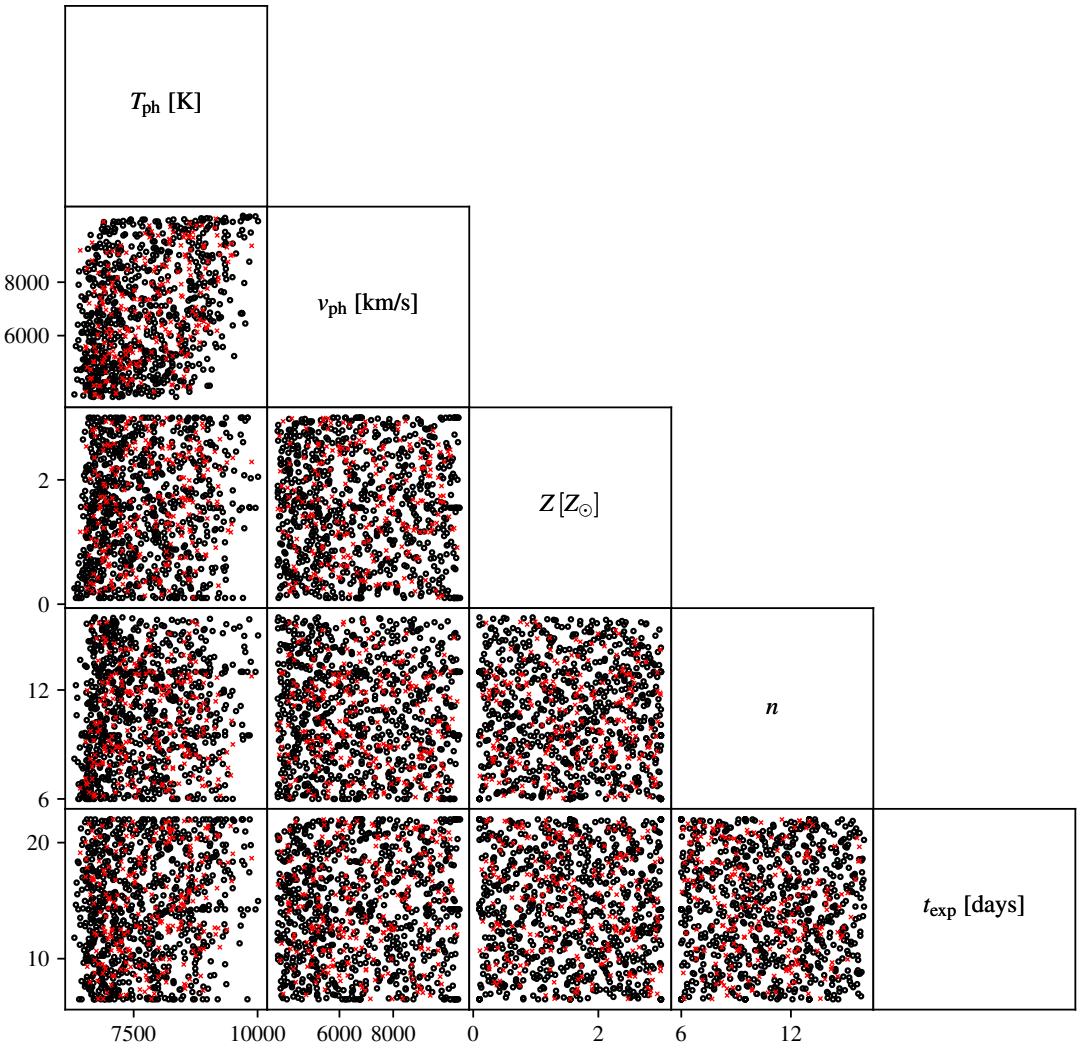

Figure 14.1.: Scatterplot matrix of the parameters of the training data (black) and test data (red) of the spectral emulator.

15. Spectral emulator

We use the synthetic spectra from the previous section to create two separate emulators: one for spectra and one for absolute magnitudes. We set up these emulators in two steps. First, we preprocess the training data and synthesize absolute magnitudes; this is followed by dimensionality reduction of the preprocessed spectra through PCA decomposition. Second, we train Gaussian processes to interpolate the spectra within the PCA space and to predict absolute magnitudes.

15.1. Preprocessing and dimensionality reduction

The synthetic spectra have a range of values that varies widely both with wavelength and between models. In addition, they contain non-negligible Monte Carlo noise. For the successful application of machine-learning techniques, it is crucial to preprocess the noisy, unscaled data to standardize them and to remove unwanted sources of variation. We start by smoothing the spectra with a fifth-order Savitzky-Golay filter (Savitzky & Golay, 1964) to reduce the effect of Monte Carlo noise. Savitzky-Golay filtering performs well in preserving the shape of spectral features, even weak ones, which makes it a popular choice for denoising astrophysical spectra (see e.g., Hügelmeyer et al., 2007; Poznanski et al., 2010; Sasdelli et al., 2015). Next, we approximately correct for the variations in the position of spectral features between models by Doppler shifting each spectrum by the photospheric velocity v_{ph}. This roughly maps the absorption minimum of a spectral feature to the same wavelength for all models. Since we do not assume a distance for fitting an observed spectrum (see Chapter 18), we can standardize the spectral library further by discarding the information about the luminosity. Specifically, we normalize the shifted synthetic spectra to have unit flux at 6000 Å; this provides a good standardization of the continuum flux levels between models since no strong line features form at this position. Finally, we apply a linear transformation to the fluxes in each wavelength bin such that in each bin the values for the full spectral library span a range from -0.5 to 0.5 (see Chapter 19). For each preprocessing step, we restrict the considered wavelength range to the minimum range needed to model the observations in Chapter 18.[1] In practice, this corresponds to a wavelength window from roughly 3200 Å to 9500 Å. In contrast, we only smooth the test spectra but do not preprocess them further: we compare them to the emulated spectra in the same fashion as for observational data.

In the final step, we reduce the dimensionality of our spectral library. Each preprocessed spectrum consists of a few thousand wavelength bins, a number which by far exceeds that of the

[1] We note that this wavelength range deviates slightly from that of the observed spectra to allow for Doppler shifting the model spectra in the preprocessing.

physical parameters used in its creation. To obtain a less correlated, more compact representation of our data, we use PCA.[2] Principal component analysis has been applied successfully to observed spectra of a wide range of astrophysical objects, including quasars (e.g., Francis et al., 1992), stars (e.g., Bailer-Jones et al., 1998), galaxies (e.g., Connolly et al., 1995), and supernovae (e.g., Sasdelli et al., 2015; Williamson et al., 2019). The basic idea is to find an orthogonal basis for the data that is a linear transformation of the original but where the axes are aligned with the directions of maximal variance. Since by construction each successive principal component explains less of the variance in the data, we can reduce the dimensionality of our dataset by truncating the basis; instead of using the full set of N_L principal component eigenvectors, where N_L is the number of spectra in the spectral library, we use only the first $N < N_\mathrm{L}$ components. We select the dimensionality N of the truncated basis through cross-validation on the training sample since our main goal is the accurate prediction of synthetic spectra. The cross-validation performance increases at first as more principal components are included but at some point levels off when the additional components stop providing meaningful information; it is at this point that we truncate the PCA basis. For the spectral emulator presented in this paper, this approach leads us to use $N = 80$ principal components, which explain 99.97 % of the total variance; this is a significant reduction compared to the original approximately 1500 wavelength bins. If necessary[3], the number of principal components can be reduced even further with only minor losses in accuracy. By projecting each preprocessed spectrum $\hat{f}_k$ onto the basis vectors ξ_i of the thus-truncated basis, we obtain a compact representation of the input data in terms of a set of N principal component weights $\{w_{ik}\}$. From these principal component weights, we can reconstruct every input spectrum as a linear combination of the principal components ξ_i and the mean spectrum $\xi_\mu = \sum_k^{N_\mathrm{L}} \hat{f}_k / N_\mathrm{L}$:

$$\hat{f}_k \approx \xi_\mu + \sum_{i=1}^{N} w_{ik} \xi_i. \tag{15.1}$$

For the selected number of principal components, the mean fractional reconstruction error for this procedure is 0.26 %.

In addition to the spectral preprocessing and the dimensionality reduction, we synthesize Johnson-Cousins B, V, I magnitudes from the unprocessed synthetic spectra.[4] These serve as training data for a separate emulator that predicts absolute photometric magnitudes for a set of model parameters v_ph, T_ph, Z, t_exp, and n. This allows us to convert the inferred parameters from the spectral fitting into a distance estimate based on the observed photometry (Chapter 18).

[2] Specifically, we use the probabilistic PCA model of Tipping & Bishop (1999) as implemented in scikit-learn (Pedregosa et al., 2011).

[3] For example, for sampling in high-dimensional parameter spaces the emulation speed may become a limitation.

[4] For our synthetic photometry, we use the filter functions of Bessell (1990).

15.2. Gaussian process interpolation

15.2.1. Spectra

To predict a spectrum for a new set of input parameters $\theta = (v_{\rm ph}, T_{\rm ph}, Z, n, t_{\rm exp})$, we have to interpolate between the principal component weights $\{w_{ik}\}$, which form the compressed version of our spectral library. We choose to model the weights w_i for each principal component ξ_i independently since by construction the weights for the different components are at least linearly uncorrelated. As in Czekala et al. (2015), we use Gaussian processes (GPs; e.g., Rasmussen & Williams, 2006) for the interpolation. Gaussian processes are a powerful probabilistic tool for regression analysis, which are steadily gaining in popularity in the astrophysical community (see, e.g., Rajpaul et al., 2015; Foreman-Mackey et al., 2017). As a nonparametric method, GPs offer increased flexibility for modeling complicated signals compared to more conventional approaches such as linear or polynomial regression.

Fundamentally speaking, GPs provide a generalization of the Gaussian probability distribution from finite-dimensional random variables to functions. Following this analogy, each GP is characterized by a mean- and a covariance function. The covariance function k controls the covariance between the distribution of random function values at any two points $\theta, \theta^{'}$ in the parameter space. As such, it determines the properties of the functions that can be drawn from the GP, including for example their smoothness, periodicity, and so forth. In the context of regression analysis, the choice of the covariance function sets the prior distribution of functions that we expect to see in the data.[5] A particularly important class of covariance functions are the so-called stationary covariance functions, which do not depend on the positions $\theta, \theta^{'}$ in the input space but only on their distance $r = ||\theta - \theta^{'}||$. The most commonly used members of this class include the squared exponential, the Matérn, and the rational quadratic covariance function (see, e.g., Rasmussen & Williams, 2006; Murphy, 2012). The type of covariance function is a hyperparameter of the machine-learning approach and can, similar to the preprocessing steps, be set based on the cross-validation performance. After some experimentation, we adopted covariance functions from the Matérn family:

$$k_{\rm Matern}(r) = \sigma_{\rm f}^2 \frac{2^{1-\nu}}{\Gamma(\nu)} \left(\sqrt{2\nu} r\right)^{\nu} K_{\nu} \left(\sqrt{2\nu} r\right). \tag{15.2}$$

Here, $\sigma_{\rm f}^2$ denotes the signal variance, ν is a parameter that regulates the smoothness of the GP, Γ is the gamma function, and K_{ν} is the modified Bessel function of the second kind. Since we do not expect the weights that encode our MC synthetic spectra to be noise free, we include an additive contribution of homoscedastic white noise in the covariance function:

$$k(r) = k_{\rm Matern}(r) + \sigma_{\rm n}^2 \, \delta(r), \tag{15.3}$$

[5] It is customary to assume a zero mean for the prior distribution of possible regression functions (see, e.g., Rasmussen & Williams, 2006).

where σ_n^2 is the noise variance and δ the Dirac delta function. We complete the description of the covariance function by defining the distance as

$$r^2(\theta, \theta') = (\theta - \theta')^\mathrm{T} M (\theta - \theta'), \tag{15.4}$$

where M can be any positive semidefinite matrix. For simplicity, we only consider diagonal matrices of the following type:

$$M = \begin{bmatrix} \frac{1}{l_{v_\mathrm{ph}}{}^2} & & & \\ & \frac{1}{l_{T_\mathrm{ph}}{}^2} & & \\ & & \ddots & \\ & & & \frac{1}{l_{t_\mathrm{exp}}{}^2} \end{bmatrix}. \tag{15.5}$$

For this choice of metric, each dimension of the input space $(v_\mathrm{ph}, T_\mathrm{ph}, Z, n, t_\mathrm{exp})$ has its own characteristic length-scale $(l_{v_\mathrm{ph}}, \ldots, l_{t_\mathrm{exp}})$ for variations in the function values.

Finally, to make predictions, we have to move from the prior distribution of functions to a posterior distribution of functions that agree with the training data. Mathematically speaking, this is achieved by conditioning the zero-mean prior GP on the observed values. The conditional GP has a nonzero mean function $w_i(\theta)$ that is determined by the values w_{ik} of the training data and the covariances $k_i(\theta, \theta_k)$ between the location θ and the training locations θ_k. The relevant expressions for the predictive mean and variance can be found in standard textbooks such as Rasmussen & Williams (2006; their Algorithm 2.1). Given a set of hyperparameters $(\sigma_\mathrm{n}^2, \sigma_\mathrm{f}^2, l_{v_\mathrm{ph}}, \ldots, l_{t_\mathrm{exp}}, \nu)$, these equations yield the interpolated values for the principal component weight as well as an estimate of the interpolation uncertainty. The parameter ν regulating the smoothness properties of the process is difficult to constrain through the data; after some experimentation, we adopted $\nu = 3/2$, corresponding to functions that are once mean-square differentiable. We set the remaining hyperparameters by numerically maximizing the marginal likelihood of the training data under the GP model. We repeat this process N times since we model the weights w_i for each principal component ξ_i independently.

Equation 15.1 allows us to predict "preprocessed" spectra $\hat{f}(\theta)$ using the trained GPs. To arrive at a spectrum that we can compare to observations, we have to reverse some of the preprocessing steps used to standardize the input spectra for PCA in Sect. 15.1. This involves inverting the linear transformation applied to map the fluxes in each bin to the range $[-0.5, 0.5]$, as well as blue-shifting the spectrum by the photospheric velocity v_ph.

15.2.2. Absolute magnitudes

In Sect. 15.1, we removed the luminosity information from the synthetic spectra to standardize them further for PCA. We train additional GPs for the prediction of the absolute magnitudes, which we need for our distance inferences in Chapter 18.

As part of the data preprocessing, we synthesized Johnson-Cousins S=$\{B,V,I\}$ magnitudes M_S from the unprocessed synthetic spectra. Before we use these as training data for the GPs, we remove the variation in the magnitudes introduced by differences in the physical sizes of the supernova models. Specifically, we transform from absolute magnitudes to magnitudes at the position of the photosphere

$$m_S^{\mathrm{ph}} = M_S + 5\log\frac{R_{\mathrm{ph}}}{10\,\mathrm{pc}}, \tag{15.6}$$

where $R_{\mathrm{ph}} = v_{\mathrm{ph}} t_{\mathrm{exp}}$. We model each bandpass with a GP with a Matérn covariance function (see, Eq. (15.2)) that has a smoothness parameter $\nu = 5/2$. The hyperparameters $(\sigma_{\mathrm{n}}^2, \sigma_{\mathrm{f}}^2, l_{v_{\mathrm{ph}}}, \ldots, l_{t_{\mathrm{exp}}})$ for the individual bandpasses are set in the same fashion as for the spectral emulator. Finally, to predict absolute magnitudes for a new set of input parameters $\theta = (v_{\mathrm{ph}}, T_{\mathrm{ph}}, Z, n, t_{\mathrm{exp}})$, we evaluate the trained GP and subtract $5\log(R_{\mathrm{ph}}/10\,\mathrm{pc})$.

16. Evaluation of the emulator performance

To allow the reliable inference of parameters from supernova spectra, it is crucial that the emulator reproduces the output of our simulation code TARDIS to high precision. We assess the predictive performance of our method by comparing the predicted spectra and absolute magnitudes to a set of independently collected test data. Our strategy for the calculation of the 225 test models is described in detail in Chapter 14 and the associated preprocessing procedure in Sect. 15.1.

16.1. Spectra

In Fig. 16.1, we compare simulated and emulated spectra for a subset of the test models; the selected subset approximately spans the range of deviations encountered in the full test data. We scaled the emulated spectra back to physical units for the comparison of spectral shapes.[1] Despite covering a wide variety of spectral appearances, including for example SEDs with very broad or very narrow features, with or without line blanketing, the agreement is excellent overall. In addition, in most cases, the deviations are within the 95% confidence interval of the emulator prediction with areas of larger residuals corresponding to regions with increased emulation uncertainties.

In order to quantify the test performance, we need to define a quality metric that expresses the mismatch between two spectra in a single number. We use the mean fractional error (MFE)

$$\mathrm{MFE} = \frac{1}{N_\lambda} \sum_{i=1}^{N_\lambda} \frac{|f_{\lambda,i}^{\mathrm{emu}} - f_{\lambda,i}^{\mathrm{test}}|}{f_{\lambda,i}^{\mathrm{test}}}, \tag{16.1}$$

where $f_{\lambda,i}^{\mathrm{test}}$ and $f_{\lambda,i}^{\mathrm{emu}}$ are the test and emulated spectra respectively, and N_λ is the number of wavelength bins. By using the MFE instead of for example the mean squared error, we give approximately the same weight to the red (low flux) and blue (high flux) parts of the spectrum. We summarize the test performance in the top left panel of Fig. 16.1, which shows a histogram of the MFEs for the entire test sample. The median MFE is 0.64 %, confirming the excellent agreement found by visual inspection. For 95 % of the test spectra the deviation is less than 1.2 %; for the remaining 5 % maximum differences of around 2 % are possible. To assess how the emulator performance varies within the parameter space, we modified the scatterplot matrix of the test parameters to include the color-coded MFE (see Fig. 16.2). The figure demonstrates that a significant fraction of the cases with appreciable mismatches can be traced back to models near

[1] As discussed in Sect. 15.1, we discard any useful luminosity information during the preprocessing of the training spectra; this means that it is only meaningful to compare spectral shapes.

the edge of the training parameter space (or even outside of it). We also notice a slight decrease in performance towards lower velocities, temperatures, and higher metallicities. This trend is to be expected since the complexity of the SED increases in these directions of the parameter space. For example, in the case of velocity, we move from a few blended features to a forest of individual metal lines; each of these lines evolves individually in a nonlinear fashion making it difficult to model the spectral evolution based on a PCA decomposition.

16.2. Absolute magnitudes

For the purpose of measuring accurate distances, it is crucial that we can accurately predict the luminosity for any combination of input parameters. We assess the accuracy of our approach by comparing the synthetic photometry of the test models to the absolute magnitudes predicted by the emulator. As shown in Fig. 16.3, the median difference between the predicted and true magnitudes is less than 0.0012 mag; this confirms that the emulator provides an unbiased estimate of the true model luminosity. The accuracy of the predictions decreases from the redder to the bluer bandpasses but is nevertheless excellent in all cases; the slight decrease can be easily explained by the different amounts of line blanketing in each filter. In all filters, 68 % of the models show differences of less than 0.007 mag corresponding to errors in the model flux of less than 0.7 %. For 95 % of the models, the errors are less than 0.02 mag yielding maximum flux errors of around 1.8 %. Thus, in virtually all cases, the accuracy of the emulator is much higher than the uncertainties in most real photometric data. Finally, in Fig. 16.4, we demonstrate that, as in the case of spectra, the emulator provides sensible estimates for the predictive uncertainties.

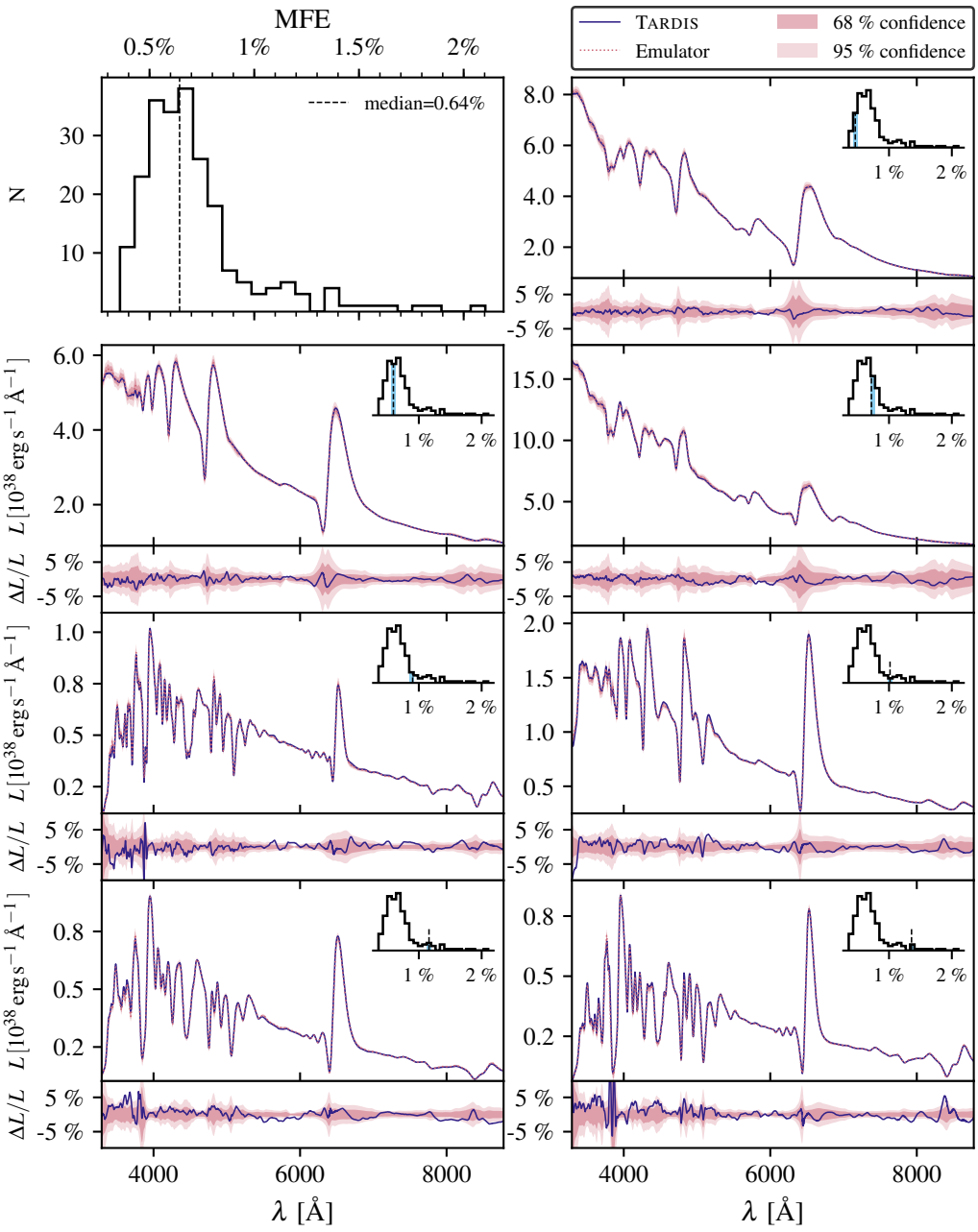

Figure 16.1.: Evaluation of the emulator performance. The test performance is summarized in the *top left panel*, which shows a histogram of the test errors; specifically, the MFE (see Eq. 16.1) is displayed. The other panels provide a direct comparison between emulated and simulated spectra for a subset of the test data. Each panel contains a histogram of the test errors, in which the position of the current model is highlighted. To highlight the subtle differences between the predicted and true spectra, the fractional difference $\Delta L/L$ is shown in the lower section of each panel (solid blue line). In both sections, the shaded regions indicate the 68 % and 95 % confidence intervals for the prediction of the emulator.

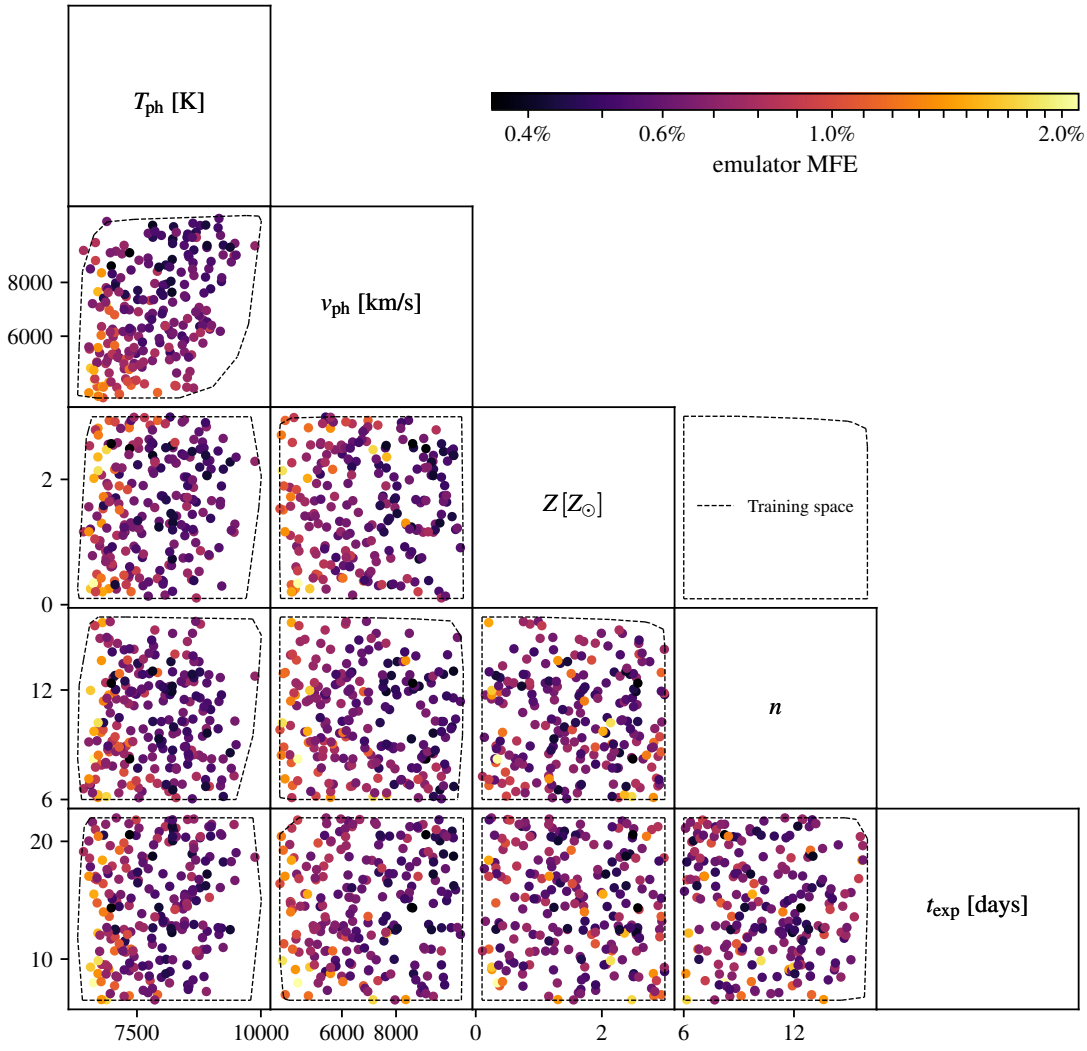

Figure 16.2.: Test errors for the spectral emulator as a function of the input parameters. We show the color-coded MFE (see Eq. 16.1) between emulated and simulated spectra for all two-dimensional projections of the test parameters. The region enclosed by the dashed black line indicates the parameter space covered by the training data.

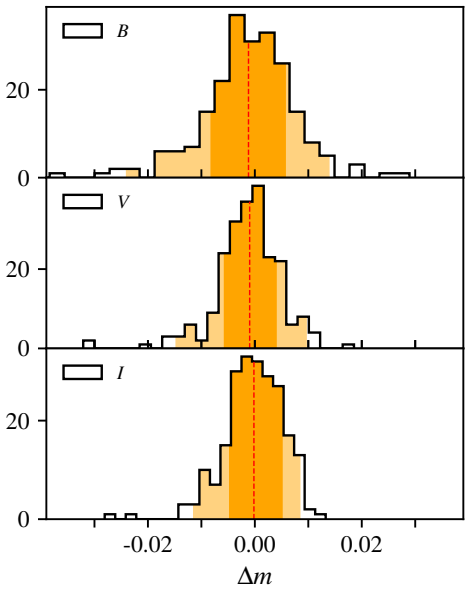

Figure 16.3.: Differences Δm between predicted and true magnitudes for the B, V, and I bandpasses. The median of each distribution is marked with a dashed red line. We indicate the central 68 % and 95 % intervals in orange and light orange respectively.

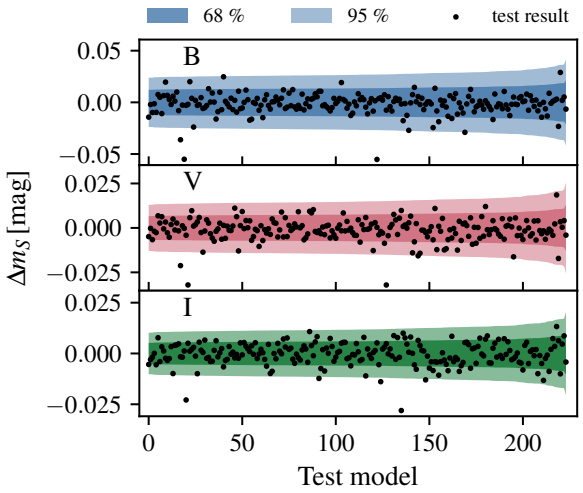

Figure 16.4.: Comparison of the predicted uncertainties to the actual differences, Δm, between predicted and true magnitudes. For each bandpass (B, V and I), we show the 68 % and 95 % confidence interval for the predicted magnitudes as well as their actual deviations from the magnitudes of the test models (denoted “test result”).

17. Learning behavior of the emulator

In this section, we address questions about the number of models needed for a desired accuracy, the adequacy of the adopted methods, and how the emulator compares to the standard approach of picking the best-fitting model from the grid.

We start by creating a learning curve for the spectral emulator as shown in Fig. 17.1. The learning curve shows the accuracy of the emulator as a function of the number of models used for training, for both the test and the training sample. We keep the number of principal components fixed, thus starting with a minimum training size of 80. In the investigated regime, the mean error on the training set is almost constant at around 0.5 %. At least part of this error can plausibly be attributed to the MC noise inherent to the models.[1] From the small training errors, we conclude that our model does not suffer from high bias, that is to say, the model is flexible enough to provide a satisfactory fit to the training data. The mean test error decreases steadily from its initial value of 1.7 % as the number of training instances is increased and quickly drops below 1 %. Finally, for the maximum training size, a test score of 0.7 % is reached. At this point, the difference between training and test score is small but non-negligible. The gap between the scores will be reduced even further as more training instances are added since the test score is still decreasing (albeit at a slower rate). We conclude that our model generalizes well and does not overfit the training data.

Finally, we compare the emulator to the often used approach of simply picking the best-fitting model from the grid. Figure 17.2 shows the test scores for both approaches as a function of the number of training instances; the plot highlights the massive reduction in the number of models that are needed to achieve a given precision. The emulator with the minimum considered training size of 80 outperforms the method of picking the nearest model even when the full set of 780 spectra is used. To get a rough estimate of how many models would be needed to match the final accuracy of 0.7 % of the emulator, we linearly extrapolate the learning curve in log-linear space; this yields on the order of 15 000 spectra. This is a conservative lower limit for the number of needed models since it generously assumes a constant learning rate.

[1] The MC noise manifests itself not only as Poisson noise in the synthetic spectra but also in terms of complicated correlated noise that arises from the MC uncertainties in the plasma state quantities.

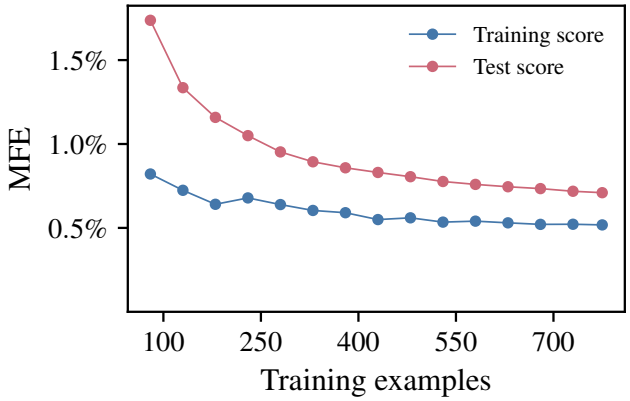

Figure 17.1.: Learning curve for the spectral emulator. The error on the training sample as well as the test sample is shown as a function of the number of models used in the training. The quoted errors are the mean of the individual errors, which in turn are the MFE for each spectrum. For each training size, we select five different realizations at random and average the resulting errors.

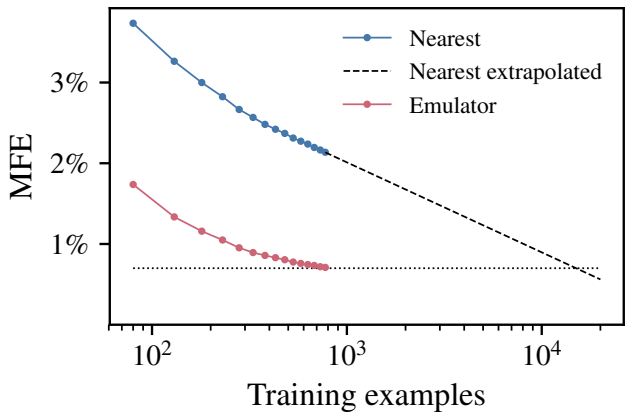

Figure 17.2.: Learning behavior of the emulator as a function of the number of spectra used in the training in comparison to the more naive approach of picking the closest spectrum.

18. Modeling observations

With the spectral emulator, we can fit SN II spectral time series in an automated fashion. For a first demonstration, we select SN 1999em and SN 2005cs as our test objects. SN 1999em is considered by many to be the prototype of a type II supernova, whereas SN 2005cs is a more peculiar, subluminous object. Both are among the best-observed type II supernovae, with extensive datasets including photometry and spectroscopy at UV, optical, and infrared wavelengths (Leonard et al., 2001, 2002; Hamuy et al., 2001; Dessart & Hillier, 2006; Pastorello et al., 2006, 2009b; Tsvetkov et al., 2006; Bufano et al., 2009). Both SNe have been studied with detailed NLTE radiative transfer models using CMFGEN (Dessart & Hillier, 2006; Dessart et al., 2008) and PHOENIX (Baron et al., 2004, 2007). Here we compare the results of our automated fits to these analyses, which have been conducted carefully by hand. In our comparison, we focus on the studies of Dessart & Hillier (2006) and Dessart et al. (2008), which model more epochs and have published the relevant inferred parameters, namely $T_{\rm ph}, v_{\rm ph}$ and n. In the final step, we infer distances to the supernovae from our fits using the tailored-expanding-photosphere method.

18.1. Likelihood for parameter inference

We use a standard multi-dimensional Gaussian likelihood function for parameter inference. In this case, the log-likelihood of an observed spectrum $f_\lambda^{\rm obs}$ with $N_{\rm pix}$ spectral bins is given by

$$\ln p(f_\lambda^{\rm obs}|\theta_{\rm SN}, E(B-V)) = -\frac{1}{2}\left(\mathrm{R}^{\mathrm{T}}\mathrm{C}^{-1}\mathrm{R} + \ln\det \mathrm{C} + N_{\rm pix}\ln 2\pi\right), \tag{18.1}$$

where

$$R = f_\lambda^{\rm obs} - f_\lambda(\theta_{\rm SN}, E(B-V)), \tag{18.2}$$

are the residuals with respect to the emulated, reddened spectrum f_λ and C is the pixel-by-pixel covariance matrix (e.g., Czekala et al., 2015). As before, $\theta_{\rm SN} = (v_{\rm ph}, T_{\rm ph}, Z, n, t_{\rm exp})$ are the parameters of our SN model and $E(B-V)$ is the color excess.[1] The residuals have pixel-to-pixel correlations mostly due to imperfections in the model calculations (see Czekala et al., 2015). For example, a slight error in the ionization balance of a given element will lead to features in the synthetic spectrum that are either systematically too weak or too strong, producing highly correlated residuals in these regions. If these correlations are not accounted for in the covariance matrix C, the uncertainties of the inferred parameters will be severely underestimated (Czekala

[1] We assume a ratio of total to selective absorption of $R_V = 3.1$ as appropriate for Milky Way-type dust.

et al., 2015). We find typical uncertainties for the photospheric temperature of the order of a few Kelvin if we only include the interpolation uncertainty and the photon count noise; thus, without a good statistical model for the correlated residuals, the inferred uncertainties are essentially meaningless. For the purpose of a first demonstration, we resort to a simple maximum-likelihood approach with homoscedastic white noise, that is to say a diagonal, constant covariance matrix. Our rationale for using homoscedastic white noise instead of a combination of the heteroscedastic photon noise and the interpolation uncertainties is that the systematic mismatches between model and observation are the dominant error component in most regions; ignoring these mismatches means that we assign highly variable and essentially meaningless weights to different parts of the spectrum.

18.2. Fitting observed spectra

We want to compare our framework for parameter inference to the quantitative spectroscopic analyses of Dessart & Hillier (2006) and Dessart et al. (2008)—detailed NLTE studies conducted carefully by hand by experts. To allow an unbiased comparison of the inferred parameters, we copy key assumptions of these studies. First, we adopt solar metallicities for the nonCNO processed elements. Second, we use the same elapsed times since explosion as utilized in the calculation of their spectral models; this is particularly important for the comparison of photospheric temperatures, which are sensitive to this parameter. Third, we adopt a color excess of $E(B-V) = 0.1$ towards SN 1999em[2] and a color excess of $E(B-V) = 0.04$ towards SN 2005s in concordance with Dessart & Hillier (2006) and Dessart et al. (2008). We redden the emulated spectra by this color excess according to the Cardelli, Clayton, & Mathis (1989) law with $R_V = 3.1$. Finally, we blueshift the observed spectra by the peculiar velocities of their host galaxies, which we assume to be $770\,\mathrm{km\,s^{-1}}$ (Leonard et al., 2002; Dessart & Hillier, 2006) for SN 1999em and $466\,\mathrm{km\,s^{-1}}$ (Dessart et al., 2008) for SN 2005s. A log of the spectra used as well as relevant model parameters such as the time since explosion utilized in the calculation of the spectral models can be found in Table 18.1.

18.2.1. SN 1999em

We model three epochs of SN 1999em, covering a time span between roughly two and four weeks after explosion. In Fig. 18.1, we show the maximum likelihood emulated spectra in comparison to the observations, highlighting the good agreement between the two.[3] For each spectral epoch, a table with the inferred maximum likelihood parameters as well as the literature values from Dessart & Hillier (2006) is attached to the plot. Despite using vastly different methods for calculating synthetic spectra and for adjusting them to match the observations, we find good

[2] This value is slightly higher than our favored reddening of $E(B-V) = 0.08$ (see Vogl et al., 2019).

[3] Nevertheless, even better agreement between models and observations would be achieved for our favored reddening of $E(B-V) = 0.08$ (see Vogl et al., 2019).

Table 18.1.: Log of modeled spectra for SN 1999em and SN 2005cs.

SN 1999em			
JD (+2 451 474.04)	Date	Source	$t_{\rm exp}$
17.9	9 Nov. 1999	H01	9.67
22.9	14 Nov. 1999	H01	11.21
27.9	19 Nov. 1999	H01	22.00$^{(a)}$
SN 2005cs			
JD (+2 453 549)	Date	Source	$t_{\rm exp}$
12.25	9 July 2005	D08	14.67
13.5	10 July 2005	F14	16.12
14.5	11 July 2005	P06	15.33
17.0	14 July 2005	P06	16.11
19.4	16 July 2005	P200	19.40

Notes. The reference JDs are the estimated times of explosion of Dessart & Hillier (2006) and Pastorello et al. (2009b). The abbreviations for the data sources are H01 for Hamuy et al. (2001), P06 for Pastorello et al. (2006), D08 for Dessart et al. (2008), F14 for Faran et al. (2014a), and P200 for spectra taken at the Palomar 200-inch Hale Telescope with DBSP. All spectra have been retrieved from the WISeREP archive (Yaron & Gal-Yam, 2012). We use the listed time since explosions $t_{\rm exp}$, as taken from Dessart & Hillier (2006) and Dessart et al. (2008), for calculating synthetic spectra with the emulator. $^{(a)}$ As the single exception, we adopt the maximum $t_{\rm exp}$ of our spectral emulator for the epoch of the 19 November 1999; this is roughly 19 % smaller than the value of $t_{\rm exp} = 27.0$ used by Dessart & Hillier (2006) .

agreement in the inferred parameters, with maximum differences of only 285 K in photospheric temperature, 351 km s^{-1} in photospheric velocity, and 0.8 in the steepness of the density profile. We visualize this in Fig. 18.4, which plots our values for $v_{\rm ph}$ and $T_{\rm ph}$ against those of Dessart & Hillier (2006). Whereas our best fit parameters for $T_{\rm ph}$ and $v_{\rm ph}$ fall below or above those of Dessart & Hillier (2006) depending on the epoch, we find systematically higher values for the power law density index n. To investigate this, we examine the influence of the steepness of the density profile on the emergent spectra in Fig. 18.2 using the epoch of 9 November 1999 as an example. From this, it becomes clear that in the discussed regime of values (density indexes between 10 and 11) the changes in the emergent spectra are small. We see that only strong lines such as Hα, which form over a wide range of velocities, are affected at all and even those only slightly.

18.2.2. SN 2005cs

We analyze five closely spaced spectral observations of SN 2005cs, between roughly two and three weeks after explosion. For the first four epochs, there are spectral models from Dessart et al. (2008) at comparable epochs, allowing a comparison of the inferred parameters. The last epoch on 16 July 2005 is used only for our measurement of the distance to the supernova in Sect. 18.3. As for SN 1999em, we show the maximum likelihood emulated spectra combined with tables of the inferred and literature parameters in Fig. 18.3. Again, we find good agreement in the inferred parameters with only few exceptions.

For the photospheric velocity, the epoch of 14 July 2005 stands out, which shows a deviation of 569 km s^{-1}. In particular, the increase in velocity compared to the previous epoch is puzzling. It can be understood in the following way: as discussed in Sect. 3.3.3 of Dessart & Hillier (2006), spectral fits yield differences on the 10 % level in the photospheric velocity depending on which set of lines the fit is optimized on. For the two epochs, our automated fits likely attribute varying weights to certain features, thus giving rise to the inconsistent velocity estimates; for example, on 11 July the Ca infrared triplet absorption is not fit well, forming at overly low velocities, whereas on 14 July the absorption minimum is matched much better.

Regarding photospheric temperature, the earliest epoch has the largest deviation, which is 767 K. We do not know for certain what causes this significant difference. Nevertheless, it is striking that the epoch with the largest deviation in temperature also has the smallest wavelength coverage. We show a full comparison of measured temperatures and velocities in Fig. 18.4.

Similar to the case of SN 1999em, our maximum likelihood fits favor slightly steeper density profiles than those proposed by Dessart et al. (2008); instead of $n = 10$, we find values between 10.9 and 12.4. As outlined in the previous section, these variations in the density profile only induce very moderate changes in the emergent spectrum and should not be overinterpreted.[4] This applies in particular to the increase of the best-fit value for n in the last two epochs; this is

[4] We note that Baron et al. (2007) have invoked similarly steep density distributions at even later epochs (see their radiative transfer model for 31 July 2005).

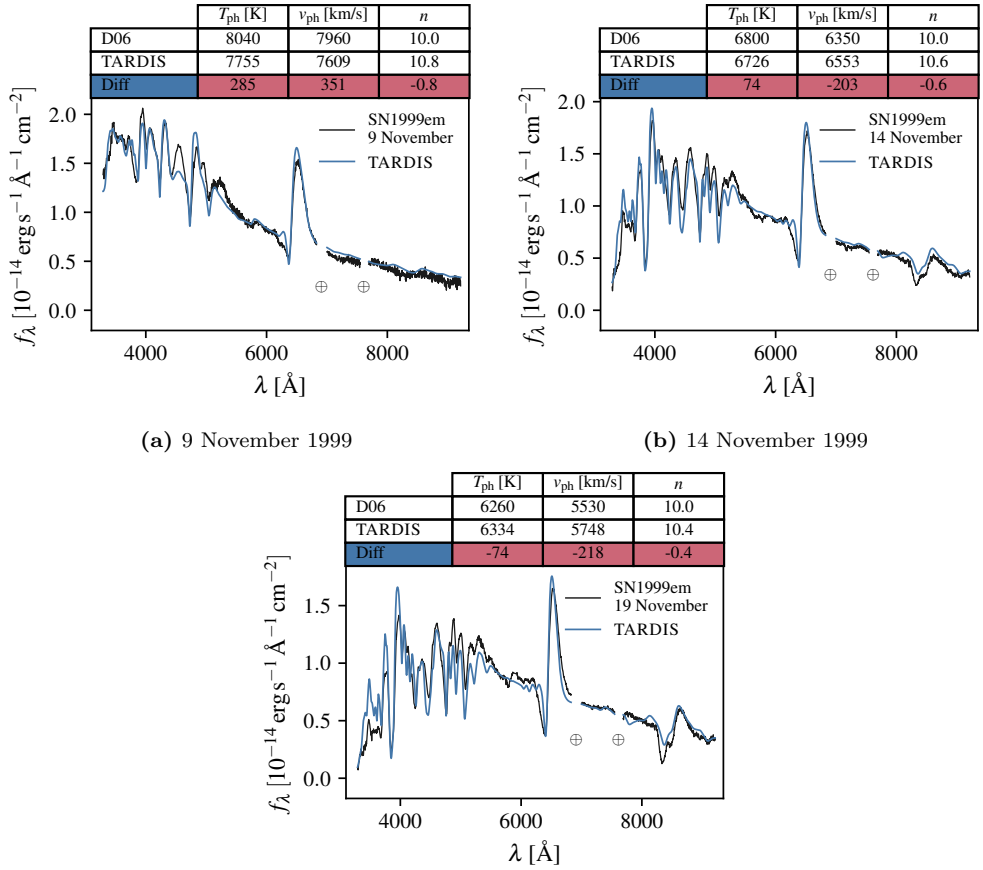

(a) 9 November 1999

(b) 14 November 1999

(c) 19 November 1999

Figure 18.1.: Spectroscopic analysis of SN 1999em. The three subfigures show comparisons between observed (black) and best-fit emulated spectra (blue); the best-fit has been determined through a maximum likelihood approach as outlined in Sect. 18.2. Each spectral comparison is combined with a table of the inferred parameters, the literature values from Dessart & Hillier (2006; D06), and the difference between the two. Since the observations have not been corrected for telluric absorption, we exclude the regions of strongest absorption from the fit (marked ⊕).

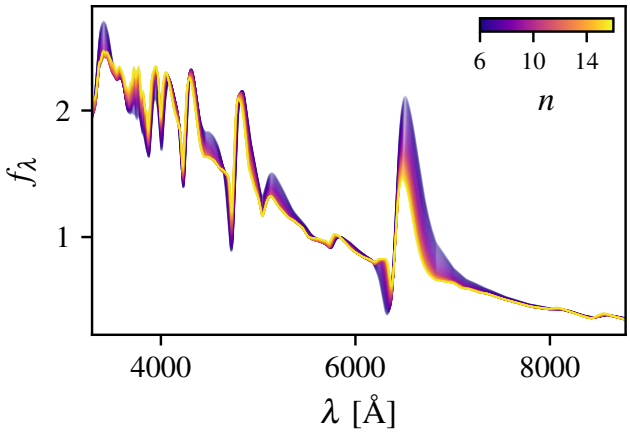

Figure 18.2.: Variation of the spectral shape with the steepness of the density profile n. We plot specific flux f_λ in arbitrary units for a sequence of emulated spectra where only the power law density index n is modified between spectra; the remaining parameters have been chosen to provide a good fit to SN 1999em for 9 November 1999 (see Fig. 18.1). We color code the plotted spectra by the power-law density index n.

likely not due to a physical effect but an artifact of our current method of using different density profiles for each epoch and our maximum likelihood approach. This will be alleviated by fitting the entire spectral time series at the same time.

18.3. Distance measurements

In the past, the need to optimize the fit quality by hand and eye combined with the high cost of radiative transfer calculations have made distance measurements from SN II spectral models (e.g., Baron et al., 2004; Dessart & Hillier, 2006) a very labor-intensive process. Automated fits based on spectral emulation revise this picture completely.

We use a variant of the tailored EPM (Dessart & Hillier, 2006; Dessart et al., 2008) to constrain the distance D to the supernovae. As a first step, we measure the photospheric angular diameter $\Theta = R_{\rm ph}/D = v_{\rm ph}t_{\rm exp}/D$ for each epoch. We compare the apparent magnitudes m_S of our best fit model,

$$m_S = M_S(\theta^*) - 5\log(\Theta) + A_S, \tag{18.3}$$

to the observed photometry ${m_S}^{\rm obs}$ for different values of Θ. Here, A_S is the broadband dust extinction for the bandpass S=$\{B,V,I\}$ and $M_S(\theta^*)$ is the predicted absolute magnitude for the best-fit parameters θ^*. We adopt the photospheric angular diameter Θ^* that minimizes the squared difference between observed and model magnitudes:

$$\Theta^* = \arg\min_{\Theta} \sum_S \left(m_S - {m_S}^{\rm obs}\right)^2. \tag{18.4}$$

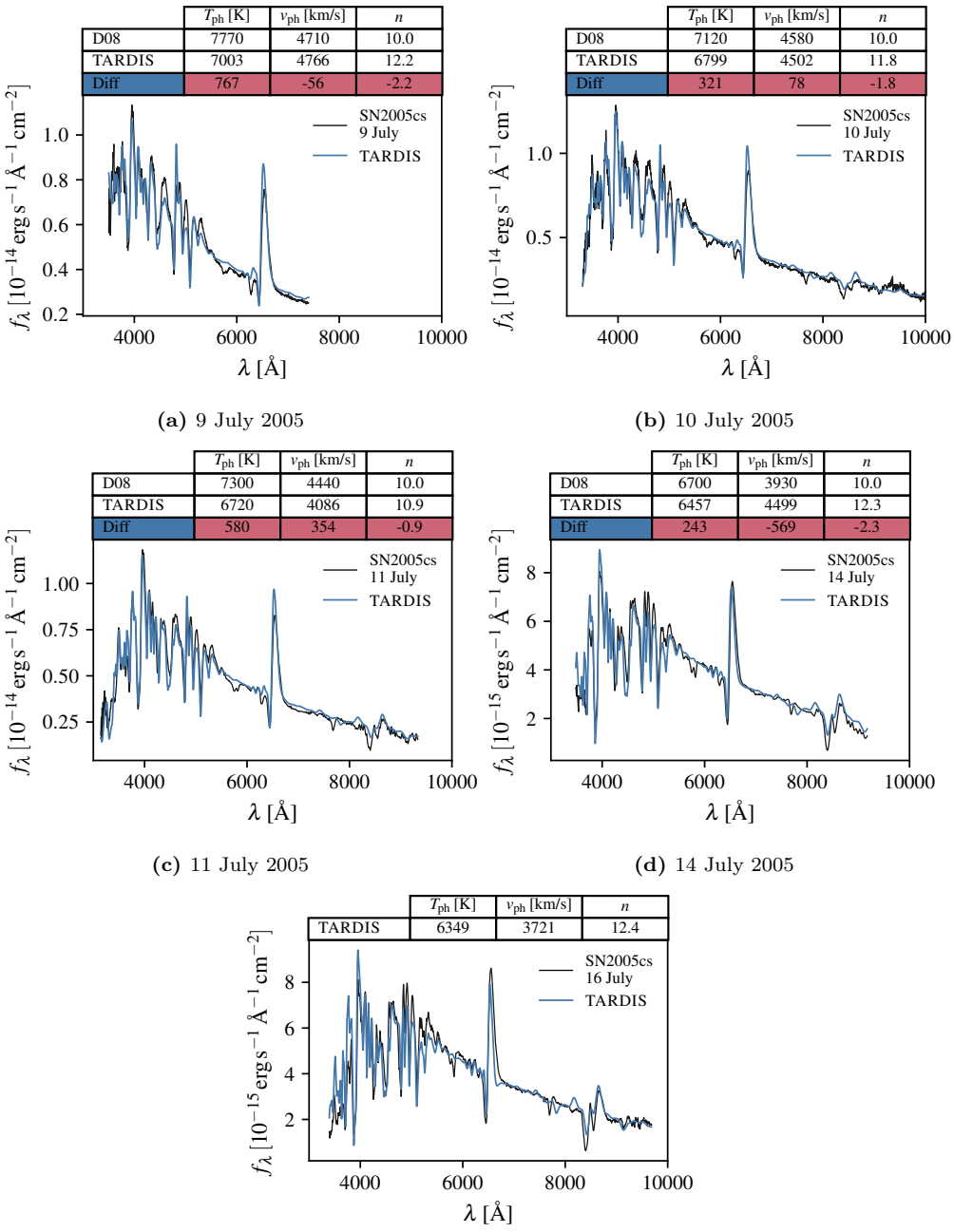

(a) 9 July 2005

(b) 10 July 2005

(c) 11 July 2005

(d) 14 July 2005

(e) 16 July 2005

Figure 18.3.: Spectroscopic analysis of SN 2005cs. See Fig. 18.1 for a description of the layout. Here, values for the parameter comparison are taken from Dessart et al. (2008; D08). In (e), we only show the inferred parameters since this epoch has not been modeled in Dessart et al. (2008).

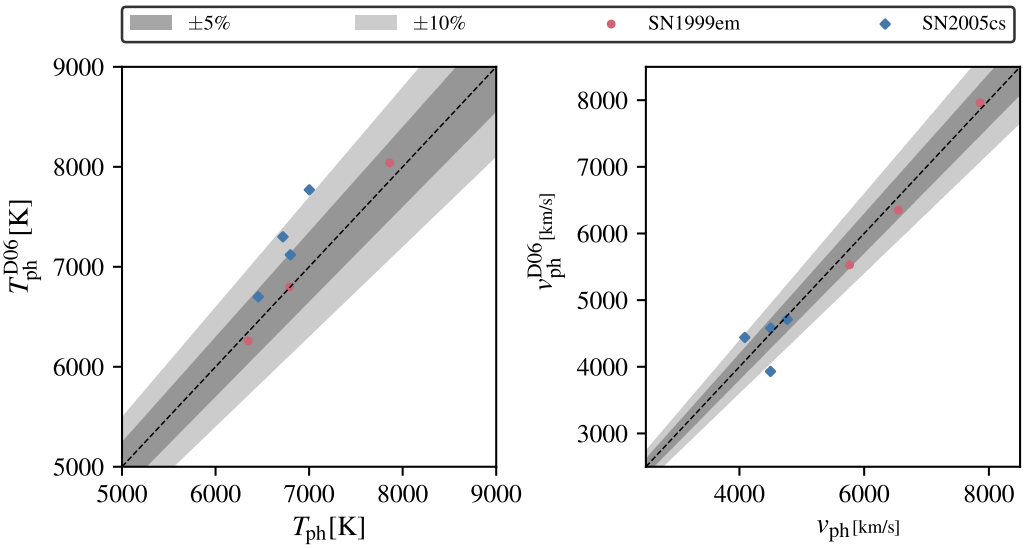

Figure 18.4.: Comparison of the photospheric temperatures $T_{\rm ph}$ and velocities $v_{\rm ph}$ inferred from our automated spectral fits to those of Dessart & Hillier (2006) and Dessart et al. (2008): $T_{\rm ph}^{\rm D06}$ and $v_{\rm ph}^{\rm D06}$. The dashed black line indicates perfect agreement between the measurements, whereas the gray shaded regions denote deviations of 5 % and 10 % respectively.

Our approach to tailored EPM is technically identical to that of Dessart & Hillier (2006) and Dessart et al. (2008) but avoids the detour of parametrizing the model magnitudes by a blackbody color temperature and a dilution factor.

Finally, we determine the time of explosion and the distance through a Bayesian linear fit to the time evolution of the ratio of the photospheric angular diameter Θ and the photospheric velocity $v_{\rm ph}$. To be more specific, we obtain the time of explosion from the intercept with the time axis and the distance from the inverse of the slope. In our analysis, we assume that the uncertainties are Gaussian and that they have standard deviations of 10 % of the measured values as in Dessart & Hillier (2006) and Dessart et al. (2008).[5] We use a half-Cauchy prior for the slope of the regression curves, corresponding to a uniform distribution for the angle between the straight lines and the time axis. We adopt informative priors for the time of explosion, which we discuss below in the context of the individual supernovae.

Our sources of photometry are Leonard et al. (2002) for SN 1999em (as listed in Table 1 of Dessart & Hillier, 2006) and Pastorello et al. (2009b) for SN 2005cs. If there is no coincident photometric observation for a given spectral epoch, we linearly interpolate the magnitudes from the nearest epochs. We list all magnitudes used in our tailored EPM analysis in Table 18.2.

[5] In the case of a full Bayesian analysis, the assumption of Gaussian uncertainties can be dropped and the posterior distribution of $\Theta/v_{\rm ph}$ can be used instead.

Table 18.2.: Interpolated *BVI* photometry for the epochs of spectral observations.

SN 1999em				
JD (+2 451 474.04)	Date	*B*	*V*	*I*
17.9	9 Nov. 1999	14.02	13.84	13.48
22.9	14 Nov. 1999	14.25	13.81	13.44
27.9	19 Nov. 1999	14.47	13.86	13.40
SN 2005cs				
JD (+2 453 549)	Date	*B*	*V*	*I*
12.25	9 July 2005	14.75	14.59	14.30
13.5	10 July 2005	14.83	14.60	14.26
14.5	11 July 2005	14.92	14.58	14.25
17.0	14 July 2005	15.09	14.67	14.25
19.4	16 July 2005	15.26	14.70	14.28

Notes. The reference JDs are the same as in Table 18.1.

18.3.1. SN 1999em

For a first demonstration of the emulator, we adopt an informative Gaussian prior for the time of explosion based on the tailored EPM analysis of Dessart & Hillier (2006), which finds $t_0 = \mathrm{JD}\ 2\,451\,474.04 \pm 1.0$. While the time of explosion for SN 1999em is not well constrained through the photometry, many objects have limits that are as tight or tighter than the adopted prior for t_0; this applies, for example, to SN 2005cs as we discuss in the following section.

With the prior for t_0 defined, we apply the tailored EPM as outlined above. We summarize the inputs as well as the results of our analysis in Fig. 18.5. In the figure, we combine a table of the ratios of photospheric angular diameter and velocity Θ/v_{ph}, a visualization of the Bayesian linear regression, and a corner plot of the inferred distance and time of explosion. We find a distance of $11.4^{+1.0}_{-0.9}\,\mathrm{Mpc}$, which is in excellent agreement with the Cepheid distance to the host galaxy of $11.7 \pm 1\,\mathrm{Mpc}$ (Leonard et al., 2003). It is important to keep in mind that the quoted uncertainties are solely statistical and depend both on the adopted prior for t_0 and the assumed uncertainties for Θ/v_{ph}. Finally, we point out that the regression is only weakly informative on the time of explosion, that is to say, the posterior distribution for t_0 is only slightly modified compared to the prior.

18.3.2. SN 2005cs

As opposed to SN 1999em, the time of explosion for SN 2005cs is constrained tightly by photometric observations. Based on the nondetection at JD = 2 453 548.43 and the detection at

Date	Time [d]	$\Theta/v_{\rm ph}$ [d/Mpc]
9 Nov 1999	17.9	1.46
14 Nov 1999	22.9	2.02
19 Nov 1999	27.9	2.56

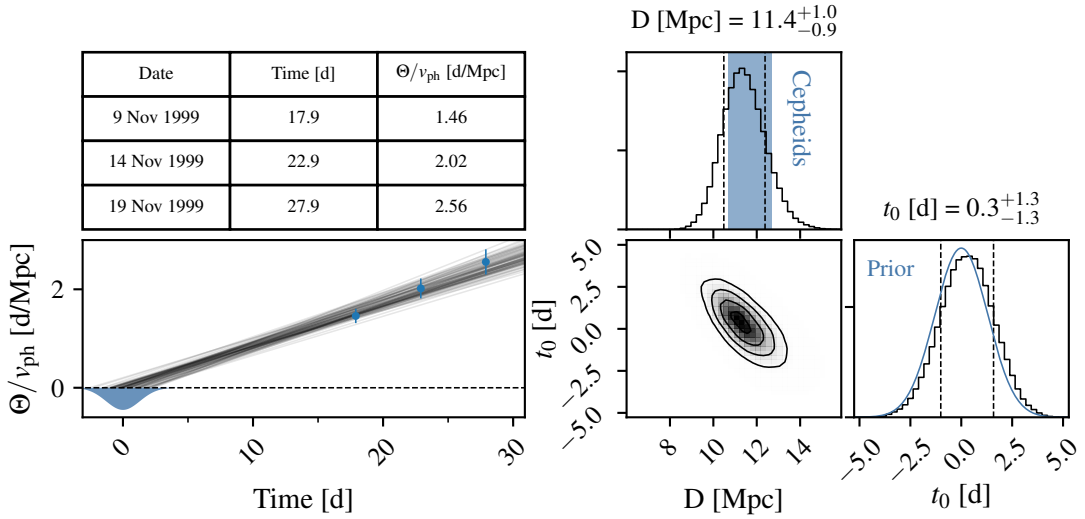

Figure 18.5.: Tailored EPM for SN 1999em. *Lower left panel*: evolution of the ratio of the photospheric angular diameter Θ and the photospheric velocity $v_{\rm ph}$ with time (blue circles). Here, we measure the time with respect to JD 2 451 474.04. We tabulate the plotted values in the *upper left panel*. Finally, we perform a Bayesian linear fit to this data. Our prior for the time of explosion is indicated by the blue shaded region. From the posterior distribution, we show 100 randomly sampled regression curves for illustrative purposes. The right half of the figure features a corner plot of the inferred parameters. Our distance measurement is in excellent agreement with the Cepheid distance of Leonard et al. (2003), which is indicated by the blue shaded region.

Date	Time [d]	$\Theta/v_{\rm ph}$ [d/Mpc]
9 July 2005	12.25	1.69
10 July 2005	13.50	1.90
11 July 2005	14.50	2.12
14 July 2005	17.00	2.01
16 July 2005	19.40	2.44

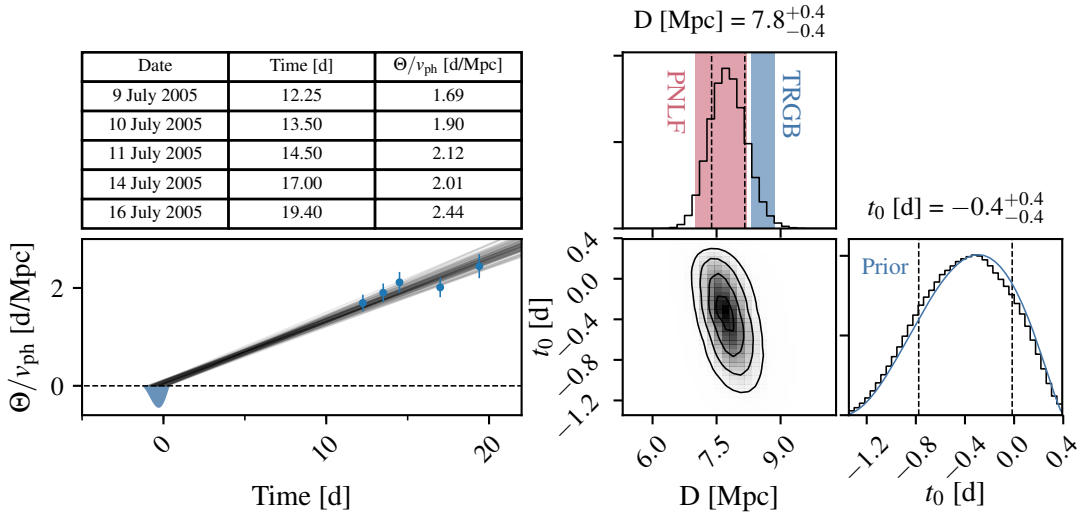

Figure 18.6.: Tailored EPM for SN 2005cs. For a description of the figure layout see Fig. 18.5. The time zero point is at JD 2 453 549.0. Within the statistical uncertainties, the inferred distance agrees with the measurement of Ciardullo et al. (2002) using the planetary nebula luminosity function (PNLF), as well as that of McQuinn et al. (2016) based on the tip of the red giant branch (TRGB).

JD = 2 453 549.41, Pastorello et al. (2009b) identify JD = 2 453 549.0 ± 0.5 as the time of shock breakout. In our prior for t_0, we make small changes to this result to incorporate two basic arguments. First, the prior probability that the first detection is coincident with the explosion should be zero. Secondly, the probability that the explosion occurred before the last nondetection should be non-negligible due to the limited depth of the image. Based on these considerations, we construct the Beta prior shown in Fig. 18.6. Our prior peaks shortly after the last nondetection and has a width that is compatible with the quoted uncertainties of Pastorello et al. (2009b). We derive the distance to the supernova as illustrated in Fig. 18.6 and obtain a value of $7.8^{+0.4}_{-0.4}$ Mpc.

In contrast to SN 1999em, the distance to SN 2005cs is not constrained through Cepheids. The NASA/IPAC Extragalactic Database (NED)[6] lists 50 individual distance measurements spanning a range of values between 2.45 Mpc and 12.2 Mpc with a median distance of 7.935 Mpc. Based on spectral modeling of SN 2005cs, Dessart et al. (2008) find a distance of 8.9 ± 0.5 Mpc using tailored EPM in the BVI bandpasses and Baron et al. (2007) $7.9^{+0.7}_{-0.6}$ Mpc with the SEAM method. Independent state-of-the-art measurements come from Ciardullo et al. (2002), who derive a distance of 7.6 ± 0.6 Mpc using the planetary nebula luminosity function (PNLF), and McQuinn et al. (2016), who infer a value of 8.58 ± 0.10 Mpc[7] from the tip-of-the-red-giant-branch (TRGB) method.

Overall, the agreement between our measurement and the results above is satisfactory given the uncertainties of the individual methods. However, the 15 % deviation to the tailored EPM distance of Dessart et al. (2008) warrants investigation. We find that roughly half of the discrepancy arises from differences in the time of explosion. From the evolution of the ratio of photospheric angular diameter and velocity, Dessart et al. (2008) obtain an explosion epoch that is earlier than ours by about a day. These latter authors explain the difference between their estimate and those based on nondetections (specifically, Pastorello et al., 2006; in their paper) with a short time delay between the beginning of the expansion and the optical brightening. After adjusting the time of explosion, the remaining deviation is around 7 % and thus within the expected range.

[6] The NASA/IPAC Extragalactic Database (NED) is operated by the Jet Propulsion Laboratory, California Institute of Technology, under contract with the National Aeronautics and Space Administration.

[7] The reported uncertainty only accounts for statistical errors. The authors speculate that the systematic uncertainty could be of order 0.05 mag in distance modulus.

19. Conclusions and outlook

In this paper, we demonstrate the use of spectral emulation to predict the SN II spectra and magnitudes generated by TARDIS (Kerzendorf & Sim, 2014; Vogl et al., 2019). The key ingredient of our approach is the creation of a low-dimensional space for the interpolation of synthetic spectra through the combination of appropriate data preprocessing and dimensionality reduction by PCA. In this space, we train Gaussian processes to predict preprocessed, dimensionality-reduced spectra for new sets of input parameters. In the final step, we reverse the preprocessing procedure to obtain a spectrum that can be compared to observations. This method emulates the output of our radiative transfer code to high precision; we demonstrate this by comparing emulated and simulated spectra for a large number of test models. On average, the emulator prediction deviates from the simulation by around 0.64 % (as measured by the MFE)—this is much smaller than both observational and model uncertainties. Not only are the interpolation uncertainties small but we can also estimate them sensibly through our use of Gaussian processes; this will allow us in the future to propagate these errors into the uncertainties of the inferred parameters.

We complement the spectral emulator with an emulator for absolute magnitudes; we have discarded the luminosity information in the spectral emulator to standardize the spectra and to obtain better predictive performance. The training data are Johnson-Cousins B, V, I magnitudes that have been synthesized from the unprocessed training spectra. We remove variations in the luminosity that result from differences in the physical sizes of the supernova models by transforming the magnitudes to the position of the photosphere; we then interpolate the transformed magnitudes using Gaussian processes. This allows us to predict absolute magnitudes with an average precision of better than 0.01 mag, which is significantly smaller than typical observational uncertainties.

The emulator is not only accurate but is also orders of magnitude faster ($\approx 10\,\mathrm{ms}$) than our simulator TARDIS ($\approx 100\,000\,\mathrm{s}$) making it possible to fit spectra automatically. We demonstrate this by performing maximum likelihood parameter estimation for spectral time series of SN 1999em and SN 2005cs. The inferred parameters of the supernovae show good agreement with those of Dessart & Hillier (2006) and Dessart et al. (2008), who studied these objects using the CMFGEN code. Similarly, the distances that we infer from our fits are consistent with the best available measurements from the literature.

As a next step, we will develop a more detailed likelihood to infer accurate uncertainties for complete parameter estimates. The emulator and an advanced likelihood will then allow the use of type IIP supernovae for accurate cosmological distance determinations.

Appendix A: Min-max normalization

Min-max normalization scales each feature (here, the fluxes in a bin) individually such that it spans the range [Min, Max] for the training data. The min-max normalized flux $f_{\lambda,ij}^{\mathrm{norm}}$ for spectrum i in bin j is given by

$$f_{\lambda,ij}^{\mathrm{norm}} = \frac{f_{\lambda,ij} - \min\limits_{i} f_{\lambda,ij}}{\max\limits_{i} f_{\lambda,ij} - \min\limits_{i} f_{\lambda,ij}} (\mathrm{Max} - \mathrm{Min}) + \mathrm{Min}. \tag{19.1}$$

This linear transformation can be easily reversed in the prediction step of the emulator.

Acknowledgements

CV thanks Andreas Floers, Marc Williamson, and Markus Kromer for stimulating discussions during various stages of this project. The authors gratefully acknowledge Stefan Taubenberger for sharing his enormous expertise in the field of supernovae and for being a key member of the supernova cosmology project that motivated this work. The authors thank the anonymous reviewer for valuable comments. This work has been supported by the Transregional Collaborative Research Center TRR33 "The Dark Universe" of the Deutsche Forschungsgemeinschaft and by the Cluster of Excellence "Origin and Structure of the Universe" at Munich Technical University. SAS acknowledges support from STFC through grant, ST/P000312/1. This research made use of TARDIS, a community-developed software package for spectral synthesis in supernovae (Kerzendorf & Sim, 2014; Kerzendorf et al., 2019). The development of TARDIS received support from the Google Summer of Code initiative and from ESA's Summer of Code in Space program. TARDIS makes extensive use of Astropy and PyNE. Data analysis and visualization was performed using MATPLOTLIB (Hunter, 2007), NUMPY (Oliphant, 2006) and SCIPY (Jones et al., 2001).

Part IV.

H_0 from the tailored-expanding-photosphere method

20. Past and ongoing observational programs

We have developed the necessary tools to measure H_0 through the tailored EPM in the preceding parts. The extended version of TARDIS from Part II allows us to produce accurate radiative transfer models for SNe II and the emulator shown in Part III makes it feasible to fit them to observed spectra. This leaves a final prerequisite for an accurate determination of H_0: high-quality spectral time series for a large sample of SNe II in the Hubble flow. Such a dataset does not exist in the literature. The primary focus of SN II observations is the physics of the explosion. Therefore, good spectral datasets with high cadence are usually only collected for nearby objects. To overcome this limitation, we have started our own observational programs.

We have two main sources of data for our future determination of H_0: the Nearby Supernova Factory (SNfactory; Aldering et al., 2002) and the ESO VLT large programme for an accurate determination of H_0 with core-collapse supernovae (adH0cc; Leibundgut et al., 2019). The SNfactory provides a completed low redshift sample of 21 SNe II with redshifts below 0.0424, which we describe in Sect. 20.1. adH0cc is an ongoing project with the aim of extending our SN II sample to higher redshifts of up to ~ 0.1. In Sect. 20.2, we outline our observing strategy for this program and give a summary of the current status.

20.1. Nearby Supernova Factory

The SNfactory (Aldering et al., 2002) is a cosmology experiment with the primary goal of collecting high-quality spectrophotometric time series for a large sample of nearby SNe Ia. The homogeneous nature of the dataset and a better handle on systematic errors are intended to make it a prime source for the calibration and study of SNe Ia, as well as the measurement of the expansion history of the Universe.

Absolute spectrophotometry is a key ingredient for achieving these science goals. The observations are made possible through the custom-built integral field spectrograph SNIFS (Lantz et al., 2004), which is mounted on the UH 88-inch telescope on Mauna Kea, Hawaii. SNIFS is designed for observations of point sources on diffuse backgrounds, as encountered in SN spectroscopy. It provides moderate-resolution spectra (~ 3 Å) with a wavelength coverage from 3300 Å to 9700 Å. The spatial resolution is 0.43 arcsec, which is achieved through a subdivision of the 6.4 by 6.4 arcsec field of view into 225 (15x15) spaxels by a microlens array. Each spaxel produces a spectrum

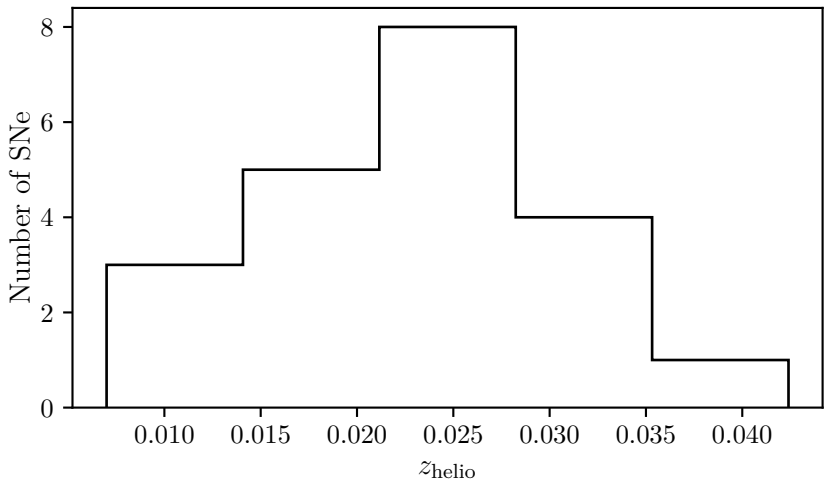

Figure 20.1.: Redshift distribution of the SNfactory SNe. The sample covers a redshift range from 0.007 to 0.0424 with a median redshift of 0.0237.

in a red and blue channel by splitting the light with a dichroic at 5100 Å, dispersing it through a grating, and recording it on a CCD. The 2D spectra are then wavelength calibrated using arc lamp spectra. These are collected after every science exposure at the same telescope orientation. Before the spectra are extracted from the resulting (x,y,λ) data cubes, the host galaxy emission is subtracted using a spectrophotometric template of the SN location as described by Bongard et al. (2011). Observations of multiple spectroscopic standard stars jointly provide the basis for the flux calibration and atmospheric extinction correction of the extracted spectra (Buton et al., 2013). This is complemented by multifilter imaging of stars close to the field of view of the spectrograph. The latter provides an estimate of the atmospheric attenuation for each exposure, which can be used to obtain an absolute flux calibration even in non-photometric conditions. The complete data reduction is performed by the SNfactory pipeline in an automated fashion (Aldering et al., 2006; Scalzo et al., 2010).

In addition to their core SN Ia cosmology project, the SNfactory collaboration has observed 21 SNe II in the Hubble flow. The objects were discovered mostly through dedicated transient surveys including the Palomar Transient Factory (PTF; Law et al., 2009), the intermediate Palomar Transient Factory (iPTF; Kulkarni, 2013), La Silla-QUEST (LSQ; Baltay et al., 2013), and the Catalina Real-Time Transient Survey (CRTS; Drake et al., 2009). The remaining targets were supplied by amateur astronomers: Tom Boles, Maurice Gavin, Ron Arbour, Koichi Itagaki, and the Italian Supernovae Search Project (ISSP). Classifications were performed on the UH-88 or taken from the literature. The SN II dataset was optimized for a determination of H_0 by means of the tailored EPM. This involved taking multiple spectra in the first month after the

Table 20.1.: Overview of the SNfactory SN II sample.

Name	RA	DEC	Host galaxy	Discovery date
PTF10tpa	23:04:40.95	−09:38:27.7	WISEA J230440.55-093830.3	2010-08-23
SN 2010hb	03:07:01.66	+46:37:20.2	UGC 02537	2010-08-24
PTF10wmf	21:56:15.69	+02:10:13.8	CGCG 377-004	2010-09-24
PTF10xlr	23:09:22.76	+01:00:03.6	SDSS J230922.92+010002.0	2010-10-03
SN 2010jc	02:40:13.97	−08:46:25.7	NGC 1033	2010-10-29
SN 2011az	12:53:53.43	+36:05:19.3	IC 3862	2011-03-18
SN 2011fd	06:46:39.85	+60:21:02.8	NGC 2273B	2011-08-20
SN 2011fv	01:18:07.80	+17:33:29.8	NGC 459	2011-08-26
SN 2011fy	18:39:53.93	+40:01:43.7	IC 4772	2011-09-17
LSQ12cer	13:17:08.45	−20:24:41.8	WISEA J131708.58-202434.9	2012-04-24
SN 2012ch	15:06:02.54	+41:25:32.7	WISEA J150602.64+412535.3	2012-05-17
SN 2012eh	01:27:31.45	+14:49:05.8	IC 1706	2012-08-20
SN 2012fs	00:37:39.38	+10:21:29.0	IC 35	2012-10-07
LSQ12fvq	01:16:36.17	−31:27:07.4	WISEA J011636.34-312714.2	2012-11-01
PTF12ljg	08:12:48.97	+46:17:00.1	SDSS J081248.90+461701.9	2012-11-22
SN 2012hi	08:39:42.02	+60:58:16.0	UGC 4512	2012-12-02
SN 2012ho	22:40:17.02	−02:25:34.1	MCG-01-57-021	2012-12-06
LSQ12hnj	05:12:24.82	−25:46:57.4	WISEA J051224.61-254658.0	2012-12-12
SN 2013bm	10:48:26.57	+38:24:07.9	UGC 05910	2013-04-16
iPTF13bjx	14:14:51.95	+36:47:28.9	KUG 1412+370	2013-05-29
SN 2013ds	16:11:29.58	+57:22:51.7	MCG +10-23-036	2013-07-01

explosion at a cadence of around five days. Taking technical, weather and observing condition constraints into account, this strategy yielded around five epochs for each object in this time window. An additional spectrum at an estimated 50 d after explosion allows us to make an internal consistency check between the EPM and the SCM of Nugent et al. (2006). Three nearby objects were followed until the end of the plateau phase. Figure 20.2 shows an example spectral time series. Table 20.1 provides a short overview of the SN II SNfactory sample. We do not list redshifts for the individual objects to facilitate the future blind analysis of the dataset, but we show a histogram of the redshift distribution in Fig. 20.1. The relatively small size of the UH-88 inch telescope limits the sample to redshifts $\lesssim 0.04$. The lower limit has been set at a redshift of ~ 0.01 because uncertainties from peculiar motions exceed $\sim 10\,\%$ below this threshold.

20.2. ESO VLT large programme

We are in the process of extending our dataset by an additional 15 to 20 SNe II at higher redshifts ($0.04 \lesssim z \lesssim 0.1$). This will significantly reduce the uncertainties from peculiar velocities compared to the more local SNfactory sample ($z \sim 0.025$). By doubling the sample size, we will also reduce

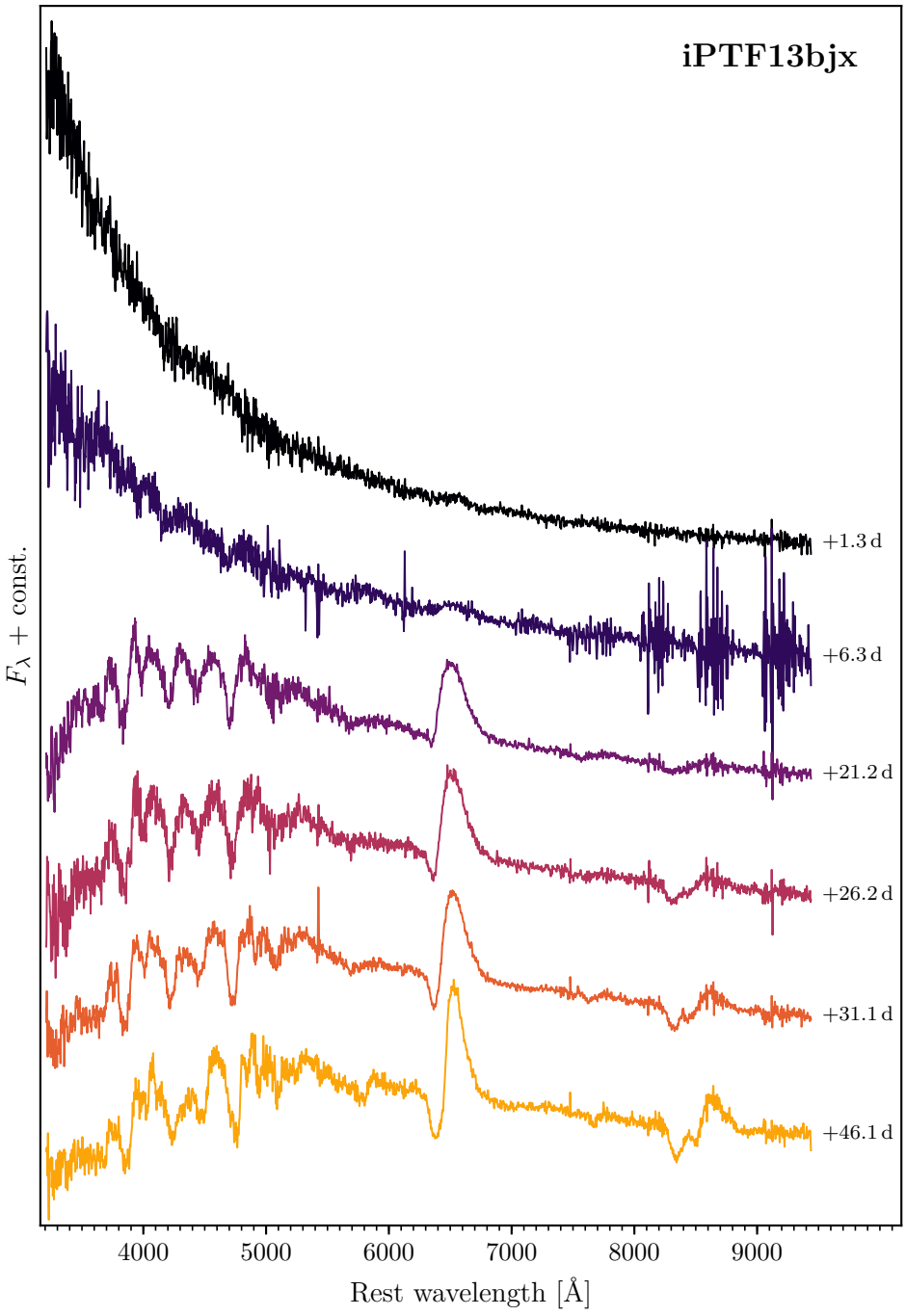

Figure 20.2.: Time series of SNIFS spectra of iPTF13bjx. Phases are reported relative to the time of explosion as estimated from an exponential light curve fit (see Sect. 21.2).

the statistical error in our H_0 measurement. Together, these improvements will provide the basis for a highly-competitive H_0 determination.

The extension of our sample is made possible through observations at the ESO 8.2m Very Large Telescope (VLT-UT1) on Cerro Paranal, Chile. The data for the targeted SNe are collected over the course of three semesters starting from October 2019 through the adH0cc large programme. We use the focal-reducer spectrograph and camera FORS2 to obtain around six epochs of low-resolution spectroscopy and $BVRI$-filter photometry for each object during the first month after explosion. We take spectra with grisms 300V and 300I (+OG590), which provides a wavelength coverage from 3400 Å to 10 200 Å at a resolution of $\sim$ 9 Å. This setup minimizes second-order contamination. Potential candidates for our program are provided by the ATLAS survey (Tonry et al., 2018), the Zwicky Transient Facility (ZTF; Kulkarni, 2018), and the Pan-STARRS Survey for Transients (Chambers et al., 2016). We screen the data streams from these sources for objects in the correct redshift range and with well-constrained explosion epochs through a custom-built webtool. Potential SNe II are identified based on contextual clues, including the host galaxy morphology, multicolor light curves, and absolute magnitudes. We have dedicated time to classify these candidates with FORS2 as part of our program: public spectroscopic surveys such as ePESSTO+ do not discover enough young SNe II in the desired redshift range due to the faintness of these objects.

To date, we have followed up six SNe II with redshifts between 0.033 and 0.166 (see Table 20.2). Five of the six targets have been classified by ourselves (e.g., Leibundgut et al., 2019; Floers et al., 2020; Hillebrandt et al., 2020); spectral typing for the final object comes from ZTF. Figures 20.3 and 20.4 illustrate the data that we have acquired for these SNe: Fig. 20.3 shows multicolor image cutouts from our FORS2 photometry and Fig. 20.4 an example spectral time series.[1] Over the next two semesters (P105 and P106), we will collect data for $\sim$ 10 more SNe to complete our sample.

[1]The plotted spectra have been quick-reduced with a modified version of the PESSTO pipeline developed by us. The pipeline is available at https://github.com/chvogl/pessto/tree/fors-pipeline.

Table 20.2.: Overview of the current adH0cc SN sample.

	Host galaxy	Discovery UT	$z_{\rm helio}$	Classifying group
SN 2019tjt	AGC 102756	Oct 26.13	0.04760	adH0cc
SN 2019uxh	WISEA J225105.53-114723.1	Nov 12.23	0.03257	adH0cc
SN 2019vew	WISEA J052749.22-052143.6	Nov 16.53	0.0419[a]	ZTF
SN 2020zs	CGCG 032-030	Jan 16.21	0.04589	adH0cc
SN 2020bcv	SDSS J095542.44+000635.1	Jan 24.47	0.166[a]	adH0cc
SN 2020cye	WISEA J123433.55+202106.3	Feb 19.37	0.06383	adH0cc

Notes. [a] Redshift determined from our FORS2 spectra based on host galaxy emission lines.

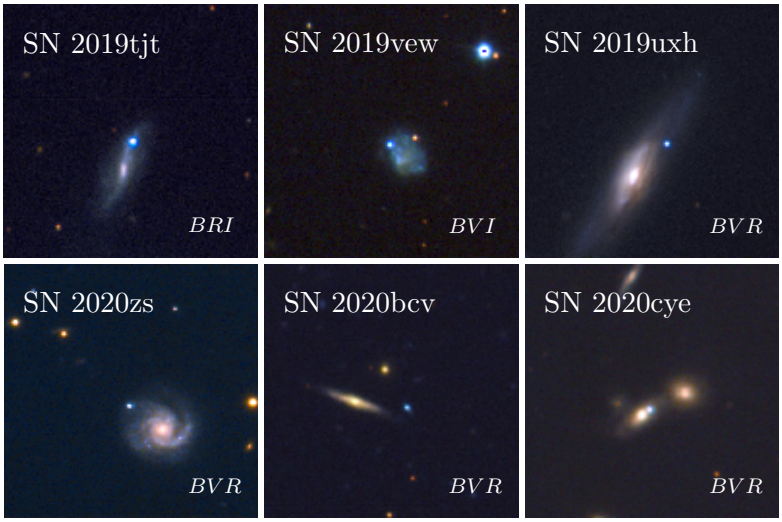

Figure 20.3.: VLT+FORS2 multicolor image cutouts of the adH0cc SNe. Individual cutouts courtesy of S. Taubenberger.

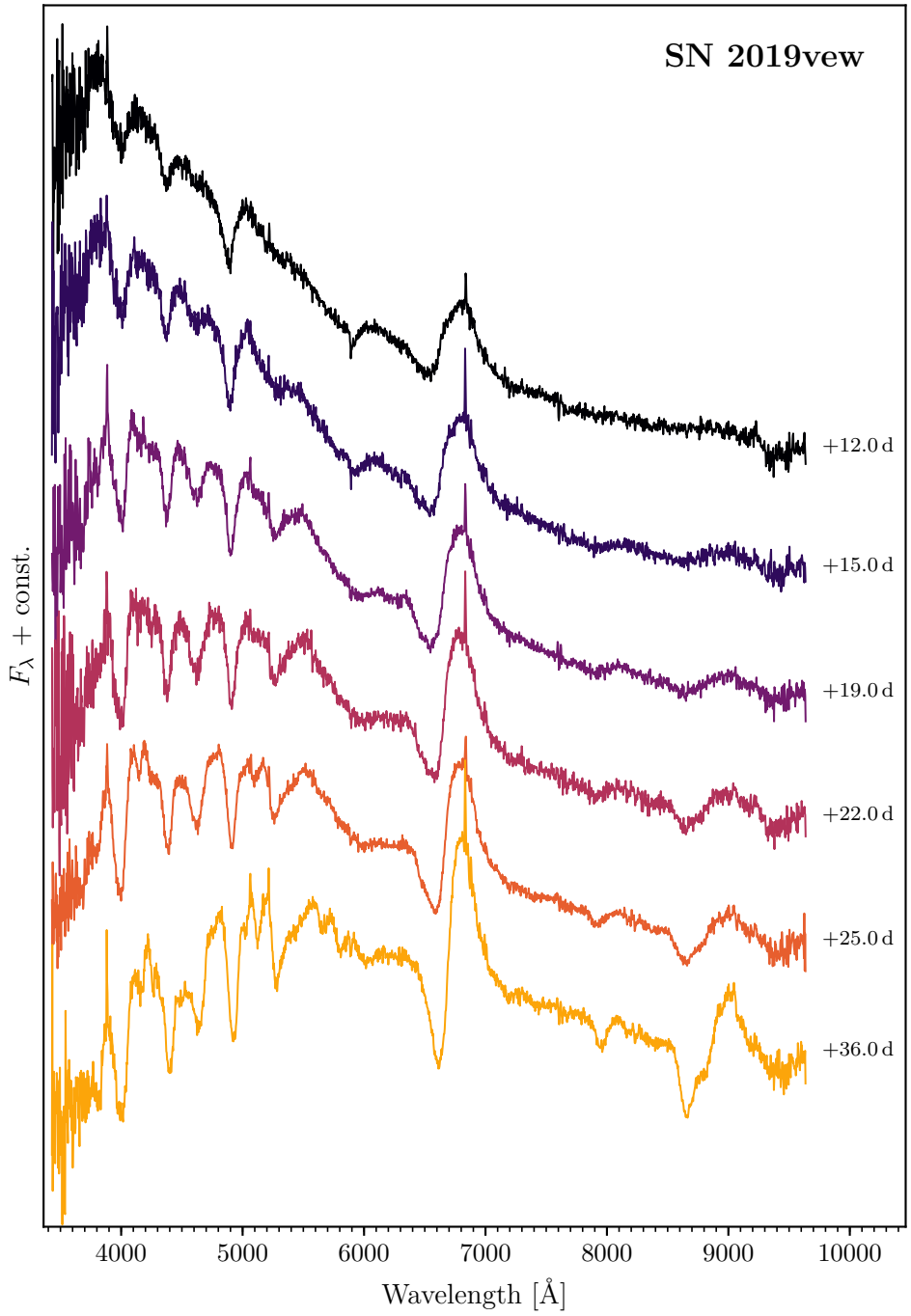

Figure 20.4.: Time series of VLT+FORS2 spectra of SN 2019vew. Phases are reported relative to the time of explosion estimated as the midpoint between the last non-detection and the first detection (MJD=58796.0). The spectra shown are quick reductions of the grism 300V data.

21. Proof-of-principle measurement

As discussed in Parts II, III and Chapter 20, we have all the basic ingredients for an accurate determination of H_0 through the tailored EPM: an accurate radiative transfer code, an innovative method to fit the models to the data, and a soon to be completed dedicated dataset of SN II spectral time series. As the conclusion to this thesis, we demonstrate the utility of the developed methodology in a proof-of-principle H_0 measurement. This demonstration constitutes the first application of the tailored EPM to SNe in the Hubble flow.

Recent years have shown an increased awareness of the importance of blind analysis in cosmology (e.g., Suyu et al., 2013; Troxel et al., 2018; Verde et al., 2019). Conducting the measurement in ignorance of its final result minimizes the danger that modeling and data analysis choices are influenced, even subconsciously, by the expected outcome. In light of the ongoing controversy, these considerations are particularly relevant for determinations of H_0.

We use data from the literature and one exemplary object from the SNfactory sample for our proof-of-principle demonstration. This way, we can perform the definite analysis of the SNfactory data in a blind fashion—as expected in state-of-the-art cosmography. We restrict our literature sample to SNe with well-constrained explosion epochs. A good estimate of the time of explosion makes it possible to determine accurate distances even to objects with very few spectra. This is crucial because only a vanishingly small number of SNe II in the Hubble flow have good spectroscopic time series. We select five objects that cover a redshift range from 0.01 to 0.04. Table 21.1 summarizes the key properties of our sample including the SNfactory supernova iPTF13bjx. The selected objects span a significant portion of the parameter space of normal SNe II. The peak luminosities range from the extremely low end of the distribution, in the case of SN 2010id ($M_V \approx -15.5$; Gal-Yam et al., 2011), to the absolute high end for SN 2012ck ($M_V \approx -18.5$; de Jaeger et al., 2019). SN 2013fs is a prominent flash-ionization event (Yaron et al., 2017). Finally, SN 2003bn, SN 2006it, and iPTF13bjx are standard SNe II similar to SN 1999em. The diversity of the sample makes it possible to tentatively test whether SNe II at the fringes of the parameter space are reliable distance indicators. This is a first step towards studying possible systematics in the H_0 measurement introduced through the sample selection process.

21.1. Observational data

We need spectra as well as BVI photometry for our tailored EPM analysis. The necessary data for the literature SNe has been retrieved from the WISeREP archive (Yaron & Gal-Yam, 2012)

Table 21.1.: Supernova sample for H_0 measurement.

Name	Host galaxy	Nondetection UT	Discovery UT	z_{helio}	z_{CMB}	E$(B-V)$ (MW)[a]
SN 2003bn	2MASX J10023529-2110531	Feb 21.00	Feb 22.33	0.01277	0.01392	0.0562
SN 2006it	NGC 6956	Sep 26.19	Oct 1.17	0.01551	0.01452	0.0850
SN 2010id	NGC 7483	Sep 11.34	Sep 15.24	0.01648	0.01524	0.0521
SN 2012ck	LOSS J191927.83+441449.2	May 15.50	May 19.50	0.04176[b]	0.04119	0.0826
SN 2013fs	NGC 7610	Oct 5.34	Oct 6.25	0.01185	0.01062	0.0346
iPTF13bjx	KUG 1412+370	May 30.22	May 31.19	0.02786	0.02846	0.0075

Notes. [a] Milky way reddening taken from Schlafly & Finkbeiner (2011).
[b] Redshift from de Jaeger et al. (2019).

or the Open Supernova Catalog (Guillochon et al., 2017). Out of the available spectra, we have selected those that fall within the parameter space of our emulator. We have discarded spectra with obvious reduction artifacts, for example, in the relative flux calibration. This leaves between one and five epochs for each SN. A list of the spectra used together with the original data sources is given in Table 21.2. For each spectral epoch, we include the interpolated values of the BVI photometry. These have been obtained through GP regression of the listed data using a squared exponential kernel (e.g., Rasmussen & Williams, 2006).[1] The tabulated spectrophotometry for iPTF13bjx—our SNfactory object—is described in Sect. 20.1. We have synthesized magnitudes for this SN in the standard Bessell (1990) photometric system from the absolute flux calibrated spectra. For SN 2012ck, we calculate K corrections from the spectra and apply them to the interpolated magnitudes; in iPTF13bjx, we perform the transformation to the SN rest frame directly on the spectrophotometry. The redshifts of the other objects are small enough that a K correction can be safely ignored.

We clean the spectral data prior to the modeling. This may include sigma clipping, trimming, and rebinning. Sigma clipping, for example, can be necessary if there are night sky subtraction residuals. For the epoch of 4 November 2013 of SN 2013fs, we have combined EFOSC2 spectra from the red and blue grisms.[2]

21.2. Time of explosion

Independent constraints on the time of explosion are essential to infer accurate distances from the spectra and photometry given in the previous section. This is particularly true for the objects with only a few or even a single spectrum. Early-time photometry provides well-constrained explosion epochs for all SNe in our sample. We will try to extract the best possible estimates for

[1] We restrict the GP fits to a suitable time interval around the spectral epochs to avoid changes in the light curve evolution time scale.
[2] Grism #11 and grism #16.

Table 21.2.: Log of modeled spectra and corresponding interpolated *BVI* photometry.

	UT date	MJD	Phase[a] [d]	*B*	*V*	*I*	Ref Photometry	Ref Spectra
SN 2003bn	Mar 12.0	52710.00	17.79	17.49	17.13	16.93	2, 4	8
SN 2006it	Oct 10.0	54018.04	12.91	18.19	17.92	—	6	8
	Oct 13.0	54020.99	15.86	18.27	17.94	—		8
SN 2010id	Sep 29.3	55468.29	15.48	19.53	18.93	18.45	1	1
	Oct 1.4	55470.40	17.59	19.60	18.93	18.47		9
SN 2012ck	Jun 13.4	56091.40	28.52	19.57	19.01	18.38	9	9
	Jun 18.4	56096.40	33.52	19.74	19.11	18.42		9
SN 2013fs	Oct 26.8	56591.82	20.77	16.65	16.41	15.97	5	7
	Oct 29.0	56594.02	22.97	16.75	16.47	16.00		7
	Nov 2.7	56598.72	27.67	16.96	16.56	16.04		7
	Nov 4.2	56600.16	29.11	17.02	16.58	16.06		3
	Nov 7.2	56603.22	32.17	17.15	16.61	16.07		7
iPTF13bjx	Jun 20.4	56463.38	21.18	18.64	18.35	18.02	10	10
	Jun 25.4	56468.37	26.17	18.96	18.46	18.05		10
	Jun 30.3	56473.32	31.12	19.22	18.54	18.09		10

Notes. (1) Gal-Yam et al. (2011), (2) Anderson et al. (2014), (3) Smartt et al. (2015), (4) Galbany et al. (2016), (5) Valenti et al. (2016), (6) Hicken et al. (2017), (7) Yaron et al. (2017), (8) Gutiérrez et al. (2017b), (9) de Jaeger et al. (2019), (10) Sect. 20.1

[a] Phases are given with respect to the time of explosion as estimated by a light curve fit (see Sect. 21.2).

the time of explosion t_0 from the early light curves: any error in t_0 propagates linearly into an error in the distance.

The common strategy of identifying the midpoint between the first detection and the last non-detection as the time of explosion is not satisfactory in this context. A simple approach like this will lead to a biased estimate of t_0—and thus the distance. We need to take into account how deep the non-detection is compared to the first detection to minimize the bias; also, the characteristic time scales for the light-curve evolution at different distances from the peak have to be considered. A simple way to include these considerations is through an exponential fit following Ofek et al. (2014) and Rubin et al. (2016). The flux f at time t is then given by

$$f(t) = f_\mathrm{m} \left(1 - \exp\left(-\frac{t - t_0}{t_\mathrm{e}}\right)\right), \tag{21.1}$$

where f_m is the peak flux and t_e is a characteristic time for the light curve rise. This simple model provides good matches to early light curves and has easily interpretable parameters. We use it to determine the times of explosion for our sample. We plan to investigate more flexible, data-driven models in the future: the restrictive functional form of the exponential fit likely leads to underestimated uncertainties in the determination of t_0.

We transform the light curves from magnitudes to flux, with the observed maximum corresponding to a flux of unity. The photometric uncertainties from the literature are converted to

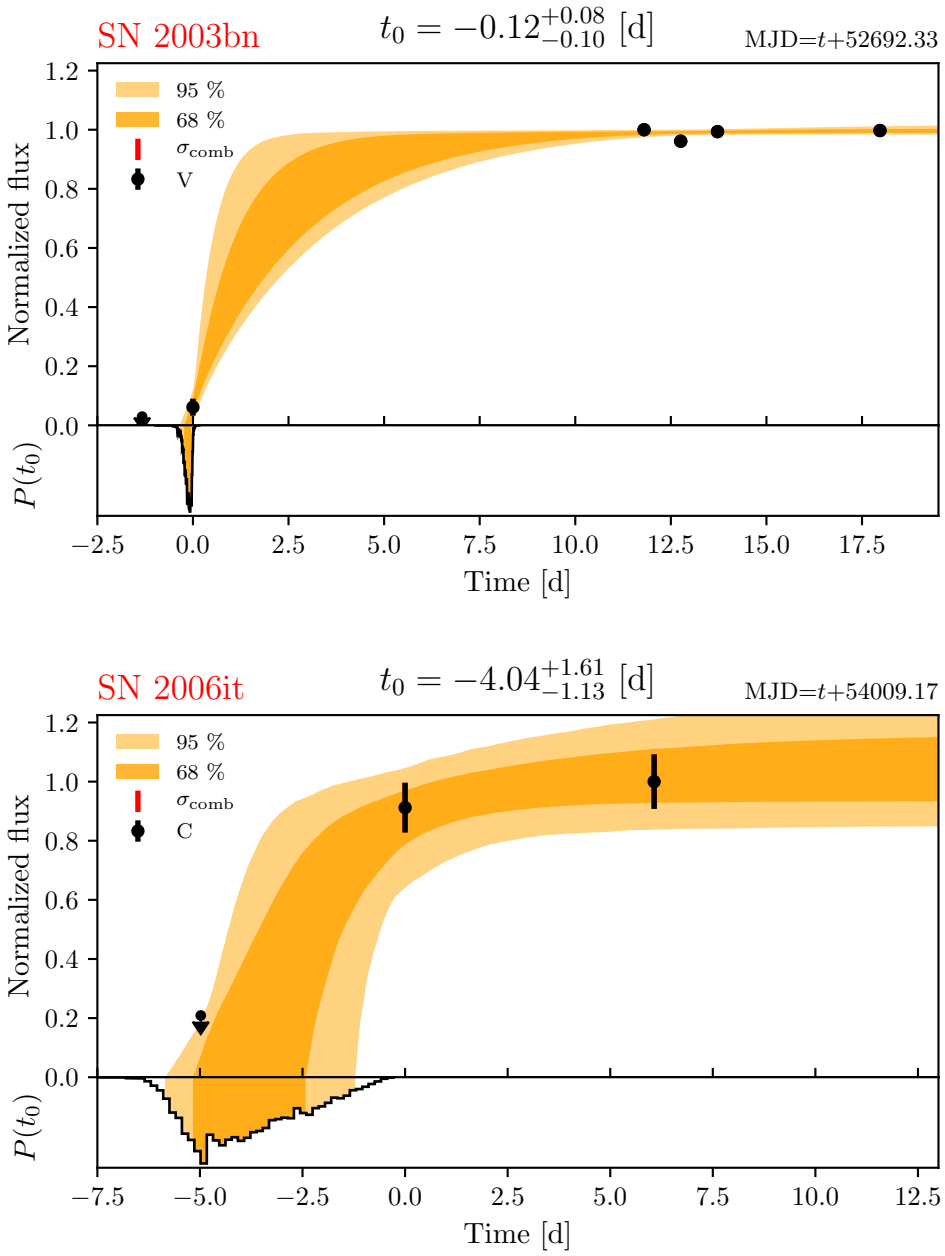

Figure 21.1.: Exponential fits to the normalized flux light curves of SN 2003bn and SN 2006it. We show the measured fluxes and their uncertainties, as reported in the literature, in black. We denote upper limits by symbols with downward arrows. Exponential fits to the data allow us to determine the time of explosion t_0: the inferred t_0 and its uncertainty is listed in the top center; the full posterior distribution is shown in the bottom panel. We visualize the exponential fit curves through their 68 % (orange) and 95 % (light orange) confidence intervals. We account for underestimated uncertainties by allowing for an additional intrinsic variance shared by all datapoints, the magnitude of which is determined in the fit. Red bars indicate the resulting inflated uncertainties σ_{comb}. Times are measured with respect to the first detection; the conversion to MJD is provided in the top right corner.

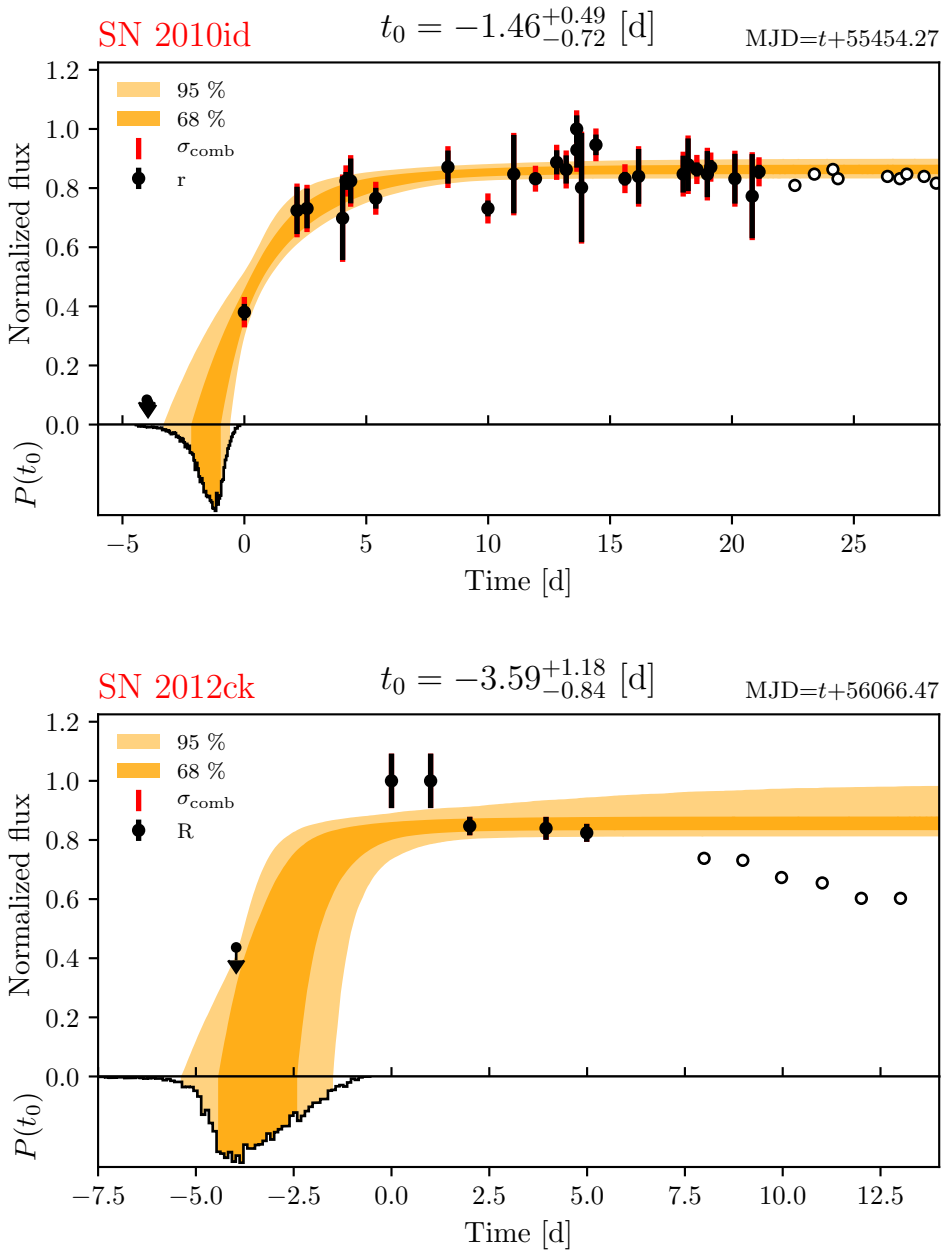

Figure 21.2.: Same as Fig. 21.1 but for SN 2010id and SN 2012ck.

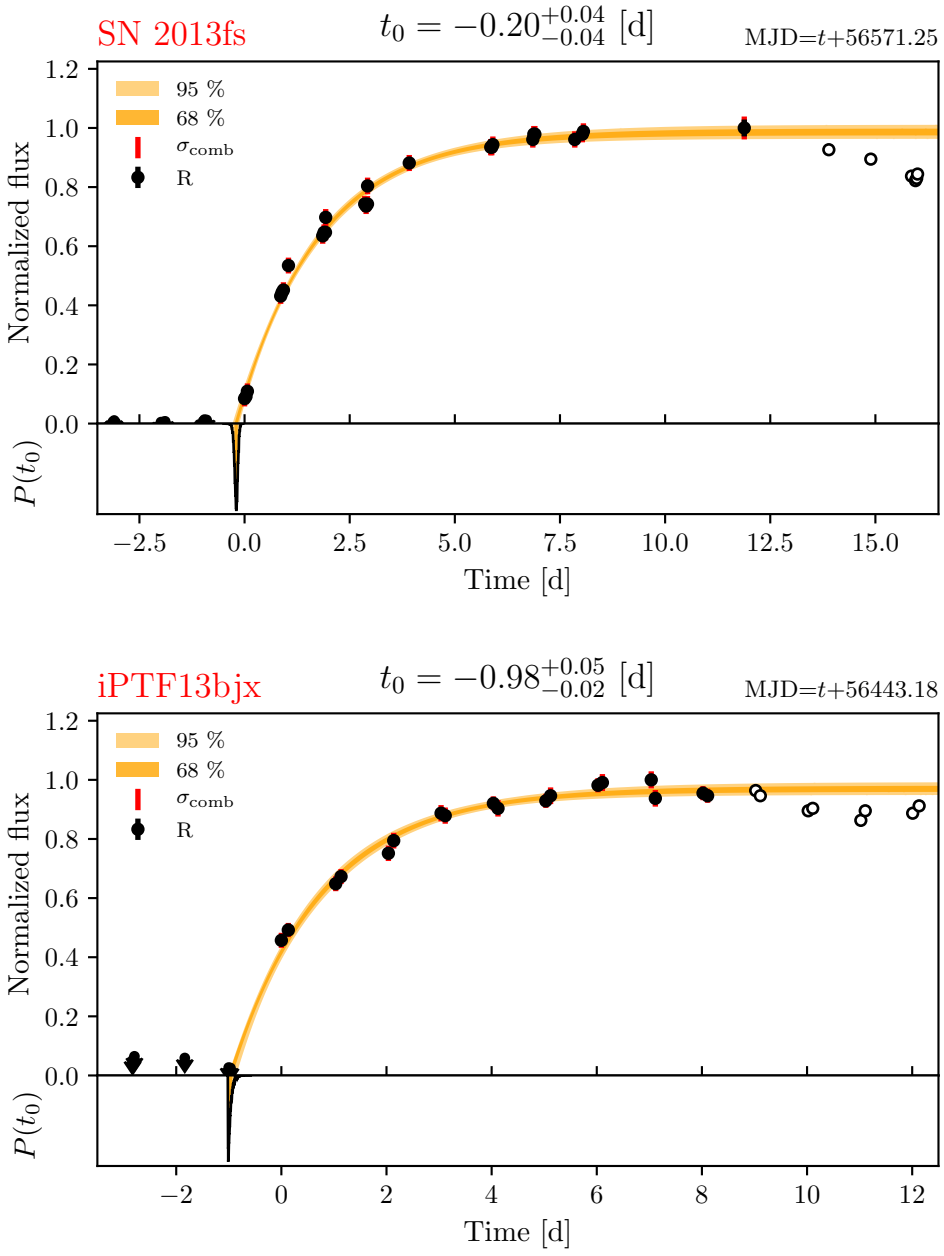

Figure 21.3.: Same as Fig. 21.1 but for SN 2013fs and iPTF13bjx.

normalized flux using linear error propagation. We then determine the parameters t_0, t_e, and f_m of our model through a Bayesian fit. The likelihood for the measured fluxes is assumed to be Gaussian. We treat upper limits in a simplified manner; the adopted likelihood is a step function in flux: uniform below the limiting flux and zero above. We add an intrinsic variance σ_i^2 to each datapoint to mitigate the effect of underestimated uncertainties on the fit. The standard deviation $\sigma_{\mathrm{comb},j}$ for the flux of data point j is thus given by

$$\sigma_{\mathrm{comb},j} = \sqrt{\sigma_i^2 + \sigma_{\mathrm{lit},j}^2}, \tag{21.2}$$

where $\sigma_{\mathrm{lit},j}^2$ is the uncertainty as reported in the literature. We determine the magnitude of the intrinsic scatter as part of the fit. The adopted prior for σ_i^2 is log-uniform between 10^{-8} and 0.075. We assume a uniform prior $\mathcal{U}$ for the light curve rise time: $\pi(t_{\mathrm{rise}}) \sim \mathcal{U}(2\,\mathrm{d}, 40\,\mathrm{d})$. We define t_{rise} as the time from the explosion to the point where the light curve rises by less than 0.01 mag/d following Gall et al. (2015) and González-Gaitán et al. (2015). This is then transformed into a distribution for the time scale of the exponential t_e. The remaining priors are $\pi(f_m) \sim \mathcal{U}(0.5, 1.5)$ and $\pi(t_0) \sim \mathcal{U}(t_{\mathrm{first}} - 10, t_{\mathrm{first}})$, where t_{first} is the time of the first detection. With the priors and likelihood defined, we can determine the time of explosion for the SNe in our sample. The light curve data used is as follows:

(i) SN 2003bn. We use a deep non-detection (21.0 mag) and detection (20.2 mag) on unfiltered NEAT images (Wood-Vasey et al., 2003) combined with V-band data from Anderson et al. (2014). Given the very blue SED at early times, the effective wavelength of the unfiltered images will be in one of the bluer bands even for a red-sensitive CCD; we adopt the V-band.[3] We conservatively assign an uncertainty of 0.5 mag to the first NEAT detection.

(ii) SN 2006it. The data used consists of a non-detection (19.2 mag) and two detections (17.6 mag, 17.5 mag) from unfiltered KAIT images (Lee & Li, 2006). We do not combine the unfiltered data with filtered photometry due to considerable mismatches.

(iii) SN 2010id. We utilize an r-band light curve from the Palomar Transient Factory (PTF; Law et al., 2009) with a cadence between one and five days as published in Gal-Yam et al. (2011).

(iv) SN 2012ck. We combine a non-detection (18.8 mag) and two detections (17.9 mag) from unfiltered KAIT images (Kandrashoff et al., 2012) with R-band photometry from de Jaeger et al. (2019). We assign an error of 0.1 mag to the two KAIT detections to account for the uncertainties in the transformation from unfiltered to R-band magnitudes.

[3] It does not make much of a difference whether we combine the unfiltered data with V or B band photometry given how far the first detection is below the peak (~ 3.5 mag).

Table 21.3.: Parameter range covered by the extended spectral emulator.

	$v_{\rm ph}$ [km s^{-1}]	$T_{\rm ph}$ [K]	Z [$Z_\odot$]	$t_{\rm exp}$ [days]	n
Min	3600	5800	0.1	6.5	6
Max	10 700	10 000	3.0	40.0	16

(v) SN 2013fs. We use an R-band light curve from the intermediate Palomar Transient Factory (iPTF; Kulkarni, 2013) with near-daily cadence as published by Yaron et al. (2017).

(vi) iPTF13bjx. We utilize the iPTF R-band light curve published by Rubin et al. (2016), which has near-daily cadence.

Our fits to these data are visualized in Figs. 21.1 to 21.3. We will directly use the plotted posterior distributions for t_0 as priors in the tailored EPM. The exponential fits yield plausible estimates for the explosion epochs but the associated uncertainties are likely underestimated. Fortunately, this is of little practical consequence for our analysis. The uncertainty in t_0 is only a minor contribution to that in H_0 for the objects with the suspiciously small errors, which are the ones with the best light curve coverage.

21.3. Distance determinations

We determine distances to the SNe in our sample through the tailored EPM. We model the observations with an extended version of the emulator from Part III, which has been complemented by ~ 700 models at later epochs. The new version calculates synthetic spectra up to around five weeks after the explosion compared to three weeks for the original. Otherwise, the parameter space is mostly unchanged. For reference, we list the updated parameter ranges in Table 21.3. The extended emulator allows us to model the observations noted in Table 21.2. For each fit, we fix the time since explosion to the estimated phase from the light curve fit (as measured in the SN rest frame). The well-constrained explosion epochs for our SNe eliminate the need to iteratively adjust the phases for the spectral models to be consistent with the results of the EPM regression (for t_0).

The determination of the host galaxy extinction poses a new challenge. In our initial studies of SN 1999em and SN 2005cs, we adopted values from the literature to facilitate the comparison with the results of Dessart & Hillier (2006) and Dessart et al. (2008). Here, we estimate the host galaxy reddening from the spectral time series. As demonstrated by Baron et al. (2000, 2007), Dessart & Hillier (2006), and Dessart et al. (2008), spectral modeling has the power to disentangle the effect of reddening and temperature on the SED due to their different impact on the line features. For each spectrum, we perform the same type of maximum-likelihood fit as for SN 1999em and SN 2005cs (see Part III) but exploring different values of the color excess. Through this procedure,

we have spectral fits and parameter estimates for a fine grid of possible values of the total color excess $E(B-V)$; the galactic reddening as listed in Table 21.1 sets the lower boundary of this grid. In the fit, we redden the synthetic spectra in the SN rest frame with the combined host and galactic reddening.[4] The favored color excess is the value that minimizes the χ^2 for the spectral fit. We adopt the unweighted average of the individual favored color excesses as our best-fit value for the spectral time series. The best-fit color excess and a total-to-selective extinction ratio of $R_V = 3.1$ then yield the reddening for the distance determination. The adopted approach is simple and leaves little room for subjective choices that can bias the H_0 measurement. However, by equally weighting the epochs, we neglect that each spectrum contains different amounts of information about the extinction. The sensitivity of the line features to temperature as well as the quality and wavelength coverage of the observation will determine how informative a given epoch is on the color excess. Finally, the method also disregards that spectra at closely spaced epochs do not provide completely independent estimates of the extinction.

We extract the ratio of the photospheric angular diameter and velocity $\Theta/v_{\rm ph}$ from the best-fitting models at the adopted reddening (see Part III for details). The respective spectral fits are visualized in Figs. 21.4 to 21.9. We use the $\{BVI\}$ bandpass combination for the EPM to make the most of the available information.[5,6] In the regression, we assume fractional uncertainties for $\Theta/v_{\rm ph}$ of 10 % following Dessart & Hillier (2006) and Dessart et al. (2008) as in Part III. We treat the uncertainties as Gaussian and uncorrelated between epochs. Based on the assumptions above, we determine the distance and time of explosion through a Bayesian linear regression to the time evolution of $\Theta/v_{\rm ph}$ as measured in the SN rest frame. The binned posterior distributions from the light curve fits serve as the priors for the time of explosion. The tailored EPM analyses, including the spectral fits, the regression, and the inferred parameters are summarized in Figs. 21.4 to 21.9. Table 21.4 lists the measured luminosity distances together with the time of explosion from the light curve fits, and the total color excess determined from the spectral time series. These quantities constitute the key results of our analysis.

21.4. Hubble constant

The main challenge in determining H_0 from the measured distances are the unknown peculiar velocities of the host galaxies: the treatment of peculiar velocity uncertainties and corrections will make a difference in the final H_0 due to the small sample size and local nature of our SNe. The situation is similar to that of the Megamaser Cosmology Project (MCP), which works with the same number of objects and at comparable redshifts ($z < 0.034$): they find values of H_0 from

[4] In principle, host and galactic reddening should be applied one after the other in the respective rest frame. However, for the small redshifts of our sample the difference between the correct and the adopted approach will be negligible.

[5] With the exception of SN 2006it for which there is no available I-band photometry; we instead use the $\{BV\}$ filter combination.

[6] The result of the tailored EPM is much less sensitive to the adopted bandpass combination than classical EPM. Our angular diameters deviate at most by a few percent between bandpass combinations.

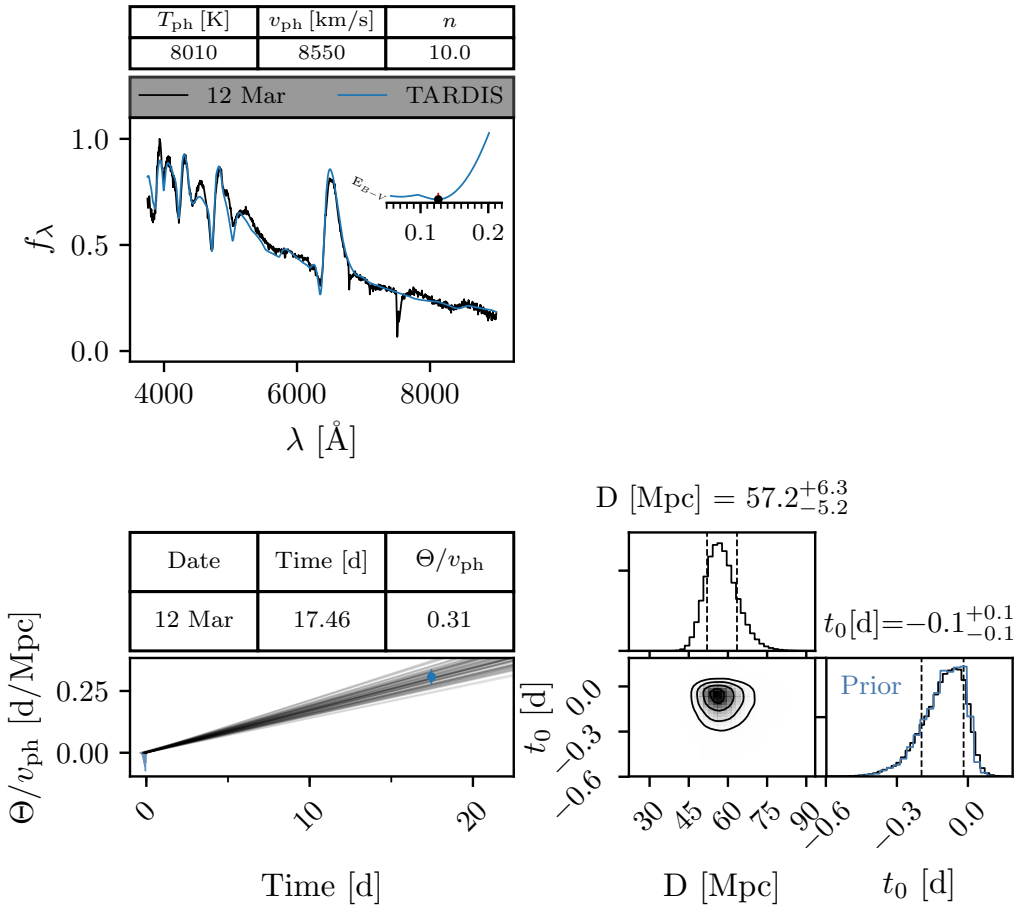

Figure 21.4.: Tailored EPM analysis of SN 2003bn. The top panel shows the maximum likelihood fits used for the distance measurement. The best-fitting emulated spectrum is depicted in blue and the de-redshifted observation in black. The flux has been normalized to the peak of the observed spectrum. A small table summarizes the most important fit parameters: photospheric temperature $T_{\rm ph}$, photospheric velocity $v_{\rm ph}$, and the power-law index of the density profile n. The inset in the panel illustrates how the fit quality, as measured by the normalized χ^2, varies with the total color excess $E(B-V)$. If multiple spectra are modeled (as is the case for other SNe), red ticks indicate the favored reddenings of the individual epochs. The black marker highlights the combined estimate for $E(B-V)$. The plotted spectral fits and the listed parameters are for this color excess. We apply the reddening correction to the synthetic spectra and not to the observations.
We use the ratios of the photospheric angular diameter and photospheric velocity $\Theta/v_{\rm ph}$ from the maximum-likelihood fits to determine the distance through a Bayesian linear regression. This is visualized in the bottom left panel, where we plot $\Theta/v_{\rm ph}$ versus time in the SN rest frame (relative to the first detection). A small table on top of the subplot lists the used values for $\Theta/v_{\rm ph}$ (in units of d/Mpc). The blue-shaded region indicates our prior on the time of explosion from the light-curve fit. We illustrate the regression through a hundred fit curves, which have been randomly sampled from the posterior. The results of the fit are summarized in the bottom right panel, which shows the posterior distributions for the distance D and the time of explosion t_0. We include the prior on t_0 in blue for comparison purposes.

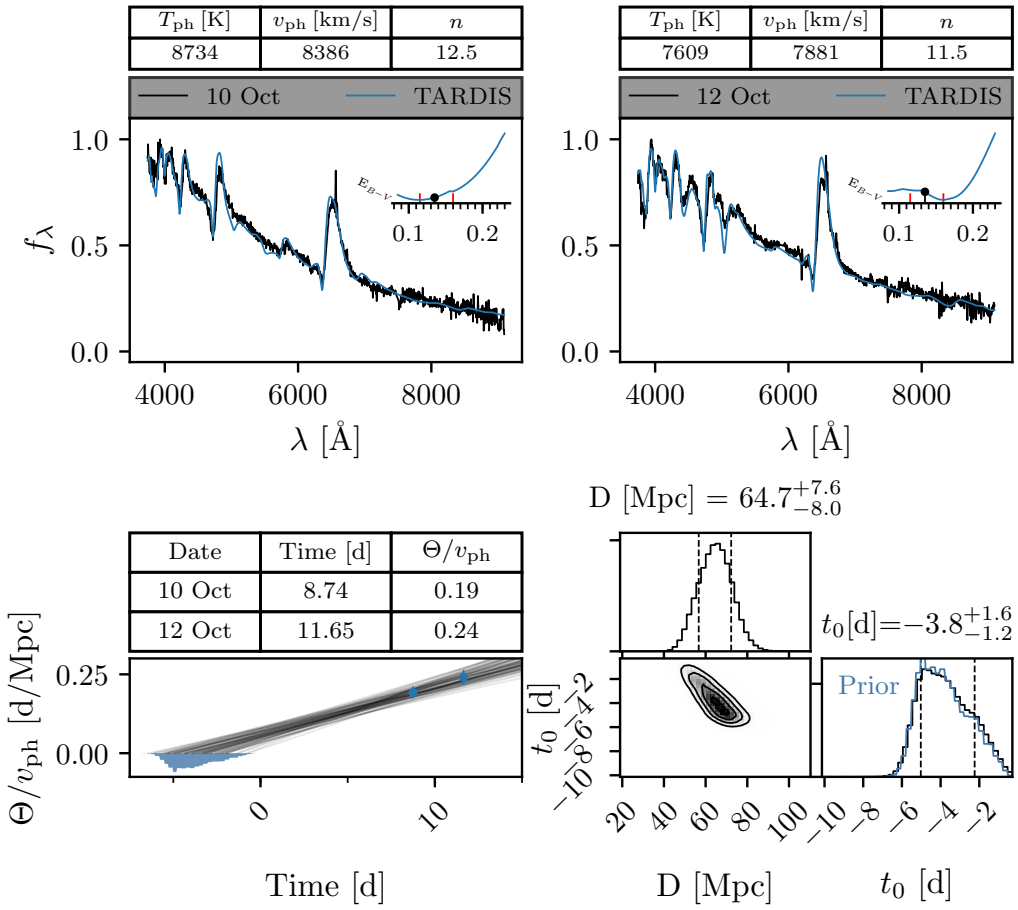

Figure 21.5.: Tailored EPM analysis of SN 2006it. See Fig. 21.4 for the figure layout.

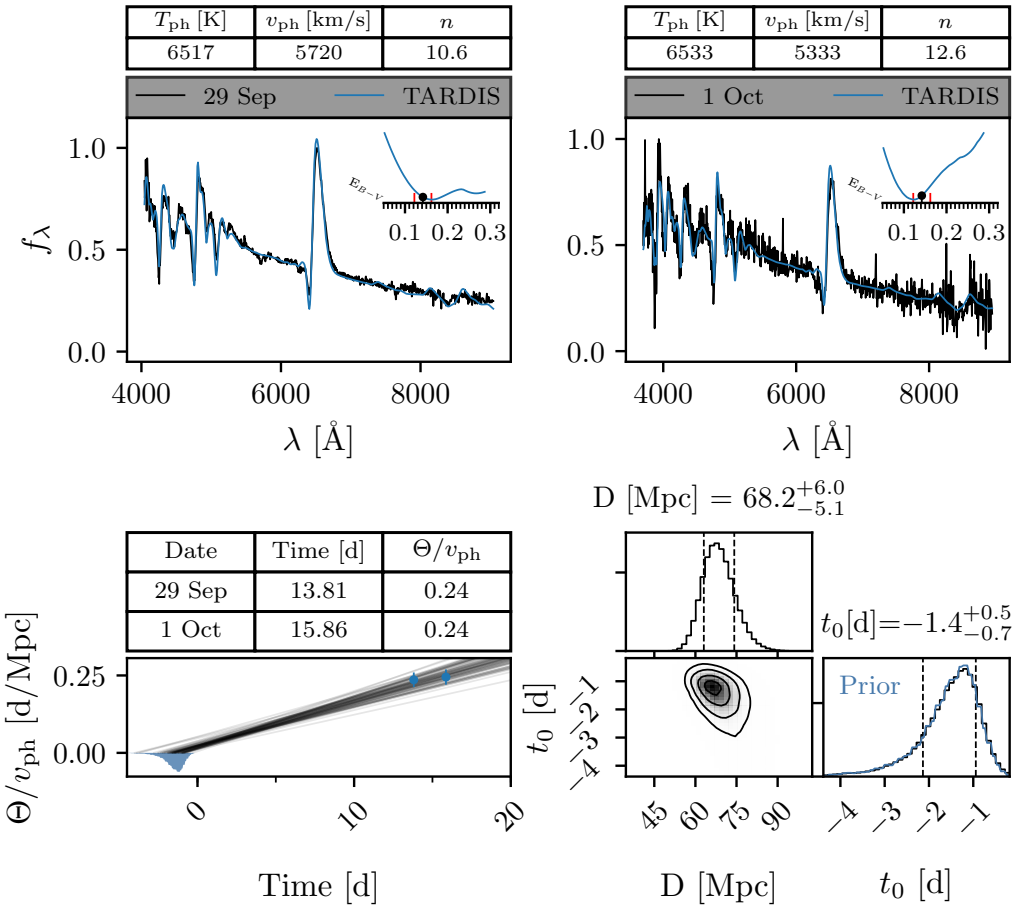

Figure 21.6.: Tailored EPM analysis of SN 2010id. See Fig. 21.4 for the figure layout.

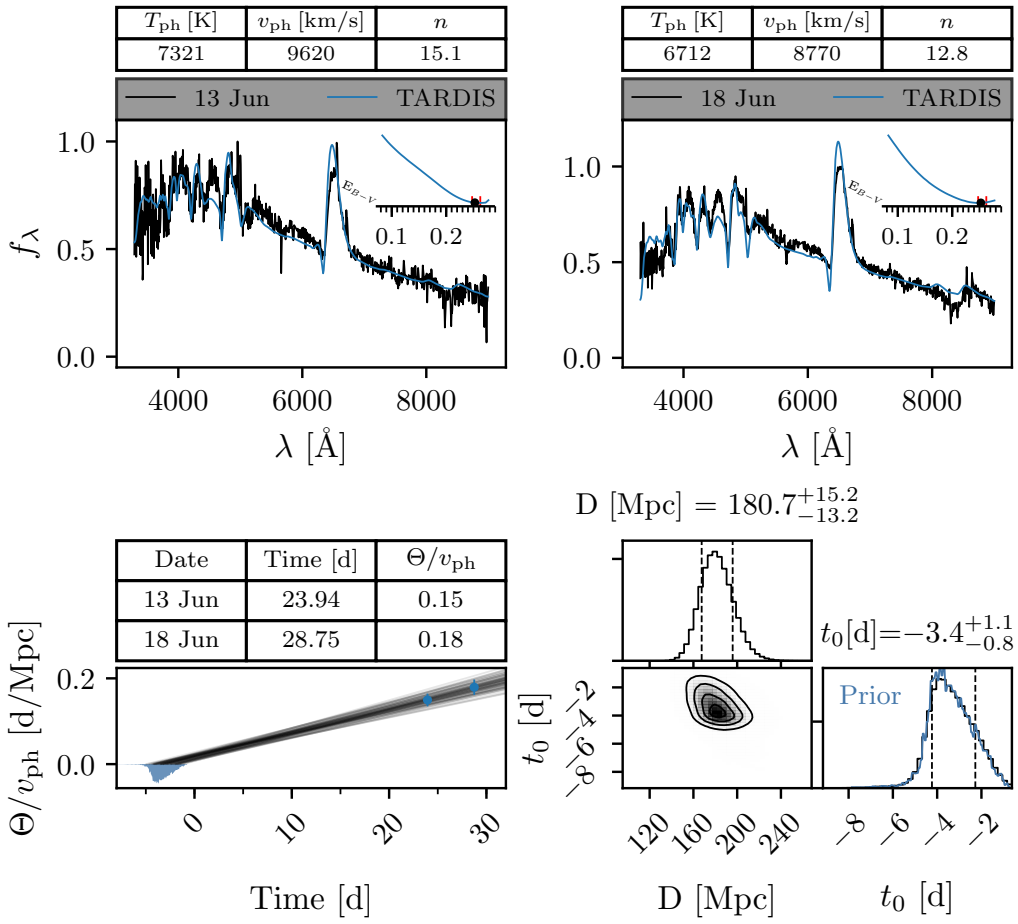

Figure 21.7.: Tailored EPM analysis of SN 2012ck. See Fig. 21.4 for the figure layout.

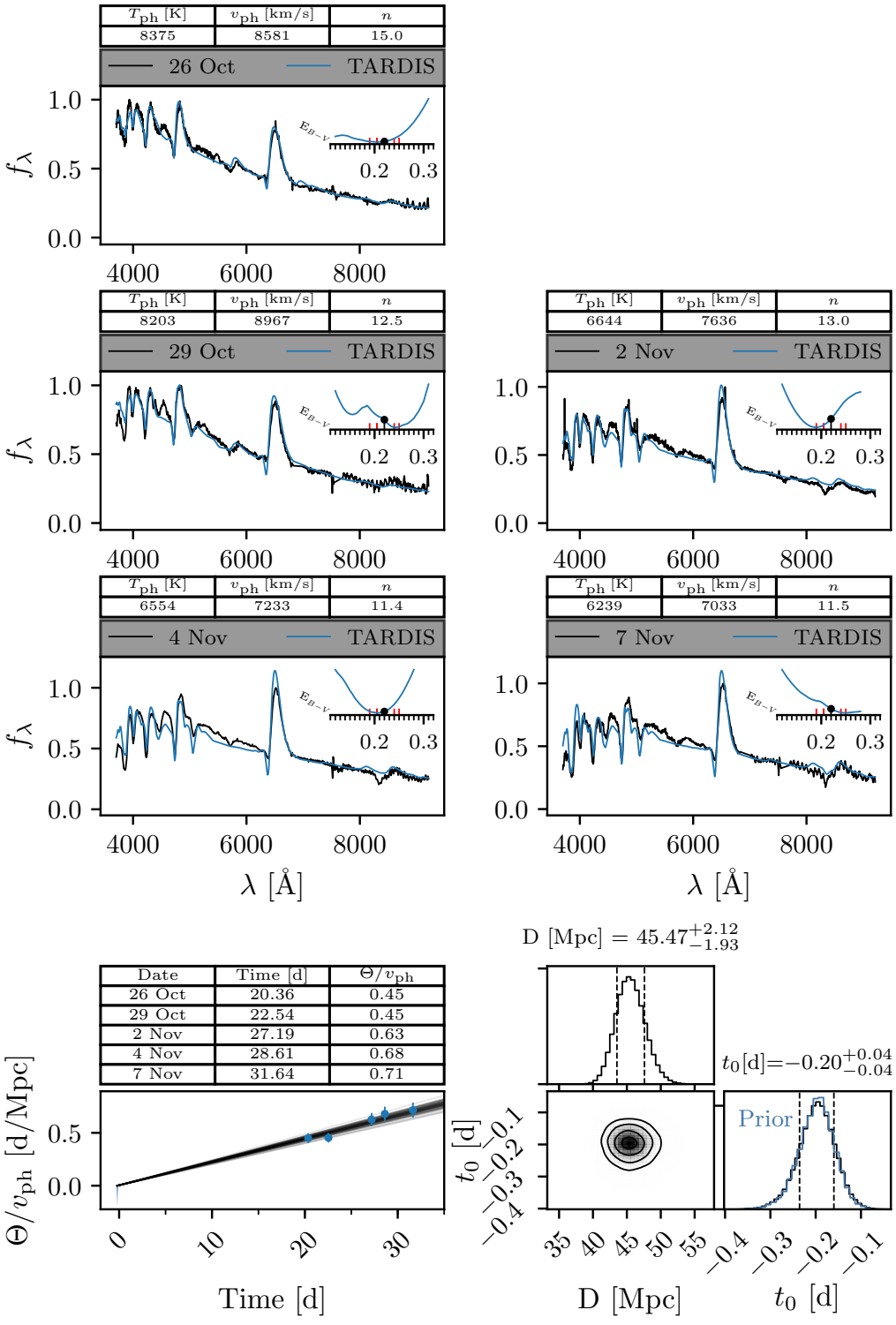

Figure 21.8.: Tailored EPM analysis of SN 2013fs. See Fig. 21.4 for the figure layout.

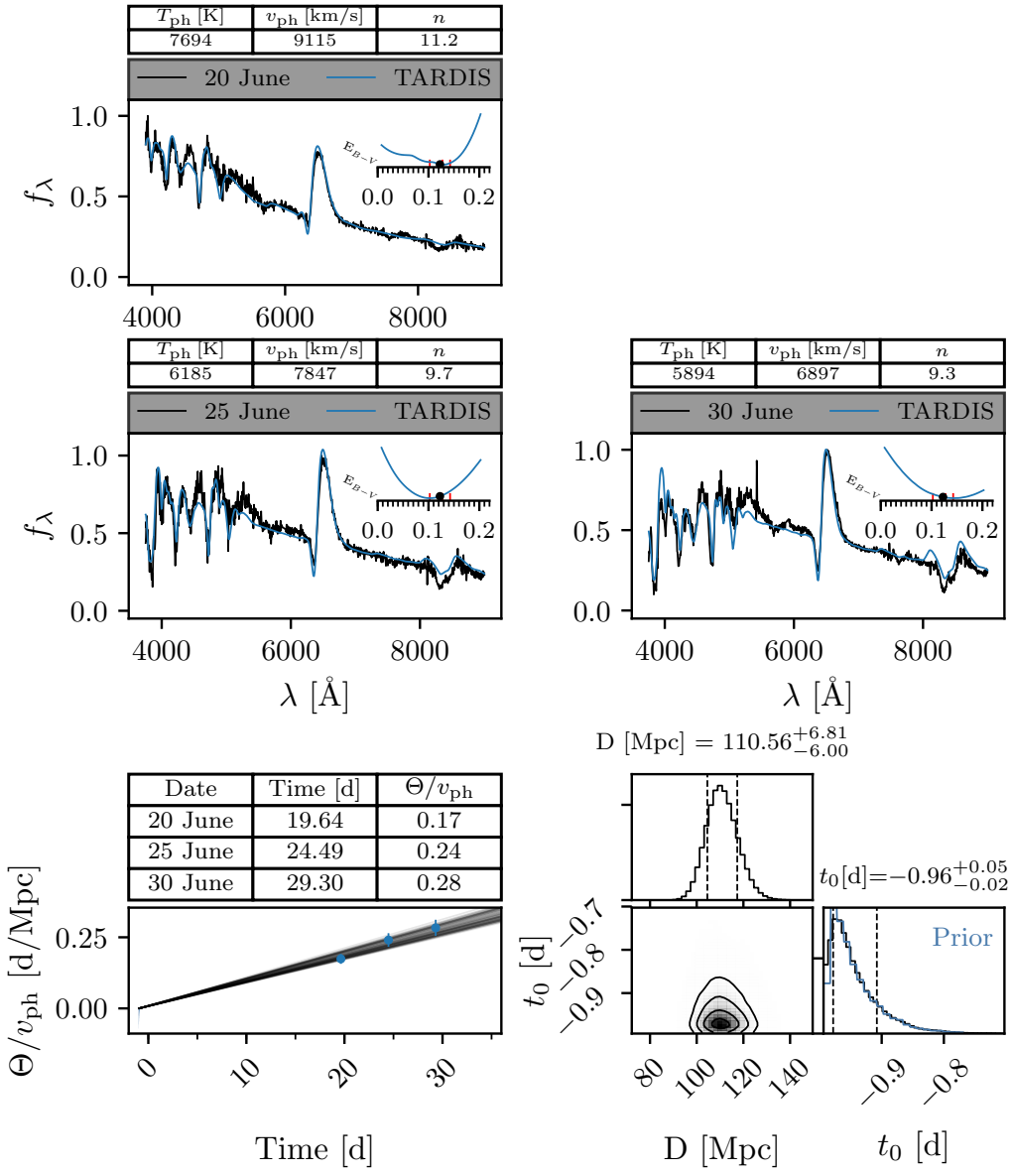

Figure 21.9.: Tailored EPM analysis of iPTF13bjx. See Fig. 21.4 for the figure layout.

$71.8\,\mathrm{km\,s^{-1}\,Mpc^{-1}}$ to $76.9\,\mathrm{km\,s^{-1}\,Mpc^{-1}}$ based on six different treatments of peculiar motions (Pesce et al., 2020) including three galaxy-flow-correction models (Mould et al., 2000; Carrick et al., 2015; Graziani et al., 2019). We adopt their fiducial model, which has the fewest assumptions, for our proof-of-principle measurement. This simple model does not use any peculiar-flow corrections but only a transformation of the heliocentric redshifts to the CMB rest frame. The treatment assumes that the measured (CMB) redshifts of galaxies z are Gaussian distributed around their true cosmological redshift $\bar{z}$:

$$\mathcal{L}_z = \frac{c}{\sqrt{2\pi\sigma_{\mathrm{pec}}^2}} \exp\left(-\frac{c^2}{2}\frac{(z-\bar{z})^2}{\sigma_{\mathrm{pec}}^2}\right). \tag{21.3}$$

We assume a velocity uncertainty σ_{pec} through peculiar motions of $300\,\mathrm{km\,s^{-1}}$ in agreement with typical values from the literature (e.g., Léget et al., 2018).[7][8] We neglect redshift measurement uncertainties because these are usually small compared to σ_{pec}. The probability distributions for the luminosity distance D_{L} and the true cosmological redshift $\bar{z}$ [Eq. (21.3)] are all we need to estimate H_0 for each SN. We randomly sample a true cosmological redshift for each distance sample from the EPM regression. We then transform these pairs into a distribution for H_0 according to

$$H_0 \approx \frac{c\bar{z}}{D_{\mathrm{L}}}\left(1 + \frac{1}{2}[1-q_0]\bar{z}\right), \tag{21.4}$$

where

$$q_0 = \Omega_{\mathrm{M}}/2 - \Omega_\Lambda \tag{21.5}$$

is the deceleration parameter. The second-order expansion in redshift is accurate to around 0.05 % for the considered redshifts and plausible cosmological parameters. We use $q_0 = -0.55$ corresponding to $\Omega_{\mathrm{M}} = 0.3$ and $\Omega_\Lambda = 0.7$ following Riess et al. (2016). The results of our analysis are relatively insensitive to this choice: for our most distant object ($z \approx 0.042$) the inferred H_0 changes only by around 1.5 % when we vary Ω_{M} between 0 and 0.5. In contrast, the difference between the adopted nonlinear expansion ($q_0 = -0.55$) and a linear Hubble law is already more than 3 %. We refrain from marginalizing over q_0 because the correction will be too small to be relevant in this exploratory study. In a final step, we construct a continuous probability distribution from the H_0 samples of each object through a Gaussian kernel-density estimate (KDE). We set the kernel bandwidth according to Scott's Rule (Scott, 1992).

We combine the H_0 constraints from the different SNe under the assumption that they are independent. In this case, the likelihood for the global H_0 is the product of the individual probability distributions, which we approximate by their KDEs.[9] Figure 21.10 illustrates our individual and combined constraints on H_0. The different objects display good agreement within

[7] This is slightly higher than the $250\,\mathrm{km\,s^{-1}}$ assumed in Pesce et al. (2020).

[8] Linear velocity addition is an excellent approximation for the low recession and peculiar velocities considered here.

[9] We adopt a flat prior for H_0 when combining the individual constraints.

Table 21.4.: Results from the tailored EPM analysis. Listed are the times of explosion from the light curve fits t_0, the total color excesses $E(B-V)$ from modeling the spectral time series, the luminosity distances D_L, and the individual constraints on H_0.

	t_0 [MJD]	$E(B-V)$	D_L [Mpc]	H_0 [km s^{-1}Mpc^{-1}]
SN 2003bn	$52692.21^{+0.08}_{-0.10}$	0.126	$57.17^{+6.30}_{-5.17}$	$73.55^{+9.26}_{-8.80}$
SN 2006it	$54005.13^{+1.61}_{-1.13}$	0.135	$64.69^{+7.57}_{-7.99}$	$68.09^{+10.64}_{-8.48}$
SN 2010id	$55452.81^{+0.49}_{-0.72}$	0.142	$68.20^{+5.98}_{-5.12}$	$67.63^{+7.23}_{-6.96}$
SN 2012ck	$56062.88^{+1.18}_{-0.84}$	0.253	$180.72^{+15.19}_{-13.16}$	$70.48^{+5.89}_{-5.67}$
SN 2013fs	$56571.05^{+0.04}_{-0.04}$	0.220	$45.47^{+2.12}_{-1.93}$	$70.48^{+7.52}_{-7.27}$
iPTF13bjx	$56442.20^{+0.05}_{-0.02}$	0.122	$110.56^{+6.81}_{-5.99}$	$78.80^{+5.40}_{-5.25}$

the uncertainties, despite likely underestimated distance errors. Neither the extremely luminous (SN 2012ck), nor the subluminous (SN 2010id) SN stands out from the rest. The same applies to the flash-ionization event (SN 2013fs). This constitutes an important finding of this proof-of-principle demonstration. However, the small sample size and the influence of peculiar velocities limit the significance of the conclusions.

Our analysis arrives at H_0=$72.28^{+2.85}_{-2.80}$ km s^{-1} Mpc^{-1} based on the six SNe used. Figure 21.11 illustrates how this measurement compares to state-of-the-art early and late Universe probes. We find good agreement with other local determinations of H_0 through distance ladders (Riess et al., 2019; Freedman et al., 2019), time-delay lensing (Wong et al., 2019), and masers (Pesce et al., 2020). Our analysis is still marginally consistent with a low H_0 as inferred from the CMB (Planck Collaboration et al., 2018) and BAO (Abbott et al., 2018), in particular, since our simple error treatment likely underestimates the uncertainties.

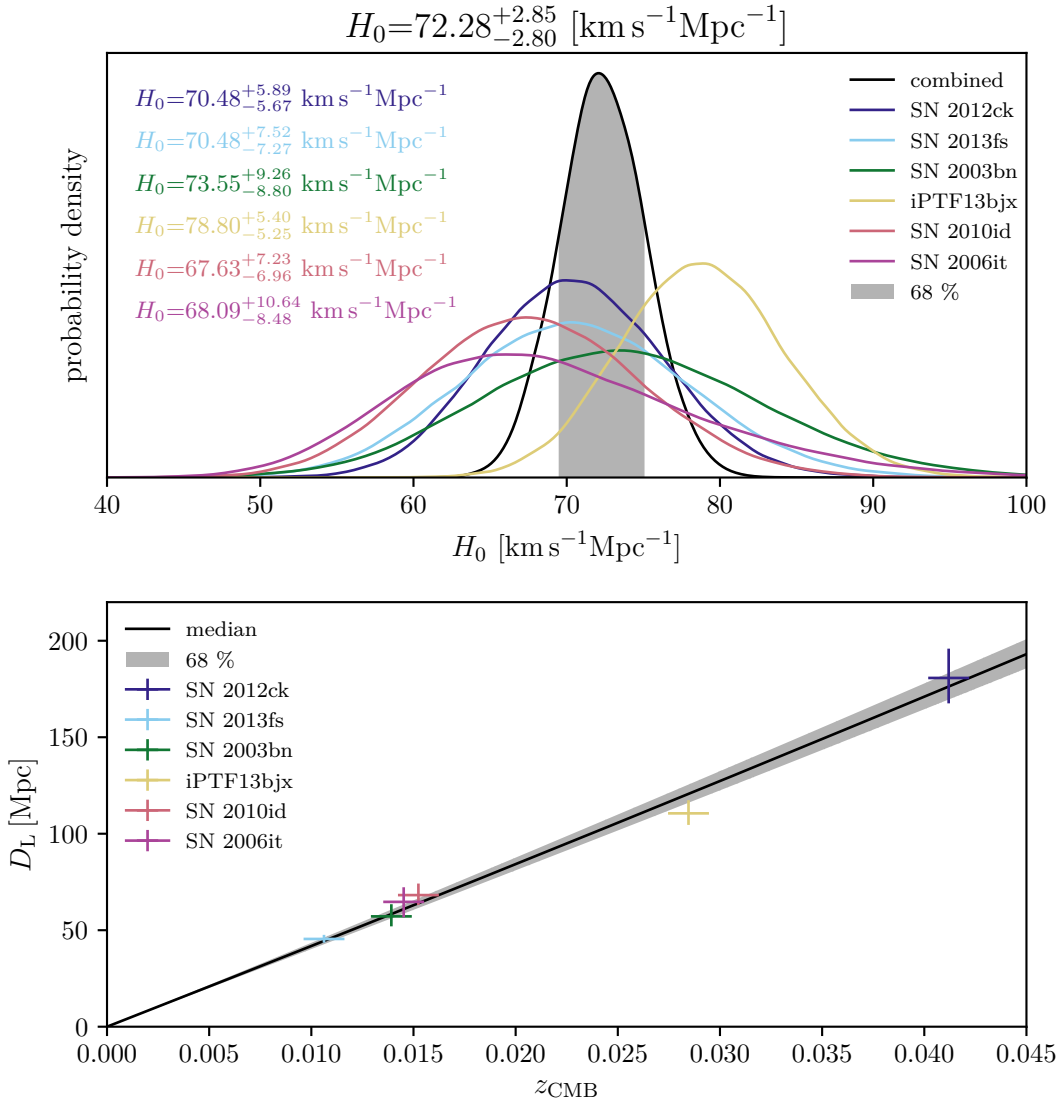

Figure 21.10.: H_0 constraints from the tailored EPM. The top panel shows the probability distributions of H_0 for the individual SNe in color and the combined estimate in black. We include the median values and 68 % confidence intervals of the distributions for ease of comparison. The bottom panel is a Hubble diagram, where we plot the luminosity distances against the CMB redshift. The black line is the redshift-distance relation for our median H_0. The gray region indicates the 68 % confidence interval of our measurement.

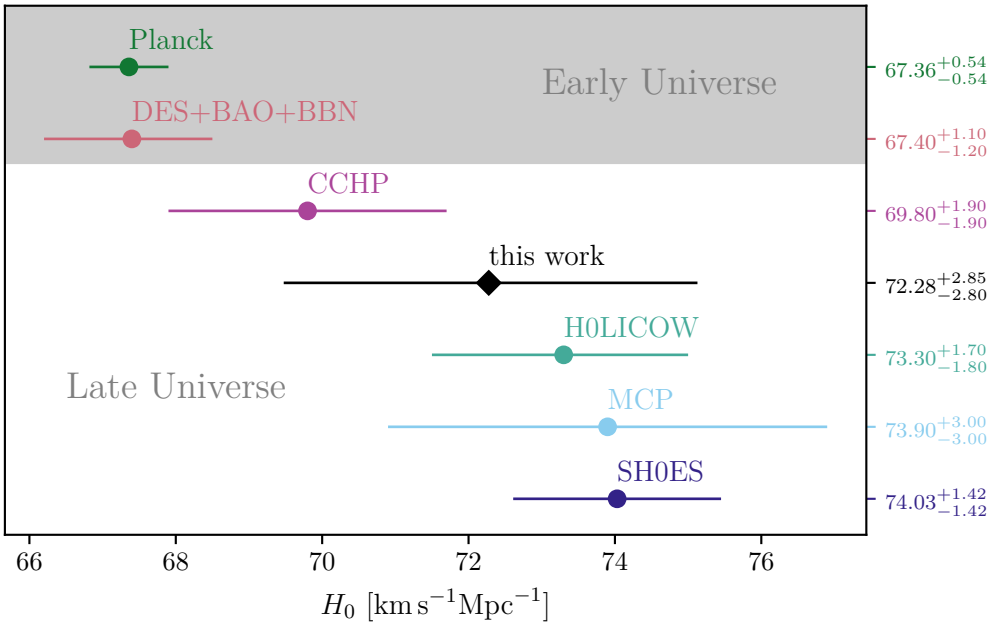

Figure 21.11.: Comparison of H_0 to competitive early and late Universe probes from the literature. On the early Universe side, we include the constraints from CMB anisotropies and lensing (Planck Collaboration et al., 2018), and an exemplary BAO measurement (DES+BAO+BBN; Abbott et al., 2018). The latter is based on Dark Energy Survey (DES) clustering and weak lensing data combined with BAO and BBN. At the other end of cosmic time, we show results from Cepheid-based (SH0ES; Riess et al., 2019) and TRGB-based (CCHP; Freedman et al., 2019) distance ladders, time-delay lensing (H0LiCOW; Wong et al., 2019), and megamasers (MCP; Pesce et al., 2020).

22. Conclusions

As Einstein put it, "Nothing happens until something moves": the paradigm shift from a static to a dynamic, moving Universe in the early twentieth century led to a revolution of our understanding of the cosmos. Accurate measurements of the current expansion rate—the Hubble constant H_0—have played a key role in developing our cosmological model: H_0 sets the size and age scale of the Universe and is thus an essential cosmological parameter (see Sect. 1.2). Measurements with as many independent probes as possible are crucial to pin it down with the necessary precision. Only in this way can we control the systematic uncertainties. This is true now more than ever in light of the ongoing discrepancy between local and global determinations of H_0, which hints at physics beyond the fiducial ΛCDM cosmological model (see Chapter 2).

Summary The objective of this thesis was to establish an independent one-step method to measure H_0 based on radiative transfer modeling of SNe II. The tailored EPM of Dessart & Hillier (2006) and Dessart et al. (2008) provides the foundation for this endeavor. The method replaces the simplified dilute-blackbody models of the classical EPM through detailed spectral fits; the increased accuracy makes competitive absolute distance measurements of SNe II possible (see Sect. 3.2). However, the improvements come at a cost: spectral fitting renders the tailored EPM an extremely complicated and time-consuming procedure. So far, it has only been applied to three nearby SNe II (Dessart & Hillier, 2006; Dessart et al., 2008). New tools are needed to enable spectral modeling of large SN samples and to realize the full potential of the tailored EPM for cosmography. We have invested substantial efforts into the creation of these tools.

To start with, we have developed a new SN II radiative transfer code that enables fast and accurate calculations of large model grids (see Part II). Our software is built on top of the one-dimensional Monte Carlo spectral synthesis code TARDIS (Kerzendorf & Sim, 2014). In its baseline version, TARDIS provides a detailed treatment of line interactions above a blackbody photosphere. This is sufficient for rapid spectral modeling of a wide variety of transients ranging from normal and peculiar SNe Ia to neutron star merges (Heringer et al., 2017; Magee et al., 2017; Watson et al., 2019). However, substantial extensions were necessary to allow us to make accurate predictions for the luminosities of SNe II based on their spectra. This requires simulating the creation and dilution of the continuum radiation (see Sect. 3.2.2). We have implemented the most important processes that couple the radiation field (directly or indirectly) to the thermal pool in TARDIS: bound-free, free-free, and collisional interactions. The macro atom scheme of Lucy (2002, 2003) allows us to model the effect of these processes on the radiation field (see Sect. 5.1.2).

Conversely, a thermal balance calculation simulates how heating and cooling by these interactions sets the temperature of the electron gas (see Sect. 5.2.3). This enables a self-consistent description of continuum formation, which would not have been possible with the previously used prescription of Mazzali & Lucy (1993). The final improvements to TARDIS concern the calculation of the excitation and ionization state: we account for the large departures from LTE, which arise in the low-density, scattering-dominated SN II atmospheres, through a full solution of the NLTE rate equations for hydrogen (see Sect. 5.2).

We demonstrate the accuracy of the extended code through spectroscopic modeling of SN 1999em. The calculation of new EPM dilution factors then showcases the utility of the tool for SN II studies based on large model grids (see Chapter 9). Our independent results allow us to critically assess the long-standing discrepancy between the correction factors of Eastman et al. (1996) and Dessart & Hillier (2005a). The two studies, which were the only ones to derive comprehensive dilution factor sets from NLTE radiative transfer models, show maximum differences of up to $\sim 50\,\%$: this constitutes one of the most important uncertainties in the classical EPM (see, e.g., Jones et al., 2009). The good agreement of our TARDIS calculations with those of Dessart & Hillier (2005a) helps to reduce this uncertainty: the dilution factors of Eastman et al. (1996) are likely too small considering also the simpler microphysics of their computations. However, differences in the model parameters—most notably the photospheric densities also partly account for the discrepancy ($\sim 10\,\%$; see Sect. 10.2). This again highlights the need to constrain the relevant SN properties through radiative transfer modeling: only in this way can we achieve percent-level accuracy in the measured distances.

The computational cost of the necessary radiative transfer calculations is considerable: it takes $\sim 1\,\mathrm{d}$ on a single core of a CPU to compute a synthetic spectrum with our code. This is the major obstacle towards automated fitting of SN spectra: calculating thousands of models for each observation to find the best-fit parameters through numerical optimization is prohibitively expensive. Instead, the best fit is usually identified "chi by eye" by a spectroscopist (e.g., Stehle et al., 2005; Magee et al., 2016; Barna et al., 2017) who can find good matches with less radiative transfer simulations. However, this is only feasible for small samples because it is highly labor intensive. We use a machine-learning spectral emulator to overcome this problem (see Part III). The emulator is trained on a set of radiative transfer models generated by our code. Through a combination of data preprocessing, PCA decomposition, and GP regression, we can predict the output of our simulations at a tiny fraction of the computational cost ($\sim 10^{-7}$). The predicted spectra agree with real calculations to better than a percent (see Chapter 16). The tremendous speedup removes the main obstacle for automated spectral fitting. To showcase this, we couple the emulator to a standard optimization algorithm and fit spectral time series of two well-studied SNe II (see Sect. 18.2). Our tailored-EPM distance estimates agree well with those from Cepheids and the TRGB (see Sect. 18.3). While our main interest here is in the cosmological application, the method also looks very promising for automated spectroscopic analyses of a large variety of transients.

We are now in the position to fit larger SN samples in a reproducible way and determine H_0. We demonstrate this for six SNe II in the Hubble flow with redshifts up to ~ 0.04 (see Chapter 21). This first-ever cosmological application of the tailored EPM arrives at H_0=$72.3^{+2.9}_{-2.8}$ km s^{-1} Mpc^{-1}. Our result is in good agreement with other local measurements through distance ladders (Riess et al., 2019; Freedman et al., 2019), time-delay lensing (Wong et al., 2019), and masers (Pesce et al., 2020). While our result favors a high H_0 as found by these late Universe probes, it is still consistent with the lower values from the CMB (Planck Collaboration et al., 2018) and BAO (Abbott et al., 2018).

Outlook We will need to reduce our uncertainties before we can determine whether our method ultimately supports the current Hubble tension or not. More and better data will play a key role in achieving this goal: the accuracy of our proof-of-principle measurement is limited through the small sample size and, at a mean SN redshift of ~ 0.02, peculiar velocity corrections. There is only limited data in the literature that meets the necessary requirements: redshifts $\gtrsim 0.01$, accurate photometry, and multiple well-calibrated spectra in the first month after the explosion. We have continued to build an optimized dataset ourselves over the last years. This includes accurate spectrophotometric time series of 21 SNe II with redshifts up to ~ 0.04 from the SNfactory (Aldering et al., 2002; see Sect. 20.1). In addition, we have recently started an observation campaign on the ESO Very Large Telescope with FORS2 that targets SNe II at higher redshifts (see Sect. 20.2). To date, this program has collected data for 6 SNe II with redshifts between 0.033 and 0.166. Over the next year, we expect to observe ~ 10 more objects. Combined, these datasets will provide the basis for a highly-competitive H_0 measurement.

However, to critically assess the Hubble tension, the estimated uncertainty will be as important as the value itself. In our proof-of-principle demonstration, we chose a simple maximum-likelihood approach and uncertainties for the relevant quantities ($\Theta/v_{\rm ph}$) from the literature (Dessart & Hillier, 2006; Dessart et al., 2008) to facilitate the analysis. In the future, we plan to extract more realistic error estimates from a full Bayesian analysis of the spectra. This will require a more sophisticated likelihood that accounts for the different sources of uncertainties in the data and the interpolation as well as systematics in the radiative transfer models (see discussion in Sect. 18.1). The uncertainties from the spectral fits and their correlations from epoch to epoch will then be used to determine the error in the distance. Finally, we will also continue to refine our radiative transfer code to achieve the best possible accuracy. This includes extending our NLTE calculation to more species and adding a treatment of charge-exchange reactions.

Conclusion We have established radiative transfer modeling of SNe II as an independent one-step method to determine H_0 in this thesis. Our proof-of-principle measurement already shows good agreement with state-of-the-art results and with better data on the way a highly-competitive determination of H_0 is in reach. This will shed more light on the current Hubble tension and help to answer whether we need physics beyond ΛCDM. With cosmology at a crossroads, it is an exciting time for SN II cosmography.

Acknowledgments

First and foremost, I would like to thank my supervisor Wolfgang Hillebrandt for the opportunity to work on this exciting research project. During my Ph.D., Wolfgang provided great support and advice, while also creating an atmosphere where I could pursue my own ideas. I am also deeply grateful to my co-supervisors Ulrich M. Nöbauer and Stuart Sim. Without their assistance, this work would not have been possible. I want to thank Uli for his continuous support during the first years of my thesis and for being the much-needed voice of reason in all the right moments. I thank Stuart for his ongoing support, countless enlightening discussions, and for always offering an open ear. Special thanks also go to Andreas Floers, Wolfgang Kerzendorf, and Stefan Taubenberger. I am grateful to Wolfgang Kerzendorf for his ongoing support, for showing me the exciting world of open-source software, and for introducing creative interdisciplinary ideas to tackle long-standing problems. I thank Stefan Taubenberger for sharing his encyclopedic supernova knowledge, for always making time when needed, and his critical eye for the relevant physics. I want to thank Andreas Floers for valuable advice on statistical methods, many shared observing nights, and countless stimulating scientific discussion over coffee at ESO. I am also grateful to Stefan and Andreas for great personal adventures, including, but not limited to, driving into a ditch on the Bolivian altiplano. Special thanks go to all the people contributing to the success of the adH0cc observational program and in particular to Bruno Leibundgut as the PI of our project. Here, I again want to extend my gratitude to Stefan Taubenberger for going above and beyond in his support of this endeavor. I thank Stefan Lietzau for sharing his enormous coding expertise and for introducing me to the idea of emulators together with Wolfgang Kerzendorf. I also wish to acknowledge the TARDIS community, who are continuously working on improving and maintaining our code, and have helped me to learn modern coding practices. Next, I would like to express my appreciation to the members of our SN meeting for creating a space of scientific exchange and lively discussion, which contributed greatly to my scientific education. I would like to offer my special thanks to Wolfgang Kerzendorf, Stefan Taubenberger, Stefan Vogl, and most importantly Stuart Sim for proofreading this manuscript and for providing valuable comments. Finally, I would like to thank my family for their support, encouragement, and the bialetti, which fueled my late-night writing endeavors.

Abbreviations

ΛCDM Λ cold dark matter. 2, 17, 31, 152, 154

adH0cc accurate determination of H_0 with core-collapse supernovae. 126, 130, 131, 155

AGN active galactic nuclei. 26–28, 31

BAO Baryon acoustic oscillations. 15, 18, 149, 151, 154

BBN Big Bang nucleosynthesis. 17, 18, 151

CCHP Carnegie-Chicago Hubble Program. 18, 151

CMB cosmic microwave background. 8, 11, 17–19, 148–151, 154

COSMOGRAIL COSmological MOnitoring of GRAvItational Lenses. 31

CRTS Catalina Real-Time Transient Survey. 127

DEB detached eclipsing binaries. 19–21, 25

EPM expanding photosphere method. 2, 33, 44–50, 54, 92, 126–128, 133, 140–150, 152–154

FLRW Friedmann–Lemaître–Robertson–Walker. 8

GP Gaussian process. 92, 134, 153

H0LiCOW H_0 Lenses in COSMOGRAIL's Wellspring. 31, 151

HST Hubble Space Telescope. 6, 19, 21, 25

IAU International Astronomical Union. 5

iPTF intermediate Palomar Transient Factory. 127, 140

ISSP Italian Supernovae Search Project. 127

KDE kernel-density estimate. 148

LIRGs luminous infrared galaxies. 28

LMC Large Magellanic Cloud. 20–22, 24, 25

LSQ La Silla-QUEST. 127

LTE local thermodynamic equilibrium. 54, 153

MCP Megamaser Cosmology Project. 28, 141, 151

NLTE non-LTE. 42, 54, 153, 154

PCA principal component analysis. 92, 153

PTF Palomar Transient Factory. 127, 139

SBF surface brightness fluctuations. 6, 19, 28

SCM standardized candle method. 28, 128

SED spectral energy distribution. 36, 37, 39, 41, 42, 50, 139, 140

SH0ES Supernovae, H_0, for the Equation of State of Dark Energy. 17, 19, 20, 25, 151

SN supernova. 2, 3, 25, 29, 33–36, 45, 47–49, 92, 126, 127, 130, 131, 133, 134, 139–142, 148–150, 152–154

SNfactory Nearby Supernova Factory. 126–128, 133, 134, 154

SN Ia Type Ia supernova. 6, 13, 15, 17–20, 24–26, 31, 32, 126, 127, 152

SN II Type II supernova. 2, 3, 18, 28, 33–40, 42–51, 54, 92, 126–128, 130, 133, 152–154

TFR Tully–Fisher relation. 6, 19, 28

TRGB Tip of the Red Giant Branch. 18, 19, 28, 92, 151, 153

ULIRGs ultra-luminous infrared galaxies. 28

VLBI Very Long Baseline Interferometry. 21, 28

VLTI Very Large Interferometer array. 21

WMAP Wilkinson Microwave Anisotropy Probe. 17

ZTF Zwicky Transient Facility. 130, 131

Nomenclature

H_0 The Hubble constant. x, 2, 3, 5, 7, 14, 17–21, 25, 26, 28, 29, 31, 33, 47, 54, 92, 126, 127, 130, 133, 134, 140, 141, 148–152, 154

a The scale factor. 8, 9

c The speed of light. 9

H_2CO Formaldehyde. 26

H II Singly-ionized hydrogen. 5

H I Neutral hydrogen. 10

Lyα Lyman-α. 8

OH Hydroxyl. 26

Bibliography

Abbott, B. P., Abbott, R., Abbott, T. D., et al. 2017, Nature, 551, 85, [arXiv:1710.05835]

Abbott, D. C. & Lucy, L. B. 1985, ApJ, 288, 679

Abbott, T. M. C., Abdalla, F. B., Annis, J., et al. 2018, MNRAS, 480, 3879, [arXiv:1711.00403]

Adams, S. M., Kochanek, C. S., Gerke, J. R., & Stanek, K. Z. 2017a, MNRAS, 469, 1445, [arXiv:1610.02402]

Adams, S. M., Kochanek, C. S., Gerke, J. R., Stanek, K. Z., & Dai, X. 2017b, MNRAS, 468, 4968, [arXiv:1609.01283]

Addison, G. E., Watts, D. J., Bennett, C. L., et al. 2018, ApJ, 853, 119, [arXiv:1707.06547]

Adhikari, S. & Huterer, D. 2019, arXiv e-prints, arXiv:1905.02278, [arXiv:1905.02278]

Aldering, G., Adam, G., Antilogus, P., et al. 2002, Society of Photo-Optical Instrumentation Engineers (SPIE) Conference Series, Vol. 4836, Overview of the Nearby Supernova Factory, ed. J. A. Tyson & S. Wolff, 61–72

Aldering, G., Antilogus, P., Bailey, S., et al. 2006, ApJ, 650, 510, [arXiv:astro-ph/0606499]

Alexeyev, E. N., Alexeyeva, L. N., Krivosheina, I. V., & Volchenko, V. I. 1988, Physics Letters B, 205, 209

Anderson, J. P., González-Gaitán, S., Hamuy, M., et al. 2014, ApJ, 786, 67, [arXiv:1403.7091]

Anderson, J. P., Gutiérrez, C. P., Dessart, L., et al. 2016, A&A, 589, A110, [arXiv:1602.00011]

Anderson, R. I., Ekström, S., Georgy, C., Meynet, G., & Saio, H. 2017, in European Physical Journal Web of Conferences, Vol. 152, European Physical Journal Web of Conferences, 06002, [arXiv:1703.01338]

Andrade, E. N. D. C. 1950, Proceedings of the Royal Society of London Series A, 201, 439

Anguita, T., Schechter, P. L., Kuropatkin, N., et al. 2018, MNRAS, 480, 5017, [arXiv:1805.12151]

Arcavi, I. 2017, Hydrogen-Rich Core-Collapse Supernovae, ed. A. W. Alsabti & P. Murdin, 239

Arnett, W. D. 1966, Canadian Journal of Physics, 44, 2553

Arnett, W. D. 1980, ApJ, 237, 541

Asplund, M., Grevesse, N., Sauval, A. J., & Scott, P. 2009, ARA&A, 47, 481, [arXiv:0909.0948]

Aubourg, É., Bailey, S., Bautista, J. E., et al. 2015, Phys. Rev. D, 92, 123516, [arXiv:1411.1074]

Baade, W. 1926, Astronomische Nachrichten, 228, 359

Baade, W. 1954, IAU Trans., 8, 397

Baan, W. A., Guesten, R., & Haschick, A. D. 1986, ApJ, 305, 830

Baan, W. A., Wood, P. A. D., & Haschick, A. D. 1982, ApJ, 260, L49

Baes, M., Verstappen, J., De Looze, I., et al. 2011, ApJS, 196, 22, [arXiv:1108.5056]

Bailer-Jones, C. A. L., Irwin, M., & von Hippel, T. 1998, MNRAS, 298, 361, [arXiv:astro-ph/9803050]

Balázs, L. G., Bagoly, Z., Hakkila, J. E., et al. 2015, MNRAS, 452, 2236, [arXiv:1507.00675]

Baltay, C., Rabinowitz, D., Hadjiyska, E., et al. 2013, PASP, 125, 683

Barbon, R., Ciatti, F., & Rosino, L. 1979, A&A, 72, 287

Barna, B., Szalai, T., Kromer, M., et al. 2017, MNRAS, 471, 4865, [arXiv:1707.07848]

Baron, E., Branch, D., & Hauschildt, P. H. 2007, ApJ, 662, 1148, [arXiv:astro-ph/0703068]

Baron, E., Branch, D., Hauschildt, P. H., et al. 2000, ApJ, 545, 444, [arXiv:astro-ph/0010614]

Baron, E., Hauschildt, P. H., Branch, D., et al. 1995, ApJ, 441, 170

Baron, E., Hauschildt, P. H., Branch, D., Kirshner, R. P., & Filippenko, A. V. 1996a, MNRAS, 279, 799, [arXiv:astro-ph/9510070]

Baron, E., Hauschildt, P. H., & Mezzacappa, A. 1996b, MNRAS, 278, 763

Baron, E., Nugent, P. E., Branch, D., & Hauschildt, P. H. 2004, ApJ, 616, L91, [arXiv:astro-ph/0410153]

Beaton, R. L., Freedman, W. L., Madore, B. F., et al. 2016, ApJ, 832, 210, [arXiv:1604.01788]

Benedict, G. F., McArthur, B. E., Feast, M. W., et al. 2007, AJ, 133, 1810, [arXiv:astro-ph/0612465]

Bersten, M. C., Benvenuto, O., & Hamuy, M. 2011, ApJ, 729, 61, [arXiv:1101.0467]

Bessel, F. W. 1838a, Astronomische Nachrichten, 16, 65

Bessel, F. W. 1838b, MNRAS, 4, 152

Bessell, M. S. 1990, PASP, 102, 1181

Bessell, M. S. & Brett, J. M. 1988, PASP, 100, 1134

Betoule, M., Kessler, R., Guy, J., et al. 2014, A&A, 568, A22, [arXiv:1401.4064]

Bhardwaj, A., Kanbur, S. M., Macri, L. M., et al. 2016, MNRAS, 457, 1644, [arXiv:1601.00953]

Bionta, R. M., Blewitt, G., Bratton, C. B., et al. 1987, Phys. Rev. Lett., 58, 1494

Blinnikov, S. 2017, Interacting Supernovae: Spectra and Light Curves, ed. A. W. Alsabti & P. Murdin, 843

Blinnikov, S., Lundqvist, P., Bartunov, O., Nomoto, K., & Iwamoto, K. 2000, ApJ, 532, 1132, [arXiv:astro-ph/9911205]

Bonanos, A. Z., Stanek, K. Z., Kudritzki, R. P., et al. 2006, ApJ, 652, 313, [arXiv:astro-ph/0606279]

Bondi, H. 1947, MNRAS, 107, 410

Bongard, S., Soulez, F., Thiébaut, É., & Pecontal, É. 2011, MNRAS, 418, 258, [arXiv:1107.4049]

Bonvin, V., Courbin, F., Suyu, S. H., et al. 2017, MNRAS, 465, 4914, [arXiv:1607.01790]

Boyle, A., Sim, S. A., Hachinger, S., & Kerzendorf, W. 2017, A&A, 599, A46, [arXiv:1611.05938]

Branch, D., Falk, S. W., McCall, M. L., et al. 1981, ApJ, 244, 780

Bufano, F., Immler, S., Turatto, M., et al. 2009, ApJ, 700, 1456, [arXiv:0906.0367]

Bunn, E. F. & Hogg, D. W. 2009, American Journal of Physics, 77, 688, [arXiv:0808.1081]

Buton, C., Copin, Y., Aldering, G., et al. 2013, A&A, 549, A8, [arXiv:1210.2619]

Caputo, F. 2008, Mem. Soc. Astron. Italiana, 79, 453

Cardelli, J. A., Clayton, G. C., & Mathis, J. S. 1989, ApJ, 345, 245

Carrick, J., Turnbull, S. J., Lavaux, G., & Hudson, M. J. 2015, MNRAS, 450, 317, [arXiv:1504.04627]

Carter, L. & Cashwell, E. 1975, Particle-transport simulation with the Monte Carlo method, Tech. rep., Los Alamos National Laboratory (LANL), Los Alamos, NM

Castor, J. I. 1972, ApJ, 178, 779

Chambers, K. C., Magnier, E. A., Metcalfe, N., et al. 2016, arXiv e-prints, arXiv:1612.05560, [arXiv:1612.05560]

Chandrasekhar, S. 1960, Radiative transfer

Cheung, A. C., Rank, D. M., Townes, C. H., Thornton, D. D., & Welch, W. J. 1969, Nature, 221, 626

Chevalier, R. A. 1976, ApJ, 207, 872

Chevalier, R. A. 1982, ApJ, 259, 302

Chiosi, C. 1990, Astronomical Society of the Pacific Conference Series, Vol. 11, The evolution of the Cepheid stars., ed. C. Cacciari & G. Clementini, 158–192

Chodorowski, M. J. 2011, MNRAS, 413, 585, [arXiv:0911.3536]

Chornock, R., Filippenko, A. V., Li, W., & Silverman, J. M. 2010, ApJ, 713, 1363, [arXiv:0912.2465]

Ciardullo, R., Feldmeier, J. J., Jacoby, G. H., et al. 2002, ApJ, 577, 31, [arXiv:astro-ph/0206177]

Clowes, R. G., Harris, K. A., Raghunathan, S., et al. 2013, MNRAS, 429, 2910, [arXiv:1211.6256]

Coe, D. & Moustakas, L. A. 2009, ApJ, 706, 45, [arXiv:0906.4108]

Cole, S., Percival, W. J., Peacock, J. A., et al. 2005, MNRAS, 362, 505, [arXiv:astro-ph/0501174]

Colgate, S. A. & White, R. H. 1966, ApJ, 143, 626

Connolly, A. J., Szalay, A. S., Bershady, M. A., Kinney, A. L., & Calzetti, D. 1995, AJ, 110, 1071, [arXiv:astro-ph/9411044]

Courbin, F., Eigenbrod, A., Vuissoz, C., Meylan, G., & Magain, P. 2005, in IAU Symposium, Vol. 225, Gravitational Lensing Impact on Cosmology, ed. Y. Mellier & G. Meylan, 297–303

Cox, D. P. 2005, ARA&A, 43, 337

Cox, J. P. 1980, Theory of stellar pulsation

Czekala, I., Andrews, S. M., Mandel, K. S., Hogg, D. W., & Green, G. M. 2015, ApJ, 812, 128, [arXiv:1412.5177]

D'Andrea, C. B., Sako, M., Dilday, B., et al. 2010, ApJ, 708, 661, [arXiv:0910.5597]

Davies, B. & Dessart, L. 2019, MNRAS, 483, 887, [arXiv:1811.04087]

Davis, T. M. & Scrimgeour, M. I. 2014, MNRAS, 442, 1117, [arXiv:1405.0105]

de Jaeger, T., Galbany, L., Filippenko, A. V., et al. 2017, MNRAS, 472, 4233, [arXiv:1709.01513]

de Jaeger, T., González-Gaitán, S., Anderson, J. P., et al. 2015, ApJ, 815, 121, [arXiv:1511.05145]

de Jaeger, T., Zheng, W., Stahl, B. E., et al. 2019, MNRAS, 490, 2799, [arXiv:1909.13813]

Dere, K. P., Landi, E., Mason, H. E., Monsignori Fossi, B. C., & Young, P. R. 1997, A&AS, 125, 149

Dessart, L., Blondin, S., Brown, P. J., et al. 2008, ApJ, 675, 644, [arXiv:0711.1815]

Dessart, L. & Hillier, D. J. 2005a, A&A, 439, 671, [arXiv:astro-ph/0505465]

Dessart, L. & Hillier, D. J. 2005b, A&A, 437, 667, [arXiv:astro-ph/0504028]
Dessart, L. & Hillier, D. J. 2006, A&A, 447, 691, [arXiv:astro-ph/0510526]
Dessart, L. & Hillier, D. J. 2008, MNRAS, 383, 57, [arXiv:0710.0784]
Dessart, L. & Hillier, D. J. 2010, MNRAS, 405, 2141, [arXiv:1003.2557]
Dessart, L. & Hillier, D. J. 2011, MNRAS, 410, 1739, [arXiv:1008.3238]
Dessart, L., Hillier, D. J., Waldman, R., & Livne, E. 2013, MNRAS, 433, 1745, [arXiv:1305.3386]
Dewdney, P. E., Hall, P. J., Schilizzi, R. T., & Lazio, T. J. L. W. 2009, IEEE Proceedings, 97, 1482
Dhawan, S., Jha, S. W., & Leibundgut, B. 2018, A&A, 609, A72, [arXiv:1707.00715]
Di Valentino, E., Linder, E. V., & Melchiorri, A. r. 2018, Phys. Rev. D, 97, 043528, [arXiv:1710.02153]
Dodelson, S. 2003, Modern cosmology
Dos Santos, P. M. & Lepine, J. R. D. 1979, Nature, 278, 34
Drake, A. J., Djorgovski, S. G., Mahabal, A., et al. 2009, ApJ, 696, 870, [arXiv:0809.1394]
Dupree, S. A. & Fraley, S. K. 2002, A Monte Carlo Primer (New York: Kluwer Academic/Plenum Publishers)
Duschinger, M., Puls, J., Branch, D., Hoeflich, P., & Gabler, A. 1995, A&A, 297, 802
Eastman, R. G. & Kirshner, R. P. 1989, ApJ, 347, 771
Eastman, R. G. & Pinto, P. A. 1993, ApJ, 412, 731
Eastman, R. G., Schmidt, B. P., & Kirshner, R. 1996, ApJ, 466, 911
Eddington, A. S. 1923, The mathematical theory of relativity
Eddington, A. S. 1930, MNRAS, 90, 668
Edmunds, M. G. 2017, Supernovae and the Chemical Evolution of Galaxies, ed. A. W. Alsabti & P. Murdin, 2455
Efstathiou, G. 2014, MNRAS, 440, 1138, [arXiv:1311.3461]
Einstein, A. 1908, Jahrbuch der Radioaktivität und Elektronik, 4, 411
Einstein, A. 1915, Sitzungsberichte der Königlich Preußischen Akademie der Wissenschaften (Berlin), 844
Einstein, A. 1917, Sitzungsberichte der Königlich Preußischen Akademie der Wissenschaften (Berlin), 142
Eisenstein, D. J., Zehavi, I., Hogg, D. W., et al. 2005, ApJ, 633, 560, [arXiv:astro-ph/0501171]
Elias, J. H., Matthews, K., Neugebauer, G., & Persson, S. E. 1985, ApJ, 296, 379
Elias-Rosa, N., Van Dyk, S. D., Li, W., et al. 2010, ApJ, 714, L254, [arXiv:0912.2880]
Elias-Rosa, N., Van Dyk, S. D., Li, W., et al. 2011, ApJ, 742, 6, [arXiv:1108.2645]
Etherington, I. M. H. 1933, Philosophical Magazine, 15, 761
Faran, T., Goldfriend, T., Nakar, E., & Sari, R. 2019, ApJ, 879, 20, [arXiv:1905.00037]
Faran, T., Poznanski, D., Filippenko, A. V., et al. 2014a, MNRAS, 442, 844, [arXiv:1404.0378]
Faran, T., Poznanski, D., Filippenko, A. V., et al. 2014b, MNRAS, 445, 554, [arXiv:1409.1536]
Fassnacht, C. D., Gal, R. R., Lubin, L. M., et al. 2006, ApJ, 642, 30, [arXiv:astro-ph/0510728]

Fausnaugh, M. M., Kochanek, C. S., Gerke, J. R., et al. 2015, MNRAS, 450, 3597, [arXiv:1412.2138]
Feeney, S. M., Peiris, H. V., Williamson, A. R., et al. 2019, Phys. Rev. Lett., 122, 061105, [arXiv:1802.03404]
Fitzpatrick, E. L. 1999, PASP, 111, 63, [arXiv:astro-ph/9809387]
Fitzpatrick, E. L., Ribas, I., Guinan, E. F., et al. 2002, ApJ, 564, 260
Floers, A., Vogl, C., Taubenberger, S., et al. 2020, Transient Name Server AstroNote, 15, 1
Foglizzo, T. 2017, Explosion Physics of Core-Collapse Supernovae, ed. A. W. Alsabti & P. Murdin, 1053
Foreman-Mackey, D., Agol, E., Ambikasaran, S., & Angus, R. 2017, AJ, 154, 220, [arXiv:1703.09710]
Francis, P. J., Hewett, P. C., Foltz, C. B., & Chaffee, F. H. 1992, ApJ, 398, 476
Fraser, M., Takáts, K., Pastorello, A., et al. 2010, ApJ, 714, L280, [arXiv:0912.2071]
Freedman, W. L., Hughes, S. M., Madore, B. F., et al. 1994, ApJ, 427, 628
Freedman, W. L. & Madore, B. F. 2010, ARA&A, 48, 673, [arXiv:1004.1856]
Freedman, W. L., Madore, B. F., Gibson, B. K., et al. 2001, ApJ, 553, 47, [arXiv:astro-ph/0012376]
Freedman, W. L., Madore, B. F., Hatt, D., et al. 2019, ApJ, 882, 34, [arXiv:1907.05922]
Freedman, W. L., Madore, B. F., Scowcroft, V., et al. 2012, ApJ, 758, 24, [arXiv:1208.3281]
Friedmann, A. 1922, Zeitschrift fur Physik, 10, 377
Friedmann, A. 1924, Zeitschrift fur Physik, 21, 326
Gaia Collaboration, Brown, A. G. A., Vallenari, A., et al. 2018, A&A, 616, A1, [arXiv:1804.09365]
Gaia Collaboration, Prusti, T., de Bruijne, J. H. J., et al. 2016, A&A, 595, A1, [arXiv:1609.04153]
Gal-Yam, A. 2017, Observational and Physical Classification of Supernovae, ed. A. W. Alsabti & P. Murdin, 195
Gal-Yam, A., Kasliwal, M. M., Arcavi, I., et al. 2011, ApJ, 736, 159, [arXiv:1106.0400]
Galbany, L., Hamuy, M., Phillips, M. M., et al. 2016, AJ, 151, 33, [arXiv:1511.08402]
Gall, E. E. E., Kotak, R., Leibundgut, B., et al. 2016, A&A, 592, A129, [arXiv:1603.04730]
Gall, E. E. E., Kotak, R., Leibundgut, B., et al. 2018, A&A, 611, A25, [arXiv:1705.10806]
Gall, E. E. E., Polshaw, J., Kotak, R., et al. 2015, A&A, 582, A3, [arXiv:1502.06034]
Gao, F., Braatz, J. A., Reid, M. J., et al. 2016, ApJ, 817, 128, [arXiv:1511.08311]
Gerke, J. R., Kochanek, C. S., & Stanek, K. Z. 2015, MNRAS, 450, 3289, [arXiv:1411.1761]
Goldhaber, G., Deustua, S., Gabi, S., et al. 1997, in NATO Advanced Science Institutes (ASI) Series C, Vol. 486, NATO Advanced Science Institutes (ASI) Series C, ed. P. Ruiz-Lapuente, R. Canal, & J. Isern, 777, [arXiv:astro-ph/9602124]
González-Gaitán, S., Tominaga, N., Molina, J., et al. 2015, MNRAS, 451, 2212, [arXiv:1505.02988]
Goobar, A., Amanullah, R., Kulkarni, S. R., et al. 2017, Science, 356, 291, [arXiv:1611.00014]
Graziani, R., Courtois, H. M., Lavaux, G., et al. 2019, MNRAS, 488, 5438, [arXiv:1901.01818]
Grogin, N. A. & Narayan, R. 1996, ApJ, 464, 92
Guillochon, J., Parrent, J., Kelley, L. Z., & Margutti, R. 2017, ApJ, 835, 64, [arXiv:1605.01054]

Guinan, E. F., Fitzpatrick, E. L., DeWarf, L. E., et al. 1998, ApJ, 509, L21, [arXiv:astro-ph/9809132]

Gutiérrez, C. P., Anderson, J. P., Hamuy, M., et al. 2014, ApJ, 786, L15, [arXiv:1403.7089]

Gutiérrez, C. P., Anderson, J. P., Hamuy, M., et al. 2017a, ApJ, 850, 90, [arXiv:1709.02799]

Gutiérrez, C. P., Anderson, J. P., Hamuy, M., et al. 2017b, ApJ, 850, 89, [arXiv:1709.02487]

Guy, J., Astier, P., Baumont, S., et al. 2007, A&A, 466, 11, [arXiv:astro-ph/0701828]

Hachinger, S., Mazzali, P. A., Taubenberger, S., et al. 2012, MNRAS, 422, 70, [arXiv:1201.1506]

Hamuy, M. 2003, ApJ, 582, 905, [arXiv:astro-ph/0209174]

Hamuy, M. & Pinto, P. A. 2002, ApJ, 566, L63, [arXiv:astro-ph/0201279]

Hamuy, M., Pinto, P. A., Maza, J., et al. 2001, ApJ, 558, 615, [arXiv:astro-ph/0105006]

Hamuy, M. A. 2001, PhD thesis, The University of Arizona

Harrison, E. 2000, Cosmology: The Science of the Universe, 2nd edn. (Cambridge University Press)

Hauschildt, P. H., Best, M., & Wehrse, R. 1991, A&A, 247, L21

Heckman, T. M. & Thompson, T. A. 2017, Galactic Winds and the Role Played by Massive Stars, ed. A. W. Alsabti & P. Murdin, 2431

Heitmann, K., Higdon, D., White, M., et al. 2009, ApJ, 705, 156, [arXiv:0902.0429]

Heringer, E., van Kerkwijk, M. H., Sim, S. A., & Kerzendorf, W. E. 2017, ApJ, 846, 15

Herrnstein, J. R., Moran, J. M., Greenhill, L. J., et al. 1999, Nature, 400, 539, [arXiv:astro-ph/9907013]

Hershkowitz, S., Linder, E., & Wagoner, R. V. 1986a, ApJ, 303, 800

Hershkowitz, S., Linder, E., & Wagoner, R. V. 1986b, ApJ, 301, 220

Hershkowitz, S. & Wagoner, R. V. 1987, ApJ, 322, 967

Hicken, M., Friedman, A. S., Blondin, S., et al. 2017, ApJS, 233, 6, [arXiv:1706.01030]

Hillebrandt, W., Taubenberger, S., Floers, A., et al. 2020, Transient Name Server AstroNote, 25, 1

Hinshaw, G., Larson, D., Komatsu, E., et al. 2013, ApJS, 208, 19, [arXiv:1212.5226]

Hirata, K., Kajita, T., Koshiba, M., et al. 1987, Phys. Rev. Lett., 58, 1490

Hoflich, P. 1991, A&A, 246, 481

Hogg, D. W. 1999, arXiv e-prints, astro, [arXiv:astro-ph/9905116]

Hogg, D. W., Baldry, I. K., Blanton, M. R., & Eisenstein, D. J. 2002, arXiv e-prints, astro, [arXiv:astro-ph/0210394]

Hosseinzadeh, G., Valenti, S., McCully, C., et al. 2018, ApJ, 861, 63, [arXiv:1801.00015]

Hu, W. & Dodelson, S. 2002, ARA&A, 40, 171, [arXiv:astro-ph/0110414]

Huang, C. D., Riess, A. G., Yuan, W., et al. 2020, ApJ, 889, 5, [arXiv:1908.10883]

Hubble, E. 1929, Proceedings of the National Academy of Science, 15, 168

Hubble, E. & Humason, M. L. 1931, ApJ, 74, 43

Hubble, E. P. 1925a, Popular Astronomy, 33, 252

Hubble, E. P. 1925b, ApJ, 62, 409

Hubble, E. P. 1926, ApJ, 64, 321

Hubeny, I. & Mihalas, D. 2014, Theory of Stellar Atmospheres

Hügelmeyer, S. D., Dreizler, S., Werner, K., et al. 2007, in Astronomical Society of the Pacific Conference Series, Vol. 372, 15th European Workshop on White Dwarfs, ed. R. Napiwotzki & M. R. Burleigh, 249, [arXiv:astro-ph/0610746]

Humason, M. L., Mayall, N. U., & Sandage, A. R. 1956, AJ, 61, 97

Humphreys, E. M. L., Reid, M. J., Moran, J. M., Greenhill, L. J., & Argon, A. L. 2013, ApJ, 775, 13, [arXiv:1307.6031]

Hunter, J. D. 2007, Computing in Science and Engineering, 9, 90

Imshennik, V. S. & Nadezhin, D. K. 1988, Soviet Astronomy Letters, 14, 449

Janka, H.-T. 2017, Neutrino-Driven Explosions, ed. A. W. Alsabti & P. Murdin, 1095

Jee, I., Komatsu, E., & Suyu, S. H. 2015, J. Cosmology Astropart. Phys., 2015, 033, [arXiv:1410.7770]

Jeffery, D. J. 1995, ApJ, 440, 810

Jerkstrand, A., Fransson, C., Maguire, K., et al. 2012, A&A, 546, A28, [arXiv:1208.2183]

Jones, D. O., Riess, A. G., Scolnic, D. M., et al. 2018, ApJ, 867, 108, [arXiv:1805.05911]

Jones, D. O., Rodney, S. A., Riess, A. G., et al. 2013, ApJ, 768, 166, [arXiv:1304.0768]

Jones, E., Oliphant, T., Peterson, P., et al. 2001, SciPy: Open source scientific tools for Python

Jones, M. I., Hamuy, M., Lira, P., et al. 2009, ApJ, 696, 1176, [arXiv:0903.1460]

Kandrashoff, M., Fuller, K., Cenko, S. B., et al. 2012, Central Bureau Electronic Telegrams, 3121, 1

Kasen, D. & Woosley, S. E. 2009, ApJ, 703, 2205, [arXiv:0910.1590]

Kelly, P. L., Rodney, S. A., Treu, T., et al. 2015, Science, 347, 1123, [arXiv:1411.6009]

Kennicutt, R. C., J. 1984, ApJ, 277, 361

Kerzendorf, W., Nöbauer, U., Sim, S., et al. 2019, tardis-sn/tardis: TARDIS v3.0 alpha2

Kerzendorf, W. E. & Sim, S. A. 2014, MNRAS, 440, 387, [arXiv:1401.5469]

Khazov, D., Yaron, O., Gal-Yam, A., et al. 2016, ApJ, 818, 3, [arXiv:1512.00846]

Kirshner, R. P. 2004, Proceedings of the National Academy of Science, 101, 8

Kirshner, R. P. & Kwan, J. 1974, ApJ, 193, 27

Kochanek, C. S. 2019, arXiv e-prints, arXiv:1911.05083, [arXiv:1911.05083]

Koopmans, L. V. E., Treu, T., Fassnacht, C. D., Bland ford, R. D., & Surpi, G. 2003, ApJ, 599, 70, [arXiv:astro-ph/0306216]

Kowal, C. T. 1968, AJ, 73, 1021

Kreisch, C. D., Cyr-Racine, F.-Y., & Doré, O. 2019, arXiv e-prints, arXiv:1902.00534, [arXiv:1902.00534]

Kulkarni, S. R. 2013, The Astronomer's Telegram, 4807, 1

Kulkarni, S. R. 2018, The Astronomer's Telegram, 11266, 1

Kuo, C. Y., Braatz, J. A., Condon, J. J., et al. 2011, ApJ, 727, 20, [arXiv:1008.2146]

Kuo, C. Y., Braatz, J. A., Lo, K. Y., et al. 2015, ApJ, 800, 26, [arXiv:1411.5106]

Kuo, C. Y., Braatz, J. A., Reid, M. J., et al. 2013, ApJ, 767, 155, [arXiv:1207.7273]
Kurucz, R. L. & Bell, B. 1995, Atomic line list
Landi, E., Del Zanna, G., Young, P. R., Dere, K. P., & Mason, H. E. 2012, ApJ, 744, 99
Lantz, B., Aldering, G., Antilogus, P., et al. 2004, Society of Photo-Optical Instrumentation Engineers (SPIE) Conference Series, Vol. 5249, SNIFS: a wideband integral field spectrograph with microlens arrays, ed. L. Mazuray, P. J. Rogers, & R. Wartmann, 146–155
Law, N. M., Kulkarni, S. R., Dekany, R. G., et al. 2009, PASP, 121, 1395, [arXiv:0906.5350]
Le Fèvre, O., Amorin, R., Bardelli, S., et al. 2014, The Messenger, 155, 37
Leavitt, H. S. 1908, Annals of Harvard College Observatory, 60, 87
Leavitt, H. S. & Pickering, E. C. 1912, Harvard College Observatory Circular, 173, 1
Lee, G. K. H., Wood, K., Dobbs-Dixon, I., Rice, A., & Helling, C. 2017, A&A, 601, A22, [arXiv:1701.00983]
Lee, N. & Li, W. 2006, Central Bureau Electronic Telegrams, 660, 1
Léget, P. F., Pruzhinskaya, M. V., Ciulli, A., et al. 2018, A&A, 615, A162, [arXiv:1804.03418]
Leibundgut, B., Schommer, R., Phillips, M., et al. 1996, ApJ, 466, L21, [arXiv:astro-ph/9605134]
Leibundgut, B., Spyromilio, J., Vogl, C., et al. 2019, Transient Name Server AstroNote, 103, 1
Lemaître, G. 1927, Annales de la Société Scientifique de Bruxelles, 47, 49
Lentz, E. J., Baron, E., Branch, D., & Hauschildt, P. H. 2001, ApJ, 557, 266, [arXiv:astro-ph/0104225]
Leonard, D. C., Filippenko, A. V., Ardila, D. R., & Brotherton, M. S. 2001, ApJ, 553, 861, [arXiv:astro-ph/0009285]
Leonard, D. C., Filippenko, A. V., Ganeshalingam, M., et al. 2006, Nature, 440, 505, [arXiv:astro-ph/0603297]
Leonard, D. C., Filippenko, A. V., Gates, E. L., et al. 2002, PASP, 114, 35, [arXiv:astro-ph/0109535]
Leonard, D. C., Kanbur, S. M., Ngeow, C. C., & Tanvir, N. R. 2003, ApJ, 594, 247, [arXiv:astro-ph/0305259]
Levesque, E. M., Massey, P., Olsen, K. A. G., et al. 2005, ApJ, 628, 973, [arXiv:astro-ph/0504337]
Li, W., Leaman, J., Chornock, R., et al. 2011, MNRAS, 412, 1441, [arXiv:1006.4612]
Lietzau, S. 2017, Master's thesis, Technical University Munich
Linder, E. V. 2011, Phys. Rev. D, 84, 123529, [arXiv:1109.2592]
Litvinova, I. I. & Nadezhin, D. K. 1983, Ap&SS, 89, 89
Lo, K. Y. 2005, ARA&A, 43, 625
López-Corredoira, M., Allende Prieto, C., Garzón, F., et al. 2018, A&A, 612, L8, [arXiv:1804.03064]
Lucy, L. B. 1999a, A&A, 344, 282
Lucy, L. B. 1999b, A&A, 345, 211
Lucy, L. B. 2002, A&A, 384, 725, [arXiv:astro-ph/0107377]
Lucy, L. B. 2003, A&A, 403, 261, [arXiv:astro-ph/0303202]
Lundmark, K. 1924, MNRAS, 84, 747
Macaulay, E., Nichol, R. C., Bacon, D., et al. 2019, MNRAS, 486, 2184, [arXiv:1811.02376]

Madore, B. F. 1982, ApJ, 253, 575
Madore, B. F. & Freedman, W. L. 1991, PASP, 103, 933
Madore, B. F. & Freedman, W. L. 2012, ApJ, 744, 132, [arXiv:1111.6313]
Madore, B. F., Mager, V., & Freedman, W. L. 2009, ApJ, 690, 389, [arXiv:0809.2598]
Magee, M. R., Kotak, R., Sim, S. A., et al. 2016, A&A, 589, A89, [arXiv:1603.04728]
Magee, M. R., Kotak, R., Sim, S. A., et al. 2017, A&A, 601, A62, [arXiv:1701.05459]
Maguire, K. 2017, Type Ia Supernovae, ed. A. W. Alsabti & P. Murdin, 293
Mamajek, E. E. 2005, ApJ, 634, 1385, [arXiv:astro-ph/0507416]
Maoz, E., Newman, J. A., Ferrarese, L., et al. 1999, Nature, 401, 351
Matthews, T. A. & Sandage, A. R. 1963, ApJ, 138, 30
Mattila, S., Smartt, S., Maund, J., Benetti, S., & Ergon, M. 2010, arXiv e-prints, arXiv:1011.5494, [arXiv:1011.5494]
Maund, J. R., Fraser, M., Reilly, E., Ergon, M., & Mattila, S. 2015, MNRAS, 447, 3207
Mazzali, P. A. & Lucy, L. B. 1993, A&A, 279, 447
Mazzali, P. A., Sauer, D. N., Pastorello, A., Benetti, S., & Hillebrandt, W. 2008, MNRAS, 386, 1897, [arXiv:0803.1383]
McQuinn, K. B. W., Skillman, E. D., Dolphin, A. E., Berg, D., & Kennicutt, R. 2016, ApJ, 826, 21, [arXiv:1606.04120]
Mihalas, D. 1978, Stellar Atmospheres, 2nd edn. (San Francisco: W. H. Freeman and Co.), 632
Mihalas, D. & Mihalas, B. W. 1984, Foundations of radiation hydrodynamics, ed. Mihalas, D. & Mihalas, B. W.
Millon, M., Galan, A., Courbin, F., et al. 2019, arXiv e-prints, arXiv:1912.08027, [arXiv:1912.08027]
Milone, E. F., Stagg, C. R., & Kurucz, R. L. 1992, ApJS, 79, 123
Minkowski, R. 1941, PASP, 53, 224
Mitchell, R. C., Baron, E., Branch, D., et al. 2002, ApJ, 574, 293, [arXiv:astro-ph/0204012]
Mörtsell, E. & Dhawan, S. 2018, J. Cosmology Astropart. Phys., 2018, 025, [arXiv:1801.07260]
Mould, J. R., Huchra, J. P., Freedman, W. L., et al. 2000, ApJ, 529, 786, [arXiv:astro-ph/9909260]
Müller, B., Melson, T., Heger, A., & Janka, H.-T. 2017a, MNRAS, 472, 491, [arXiv:1705.00620]
Müller, T., Prieto, J. L., Pejcha, O., & Clocchiatti, A. 2017b, ApJ, 841, 127, [arXiv:1702.00416]
Murphy, K. P. 2012, Machine Learning: A Probabilistic Perspective (The MIT Press)
Nagao, T., Cikota, A., Patat, F., et al. 2019, MNRAS, 489, L69, [arXiv:1907.10505]
Niemela, V. S., Ruiz, M. T., & Phillips, M. M. 1985, ApJ, 289, 52
Nomoto, K. 1984, ApJ, 277, 791
Nomoto, K. & Leung, S.-C. 2017, Electron Capture Supernovae from Super Asymptotic Giant Branch Stars, ed. A. W. Alsabti & P. Murdin, 483
Nugent, P., Sullivan, M., Ellis, R., et al. 2006, ApJ, 645, 841, [arXiv:astro-ph/0603535]
Ofek, E. O., Arcavi, I., Tal, D., et al. 2014, ApJ, 788, 154, [arXiv:1404.4085]
Oke, J. B. & Sandage, A. 1968, ApJ, 154, 21
Oliphant, T. E. 2006, Guide to NumPy, Provo, UT

Oort, J. H. 1932, Bull. Astron. Inst. Netherlands, 6, 249

Osterbrock, D. E. 1974, Astrophysics of gaseous nebulae (San Francisco: W. H. Freeman and Co.)

Paczynski, B. 1997, in The Extragalactic Distance Scale, ed. M. Livio, M. Donahue, & N. Panagia, 273

Panagia, N., Gilmozzi, R., Macchetto, F., Adorf, H. M., & Kirshner, R. P. 1991, ApJ, 380, L23

Paraficz, D. & Hjorth, J. 2009, A&A, 507, L49, [arXiv:0910.5823]

Pastorello, A., Crockett, R. M., Martin, R., et al. 2009a, A&A, 500, 1013, [arXiv:0904.0637]

Pastorello, A., Sauer, D., Taubenberger, S., et al. 2006, MNRAS, 370, 1752, [arXiv:astro-ph/0605700]

Pastorello, A., Valenti, S., Zampieri, L., et al. 2009b, MNRAS, 394, 2266, [arXiv:0901.2075]

Patat, F., Barbon, R., Cappellaro, E., & Turatto, M. 1994, A&A, 282, 731

Peacock, J. A. 1999, Cosmological Physics

Peacock, J. A. 2008, arXiv e-prints, arXiv:0809.4573, [arXiv:0809.4573]

Pedregosa, F., Varoquaux, G., Gramfort, A., et al. 2011, Journal of Machine Learning Research, 12, 2825

Peebles, P. J. E. 1993, Principles of Physical Cosmology

Perlmutter, S., Aldering, G., Goldhaber, G., et al. 1999, ApJ, 517, 565, [arXiv:astro-ph/9812133]

Perlmutter, S. A., Deustua, S., Gabi, S., et al. 1997, in NATO Advanced Science Institutes (ASI) Series C, Vol. 486, NATO Advanced Science Institutes (ASI) Series C, ed. P. Ruiz-Lapuente, R. Canal, & J. Isern, 749, [arXiv:astro-ph/9602122]

Pesce, D. W., Braatz, J. A., Reid, M. J., et al. 2020, ApJ, 891, L1, [arXiv:2001.09213]

Phillips, M. M. 1993, ApJ, 413, L105

Phillips, M. M. & Burns, C. R. 2017, The Peak Luminosity - Decline Rate Relationship for Type Ia Supernovae, ed. A. W. Alsabti & P. Murdin, 2543

Phillips, M. M., Lira, P., Suntzeff, N. B., et al. 1999, AJ, 118, 1766, [arXiv:astro-ph/9907052]

Pietrzyński, G., Graczyk, D., Gallenne, A., et al. 2019, Nature, 567, 200, [arXiv:1903.08096]

Pistinner, S. & Shaviv, G. 1994, ApJ, 432, 302

Planck Collaboration, Ade, P. A. R., Aghanim, N., et al. 2014a, A&A, 571, A1, [arXiv:1303.5062]

Planck Collaboration, Ade, P. A. R., Aghanim, N., et al. 2014b, A&A, 571, A16, [arXiv:1303.5076]

Planck Collaboration, Aghanim, N., Akrami, Y., et al. 2018, arXiv e-prints, arXiv:1807.06209, [arXiv:1807.06209]

Polshaw, J., Kotak, R., Chambers, K. C., et al. 2015, A&A, 580, L15, [arXiv:1509.00507]

Popov, D. V. 1993, ApJ, 414, 712

Potashov, M. S., Blinnikov, S. I., & Utrobin, V. P. 2017, Astronomy Letters, 43, 36, [arXiv:1707.02177]

Poulin, V., Smith, T. L., Karwal, T., & Kamionkowski, M. 2019, Phys. Rev. Lett., 122, 221301, [arXiv:1811.04083]

Poznanski, D., Butler, N., Filippenko, A. V., et al. 2009, ApJ, 694, 1067, [arXiv:0810.4923]

Poznanski, D., Nugent, P. E., & Filippenko, A. V. 2010, ApJ, 721, 956, [arXiv:1008.0877]
Prantzos, N., Doom, C., Arnould, M., & de Loore, C. 1986, ApJ, 304, 695
Przybilla, N. & Butler, K. 2004, ApJ, 609, 1181, [arXiv:astro-ph/0406458]
Pskovskii, I. P. 1977, Soviet Ast., 21, 675
Pskovskii, Y. P. 1984, Soviet Ast., 28, 658
Quimby, R. M., Wheeler, J. C., Höflich, P., et al. 2007, ApJ, 666, 1093, [arXiv:0705.3478]
Rajpaul, V., Aigrain, S., Osborne, M. A., Reece, S., & Roberts, S. 2015, MNRAS, 452, 2269, [arXiv:1506.07304]
Rasmussen, C. E. & Williams, C. K. I. 2006, Gaussian Processes for Machine Learning (The MIT Press)
Refsdal, S. 1964, MNRAS, 128, 307
Refsdal, S. 1966, MNRAS, 134, 315
Reid, M. J., Braatz, J. A., Condon, J. J., et al. 2009, ApJ, 695, 287, [arXiv:0811.4345]
Reid, M. J., Braatz, J. A., Condon, J. J., et al. 2013, ApJ, 767, 154, [arXiv:1207.7292]
Reid, M. J. & Honma, M. 2014, ARA&A, 52, 339, [arXiv:1312.2871]
Ribas, I., Fitzpatrick, E. L., Maloney, F. P., Guinan, E. F., & Udalski, A. 2002, ApJ, 574, 771, [arXiv:astro-ph/0204061]
Ribas, I., Jordi, C., Vilardell, F., et al. 2005, ApJ, 635, L37, [arXiv:astro-ph/0511045]
Riess, A. G., Casertano, S., Yuan, W., et al. 2018a, ApJ, 855, 136, [arXiv:1801.01120]
Riess, A. G., Casertano, S., Yuan, W., et al. 2018b, ApJ, 861, 126, [arXiv:1804.10655]
Riess, A. G., Casertano, S., Yuan, W., Macri, L. M., & Scolnic, D. 2019, ApJ, 876, 85, [arXiv:1903.07603]
Riess, A. G., Filippenko, A. V., Challis, P., et al. 1998, AJ, 116, 1009, [arXiv:astro-ph/9805201]
Riess, A. G., Macri, L. M., Hoffmann, S. L., et al. 2016, ApJ, 826, 56, [arXiv:1604.01424]
Riess, A. G., Press, W. H., & Kirshner, R. P. 1996, ApJ, 473, 88, [arXiv:astro-ph/9604143]
Rigault, M., Aldering, G., Kowalski, M., et al. 2015, ApJ, 802, 20, [arXiv:1412.6501]
Rigault, M., Brinnel, V., Aldering, G., et al. 2018, arXiv e-prints, arXiv:1806.03849, [arXiv:1806.03849]
Rodney, S. A., Riess, A. G., Scolnic, D. M., et al. 2015, AJ, 150, 156
Rodríguez, Ó., Clocchiatti, A., & Hamuy, M. 2014, AJ, 148, 107, [arXiv:1409.3198]
Roman, M., Hardin, D., Betoule, M., et al. 2018, A&A, 615, A68, [arXiv:1706.07697]
Romaniello, M., Primas, F., Mottini, M., et al. 2008, A&A, 488, 731, [arXiv:0807.1196]
Rose, B. M., Garnavich, P. M., & Berg, M. A. 2019, ApJ, 874, 32, [arXiv:1902.01433]
Rubin, A., Gal-Yam, A., De Cia, A., et al. 2016, ApJ, 820, 33, [arXiv:1512.00733]
Ruel, J., Bazin, G., Bayliss, M., et al. 2014, ApJ, 792, 45, [arXiv:1311.4953]
Rust, B. W. 1974, PhD thesis, Oak Ridge National Lab., TN.
Samtleben, D., Staggs, S., & Winstein, B. 2007, Annual Review of Nuclear and Particle Science, 57, 245, [arXiv:0803.0834]
Sandage, A. 1958, ApJ, 127, 513

Sandage, A. 1964, ApJ, 139, 416
Sanders, N. E., Soderberg, A. M., Gezari, S., et al. 2015, ApJ, 799, 208, [arXiv:1404.2004]
Sarangi, A., Matsuura, M., & Micelotta, E. R. 2018, Space Sci. Rev., 214, 63
Sasdelli, M., Hillebrandt, W., Aldering, G., et al. 2015, MNRAS, 447, 1247, [arXiv:1411.4424]
Sasdelli, M., Ishida, E. E. O., Vilalta, R., et al. 2016, MNRAS, 461, 2044, [arXiv:1512.06810]
Savitzky, A. & Golay, M. J. E. 1964, Analytical Chemistry, 36, 1627
Scalzo, R. A., Aldering, G., Antilogus, P., et al. 2010, ApJ, 713, 1073, [arXiv:1003.2217]
Schlafly, E. F. & Finkbeiner, D. P. 2011, ApJ, 737, 103, [arXiv:1012.4804]
Schmidt, B. P., Kirshner, R. P., & Eastman, R. G. 1992, ApJ, 395, 366, [arXiv:astro-ph/9204004]
Schmidt, B. P., Kirshner, R. P., Eastman, R. G., et al. 1994, ApJ, 432, 42
Schmidt, M. 1963, Nature, 197, 1040
Schmutz, W., Abbott, D. C., Russell, R. S., Hamann, W. R., & Wessolowski, U. 1990, ApJ, 355, 255
Scott, D. W. 1992, Multivariate Density Estimation
Seaton, M. J. 1962, in Atomic and Molecular Processes, ed. D. R. Bates (New York: Academic Press), 375
Shapiro, P. R. & Sutherland, P. G. 1982, ApJ, 263, 902
Shussman, T., Waldman, R., & Nakar, E. 2016, arXiv e-prints, arXiv:1610.05323, [arXiv:1610.05323]
Sim, S. A. 2017, Spectra of Supernovae During the Photospheric Phase, ed. A. W. Alsabti & P. Murdin, 769
Sim, S. A., Drew, J. E., & Long, K. S. 2005, MNRAS, 363, 615, [arXiv:astro-ph/0508103]
Slipher, V. M. 1913, Lowell Observatory Bulletin, 1, 56
Slipher, V. M. 1915, Popular Astronomy, 23, 21
Slipher, V. M. 1917, Proceedings of the American Philosophical Society, 56, 403
Slipher, V. M. 1921, Popular Astronomy, 29, 128
Smartt, S. J. 2009, ARA&A, 47, 63, [arXiv:0908.0700]
Smartt, S. J. 2015, Publications of the Astron. Soc. of Australia, 32, e016, [arXiv:1504.02635]
Smartt, S. J., Valenti, S., Fraser, M., et al. 2015, A&A, 579, A40, [arXiv:1411.0299]
Soares-Santos, M., Palmese, A., Hartley, W., et al. 2019, ApJ, 876, L7, [arXiv:1901.01540]
Sobolev, V. V. 1957, Soviet Ast., 1, 678
Söderhjelm, S. 1999, A&A, 341, 121
Sorce, J. G., Tully, R. B., Courtois, H. M., et al. 2014, MNRAS, 444, 527, [arXiv:1408.0729]
Spiro, S., Pastorello, A., Pumo, M. L., et al. 2014, MNRAS, 439, 2873, [arXiv:1401.5426]
Staggs, S., Dunkley, J., & Page, L. 2018, Reports on Progress in Physics, 81, 044901
Stehle, M., Mazzali, P. A., Benetti, S., & Hillebrandt, W. 2005, MNRAS, 360, 1231, [arXiv:astro-ph/0409342]
Stein, M. 1987, Technometrics, 29, 143
Steinacker, J., Baes, M., & Gordon, K. D. 2013, ARA&A, 51, 63, [arXiv:1303.4998]

Stromberg, G. 1925, ApJ, 61, 353
Sukhbold, T. & Adams, S. 2019, arXiv e-prints, arXiv:1905.00474, [arXiv:1905.00474]
Sukhbold, T., Ertl, T., Woosley, S. E., Brown, J. M., & Janka, H. T. 2016, ApJ, 821, 38, [arXiv:1510.04643]
Suyu, S. H., Auger, M. W., Hilbert, S., et al. 2013, ApJ, 766, 70, [arXiv:1208.6010]
Suyu, S. H., Bonvin, V., Courbin, F., et al. 2017, MNRAS, 468, 2590, [arXiv:1607.00017]
Taddia, F., Sollerman, J., Fremling, C., et al. 2016, A&A, 588, A5
Takáts, K. & Vinkó, J. 2006, MNRAS, 372, 1735, [arXiv:astro-ph/0608430]
Takeda, Y. 1990, A&A, 234, 343
Takeda, Y. 1991, A&A, 245, 182
Tatischeff, V. & Gabici, S. 2018, Annual Review of Nuclear and Particle Science, 68, 377, [arXiv:1803.01794]
Taubenberger, S. 2017, The Extremes of Thermonuclear Supernovae, ed. A. W. Alsabti & P. Murdin, 317
Taubenberger, S., Suyu, S. H., Komatsu, E., et al. 2019, A&A, 628, L7, [arXiv:1905.12496]
Tipping, M. E. & Bishop, C. M. 1999, Journal of the Royal Statistical Society: Series B (Statistical Methodology), 61, 611
Tonry, J. L., Denneau, L., Heinze, A. N., et al. 2018, PASP, 130, 064505, [arXiv:1802.00879]
Tonry, J. L., Dressler, A., Blakeslee, J. P., et al. 2001, ApJ, 546, 681, [arXiv:astro-ph/0011223]
Treu, T. & Marshall, P. J. 2016, A&A Rev., 24, 11, [arXiv:1605.05333]
Tripp, R. 1998, A&A, 331, 815
Troxel, M. A., MacCrann, N., Zuntz, J., et al. 2018, Phys. Rev. D, 98, 043528, [arXiv:1708.01538]
Tsvetkov, D. Y., Volnova, A. A., Shulga, A. P., et al. 2006, A&A, 460, 769, [arXiv:astro-ph/0605184]
Tully, R. B., Courtois, H., Hoffman, Y., & Pomarède, D. 2014, Nature, 513, 71, [arXiv:1409.0880]
Turatto, M. 2003, Classification of Supernovae, ed. K. Weiler, Vol. 598, 21–36
Turner, D. G., Abdel-Sabour Abdel-Latif, M., & Berdnikov, L. N. 2006, PASP, 118, 410, [arXiv:astro-ph/0601687]
Ugliano, M., Janka, H.-T., Marek, A., & Arcones, A. 2012, ApJ, 757, 69, [arXiv:1205.3657]
Utrobin, V. P. & Chugai, N. N. 2005, A&A, 441, 271, [arXiv:astro-ph/0501036]
Valenti, S., Howell, D. A., Stritzinger, M. D., et al. 2016, MNRAS, 459, 3939, [arXiv:1603.08953]
Valenti, S., Sand, D., Stritzinger, M., et al. 2015, MNRAS, 448, 2608, [arXiv:1501.06491]
Van Dyk, S. D. 2017, Supernova Progenitors Observed with HST, ed. A. W. Alsabti & P. Murdin, 693
van Regemorter, H. 1962, ApJ, 136, 906
Verde, L., Treu, T., & Riess, A. G. 2019, Nature Astronomy, 3, 891, [arXiv:1907.10625]
Vogl, C. 2016, Master's thesis, Technical University Munich
Vogl, C., Sim, S. A., Noebauer, U. M., Kerzendorf, W. E., & Hillebrandt, W. 2019, A&A, 621, A29, [arXiv:1811.02543]
Wagoner, R. V. 1981, ApJ, 250, L65

Walsh, D., Carswell, R. F., & Weymann, R. J. 1979, Nature, 279, 381

Wang, L. & Wheeler, J. C. 2008, ARA&A, 46, 433, [arXiv:0811.1054]

Watson, D., Hansen, C. J., Selsing, J., et al. 2019, Nature, 574, 497, [arXiv:1910.10510]

Weaver, H., Williams, D. R. W., Dieter, N. H., & Lum, W. T. 1965, Nature, 208, 29

Wesselink, A. J. 1946, Bull. Astron. Inst. Netherlands, 10, 91

Williamson, M., Modjaz, M., & Bianco, F. B. 2019, ApJ, 880, L22, [arXiv:1903.06815]

Wong, K. C., Suyu, S. H., Chen, G. C. F., et al. 2019, arXiv e-prints, arXiv:1907.04869, [arXiv:1907.04869]

Wood, K. & Reynolds, R. J. 1999, ApJ, 525, 799, [arXiv:astro-ph/9905289]

Wood-Vasey, W. M., Aldering, G., Nugent, P., Mulchaey, J., & Phillips, M. 2003, IAU Circ., 8088, 2

Yaron, O. & Gal-Yam, A. 2012, PASP, 124, 668, [arXiv:1204.1891]

Yaron, O., Perley, D. A., Gal-Yam, A., et al. 2017, Nature Physics, 13, 510, [arXiv:1701.02596]

Yip, C. W., Connolly, A. J., Vanden Berk, D. E., et al. 2004, AJ, 128, 2603, [arXiv:astro-ph/0408578]

Young, T. R. 2004, ApJ, 617, 1233, [arXiv:astro-ph/0409284]

Yusef-Zadeh, F., Morris, M., & White, R. L. 1984, ApJ, 278, 186

Kramida, A., Yu. Ralchenko, Reader, J., & and NIST ASD Team. 2019, NIST Atomic Spectra Database (ver. 5.7.1), [Online]. Available: `http://physics.nist.gov/asd` [Tue Nov 05 2019]. National Institute of Standards and Technology, Gaithersburg, MD. DOI: `https://doi.org/10.18434/T4W30F`